## Title

Synthesis, Characterization, and Fabrication of Boron Nitride and Carbon Nanomaterials, their Applications, and the Extended Pressure Inductively Coupled Plasma Synthesis of Boron Nitride Nanotubes



## Author

Fathalizadeh, Aidin

## Publication Date

2016

Peer reviewed|Thesis/dissertation

# Synthesis, Characterization, and Fabrication of Boron Nitride and Carbon Nanomaterials, their Applications, and the Extended Pressure Inductively Coupled Plasma Synthesis of Boron Nitride Nanotubes

by

Aidin Fathalizadeh

A dissertation submitted in partial satisfaction of the

requirements for the degree of

Doctor of Philosophy

in

Physics

in the

Graduate Division

of the

University of California, Berkeley

Committee in charge:

Professor Alex K. Zettl, Chair

Professor Michael F. Crommie

Professor Liwei Lin

Spring 2016

Synthesis, Characterization, and Fabrication of Boron Nitride and Carbon Nanomaterials, their Applications, and the Extended Pressure Inductively Coupled Plasma Synthesis of Boron Nitride Nanotubes



Aidin Fathalizadeh

Abstract

Synthesis, Characterization, and Fabrication of Boron Nitride and Carbon Nanomaterials, their Applications, and the Extended Pressure Inductively Coupled Plasma Synthesis of Boron Nitride Nanotubes

by

Aidin Fathalizadeh

Doctor of Philosophy in Physics

University of California, Berkeley

Professor Alex K. Zettl, Chair

Nanoscale materials made of carbon, boron, and nitrogen, namely BCN nanostructures, exhibit many remarkable properties making them uniquely suitable for a host of applications. Boron nitride (BN) and carbon (C) nanomaterials are structurally similar. The forms studied here originate from a two-dimensional hexagonally arranged structure of $sp^2$ bonded atoms. These nanomaterials exhibit extraordinary mechanical and thermal properties. However, the unique chemical compositions of carbon and boron nitride result in differing electrical, chemical, biological, and optical properties. In this work, we explore the single layer sheets of $sp^2$ bonded carbon (graphene), and their cylindrical forms (nanotubes) of carbon and boron nitride.

In the first part of this work, we look at carbon based nanomaterials. In Chapter 2, the electron field emission properties of carbon nanotubes (CNTs) and their implementation as nanoelectromechanical oscillators in an integrated device will be discussed. We show a technique hereby a single CNT is attached to a probe tip and its electron field emission characterized. We then delve into the fabrication of a field emitting CNT oscillator based integrated device using a silicon nitride membrane support. We then present the electron field emission capabilities of these devices and discuss their potential use for detection of nuclear magnetic resonance (NMR) signals.

Graphene is the subject of study in Chapter 3. We begin by extensively examining the synthesis of graphene using a chemical vapor deposition (CVD) process, ultimately establishing techniques to control graphene domain size, shape, and number of layers. We then discuss the application of the single-atom thick, but ultra-mechanically strong graphene as a capping layer to trap solutions in a custom fabricated silicon nitride membrane to enable transmission electron microscopy (TEM) of liquid environments. In this manner, the volume and position of liquid cells

for electron microscopy can be precisely controlled and enable atomic resolution of encapsulated particles.

In the second portion of this work, we investigate boron nitride nanostructures and in particular nanotubes. In Chapter 4, we present the successful development and operation of a high-throughput, scalable BN nanostructures synthesis process whereby precursor materials are directly and continuously injected into a novel high-temperature, *Extended-Pressure Inductively-Coupled* plasma system (EPIC). The system can be operated in a near-continuous fashion and has a record output of over 35 g/hour for pure, highly crystalline boron nitride nanotubes (BNNTs). We also report the results of numerous runs exploring the wide range of operating parameters capable with the EPIC system.

In Chapter 5, we examine the impurities present in as-synthesized BNNT materials. Several methods of sample purification are then investigated. These include chemical oxidation, using both gas and liquid phase based methods, as well as physical separation techniques.

The large scale synthesis of BNNTs has opened the door for further studies and applications. In Chapter 6, we report a novel wet-chemistry based route to fill in the inner cores of BNNTs with metals. For the first time, various metals are loaded inside of BNNTs, forming a plethora of structures (such as rods, short nanocrystals, and nanowires), using a solution-based method. We are also able to initiate and observe dynamics of the metallic nanoparticles, including their movement, splitting, and fusing, within a BNNT.

# To آنا and آتا

# Contents

# List of Figures

# Acknowledgments

I am forever grateful to many who have played a critical role during my journey through graduate school. Foremost among them is my teacher and advisor Alex Zettl. You gave a young student a challenge and let him run with it. The space you have shaped nurtures independent innovation, at the same time fostering collaboration among such diverse and welcoming colleagues, making the lab a genuinely creative and enjoyable experience. Thank you for believing in me, guiding me, and allowing me the freedom to play, learn, grow, and fly.

I thank the other members of my dissertation committee, Professor Mike Crommie and Professor Liwei Lin, for taking the time to read through and offering words of encouragement on this work. I must also thank them alongside Professor Steven Louie for serving on my qualifying exam committee and motivating me to strengthen my knowledge of the fundamentals.

I am grateful for all of the assistance and seemingly unending levels of bureaucracy that Gee Gee Lang and Laura King have had to navigate over the years. Your hard work and selfless attitude day in and day out make everything we do in the lab possible. Anne Takizawa, Donna Sakima, and Claudia Trujillo, you all have been a bedrock of support for me since I first started at Berkeley and I thank you for the immense service you do to keep the entire department afloat.

Over the course of the last few years, the friends and colleagues I have had the privilege to work with in the Zettl group became something of a second family for me. I am grateful to my partner in crime, Thang Pham, I hold our friendship dear and appreciate our many collaborations in the lab or at the gym. You've grown to become an exemplary scientist and scholar. The many hours we worked side-by-side on EPIC will remain one of the highlights of my grad student career, times that I will always cherish. Here's to many more victory celebrations over root beers. To Willi Mickelson, for your mentorship, guidance, and scientific rigor. Thank you for always inspiring us to aim high and work hard. You taught me to be about that action, boss! To Oscar Vazquez Mena, for the invigorating political discussions, the hours of laughs, and for being the admirable model of a passionate scientist dedicated to service. Keep running, keep dancing. To Haider Rasool, for the many ruminations on life and the guidance you've given me in and outside the lab. Your friendship is treasured, your honesty appreciated, your openness praiseworthy. To my mentee, Harvey Vazquez, whose energetic youthfulness proved contagious. You'll soar high. To Seita Onishi, with whom I first collaborated, experiencing the value of teamwork. Thank you for sharing a desk, your stories, and gymnastics tips with me. To Benji Alemán; your intelligence, compassion, and direction lead me to embark on this journey with

the Zettl group. You are a natural born leader and teacher. To Michael Rousseas. Thank you for showing me the ropes early on, the numerous BN pow wows, and doing the heavy lifting. You have a heart of gold. To Hamid Barzegar. You are a trusting companion and clever colleague; thank you for your insight and illuminating advice. To Ashley Gibb; bright and benevolent, it was always a joy catching up with you. You serve as the glue to keep generations of Zettlites in touch. To Sally Turner, the young prizefighter whose ascent will surely shake up the world. Stay fierce. To Gabe Dunn; your big heart and BBQs kept my soul and stomach well nurtured. To Matt Gilbert. The dedication you have for your craft is sincerely commendable. Keep knocking those doors down. To Brian Shevitski, for being genuine and colorful. To Jong Min Yuk, thank you for exchanging ideas, TEM expertise, and exuding happiness everywhere you go. To Jairo Velasco Jr., for showing me patience and teaching me about the STM. Once you are world famous, I'll be able to say I knew you back when. To Aiming Yan, whose work ethic is truly motivating. To Onur Ergen, for dreaming big and pushing boundaries. To Claudia Ojeda-Aristizabal, so sharp and so kind; your presence immediately brightens up the room. To Jiyoung "the Juiceman" Chang, for elevating 105 Birge to the status of legendary; your financial advice are gems. To Qin Zhou, your curiosity knows no bounds, your stories keep us rolling on the floor laughing. Climb on. To Kris Erickson, for keeping the lab hyped up with your radiant spirit and electronic dance music. To Anna Zaniewski, for getting me excited about teaching again and leading by example, be it in the lab or through Compass. To Vivek Adiga, for your honesty and realness. To Anna Goldstein, my fellow Carolina tarheel. To Allen Sussman, for the many antics and keeping the workplace cool. To Will Regan, your wisdom always appreciated. To Will Gannett, my sailing buddy *par-excellence*. To Nasim Alem, for your unrelenting support. To the all the rest of my Zettl family, Gerard Leyva, Kwanpyo Kim, Maria Schriver, Zhengzong Sun, Jian Hao Chen, Waqas Khalid, Mehdi Jamei, Matthias Loster, Wu Shi, and collaborators Shaul Aloni, Christophe Goze-Bac, and Mohamad Akel. It's been a great honor and a lot of fun.

This incredible voyage would not have been possible without the support of countless friends and family outside the department as well. To all of the amazing, free-spirited, creative, loving, quirky, intelligent, caring, passionate, life-long compañeros I've been blessed to live with in the co-ops at Rochdale and HIP House. Too many to list here, thank you for the countless kitchen table discussions, epic adventures, and persistent encouragement.

Most important of all, I must thank my family for being the spring which has brought me to life and nourished me ever since. To my parents for having the courage and strength to leave your families and the only lives you had ever known to come to a foreign land with two little kids and struggle for years in the hopes of a

better future for your son and daughter. Thank you for the sacrifices, for teaching me to question and be inquisitive, and for loving me endlessly. To my sister, Dr. Alisan Fathalizadeh, for always caring and being available. You are a true inspiration to me and a beacon of light for all of the lives you touch. To my family back home in Tabriz and Khoy, those still with us and the loved ones who've moved on; though we are far, I carry you all in my heart and I feel you lift me higher every day.

# Chapter 1

# Introduction

The graphite of pencil lead we use daily to sketch a drawing or compose a poem couldn't be more different in appearance and function than the precious diamonds of gems so valued and gifted to loved-ones. Yet they are both composed of just pure carbon. The former is soft and darker in color than the extremely hard and optically transparent diamond. Graphite is a semimetal with zero energy bandgap whereas diamonds are insulating. As we shall see, the fundamental differences between these two carbon materials originate in their distinct bonding structures.

Many of the remarkable properties that nanoscale materials made of carbon, boron, and nitrogen, namely the $B_xC_yN_z$ nanostructures explored throughout this work, originate from the 2D hexagonal network of $sp^2$ bonded atoms. We begin by first briefly exploring carbon and its various allotropes formed from various bonding structures. We then introduce several boron nitride structures which share many similar morphologies and configurations as their carbon counterparts. Key differences are also underscored. Through this background, we hope to introduce the materials which are the subjects of our investigations and in doing so, highlight the key aspects of these materials, such as electron field emission or synthesis of, which are the focus of the research efforts presented in the ensuing chapters of this work.

## 1.1 Carbon

With an atomic number of 6, the electronic configuration of the ground state of a carbon atom is given as $1s^2 2s^2 2p^2$. It contains 4 valence electrons which can organize to form several different types of carbon-carbon bonds. In particular, the 2s and 2p atomic orbitals are relatively close enough in energy that they can mix to

form new hybrid orbitals during bond formation. During this process of hybridization, the hybrid orbitals take on new shapes and energies relative to the separate atomic orbitals. In general, the mixing of one 's' orbital with *n* number of 'p' orbitals results in $sp^n$ hybridization, where $n$ = 1, 2, or 3.

### 1.1.1 $sp^3$ Hybridization

The ground state of carbon has 2 paired electrons in its 2s orbital and 2 unpaired electrons in its p orbitals. In a crystal of diamond, the three 2p orbitals will combine with the 2s orbital to form four hybridized "$sp^3$" orbitals. In such a hybridized bonding structure, each carbon atom will form four bonds at 109° with respect to other bonds in a tetrahedral geometry. The strong covalent bonding of carbon atoms with four other carbon atoms to form an interconnected 3D network leads to the extreme hardness of diamonds.

### 1.1.2 $sp^2$ Hybridization

In graphite, the 2s orbital will combine with only two of the 2p orbitals of the carbon atom to form three hybridized "$sp^2$" orbitals. One 2p orbital remains unhybridized and forms a π-bond perpendicular to the trigonal planar geometry of the three $sp^2$ hybrid orbitals. The very strong in-plane bonds of the electrons in the $sp^2$ orbitals form σ-bonds at 120° with respect to one another. The electrical conductivity of graphite is due to the delocalization of the 2p electrons, whereas no free electrons are leftover in the carbon bonding scheme of the insulating diamond structure. Furthermore, the $sp^2$ C-C bonds of graphite are much stronger than the $sp^3$ bonds in diamonds.

The bonding of each carbon atom with three others at a uniform bond angle of 120° in-plane creates a single layer crystal lattice consisting of carbon atoms in a hexagonal arrangement, as depicted in Figure 1.1a. The 2D single layer hexagonal network of carbon atoms is called graphene and the stacking of multiple graphene sheets atop one another forms the 3D bulk graphite. As illustrated in Figure 1.1b, the graphitic sheets are typically stacked in an *ABAB* configuration where carbon atoms in adjacent layers are shifted and are not simply loaded atop one another. Such a scheme is referred to as Bernal stacking. The in-plane distance between nearest neighbor carbon atoms, $a_{c\text{-}c}$, the in-plane lattice constant which refers to the distance between alternative carbon atoms, $a_o$, and the c-axis lattice constant which is the distance between two alternative graphene sheets, $c_o$, are presented in Figure 1.1. The interlayer spacing between adjacent graphene sheets is given as $c_o/2$ = 3.35 Å. The graphitic sheets are held together by weak van der Waals forces, which is why

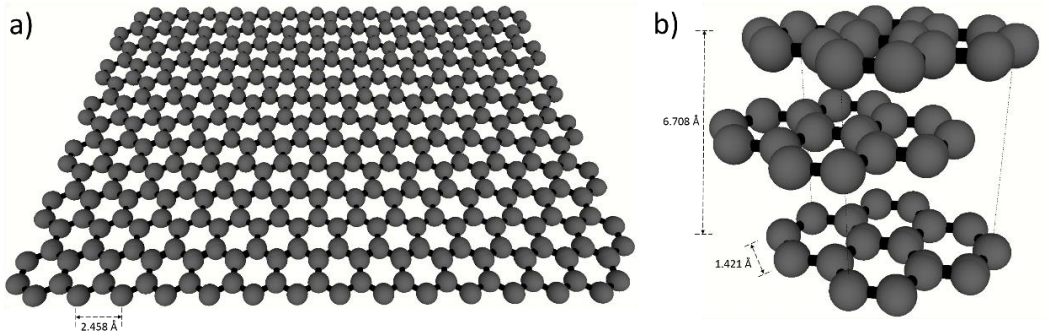


Figure 1.1: Graphene lattice structure as (a) a monolayer and (b) Bernal stacked.

this material is soft and easy to split apart, as is done when a pencil's lead is sheared across a piece of paper in drawing a line.

### 1.1.3 sp Hybridization

In some molecules, such as the hydrocarbon acetylene ($C_2H_2$), the 2s orbital of a carbon atom will mix with only one 2p orbital to yield two "sp" hybrid orbitals oriented at a bond angle of 180°, i.e. in a linear arrangement. The two remaining 2p orbitals will maintain their perpendicular orientation with respect to the linear molecule. The electrons of the 2p orbitals which are not part of the sp hybridized orbital will bond with the respective electrons of the 2p orbitals of the other carbon atom. The linearly bond carbon atoms will be held together by three bonds, a single σ-bond and two π-bonds. The C-C bond dissociation energy of $sp^3$ hybridized C in diamonds is 347 kj/mol, that of $sp^2$ C in graphene is 480 kj/mol, and that of sp hybridized C in acetylene is 835 kJ/mol. Their respective bond lengths are 1.54 Å, 1.42 Å, and 1.20 Å.

### 1.1.4 $C_{60}$

Allotropes of $sp^2$ bonded carbon exist in addition to graphene discussed above. Early studies were focused on molecules of carbon arranged to form hollow spheres, aptly named Buckminsterfullerene or "Bucky balls" in light of their resemblance to the geodesic dome structures of Buckminster Fuller. Consisting of 60 $sp^2$ bonded carbon atoms arranged like a soccer ball with C atoms positioned at the corner of 12 pentagons and 20 hexagons, the molecule is also called $C_{60}$. The van der Walls diameter of $C_{60}$ molecule is ~1nm. First investigated in 1985, Harold Kroto,

Robert Curl, and Richard Smalley were later awarded the 1996 Nobel Prize in Chemistry for their roles in the discovery of fullerenes.

### 1.1.5 Carbon Nanotubes

Carbon nanotubes (CNTs) are the nanoscale hollow cylindrical structures obtained from the rolling of graphene or graphitic sheets. They can either be single-walled (SWCNTs) or multiwalled (MWCNTs) depending on whether the nanotube is made up of one or several coaxial graphene shells. Attempting to produce fullerenes, carbon nanotubes were recognized as such in 1991 in the carbonaceous soot of graphite electrodes subjected to an arc-discharge[1].

CNTS are primarily characterized by their lengths, diameters, wall crystallinity, and the manner in which they are rolled. This last classification is referred to as chirality and can be visualized in the case of a SWCNT by imagining a single graphene sheet which can be rolled up along in a number of manners to obtain different tube axes. As depicted in Figure 1.2a, $a_1$ and $a_1$ are the unit vectors of graphene in real space from which any other lattice point can be obtained as a linear combination of $a_1$ and $a_2$. A SWCNT is described by its chiral vector, written as $C_h = na_1+ma_2$, where $n$ and $m$ are integers and oftentimes expressed as $(n,m)$ for short. The chiral vector points in a direction on the graphene sheet which is perpendicular to the axis of the nanotube it describes with a magnitude that spans the circumference of the nanotube. Hence the magnitude of the circumference of the nanotube is $|C_h|=a(n^2+m^2+nm)^{½}$ where $a$ is the length of the basis vectors, which for graphene is 2.46 Å. The nanotube diameter is then given by $d = C_h/\pi$. The chiral angle of the tube is defined as $\theta = \sin^{-1}\left(\frac{m\sqrt{3}}{2n+m}\right)$. A nanotube that is rolled up along the direction of $a_1$ so that the points (0,0) and $(n,0)$ will be together will form a "zigzag" nanotube as the two ends of the tube will have zigzag-shaped edge terminations. The CNT of Figure 1.2b is a (14,0) zigzag nanotube. If the graphene sheet is rolled so that the point (0,0) coincides with a point $(n,n)$, then the nanotube edges will have an armchair-shaped termination and are called "armchair" nanotubes. The chiral angles of zigzag and armchair nanotubes are 0° and 30° respectively. Nanotubes that are neither zigzag nor armchair are referred to as "chiral".

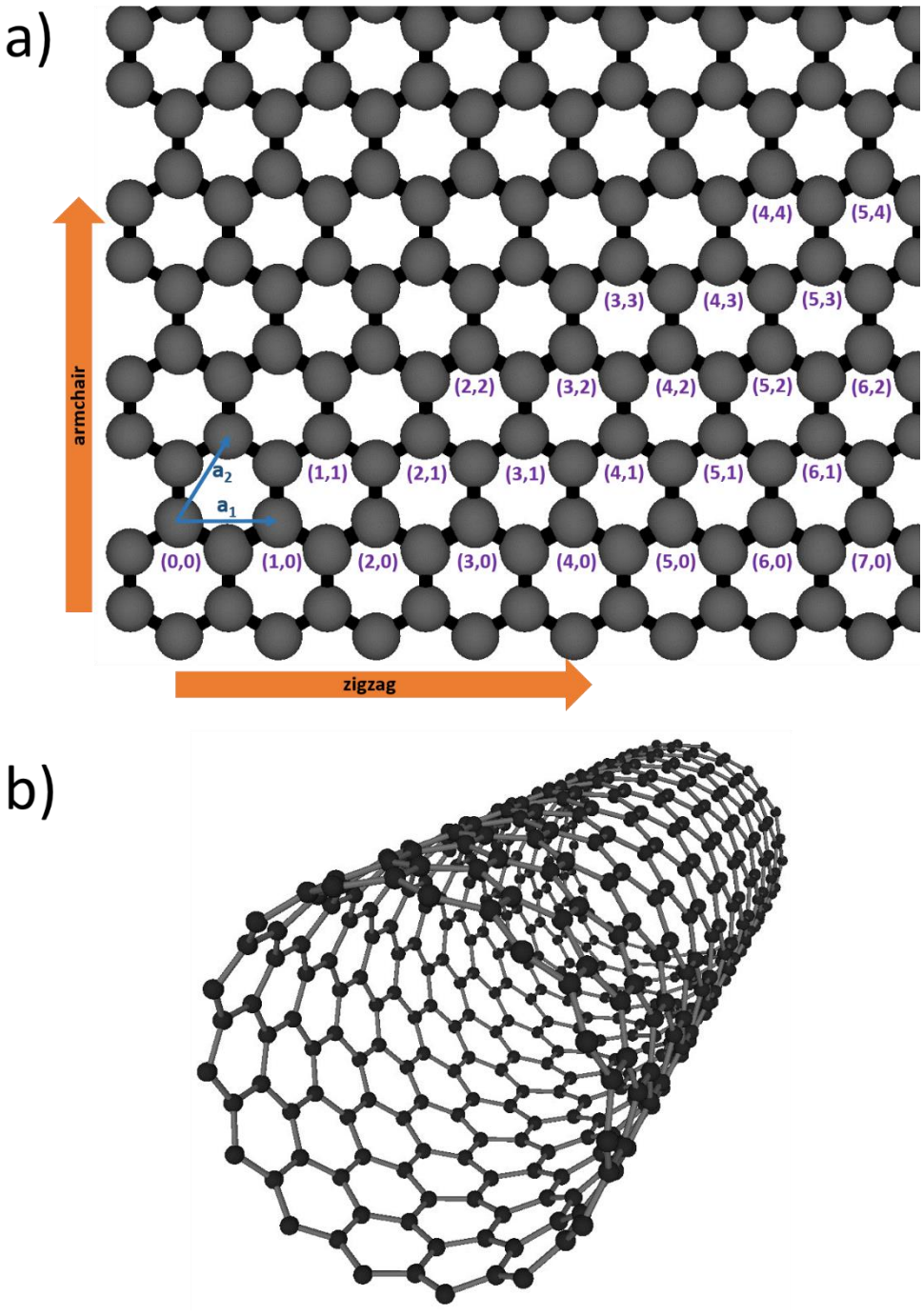


Figure 1.2: Carbon nanotube structure.(a) Graphene sheet with vector (*n*,*m*) determining chiral vector for the formation of a SWCNT, (b) (14,0) zigzag SWCNT.

Unlike the zero-bandgap sheets of graphene which make up their walls, SWCNTs can be semiconducting or semimetallic. In general, an (*n*,*m*) nanotube will be semimetallic when $n - m = 3p$, where $p$ is an integer. Otherwise it is semiconducting. MWCNTs are always semimetallic, regardless of their diameters and chiralities. Semiconducting SWCNTs will have bandgaps dependent on their chiralities. Optical characterization techniques, such as spectroflourometry, can be used to identify relative quantities of each type of semiconducting SWCNT in a sample. This is possible because of the unique 1D density of states (DOS) in carbon nanotubes which is noncontinuous and exhibits discontinuous spikes called Van Hove singularities. Prominent optical transitions occur between these singularities in the DOS, which depend on the nanotube structure, and can thus be used to characterize nanotube chiralities.

Numerous techniques have been implemented to synthesize carbon nanotubes to varying degrees of success, three of the more prominent methods which we briefly mention here. Initial discoveries were made through the arc-discharge of graphitic electrodes[1]. In an inert gas atmosphere, usually in a vacuum atmosphere, a voltage is applied to the two electrodes which when brought in close proximity to one another, will result in an electric arc discharged between the graphitic rods wherein local temperatures reach well above 6000 °C. Laser ablation methods produce similar results by focusing high power lasers on carbon-containing targets to sublimate them[2]. Chemical vapor deposition processes are perhaps the most controllable and involved the decomposition of a carbonaceous gas on a catalytic medium, such as metallic nanoparticles[3,4]. CVD enables patterned and aligned growth of carbon nanotubes and has been demonstrated as a viable option for larger scale production with commercial success. Carbon nanotube synthesis is further discussed in Chapter 2 where we investigate the synthesis of boron nitride nanotubes at length.

## 1.2 Boron Nitride

The group IV element of carbon has a very rich chemistry, forming various allotropes with remarkable properties as will be elucidated throughout this thesis. Boron and nitrogen, its neighbors on the periodic table from group III and group V, form an isoelectronic bond to those of C – C and hence exhibit the heteroatomic analogue of many of the carbon allotropes.

The electronic configuration of the ground state of a boron atom is given as $1s^2 2s^2 2p^1$ and that of nitrogen is $1s^2 2s^2 2p^3$. The 3 valence electrons of boron and the 5 of nitrogen in their 2s and 2p atomic orbitals can organize to form new hybrid

orbitals, leading to several different types of boron-nitrogen bonds. As in the case of carbon, the hybrid orbitals of BN will have new shapes and energies.

### 1.2.1 $sp^3$ Hybridization

During $sp^3$ hybridization, the 2s and three 2p orbitals of boron and nitrogen will combine to form four hybridized $sp^3$ orbitals. Three of the $sp^3$ orbitals of boron will possess unpaired electrons whereas for nitrogen in the bond, one $sp^3$ orbital will contain a paired set of electrons and the other three $sp^3$ orbitals will have one electron each. $Sp^3$-bonded BN may take the wurtzite phase (*w*-BN) or cubic phase (*c*-BN), the latter consisting of tetrahedrally-bonded boron and nitrogen atoms[5].

### 1.2.2 $sp^2$ Hybridization

In hexagonal boron nitride (*h*-BN), the 2s orbital will combine with two of the 2p orbitals to form three hybridized $sp^2$ orbitals and leave the $2p_z$ orbital. The three $sp^2$ orbitals of boron contain one unpaired electron each leaving the $2p_z$ orbital vacant while four electrons fill the three $sp^2$ orbitals of nitrogen with one additional electron in its $2p_z$ orbital. The very strong in-plane bonds of the electrons in the $sp^2$ orbitals form σ-bonds at 120° with respect to one another, which for a network of BN will produce a layered lattice consisting of alternating boron and nitrogen atoms in a hexagonal configuration, as depicted in Figure 1.3a. The 3D bulk *h*-BN is assembled from layers of stacked *h*-BN sheets arranged in an *AA′* sequence such that boron atoms in one layer lay directly atop nitrogen atoms in an adjacent layer. This is illustrated in Figure 1.3b. The in-plane distance between nearest neighbor carbon atoms, $a_{B\text{-}N}$, the in-plane lattice constant which refers to the distance between nearest boron or nitrogen atoms, $a_o$, and the c-axis lattice constant which is the distance between to alternative *h*-BN sheets, $c_o$, are presented in Figure 1.3. The interlayer spacing between adjacent *h*-BN sheets is given as $c_o/2$ = 3.33 Å. In rhombohedral phase BN (*r*-BN), single layer sheets of *h*-BN are stacked following a threefold *ABC* sequence with BN rings in adjacent layers out of alignment.

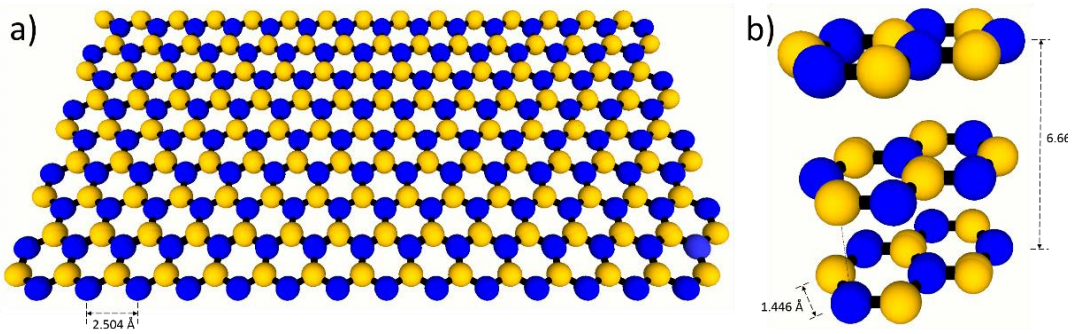


Figure 1.3: *h*-BN lattice structure as (a) a monolayer and (b) stacked in *AA*' configuration.

### 1.2.3 Boron Nitride Nanotubes

Boron nitride nanotubes (BNNTs) are the heteroatomic analogue to the carbon nanotube with alternating boron and nitrogen atoms of *h*-BN sheets rolled into a cylindrical configuration. They are predominantly multiwalled (MWBNNTs), consisting of several concentric shells, with the single-wall configuration (SWBNNTs) more difficult to obtain. This is due to the iconicity of BNNTs, which does not occur in CNTs, with nitrogen atoms of one layer tending to bond ionically with boron atoms of an adjacent layer and vice versa. Hence the double-walled and multiple layer structures are more stable than nanotubes with a single wall. Nevertheless, SWBNNTs have been achieved[6], including in our novel synthesis process described in Chapter 4. The chirality of BNNTs can also be designated in a similar manner to that of CNTs previously described. As depicted in Figure 1.4a, $a_1$ and $a_1$ are the unit vectors of a single *h*-BN sheet in real space and a SWBNNT is described by its chiral vector, labeled by the integers (*n,m*). Resultantly, (*n*,0) SWBNNTs are zigzag nanotubes, (*n,n*) SWBNNTs are armchair nanotubes, and all other general (*n,m*) SWBNNTs are chiral nanotubes. The SWBNNT of Figure 1.4b is a (14,0) zigzag nanotube. The circumference, chiral angles, and diameters of these tubes follow the same formulas previously presented in the discussion about CNTs.

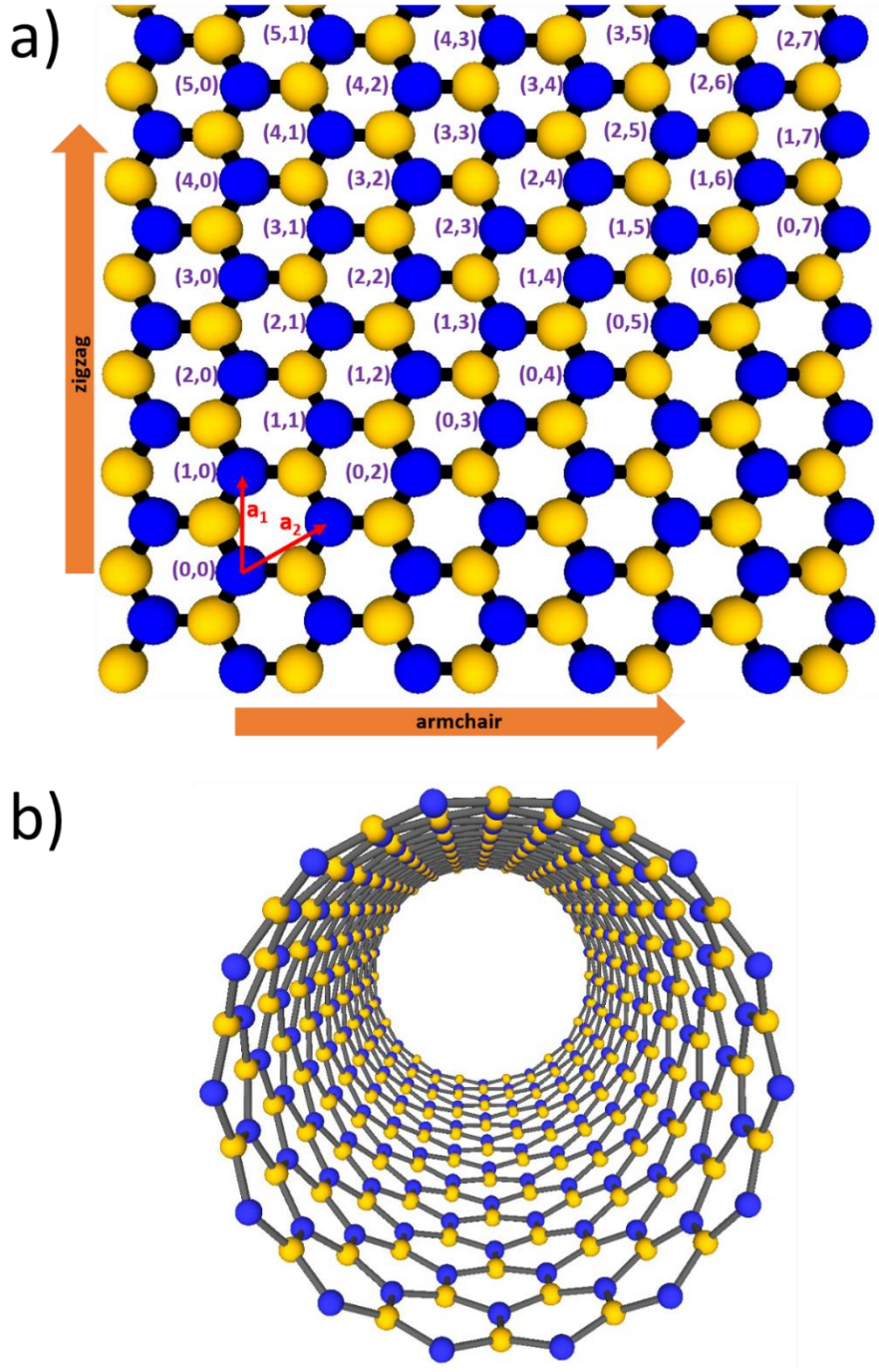


Figure 1.4: Boron nitride nanotube structure.(a) *h*-BN sheet with vector (*n*,*m*) determining chiral vector for the formation of a SWBNNT, (b) (14,0) zigzag SWBNNT.

Many of the same techniques which have been used to yield CNTs have also been attempted with BNNTs. The synthesis of BNNTs, however, has proven to be much more difficult as most of the methods which work so well for CNT growth have not been able to produce high quality BNNTs en masse. BNNT synthesis, and in particular a novel method utilizing an Extended Pressure Inductively Coupled (EPIC) plasma system to produce very long, high quality, few-walled BNNTs and other nanomaterials on a large scale, is the subject of Chapter 4.

## 1.3 Nanotube Properties

The differences in the key properties of CNTs and BNNTs principally originate from the symmetry breaking in the later structures with the incorporation of two different atomic species, namely boron and nitrogen, in the unit cell. In $sp^2$ hybridized BN bonds, electrons are localized at the nitrogen atoms. The B-N pairs will thus posses a local dipole moment due to the greater electronegativity of the nitrogen atoms. The covalent B-N bond is thus ionic in nature as well. The polarity of BNNTs in contrast to its absence in CNTs leads to dissimilar optical and electronic characteristics of these nanostructures.

### 1.3.1 Electronic

Unlike their carbon counterparts, BNNTs are a wide bandgap material with a bandgap of ~ 5.5 eV, independent of tube diameter and chirality[7]. They are good electrical insulators, in contrast to CNTs which may be semiconducting or semimetallic. Zigzag BNNTs will have a direct bandgaps whereas those of armchair BNNTs will be indirect[7].

#### 1.3.1.1 Bandgap Modification

A number of methods have been proposed and carried out to modify the bandgap of BNNTs. This includes chemical doping with carbon[8], after which they exhibit electric transport properties similar to semiconducting material properties[9]. Fluorine-doped BNNTs have also exhibited a marked decrease in their electrical resisitivities[10]. First principles density functional calculations predict radial deformations of BNNTs will also modify the material's bandgap, decreasing it by as much as 3 eV in zigzag nanotubes subjected to transverse pressures ~10 GPa[11]. This phenomena as well as the experimental attainment of such collapsed BNNTs whose bandgaps may be significantly altered are explored in Chapter 4.

Furthermore, theoretical calculations indicate a great reduction of the bandgap may be obtained in the presence of a strong transverse electric field[12]. This Stark effect is analogous to the standard Stark effect where molecular and atomic spectral lines will shift under the influence of an externally applied electric field. The insulating nature of BN results in reduced screening and hence a larger electric potential difference builds up between opposite sides of the tube, resulting in the accumulation of electrons and holes on opposite parts of the tube. The effect is more pronounced for larger diameter tubes and does not depend on chirality. The reversible tuning of a BNNT bandgap was experimentally achieved in the Zettl group using the tip of a scanning tunneling microscope (STM) to assert a local transverse electric field and probe the electric properties of a BNNT[13].

### 1.3.2 Piezoelectricity

Owing to their intrinsically polar nature, nanotubes of boron nitride unlike carbon are piezoelectric, meaning that electric charges can be generated in response to elastic deformations of the tube. Nakhmanson *et al.* calculated that BNNTs may have a better piezoelectric response than many piezoelectric polymers[14]. The first experimental signs of piezoelectricity in BNNTs were reported following the bending of a BNNT inside a TEM[15]. Based on measured current-voltage curves, the transformation between insulating and semiconducting could be reversed as the tube was deformed and reloaded.

### 1.3.3 Electron Field Emission

The very high aspect ratio of nanotubes makes them excellent candidates as electron field emitters. When subjected to voltages near 100 V, electrons can be emitted from a carbon nanotube tip into a vacuum atmosphere with currents on the order of 0.1mA achievable [REF]. This extraordinary current density from such a small system makes them excellent candidates as electron sources, which are important in many industrial fields such as lighting and displays. The field emission from CNTs and the utilization of this property for signal transduction is explored in Chapter 2. Field emission from BNNTs has also been studied experimentally by the Zettl group using a nanomanipulation stage inside a TEM[16]. With higher field-emission onset voltages than CNTs, stable field emission currents with little noise were obtained from BNNTs.

### 1.3.4 Optical

Optically, pure BNNTS are white while CNTs are black. BNNTs exhibit luminescence emissions in the ultraviolet range when excited by electrons or photons[17–19]. The emission spectrum of CNTs depends on their chiralities, but typically emit in infrared light[20–22]. CNTs have several prominent Raman active modes, including the G band at 1580 $cm^{-1}$ and the D band at 1350 $cm^{-1}$ [23]. BNNTs, however, possess only a single prominent Raman peak near 1370 $cm^{-1}$.

### 1.3.5 Mechanical

The two types of nanotubes exhibit phenomenal mechanical properties. The Young's modulus is a measure of how much a material is deformed for a certain amount of force per unit area applied to it. Theoretical calculations based on tight-binding models predict that both CNTs and BNNTs will have similar, exceptionally high Young's moduli with that of the heteroatomic structure being slightly lower. In particular, pristine CNTs are expected to reach as high as 1.25 TPa while those of defect free BNNTs are closer to 0.9 TPa[24]. The experimentally measured values for the Young's modulus of CNTs based on the literature vary widely from 0.6 to 5 TPa, but are mostly near 1 TPa[25]. By observing the thermal vibration amplitude of a cantilevered BNNT in a transmission electron microscope (TEM), the Zettl research group measured an elastic modulus of 1.2 TPa[26]. This gives BNNTs the record for the highest elastic modulus of any insulating fiber. Using an atomic force microscope (AFM) piezo driven stage integrated into a TEM, forces on individual MWBNNTs tubes were applied until they succumb to bending[27]. Values of 0.5-0.6 TPa were obtained on these tubes which were grown via the boron oxide chemical vapor deposition (BOCVD) method and hence were more defective than the arc-discharge grown tubes of Chopra *et al.*

### 1.3.6 Thermal

BNNTs are significantly more resistive to thermal oxidation than their carbon counterparts. The early studies of Chen *et al.* showed that highly crystalline ball-milled BNNTs may be stable up to 900 °C, with an onset of oxidation near 800 °C compared to 400 °C for CNTs under similar conditions[28]. Highly crystalline BNNTs synthesized using high-temperature methods are stable in air at temperatures approaching 1000 °C [29,30]. The exact temperature of decomposition depends on the quality of nanotubes, with certain synthesis methods more conducive to producing

more pristine and defect free tube walls. The oxidation of BNNTs will be discussed further in Chapter 5.

Theoretical calculations indicate that both CNTs and BNNTs ought to exhibit very high thermal conductivities, upwards of 6000 W/mK for SWCNTs at room temperature[31]. Experimentally verified thermal conductances of ~ 3500 W/mK have been measured for SWCNTs[32]. Assuming similar phonon mean free paths, BNNTs are predicted to have greater thermal conductivities than CNTs at lower temperatures[33]. The high thermal conductivity of CNTs is predominantly due to acoustic phonons, whereas that of BNNTs is exclusively from phonons[34]. The Zettl research group measured room temperature thermal conductivities of MWBNNTs ranging from 180-300 W/mK[34]. These tubes, however, were larger diameter with multiple walls and noting that only the outer shells contribute to thermal transport in nanotubes[35], these values can be improved for highly crystalline BNNTs with smaller diameters and few number of walls.

## 1.4 BxCyNz Materials

Many other $B_xC_yN_z$ compounds exist which are discussed in greater detail as they come up throughout this work. These include boron which can be an amorphous, appearing brown in color, or a shiny black crystalline phase, namely *α-rhombohedral*[36], *β-rhombohedral,* or *tetragonal*. Interestingly, *β-rhombohedral* boron is the second hardest pure elementary compound after diamonds. Boron carbide ($B_4C$) will be utilized in Chapter 4, and is the third hardest known material, after diamonds and *c*-BN. Carbon nitride has been theoretically predicted to take on several forms, including *β*-$C_3N_4$, *α*-$C_3N_4$, cubic-$C_3N_4$, pseudocubic-$C_3N_4$, and graphitic-$C_3N_4$[37]. Nanoscale carbon nitride consisting of C and N in various mixtures and conditions of phase separation have been experimentally achieved[38–40].

Compounds consisting of all three elements, namely $B_xC_yN_z$, are expected to take on similar morphologies to those of carbon and boron nitride discussed above owing to their structural likeness. These include hexagonal–$B_xC_yN_z$ (*h*–$B_xC_yN_z$), cubic–$B_xC_yN_z$, and nanoscale hybrids such as $B_xC_yN_z$ nanotubes. *h*–$B_xC_yN_z$ is quite attractive as its bandgap may be modified in-between the semimetallic graphite sheets and those of the insulating *h*-BN by controlling the chemical composition of the structure. Similarly, the bandgap of $B_xC_yN_z$ nanotubes should be predominantly determined by its atomic composition. Most $B_xC_yN_z$ compounds, however, tend to be mixtures of phase separated regions of carbon and boron nitride. In the case of nanotubes, radial phase-separation of discrete carbon and boron nitride shells have been observed in attempts to synthesize $B_xC_yN_z$ nanotubes[17].

# Chapter 2

# Carbon Nanotubes: Field Emission and CNT Integrated Device Fabrication

## 2.1 CNT Electromechanical Systems

Here we focus on studying a system which has attracted a great deal of research efforts by both academic and industrial circles since its synthesis in 1991, namely the carbon nanotube (CNT). The cylindrical network of $sp^2$ bonded carbon atoms boasts a number of exotic properties, some of which have been highlighted in the introductory chapter. A high Young's modulus of ~ 1TPa, nearly 100 times that of steel, and a large tensile strength of ~100 GPa, approximately 300 times that of steel, is a result of the strong σ-bonds between carbon atoms in the rolled hexagonal network of carbon. In combination with a very low mass density of $\rho$ = 1.3 g/cm$^3$, CNTs have a specific strength of ~50,000 kN·m/kg which is the highest of any known materials. CNTs thus serve as excellent resonating systems with high quality factors capable of high resonance frequencies. Furthermore, the electrically conducting nature of multiwalled nanotubes and their incredibly high length to diameter aspect ratios enable very high local enhancement of an electric field for a voltage biased nanotube. CNTs are thus excellent electron field emitters. CNTs present a potentially defect-free nanoelectromechanical system with extraordinary mechanical and electrical properties.

In the devices and applications we explore in this chapter, the field emission of electrons from carbon nanotube (CNT) tips is a critically important physical process that must be investigated and characterized[41,42]. Field-emission currents, and specifically its modulation in response to oscillations of the singly-clamped suspended CNT, will enable the transduction of a nanotube's mechanical motion in response to external stimuli into an electrical signal. Obtaining a stable, reproducible

field-emission current from nanotubes integrated into portable devices possesses many challenges, but is a first step in the ultimate implementation of field-emitting CNT oscillator devices for various applications, such as in the detection of nuclear magnetic resonance signals.

## 2.2 Electron Field Emission

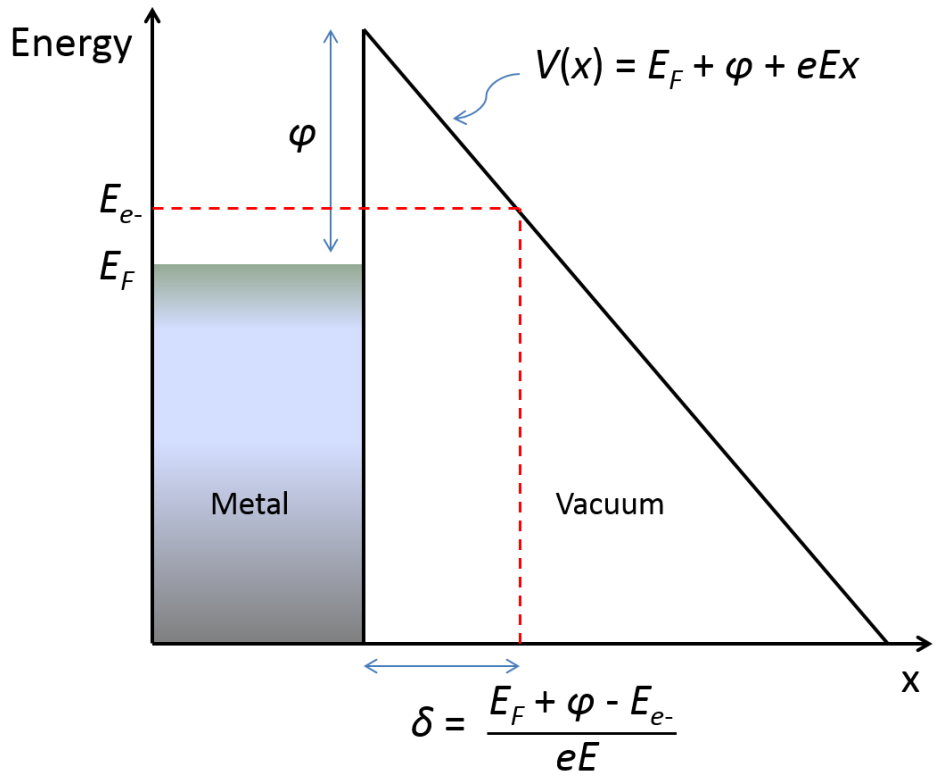


Figure 2.1: Electron Field Emission. An electron of energy $E_{e-}$ tunnels across a barrier of width $\delta$ from a metal with work function $\varphi$ and Fermi energy $E_F$ for an applied electric field $E$.

There are several basic mechanisms for the emission of electrons from a source. In thermionic emission, electrons are ejected from heated filaments as electrons gain enough thermal energy to overcome the material's work function. In photoemission, the electron ejection energy is supplied by incident radiation, such as light. Field emission, on the other hand, is a quantum mechanical effect[43]. As diagramed in Figure 2.1, when a sufficiently large external electric field is applied,

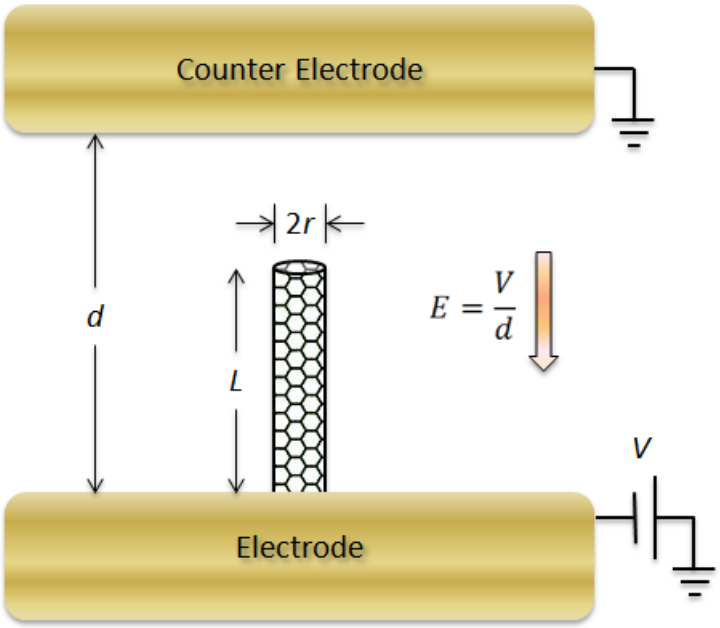


Figure 2.2: CNT field emission geometry.

electrons can tunnel through the energy barrier from a conducting material to vacuum. A larger electric field will reduce the potential barrier for tunneling, enabling greater tunneling currents. For many applications, including those described in this chapter, field emission is preferred over thermally induced methods because no heating is required and the emission current can be controlled to a great degree with just the applied external field. The monochromatic nature of a field emitted electron beam is also critical in many applications, as in electron microscopy.

The fundamental physical principles governing electron field emission were proposed by Fowler and Nordheim[44]. The current density of field-emitted electrons abides by the Fowler-Nordheim law,

$$J = c_1(\beta E_{ext})^2 \exp\left(-\frac{c_2}{\beta E_{ext}}\right) \quad (2\text{-}1)$$

where $E_{ext}$ is the external applied electric field, $\beta$ is the field enhancement factor, and $c_1$ and $c_2$ are constants involving fundamental constants and the conducting material's work function. Experimentally, the applied voltage, $V$, is controlled and is related to the applied field as $E_{ext} = V/d$ for an interelectrode spacing of $d$. The highly curved tip of a CNT as well as its high aspect ratio result in a local electric field at the tip end that is much greater than the externally applied electric field[41]. This

local electric field dictates the energy electrons near the emitting end of a conductor possess and is written as $E_{loc} = \beta E_{ext}$, which is the factor that appears in the Fowler-Nordheim expression.

The field enhancement factor is a measure of the field concentration, but is also the only variable in equation (2-1) that depends on geometry. For an anode-cathode distance, *d*, much larger than the length of the carbon nanotube, *L*, as illustrated in Figure 2.2, the enhancement factor can be approximated as $\beta = L/r + 3.5$ for a nanotube with tip radius *r* [45]. For a field-emitting CNT undergoing mechanical vibrations, the distance of the tip end from the electrode to which it is attached, *L*, will vary and hence modulate $\beta$. Through this mechanism, the mechanical motion of a nanotube can be gauged by measuring the electrical output of its field emission current.

## 2.3 CNT-Tipped Probes

The characterization of nanotube properties has proven challenging in great part due to the very small nature of these materials. Many early studies were conducted on groups of nanotubes, such as mats, bundles, or films. For instance, de Heer *et al.* first reported electron field emission from CNTs using aligned films of CNTs[41] and soon after Collins *et al.* demonstrated a robust electron field emission from bundles of CNTs[42]. Such measurements gauge the average properties of CNTs. In order to probe an individual nanotube and, for instance, take advantage of its extraordinary features such as tremendous aspect ratio for field enhancement, we must employ methods than enable the manipulation and characterization of individual CNTs.

In this chapter, we present studies on the electron field emission from individual CNTS with an aim towards CNT integrated device fabrication using two techniques. The first presented in this section 2.3 involves a bottom up fabrication process whereby CNTs are attached onto probe tips using piezo driven nanomanipulation stages. This is carried out in a high resolution imaging environment of an electron microscope which enables real time observation of nanoscaled materials such as CNTs. These efforts are built upon previous work done in the Zettl group, including the pioneering studies of John Cumings.

### 2.3.1 Fabrication

We begin by describing the assembly of CNT-probe tips. The first step in the fabrication of a CNT onto to the end of a probe, such as a tungsten wire or atomic

force microscope (AFM) tip is the preparation of the CNT sample. In order to make contact with an individual CNT, a substrate must be prepared with nanotubes hanging over and protruding from the substrate edge. Arc-discharge synthesized multiwall carbon nanotubes were sonicated in a solution of isopropanol (IPA) and spin cast onto a Au coated Si substrate. 5 nm of Ti followed by 30 nm of Au were deposited via electron beam (ebeam) deposition onto a piranha etched Si substrate, roughly 2 x 3 cm. The piranha solution is a combination of concentrated sulfuric acid with 30% hydrogen peroxide in a 3:1 ratio. After spin casting the tubes on, the substrate was heated in air at 100 °C for 10 minutes to remove residual IPA. A small line was then scribed near the edge of the substrate, which was then cracked over a thin wire. The edge of the substrate which has a slight overhang is the piece that will then be placed on the attocube stage for extracting nanotubes (See Appendix A). Previous experiments in the Zettl group have utilized electrophoresis to drop cast CNTs in-between to parallel razor blades biased with some AC voltage in order to obtain nanotubes protruding off of an edge[46]. The success rate for that technique was reportedly 10% [47]. The method employed here is cleaner, always produces tubes overhanging the substrate edge, and can be used for any type of nanotube, including wide-bandgap boron nitride nanotubes. In Figure 2.3a, a SEM image reveals the Au-coated substrate's edge on the left with plenty of protruding nanotubes.

Once the sample of CNTs has been prepared, the probe tip itself must be crafted. Scanning probe microscopy (SPM) tips were created from 300 µm thick tungsten wire (99.95%) etched in a bath of 2 N NaOH as the electrolyte. A constant-voltage power supply with an automatic switch off control is used to bias the tip and stainless steel counter electrode. The etching rate is enhanced at the NaOH surface, producing a neck in the wire which eventually breaks. If too much wire is submerged in solution, when the bottom portion is etched off, recoil of the sharpened end will result in a bulbous tip, present to some extent in the tungsten tip of Figure 2.3b and clearly in the probe tip of Figure 2.6. In our setup, wires broke after ~ 5 min, during which the current through the cell dropped quickly below a pre-set limit, automatically shutting off the power supply.

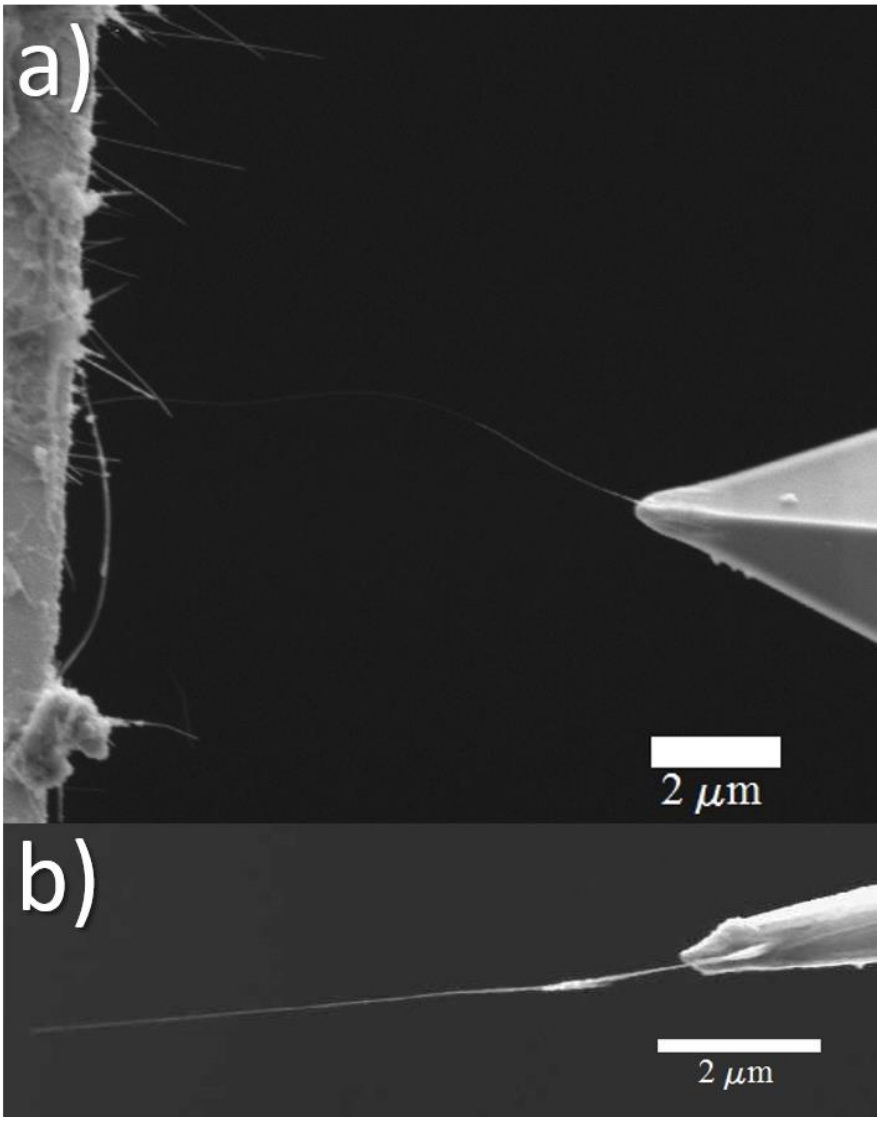


Figure 2.3: CNT-tipped probes.(a) Overhanging CNTs on substrate and CNT-AFM tip and (b) CNT-SPM tip. SPM tip is a tungsten wire.

In order to directly manipulate and gauge a single CNT, a nanomanipulator stage (attoCUBE ANPz100 with ANC 150 controller) is used in-situ inside a FEI Sirion XL-30 scanning electron microscope (SEM). Both the Si substrate with CNTs overhanging one edge and the sharpened W tip are loaded onto the attocube stage facing one another. A simple modification of the loading stage enables one to follow a similar procedure in attaching CNTs onto AFM cantilevers. The course movement

of the piezoelectric stage enables millimeter scale translation of the SPM tip in all three axes. Once the tip is brought close to the edge of the substrate, finer movements on the order of nanometers allow for gradually approaching an overhanging CNT from underneath. The probe can then be raised to make contact with the CNT, evidenced by the sudden bending of the nanotube to adhere to the tip end via van der Waals forces.

The CNT can then be attached to the W tip by focusing the electron beam onto the region of overlap. Carbonaceous species present in the SEM chamber will be deposited onto the junction, welding the two together with amorphous carbon. This bond, however, was found to be rather weak and easily broke upon slight translation of the probe tip. A much stronger mechanical attachment was achieved with the use of a gas introduction system (GIS) wherein Pt metalorganic gas precursor is introduced into the SEM chamber and decomposes under the electron beam to deposit a layer of Pt. By using the SEM's selected area scanning feature to raster the electron beam over just the nanotube-tip junction with the GIS valve fully open, a layer of material visibly accumulates conformally over the junction with little deposition elsewhere. The Pt deposition is clearly visible in Figure 2.3 and Figure 2.6 as the thicker, brighter region where the nanotube overlaps the tip end.

Once a strong attachment has been attained, the nanotube is then removed from the substrate edge. By using the SEM's line scan feature to raster the beam perpendicular to the axis of the nanotube, it is possible to cut the tube to any desired length. At the risk of damaging the nanotube and with no control over final length, running a large enough current through the tip-nanotube-Au substrate circuit can also be used to sever the nanotube. Simply translating the probe laterally away will also detach the nanotube from the substrate as demonstrated in Figure 2.3a where a CNT has been attached to an AFM cantilever head and is being pulled away from the substrate, bending in the process. As SEM image of an 8μm long multiwalled CNT attached to an SPM tip is present in Figure 2.3b.

### 2.3.2 Field Emission Characterization

Utilizing the electrical feed through connections on the SEM, characterizing the field emission of the nanotube – SPM tip was conducted in-situ once the probe was prepared. When loading the CNT-containing Au-coated substrate, the stationary stage and the top of the substrate should be in electrical contact to ensure that the top of the substrate is grounded and not in electrical contact with the mobile stage where the probe (etched tungsten wire) is loaded. The Keithley voltage source (Keithley 2400 Sourcemeter) external to the SEM provides the voltage bias to the nanotube-probe tip once all electrical connections are properly made (Appendix A).

The top of the substrate, coated with conducting metal layers and grounded to the stationary stage, serves as the counter electrode in these experiments. The nanotube-SPM tip can be positioned at any desired distance from this counter electrode. When viewing the nanotube-counter electrode setup live in the SEM, applying higher bias voltages distorts the image as electrons from the field emitting gun interact with the charged tip. When the threshold voltage for electron field emission is reached, the secondary electron detector of the SEM becomes saturated. In order to prevent this and not bombard the nanotube with additional electrons, the SEM electron beam was blanked during current-voltage (I-V) measurements.

The I-V measurements of a nanotube with length 4.5 µm located 11 µm away from the counter electrode are presented in Figure 2.4. After a certain threshold voltage near 51 V, the current increases nearly exponentially with increasing voltage and approaches a few µA in magnitude at bias voltages above 70 V. From the Fowler-Nordheim inset plot, there is a clear linear relationship between $\ln(I/V^2)$ and $(1/V)$ for a range of higher voltage values, denoted by the orange line, indicating a region of field emitted current consistent with the Fowler Nordheim equation. Positively voltage biasing the nanotube-tip did not produce any marked current. The field amplification factor, $\beta$, depends only on the geometric shape of the emitter, its work function, $\varphi$, and the inter-electrode distance, $d$. We can estimate $\beta$ in the context of the Fowler-Nordheim model from the slope of the Fowler-Nordheim plot which is equal to $(6.87 \times 10^9 \text{ V eV}^{-3/2} \text{ m}^{-1}) * \phi^{3/2} d/\beta$ [48]. Assuming a work function of $\varphi$ = 5eV for a MWCNT[49], the field enhancement factor is calculated to be 2100. Such a large β is greater than that measured for MWCNT films[50] and is primarily attributed to the very high aspect ratio

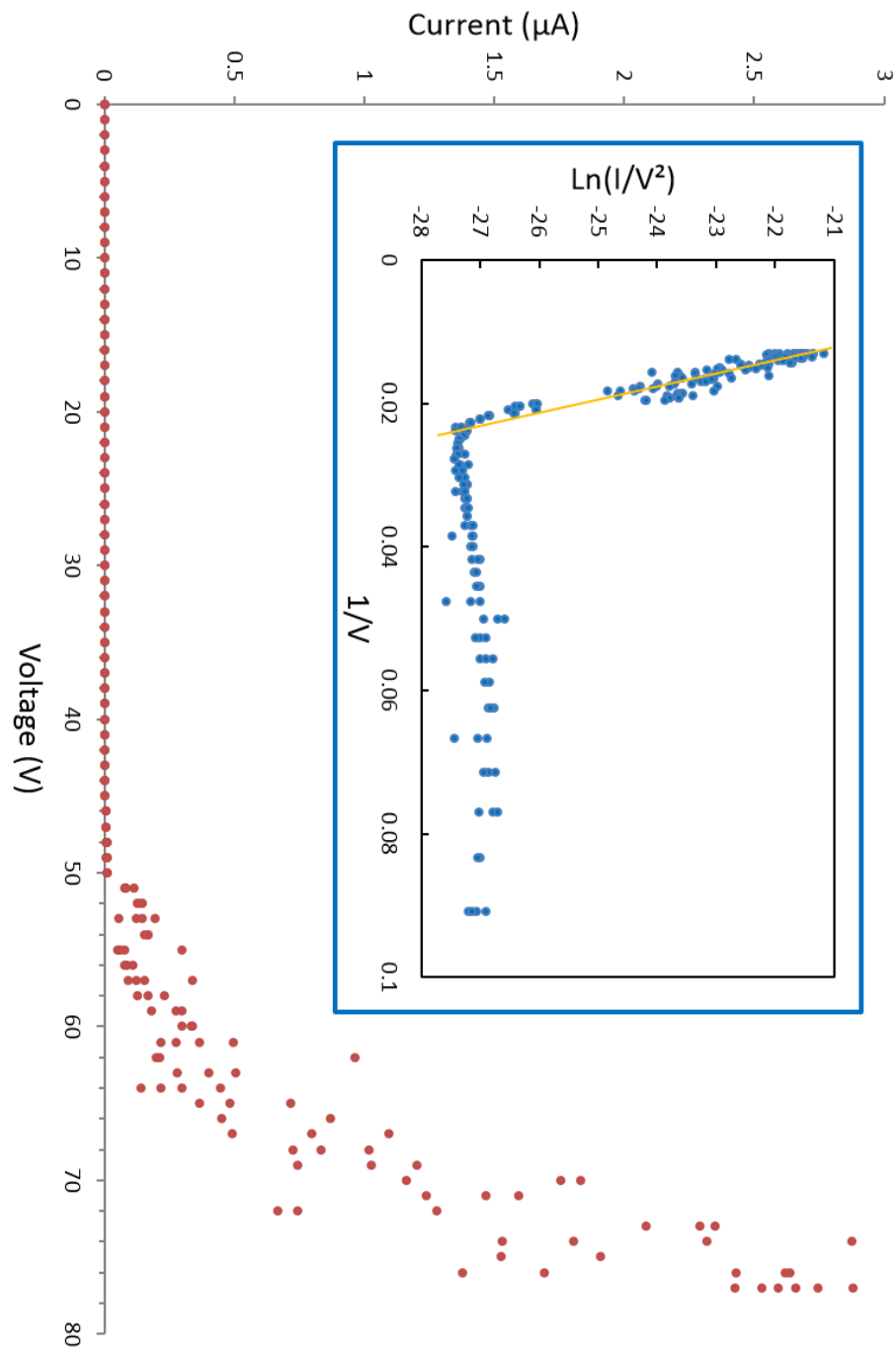


Figure 2.4: Field emission from CNT-SPM tip.I-V curve and (inset) Fowler-Nordheim plot.

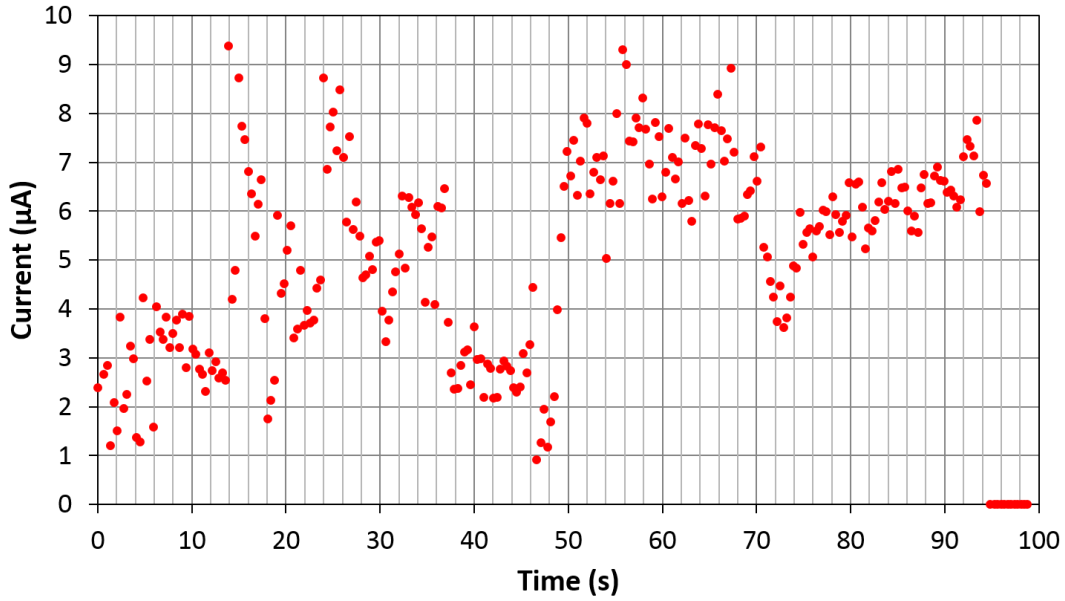


Figure 2.5: CNT-SPM tip field emission stability. CNT of length 4.5 μm positioned 280 nm from counter electrode biased at -70 V.

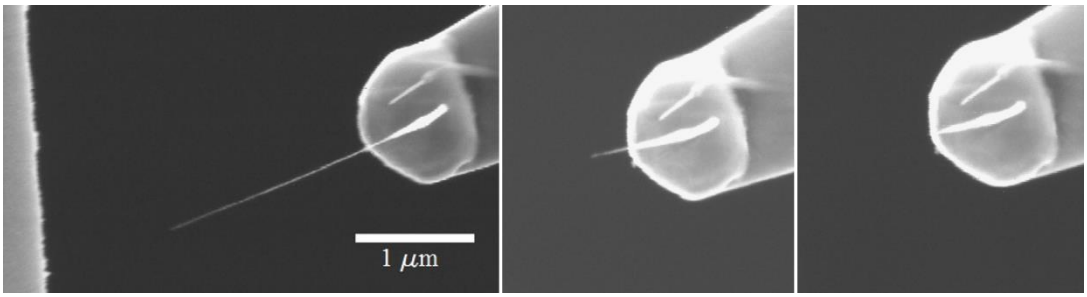


Figure 2.6: CNT damage during field emission. CNT attached to SPM tip is gradually burnt off and shortened during field emission of electrons from the CNT.

of the nanotube. From the above approximation for the field enhancement factor in terms of the aspect ratio of the conductor, the corresponding tube diameter is calculated to be ~ 4 nm, consistent with the diameters observed in this CNT batch.

A critical factor in gauging the practical application of a field emitter is its stability. The degradation of the nanotube emitter attached to a SPM tip is evaluated by assessing the field emission current at a constant voltage. The stability of a 4.5 µm long nanotube attached to a W tip located 280 nm from its counter electrode at a constant bias voltage of -70V is presented in Figure 2.5. The current is seen to fluctuate between 1 and 9 µA, occasionally exhibiting several regions of moderate instability. The fluctuations of current decrease over time with complete burnout of the tube after 95 seconds. Current fluctuations are likely due to chemisorption and removal of surface adsorbates during field emission. Over time as more material is removed from the CNT surface, the emission current becomes more stable. From 75 s to 95 s, the emission current gradually increases until it completely cuts off. This indicates a gradual shortening of the CNT as carbon atoms are ejected until the tube has been etched off. The series of SEM images of Figure 2.6 show a nanotube-SPM tip during a series of field emission trials revealing a gradual shortening of the nanotube end until it is completely destroyed. It is unclear whether outer layers of the tube are etched away first as has been reported elsewhere[51]. No damage occurred to the Au-coated substrate counter electrode during field emission trials.

Preliminary examination of the time dependence of the field emission current for a fixed bias did not reveal any step-like behavior as has been reported elsewhere[50]. Our experiments were conducted in the higher pressure chamber of the SEM (base pressure of $5.6 \times 10^{-5}$ Torr) where noise will be more dominant than in the high vacuum environment of the TEM ($10^{-7}$ Torr). Detecting discrete current levels is more difficult in a higher pressure chamber due to the greater adsorption and interaction of particles from the residual gas with the nanotube. Furthermore, switching between discrete current levels occurs at low current values[50]. The frequency of shifting between discrete levels increases with greater current. Noisy currents without clear steps are more likely for currents in the µA regime[50]. The temporal resolution of the data acquisition in our setup was 350 ms.

### 2.3.3 CNT-SPM Field Emission Improvement

A number of efforts can be employed to improve the stability of field emission and overall utilization of CNT – SPM probes for other purposes, such as scanning tunneling microscopy (STM) or as biological probes. Firstly, the etching of the W tips should be optimized in order to ensure ideal protrusion size, shape, and cleanliness. A dull, ragged, or broad tip end may result in a much weaker attachment of the CNTs.

Furthermore, the geometric structure of the W tip end as well as that of the attached nanotube determine the electric field enhancement factor β. Numerous studies have been reported on improving the etching of W to create sharpened STM tips[52–55]. The macroscopic and microscopic geometries of a tip can be characterized by optical microscopy as well as SEM and TEM respectively.

A contaminated or oxidized tip may also result in an unstable tunnel junction. W tips are particularly susceptible to contamination during etching, such as by $H_20$, hydrocarbons, or residual NaOH etchant. A thin layer of tungsten oxide almost certainly forms as well. It has been suggested that a lower etching voltage results in less oxide formation[52]. One could chemically etch away the $WO_3$ without damaging the sharpened W tip using hydrofluoric acid as well. TEM imaging can be used to observe any oxide layer and estimate its thickness[53]. Oxide on the tip could also be revealed in scanning tunneling spectroscopy (STS) data where a non-pure-metal junction could be discerned for a nonlinear I-V curve and the appearance of a gap near zero bias voltage[56].

In some applications where electrical contact only through the CNT is desired, as in microelectrodes for the biological probing of cells, an insulating layer coating the outside of the much longer tungsten wire may be desired. This can be achieved via coating by paralyene[57] or some other epoxy resin[58] and using a laser to remove the insulation at the end. This has the great advantage that the rigid W wire can be bent slightly without damaging the conformal insulation.

## 2.4 CNT Integrated Devices

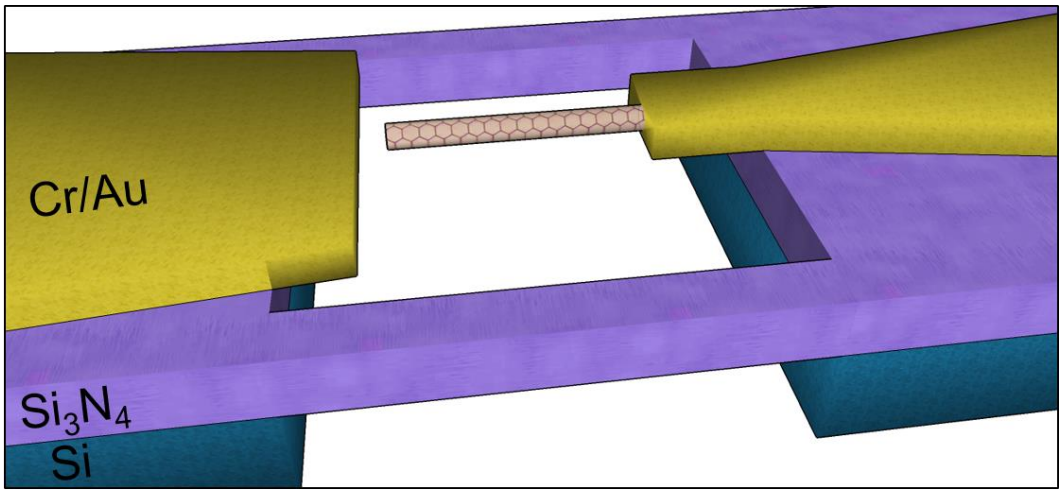


Figure 2.7: SiN-based CNT integrated device schematic. A singly-clamped CNT is suspended in-between two metal electrodes in a geometry to enable electron field emission from and oscillation of the CNT.

The manipulation of individual carbon nanotubes lends itself to characterizing fundamental properties of these structures, such as electron field emission or electrochemical characteristics. Individual probes can be fabricated in a "bottom-up" manner with the attachment and customization of an individual nanotube's geometry. The process, however, is tedious and is not easily scalable. A potentially scalable method for the production of nanotube-SPM tips may involve the synthesis via chemical vapor deposition of CNTs off of W tips coated with some type of catalyst, such as iron nanoparticles. Major hurdles employing this method include selectively growing just one or a few nanotubes off of W tips as well as controlling the orientation and length of nanotubes. Such efforts are being pursued in the Zettl group by the team of Gabe Dunn, with initially promising results. Furthermore, great care is necessary in transferring such probes, as they tend to be mechanically fragile and susceptible to electrostatic discharge.

With the aim of addressing many of these shortcomings, we pursued the use of customizable SiN-based devices. The implementation of SiN membranes for a host of studies was pioneered in the Zettl group by Gavi Begtrup, including for the investigation of MWCNT thermal conductivities as well as the fabrication of nanoelectromechanical memory devices[59]. By integrating CNTs

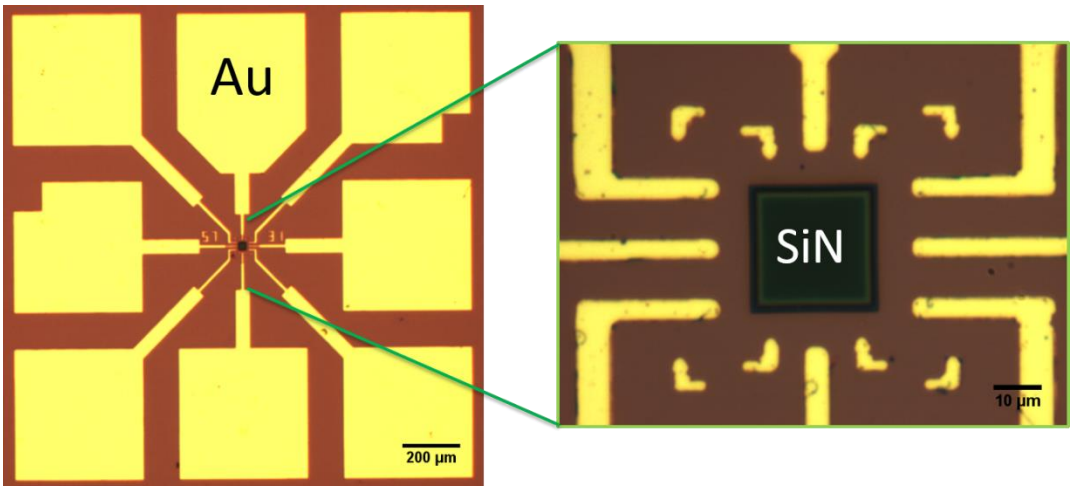


Figure 2.8: Optical images of SiN membrane devices. Yellow pads and tracks are Au electrical contacts and the dark square in the center is the suspended SiN window.

onto SiN based devices, we can customize the geometry and placement of electrical contacts as well as side gates. These chips can also be integrated into electrical circuits and systems beyond the chamber of an electron microscope. For instance, by incorporating them onto dual in-line packages (DIP), they are much less vulnerable to damage during transport and can be mounted onto printed circuit boards or inserted into standard sockets.

Using SiN membrane based chips, my colleague Seita Onishi and I sought to fabricate a fully integrated oscillating NEMS device based on a field-emitting singly-clamped CNT. Figure 2.7 is an illustration of our device showing a CNT fully suspended over an etched trench, contacted at one end by a metal electrode opposite a counter electrode. In this geometry, we are able to test for field emission of the CNTs integrated onto these devices, the first step in realizing the electromechanical capabilities of this system.

### 2.4.1 Fabrication

The greatest challenges thus far encountered have been in the fabrication of the SiN membrane based CNT devices. Figure 2.8 is an optical image of SiN membrane device showing the macroscopic electrical contact pads. Eight gold plated contact pads tapper down to eight thin leads (which we will henceforth refer to as

"tracks"), as seen in the magnified image on the right, which are positioned just outside of 20 x 20 μm window of SiN. The region of the window has been back etched so that the 10 – 40 nm thick SiN membrane is suspended. The relatively small window size and thickness of SiN has been engineered to make them quite robust, rarely rupturing if accidently dropped. The gold plated contact pads can easily be contacted by probes for electrical characterization underneath a standard optical microscope at 10x magnification. A detailed description of the microfabrication of SiN membranes is presented in the PhD thesis of Gavi Begtrup[59]. A typical Si wafer is patterned with many arrays of the design presented in Figure 2.8, which can be cleaved into 2 x 2 arrays, roughly 3.5 cm in length, which fit nicely onto the chuck of a spin coater.

Upon cleaving, the substrates must first be cleaned in order for the CNTs to stick to the SiN surface, otherwise they could be moved about during later processing steps. This could be achieved via a light oxygen plasma etch or by a rinse in acetone followed by isopropanol with the best adhesion following an etch in piranha solution (3:1 mixture of $H_2SO_4$ to 30% $H_20_2$).

A nanoscale electron beam lithographic technique is implemented to create the devices, as illustrated in Figure 2.9. Starting with cleaned SiN chip (Figure 2.9a), arc-discharge synthesized CNTs sonicated in IPA are spin coated onto the substrates (Figure 2.9b). An SEM equipped with the commercial NPGS (Nanometer Pattern Generation System) can be used to identify and then lay contacts to deposited CNTs. Briefly, an SEM mapping of the sample with alignment markers (the eight L-shaped structures outside the SiN window) is taken. Once potential CNT candidates located over the SiN window are identified, a CAD file in conjunction with the NPGS software is used to map out the regions of electron beam exposure. This pattern will dictate where subsequent metal contacts will be deposited. A thin layer of PMMA resist is then spin coated onto the substrate containing the CNTs (2000 RPM of PMMA A4 for 60 seconds) and baked (180 °C for 20 min.). The substrate is then loaded into the SEM, the SEM prepared for electron-beam writing, and then using the NPGS, the prepared pattern written onto the PMMA covered substrate. The resist is then developed in a 1:3 diluted solution of methyl isobutyl ketone (MIBK) in IPA for 90 seconds followed by rinsing (IPA for 15 sec, deionized water for 15 sec). The metal contacts can then be sputtered or deposited onto the substrate. We used electron beam deposition to lay a 5 nm layer of Ti followed by 30 nm of Au. If the electrodes have been patterned so they extend far and thinly

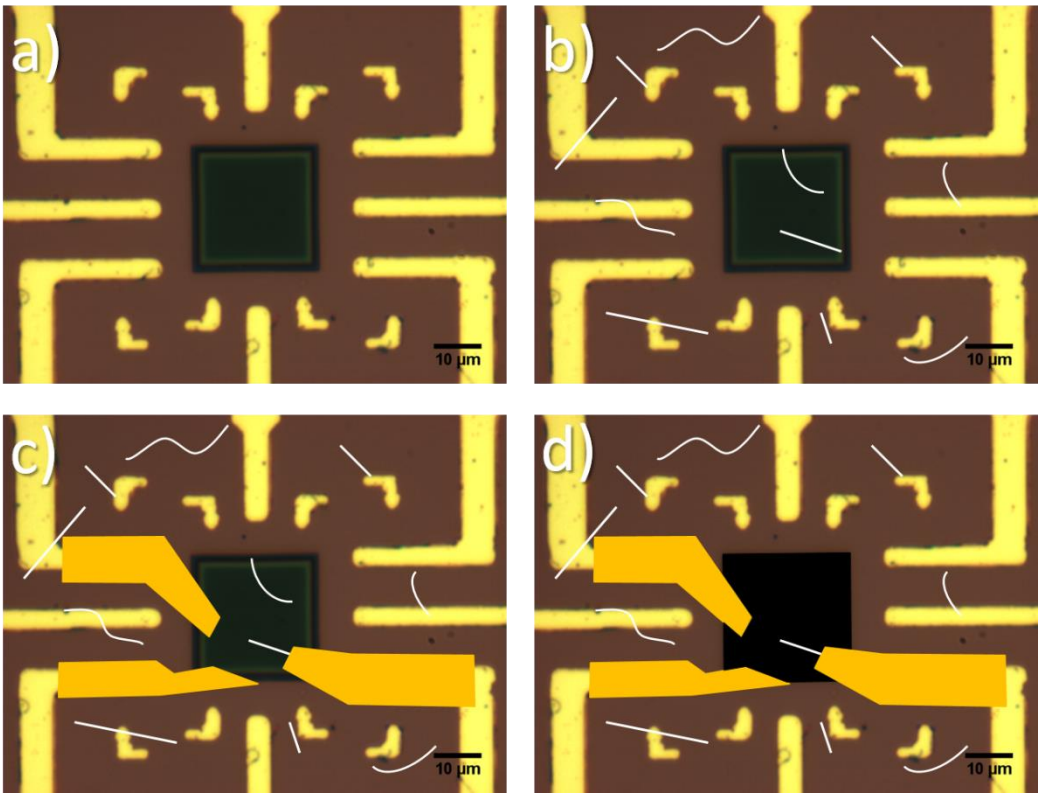


Figure 2.9: CNT integrated device fabrication. Starting with the SiN membrane device (a), CNTs (white lines) are spun cast onto the chip. Cr/Au electrical contacts (yellow) are nanolithographically patterned (c), followed by a final plasma etching of the SiN membrane window to leave the CNT suspended (d).

over the SiN window, it may be necessary to deposit a thicker layer of metal to prevent drooping or potential breakage of the final electrical contacts.

The PMMA resist can then be lifted off in acetone overnight or in heated acetone for a few hours. If the layer of metal is too thick or the features of patterned metal too close to one another, liftoff may not occur. Forcefully spraying the substrate using a syringe can help peel off these metal layers keeping the SiN membrane intact. Following a successful liftoff, the CNT should be in good electrical contact with at least one and ideally multiple Au contact pads and not in contact with any counter electrodes or side gates, as illustrated in Figure 2.9c.

The SiN window is then removed in order to leave the CNT fully suspended by reactive ion etching. 50 sccm of $SF_6$ at 200 W for 30 seconds in the commercial

Plasma Etch system was sufficient to etch through the 10 – 50 nm of SiN with little damage to the tube. The final chip with fully suspended CNT and corresponding electrodes and side gates, as depicted in Figure 2.9d, can then be loaded into the vacuum probe station for electrical characterization.

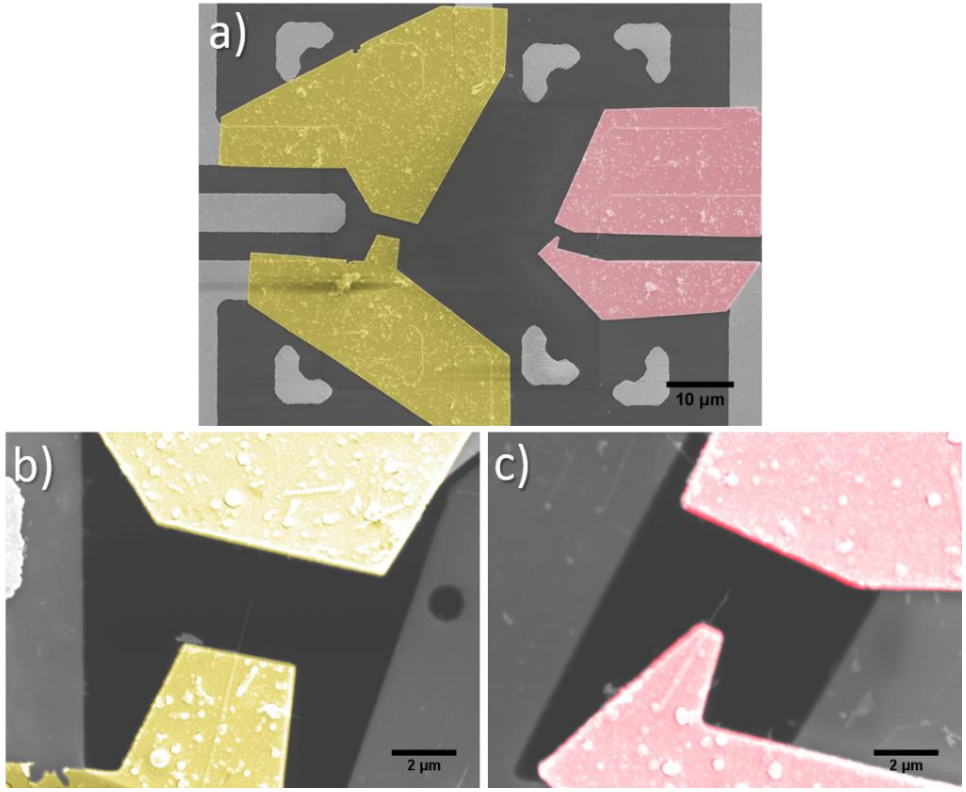


Figure 2.10: CNT integrated device (SEM image). (a) Low magnification SEM image of SiN membrane chip with two pairs of electrode-counter electrodes. (b) and (c) are higher magnification SEM images of suspended CNTs attached to an electrode and not in contact with the counter electrode. The falsely colored pairs of electrodes in (b) and (c) correspond to the falsely colored yellow and pink pairs of electrodes in (a) respectively.

An SEM image of a fabricated device with two suspended CNTs integrated onto the SiN membrane chip is presented in Figure 2.10. In Figure 2.10a, a lower magnification image shows the entire region of the SiN window before it has been etched. The ebeam deposited metal electrodes and counter electrodes have been false colored yellow and pink corresponding to the two different anode-cathode pairs. Both of the yellow electrodes, as well as the one pink counter electrode, are seen to be in electrical contact with two sets of tracks, each leading to a larger Au contact pad. This is done to ensure at least one Au contact pad is in contact with the deposited electrodes as sometimes during processing, tracks are damaged and disconnected. Figure 2.10b and Figure 2.10c are higher magnification SEM images of the two CNTs fully suspended following etching of the SiN membrane. The false-colored yellow and pink pairs of electrodes in Figure 2.10b and Figure 2.10c correspond to those same colored pairs in Figure 2.10a. The metal electrode has been deposited over a bulk of the CNT to ensure strong mechanical rigidity as well as electrical contact and a portion of the tube visibly extends beyond the electrode. Both suspended CNTs are perpendicularly oriented with respect to their counter electrodes and are free of visible contamination. Both sets of electrode surfaces are noticeably rough due to the small degree of "spitting" of Au during ebeam deposition. Similar devices were fabricated where only one CNT is contacted on a chip instead of two. In this manner, there would be greater room for the addition of side gate electrodes, which are not included in simpler anode-cathode geometry of the device in Figure 2.10.

### 2.4.2 Electrical Biasing of Devices

The CNT oscillator devices were loaded into a vacuum probe station (Desert Cryogenics) by gluing the substrate onto the stage with graphite conductive adhesive (Electron Microscopy Sciences). Once the chamber is pumped down to ~$10^{-7}$ Torr and the gold-tipped probes placed on respective Au contact pads, LabVIEW software is used to control the voltage put out by a Keithley 2410 Sourcemeter. Devices were initially characterized by voltage biasing nanotube electrodes negatively, from 0 down to -100V. For devices which exhibited exponential current increase after some threshold voltage characteristic of Fowler-Nordheim field emission, the nanotubes were then positively biased to make sure the observed I-V behavior was due to electron field emission and not some type of electrical shorting.

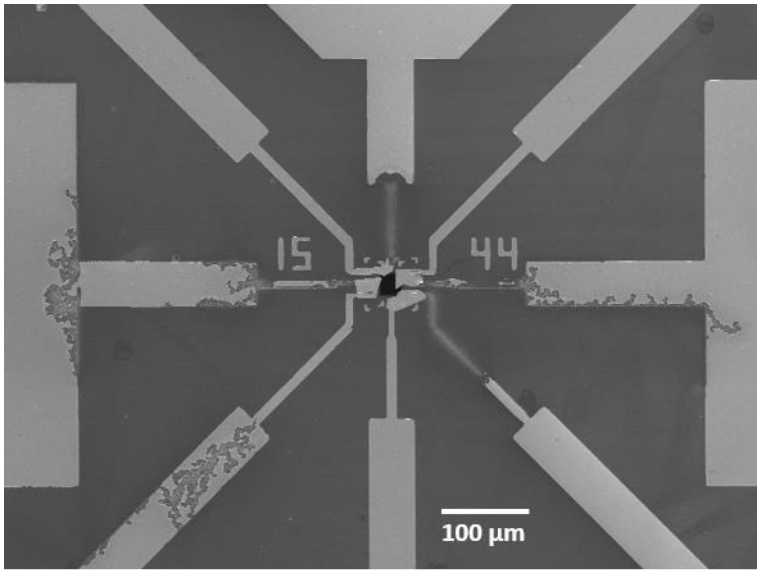


Figure 2.11: High voltage chip damage. SEM image reveals damage to contact pads, tracks, and electrodes when the device is biased at high enough voltages.

Oftentimes, many Au contact pads or tracks were damaged or completely removed during electrical biasing experiments at high enough voltage, as illustrated in Figure 2.11. Further investigations revealed current leakage through the Si substrate during biasing of the Au contact pads. We speculate the SiN insulating layers are compromised during processing, resulting in this current leakage from the metal contacts through the insulating layers to the underlying Si substrate when the contacts are biased at high enough voltage. SEM images of damaged devices reveal a propensity for Au electrode damage near the edges, perhaps indicative of etching underneath these regions during plasma treatment. The small dimensions of the patterned electrical contacts also result in a higher likelihood of failure due to electromigration from large power and current densities. Current densities as high as 6000 A/cm$^2$ regularly flowed through the thinner electrical contacts, approaching the threshold current densities for electromigration damage observed in thin Au films, but still roughly an order of magnitude less than reported elsewhere[60]. Hence the thin adhesion layer of Cr, only 1 nm thick, may not be sufficient to form a uniform layer in-between the Au layer on top and the SiN membrane beneath it, resulting in the lift off of Au at somewhat high current densities.

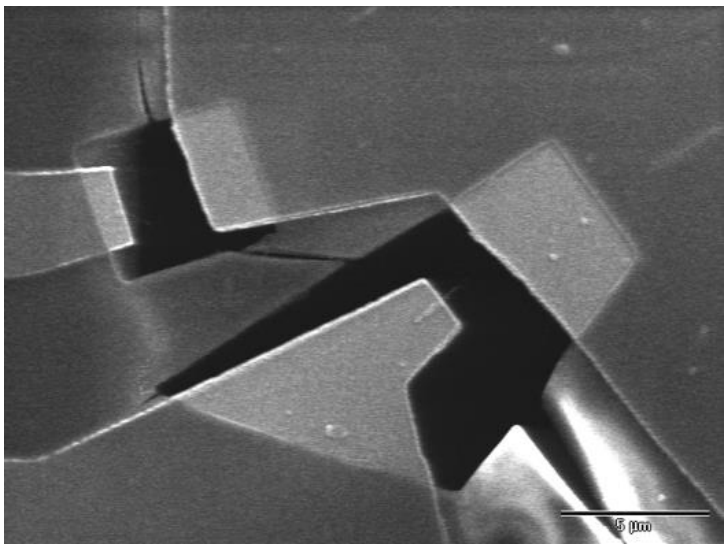


Figure 2.12: PMMA etch mask. SEM image of a chip with two pairs of electrodes with two suspended CNTs. A layer of PMMA over the entire chip acts as an etch mask except in the region near the suspended CNTs.

Various routes were pursued to solve this recurring problem of electrical contact damage. The insulating layers between the metal contacts and the underlying Si substrate were likely compromised during the SF6 reactive ion etching process which was used to etch through the SiN window. This may be due to the formation of pinholes in these layers. To remedy this, prior to the final etching of the SiN windows, a second nanolithographic step was followed to leave a layer of PMMA over the whole substrate except over the region we desired to etch, namely around the to-be suspended nanotubes. An SEM image of such an etch mask with two nanotube devices on the same substrate is depicted in Figure 2.12. The PMMA mask can be seen to cover everything except polygonal regions centered at the two nanotubes (the brighter regions being the exposed electrode and counter electrodes). Tears in the PMMA can also be observed close to these etched regions, but otherwise the rest of the substrate is covered by a layer of PMMA. Ultimately, two layers of PMMA coating the substrate prior to reactive ion etching were found to be necessary in order to prevent current leakage through insulating layers.

Efforts were also undertaken to fabricate customized SiN membranes. Maintaining nearly the same electrode pattern described above, Seita Onishi fabricated a new batch of devices with a thicker 200 nm layer of SiN. Current leakage through the Si substrate was no longer detected during high voltage biasing of

nanotubes, but damage to electrode tracks continued to be a problem. In future designs, the width and height of the contact tracks should be increased with careful consideration of the destructive effect of large current densities passing though contacts with small cross sectional area. A thicker adhesion layer, in this case of Cr, is also advised to reduce the likelihood of metal contact damage during high voltage biasing. Using the already-fabricated SiN membrane devices, these effects can be mitigated by depositing thicker and wider metal contact layers over the prepatterned tracks during the lithographic step of Figure 2.9c when the nanotube electrode and counter electrode are created.

### 2.4.3 Field Emission Characterization

The result of sweeping the bias voltage of a suspended nanotube on a SiN membrane device is presented in Figure 2.13. The nanotube is 1.1 μm long and located 0.85 μm from its counter electrode. After approximately 65 V, the current increases with greater voltage in accord with the Fowler-Nordheim equation for electron field emission. Below this onset voltage of 65V, the device is "off" with currents below 0.01 μA. In the inset of Figure 2.13, the plot of ln(I/V2) vs. (1/V) reveals a region of linear correlation in agreement with the Fowler-Nordheim equation. Once again assuming a CNT work function of $\phi$ = 5 eV, the field enhancement factor is calculated from the slope of this line to be $\beta$ = 100. The threshold voltage for field emission is greater here than for the nanotube-SPM tip of section 2.3.2. Geometric factors, such as the layout of the anode-cathode pair, in this SiN based device may play an important role in the distribution of electric field and hence field emission properties of the CNTs.

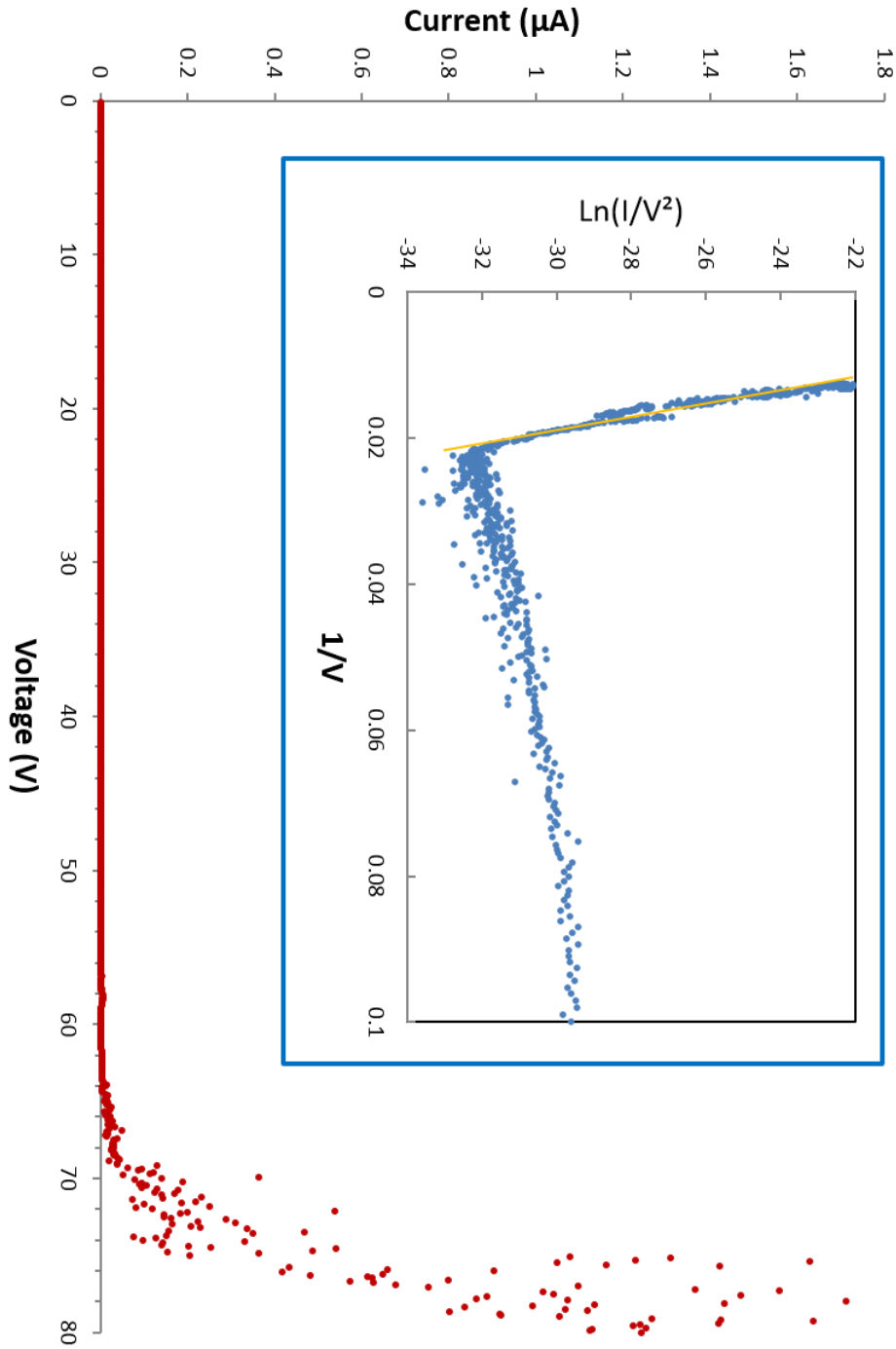


Figure 2.13: Field emission from CNT integrated device.I-V curve and (inset) Fowler-Nordheim plot.

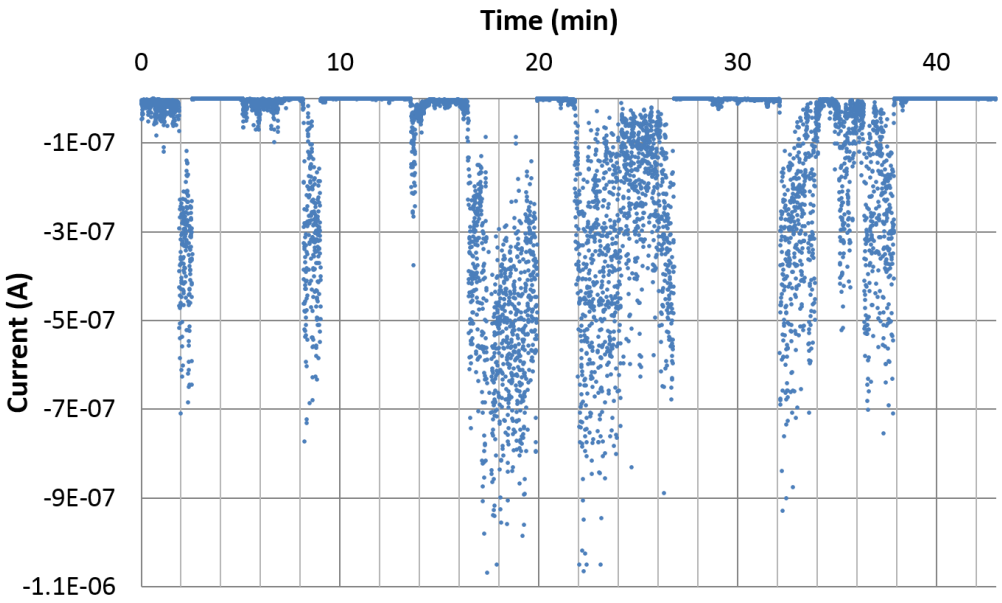


Figure 2.14: CNT integrated device field emission stability. CNT of length 1.1 µm positioned 850 nm from counter electrode biased at -69 V.

The long-term stability of the suspended CNT devices was evaluated by measuring emission currents over an extended period of time. The results of biasing the same 1.1 µm long CNT examined above at a constant voltage of -69 V are presented in Figure 2.14. A greatly fluctuating current was detected for up to 40 min. The fluctuations are attributed to the adsorption and desorption of particles from the environment. This includes chemisorption on the CNT from reactions with lingering water and other molecules in the $10^{-7}$ Torr remnant gas of the probe station vacuum chamber. Such fluctuations can be significantly reduced when devices are operated at lower chamber pressures and by using feedback stabilization mechanisms[41]. SEM inspections of the devices after electrical measurements reveal some nanotubes sustained little damage. Those subjected to prolonged field emission until failure were visibly shortened. Some devices were electrically studied multiple times, acting as robust field emitters.

As a control, devices were lithographically fabricated on the SiN membrane devices with a long metal electrode tapering down to a sharp tip at a distance of 1.5 µm from a metal counter electrode. No field emitting current was measured for these devices when the electrode was negatively biased up to -120 V. Furthermore, CNT devices which did exhibit field emission currents were also positively voltage biased up to 120 V with no significant current increases. These indicate that in devices such as those measured in Figure 2.13 and Figure 2.14, field emission of

electrons occurs from the CNT itself rather than any metal electrodes. With no detectable current when reverse biased, the CNT devices function as diodes.

Further studies of the suspended CNT devices will be necessary in order to fabricate chips for which field emission currents are reproducibly produced. Exploring various geometries for the electrodes and nanotubes as well as variations in metal contact composition and thickness, field emitting currents were measured from roughly 10% of chips. Ideally, tubes with small diameters and sharp tips should be contacted by electrodes during the design process, although this is quite difficult to discern in the SEM alone. Efforts will also need to focus on preventing deterioration of nanotubes and electrodes during field emission. This can be achieved by operation in high vacuum environments.

## 2.5 CNT NEMS Devices

Gauging and characterizing the field emission from suspended nanotubes on SiN membrane devices is a critical step in the ultimate implementation of these chips as nanoelectromechanical systems (NEMS). The magnitude of the field emitting current is highly sensitive to the position of the emitting nanotube tip with respect to the counter electrode. To understand this, recall the Fowler-Nordheim equation for electron field emission current density presented in equation (2-1). The field enhancement factor, $\beta$, is the only variable in this equation that depends on the system's geometry. As the nanotube oscillates at some amplitude, the position of the CNT tip end varies with respect to the electrodes. This variation in the geometric position of the tip end will modify $\beta$ and hence the magnitude of field emitting current as governed by equation (2-1). Physically, the electric field concentration near the CNT tip is modulated during nanotube oscillation. As previously discussed, the field enhancement factor can be approximated as $\beta \approx 3.5 + L/r$ , where *L* is the distance from CNT tip end to the electrode it's attached to and *r* its radius.

Since the field emission current couples strongly to the mechanical motion of a CNT resonator, the high-frequency nanometer amplitude of the tube's motion can be transduced into a detectable electrical signal. This mechanism has been utilized in previous studies, as in the development of the nanotube radio[61], highly sensitive mass detectors[62], and sustained self-oscillators[63]. These achievement, however, were confined to the high vacuum column of a TEM. Furthermore, a novel scheme has been proposed for implementing CNT resonators as parametric amplifiers[64]. Using the SiN membrane chips and the straight forward lithographic fabrication techniques described in section 2.4.1, we are now able to produce stand-alone nanotube oscillator devices which show great promise for studying these phenomena and integration into many other systems.

## 2.6 Nano-antennae for NMR Signal Detection

In collaboration with the group of Christophe Goze-Bac at the University of Montpellier, we sought to implement the suspended CNT oscillator devices developed here as nano-antenna for the detection nuclear magnetic resonance (NMR) signals. NMR is used extensively in medical diagnostics, such as in magnetic resonance imaging (MRI), as well as in spectroscopy for analysis of chemical or biological samples[65]. In some applications, the test samples may be very small with volumes near or below a microliter. Most conventional NMR-based devices are far too large and thus a suitably sized NMR device with high spatial resolution and sensitivity to a low number of nuclear spins is necessary.

### 2.6.1 Nuclear Magnetic Resonance

We begin by briefly discussing the physical principles behind NMR. When atoms possessing a spin are in the presence of a magnetic field, its associated magnetic moment takes on quantized orientations. For spin ½ particles, such as electrons or $^1$H (protons), the orientation can either be parallel or antiparallel to the external magnetic field, with those oriented parallel having lower energy. The energy difference between the two states is $\Delta E = h\nu_L$ , where *h* is Planck's constant and the transition frequency for magnetic resonance is given by the Larmor frequency, $\nu_L = \gamma \cdot B_o/2\pi$. Here $B_o$ is the applied magnetic field and $\gamma$ is the gyromagnetic ratio which is a property of the atoms. The atomic specificity of $\gamma$ enables the use of NMR to analyze and differentiate chemical samples. In the presence of a static magnetic field, the alignment of nuclear spins produces a macroscopic magnetization, *M*, of the sample oriented parallel to the externally applied field. By applying an excitation magnetic field perpendicular to the static

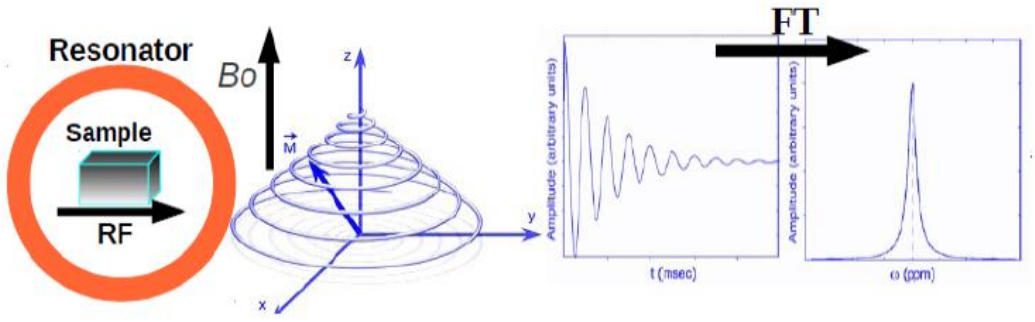


Figure 2.15: NMR signal emission. (Image courtesy of C. Goze-Bac.)

magnetic field with a magnitude oscillating at the Larmor frequency, protons may be excited into the higher energy state, perturbing the orientation of the macroscopic magnetization. When the excitation radiofrequency (RF) signal is turned off, the nuclear spins will relax to their lower energy state resulting in the magnetization precessing about $B_o$. The magnetization will fall back into alignment with the externally applied magnetic field, in the process precessing about it at the Larmor frequency, as depicted in Figure 2.15.

The RF signal emitted during relaxation is an exponentially damped sinusoidal signal called the free induction decay (FID). The FID signal is measured as an intensity across time and is Fourier transformed in order to discern the constituent frequencies, for instance by an NMR spectrometer. The FID is the culmination of signals detected from the relaxation of many different nuclei in the sample, each with its own characteristic sinusoidal frequency of decay. Hence by analyzing the frequency spectrum of the FID for a static uniform magnetic field, the elemental composition of a sample can be discerned. Furthermore, as the Larmor frequency detected in the emitted signal is proportional to the externally applied magnetic field, changing the later will result in the measurement of a different signal frequency. In this manner, applying a magnetic field gradient to a sample enables spatial resolution of the signal sources. This is critical for the implementation of NMR in MRI techniques.

### 2.6.2 NMR Resonance Techniques

Most traditional NMR techniques use induction detection methods, whereby a short radiofrequency pulse is applied inductively via a transmitting coil and the resulting nuclear precession signal measured inductively via a pickup coil[66]. These methods have many shortcomings, including restrictions on sample size due to coil geometries and poor spatial resolution of signals. Furthermore, electronic coupling between the transmitter and receiving coils is also problematic, oftentimes resulting in the saturation of received signal despite numerous attempts to mitigate this such as by positioning the two coils perpendicular to one another or by using quarter wave lines to mismatch signals[67,68]. Magnetic resonance force microscopy (MRFM) based on the mechanical measurement of small magnetic forces between the nuclear spins of a sample and a nearby magnetic tip's high field gradient allow for much greater spatial resolution of signals, including detection of individual electron spin[69–71]. However, standard MRFM techniques require samples be positioned onto microscale cantilevers, restricting sample type as well as maximum size[72], and involve tedious fabrication processing. Capacitive coupling readout methods have also been utilized to detect the electric field associated with the precessing magnetic field of nuclear

spins[73]. Such methods also suffer from poor spatial resolution and require specialized and time consuming experimental setups.

### 2.6.3 CNT-Based NMR Signal Detection

Here we propose the utilization of field-emitting CNT devices as nano-antennae for the detection of the FID signal of NMR. Figure 2.16 is a proposed schematic of such a setup. As has been demonstrated in the case of the nanotube radio, CNT field emitters act as excellent candidates in detecting electromagnetic signals[61]. Upon negatively biasing the CNT, such as via a voltage source or battery, negative charge accumulates on the tube with a much higher charge concentration near tip end[63]. The RF signal emitted from a precessing nuclear or electron spin can then couple to the charged nanotube, forcing it to mechanically oscillate. Mechanical vibrations are transduced into electrical signals via the modified field emission current[74].

The vibrational response of the nanotube to an RF signal is greatly enhanced when the frequency of the incoming wave is near the nanotube's frequency. The later can be tuned during operation. Physically shortening the tube, and hence permanently readjusting its resonance frequency, can be carried out by increasing the field-emission current so as to eject carbon atoms from the tip end[75]. In this manner, Jensen *et al.* have demonstrated nanotube resonance frequency adjustment from 350 to 100 MHz[61]. Furthermore, slight adjustments to the voltage bias between electrodes will modify the nanotube's tension, allowing for reversible finer tuning of its resonance frequency.

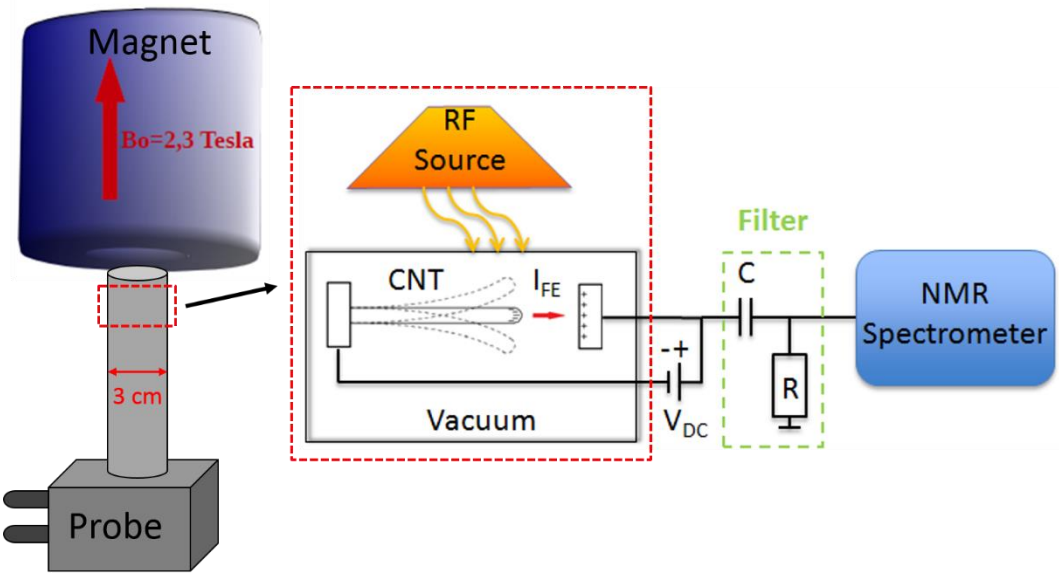


Figure 2.16: Schematic of CNT field emitters for NMR signal detection.

In considering the suitability of CNT field-emitters for NMR signal detection, we note the relevant frequencies to be measured. The Larmor frequency for $^1$H varies from 43 – 170 MHz when placed within magnetic fields in the 1 – 4 T range. In order to calculate the resonant frequency of our singly-clamped CNT oscillators, we can use classical Euler-Bernoulli elastic beam theory[76]. In our devices, the CNT is clamped at one end by ebeam deposited metal electrodes, which we assume here are rigid and are at a fixed angle to the clamped end of the nanotube. Assuming a cantilevered beam, the other end of the tube is free to move. In the Rayleigh-Ritz approximation and neglecting the effect of tension, the wave equation for our CNT beam becomes

$$\rho A \frac{\partial^2}{\partial t^2} y(x,t) = -\frac{\partial^2}{\partial x^2}\left( YI \frac{\partial^2}{\partial x^2} y(x,t) \right) \tag{2-2}$$

where $y(x,t) = y(x)\exp(-i\omega t)$ is the transverse displacement of the beam along its length, $Y$ is the Young's modulus, $I$ is the aerial moment of inertia, $\rho$ is the mass density, and $A$ is the cross-sectional area[77].

The fundamental resonant frequency of a MWCNT is found to be

$$f_o = 0.56\sqrt{\frac{YI/L^3}{\rho AL}} = 0.56\sqrt{\frac{YI/L^3}{m_{CNT}}} \tag{2-3}$$

where $m_{cnt}$ is the mass of the MWNT[78]. In the case of a transverse force applied at the end of the beam, i.e. a point-load, as we assume here in the case of concentrated charges near the nanotube tip's end, the effective spring constant is

$$k_{eff} = \frac{3YI}{L^3} \tag{2-4}$$

where the aerial moment of inertia for a MWCNT of inner radius $r_i$ and outer radius $r_o$ is

$$I = \pi\frac{{r_o}^4 - {r_i}^4}{4} \tag{2-5}$$

The MWCNTs used here vary in diameter, but typically range from 4 – 8 nm. From equation (2-3), the resonant frequencies of such MWCNTs occur in the 10 – 100 MHz range for nanotubes of length less than 1 µm. Hence by a combination of careful electrode design to determine nanotube lengths and tuning resonance as described above, our CNT field-emitting devices are suitable for detecting the NMR relevant frequency ranges.

A key factor in determining the amplitude as well as bandwidth of nanotube vibrations near resonance is the quality factor, *Q*. *Q* is defined as the ratio of elastic energy stored in the resonator to the energy lost during each cycle of oscillation. It is related to an oscillator's rate of dampening, *Γ*, by

$$Q = \frac{\omega_o}{\Gamma} \tag{2-6}$$

where $\omega_o$ is the oscillator's resonance frequency and can be measured experimentally as the ratio of $\omega_o$ to the width of the resonance peak, $Q = \omega_o/\Delta\omega$[79]. The resonance frequency is physically determined as

$$\omega_o = \sqrt{\frac{k_{eff}}{m_{eff}}} \tag{2-7}$$

where the effective mass of the nanotube is determined from Euler-Bernoulli theory to be $m_{eff}$ = 0.24 $m$ and its effective spring constant is dependent on the nanotube's geometry and Young's modulus. Preliminary CNT field emitting devices exhibited quality factors around 50. This is in part due to energy loss via friction in the relatively low vacuum environment of the chamber, manifesting in viscous dampening of the resonator, adsorption of molecules onto the CNT surface, and non-rigid clamping of the CNT to its metal electrode support[80]. Careful design and deposition of uncontaminated, thicker metal electrodes will be critical to obtain better Q values. Quality factors on the order of $10^4$ have been reported for singly clamped nanotube oscillators[62].

We now consider the sensitivity of the field-emitting CNT device in detecting electromagnetic waves. For a damped, driven harmonic oscillator, the amplitude of vibrations as a function of driving frequency is given by

$$|y(\omega)| = \frac{F/m}{\sqrt{(\omega^2 - {\omega_o}^2)^2 + \omega^2 \Gamma^2}} \tag{2-8}$$

where $y$ is the displacement of the mass, $m$, from its equilibrium position, and $F$ is the amplitude of the time varying force acting on the mass with driving frequency $\omega$. For nanotubes driven by an oscillating electric field, the displacement becomes

$$|y(\omega)| = \frac{qE/m_{eff}}{\sqrt{(\omega^2 - {\omega_o}^2)^2 + (\omega\omega_o/Q)^2}} \tag{2-9}$$

where $q$ is the charge on the nanotube tip and $E$ the amplitude of the incoming electric field. The amount of charge at the nanotube tip is a key parameter in determining its sensitivity to external electromagnetic fields and can be calculated as[45]

$$q = 4\pi\epsilon_o E_{ext} L r \left(1 + \frac{r}{2L}\right) \tag{2-10}$$

where $L$ is the length of the nanotube protruding from the electrode and $r$ its radius. For a nanotube with $L$ = 2 μm and $r$ = 5 nm in an applied field of $E_{ext} \approx 10^7$ V/m, the tip will have approximately 1 x $10^{-17}$ C of charge, corresponding to about 100 electrons.

The force sensitivity of the CNT oscillators to detecting electromagnetic waves is limited by the noise in the system. The dominant source of mechanical noise for CNT oscillators at room temperature is from thermal vibrations. The thermal fluctuations in force experienced by the nanotube cantilever is

$$S_F = 4k_B T m_{eff} \Gamma \tag{2-11}$$

where $k_B$ is the Boltzmann constant and $T$ the nanotube temperature. The minimum force detectable by the oscillator in a bandwidth $\Delta f$ is $\sqrt{S_F \Delta f}$, hence the CNT resonators can detect a minimum electric field amplitude given by

$$E_{min} = \left(\frac{1}{q}\right) \cdot \sqrt{\frac{4k_B T m_{eff} \omega_o \Delta f}{Q}} \tag{2-12}$$

For the experimentally relevant values of $T$, $\omega_o$, and $Q$, and using $m_{cnt} = 2 \times 10^{-21}$ kg[62], we calculate a minimum measurable field near 0.1 $V/m/\sqrt{Hz}$. Jensen *et al.* report an experimental minimum sensitivity of 1 $V/m/\sqrt{Hz}$ for similar CNT resonators implemented for RF detection[61]. We can compare this to a reported value of an NMR signal field strength. Prance *et al.* measured the magnitude of the component of the magnetic field due to the precessing spins was in the nT range for a sample of glycerne in a static magnetic field of 43 mT corresponding to a precession frequency of 1.825 MHz, range[73]. This particular value corresponds to electric field strengths whose magnitude is on the lower end of our device's theoretical sensitivity, but can be significantly increased under the influence of larger applied magnetic fields. The signal-to-noise ratio of the NMR signal will be enhanced as the ratio of nuclei in the lower energy state to those in the higher energy state increases. We also note that the magnitude of NMR signals are proportional to the molar mass of the sample and hence increasing sample concentration, and investigating more hydrogen rich compounds, should produce NMR response signals detectable by the field emitting CNT oscillator devices.

Further modifications would improve the performance of the SiN-based CNT devices for NMR applications. With the simple fabrication of additional metal electrodes, the CNT could be electrostatically damped by a side gate, hence altering its quality factor, in order to modify and increase the bandwidth detected[81]. A CNT can be made more sensitive to weaker fields by cooling the devices, improving the quality factor of the nanotube resonator, and by using longer or thinner nanotubes. For NMR signal detection, placement of the sample close to the nanotube probe will

be important. The effect of excitation RF signals on the charged nanotubes must also be carefully considered.

# Chapter 3

# Graphene: CVD Synthesis and Fabrication of Next-Generation Graphene Liquid Cells

## 3.1 Graphene

We now shift our focus to the synthesis and application of another carbon nanomaterials, namely graphene. Graphene is formed by $sp^2$ bonded carbon atoms in a hexagonal lattice exactly one atom in thickness. Its unique bonding structure and 2D layered nature have made this one of the most exciting and promising materials to study. The 2010 Nobel Prize in Physics was awarded to Andre Geim and Konstanin Novoselov for their initial efforts at isolating a single sheet of graphite and studying its electric transport properties in 2004[82]. Since then, graphene has been explored extensively in both academia and industry and a new field of study has emerged, namely that of 2D layered materials[83]. In this chapter, we investigate the synthesis of graphene and take advantage of some of its remarkable properties, such as its unmatched mechanical strength, superb electrical and thermal conductivities, and ultra-thin nature, in developing the next generation of graphene liquid cells for transmission electron microscopy of liquid environments.

### 3.1.1 Structure and Properties

A layer of graphene is depicted in Figure 1.1, showing the honeycomb lattice structure characteristic of a sheet of carbon atoms bonded to three other carbon atoms via $sp^2$ hybridization. The carbon-carbon bond length is 0.142 nm. Bulk graphite is formed by stacked layers of graphene held together by van der Waals

forces at a distance of 0.335nm. The strong $sp^2$ hybridized σ-bonds between carbon atoms makes graphene one of the strongest known materials. Using a nano-indentation technique to poke on the surface of a suspended sheet of graphene, a Young's modulus of ~ 1 TPa and an intrinsic strength of 130 GPa was reported[84]. Nevertheless, it is extremely flexible and capable of conforming to nanoparticles it is transferred upon[85]. Indeed, graphene has garnered much excitement for potential use in flexible and wearable electronics[86,87].

Theoretical tight-binding calculations conducted as early as 1947 reveal a unique band structure for single layer graphite[88]. In particular, the energy dispersion near the Fermi energy, $E_F$, is linear with zero bandgap, making it a semimetal. This linear band structure results in electrons near $E_F$ behaving as massless Dirac fermions. Furthermore, graphene has extremely high electron mobilities with reports of room temperature mobilities as high as ~ 200,000 $cm^2/V{\cdot}s$ reported for suspended graphene, the highest of any material[89]. Graphene's extraordinary electrical properties are discussed in greater depth in several review articles[90–92]

Graphene also possess an exceptionally high thermal conductivity. Room temperature thermal conductivities of ~5000 W/mK were measured for suspended graphene[93]. This is greater than 10 times the best metallic heat conductors, including copper, silver, and gold. Heat transfer in carbon materials, including graphene, is predominantly carried out via acoustic phonons. The strong covalent $sp^2$ bonds between atoms allows for efficient heat transfer via lattice vibrations. Several reviews on the thermal properties of graphene and its implication on potential applications are avaliable[94,95].

## 3.2 Graphene Synthesis

Graphene has been produced using a number of different techniques. Original studies of the properties of graphene were conducted on samples obtained from the mechanical exfoliation of bulk graphite. This can be accomplished by peeling the layered material apart multiple times using adhesives until a few or single layer of the graphite is obtained[82]. In addition to this "scotch-tape" method, scalable levels of graphene can be obtained from the exfoliation of graphite in liquids[96,97]. Mechanical exfoliation produces highly crystalline flakes with high room temperature carrier mobilities of ~ 10,000 $cm^2/V{\cdot}s$ [82] on Si substrates and up to 200,000 $cm^2/V{\cdot}s$ when suspended[82,89], but the flake sizes are small with little control over final geometry. The thermal decomposition of single crystal silicon carbide[98,99] as well as the chemical reduction of graphene oxide films[100,101] have also served as routes to synthesize graphene. SiC wafers, however, are relatively expensive and make

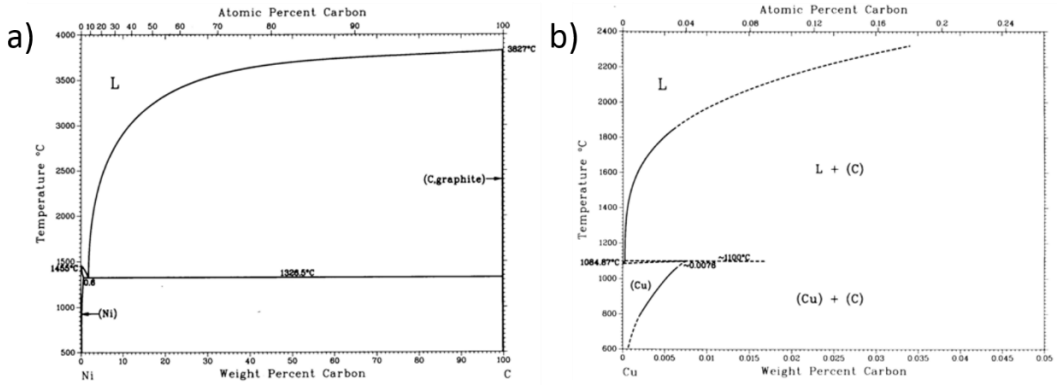


Figure 3.1: Binary phase diagrams for (a) Ni-C and (b) Cu-C

transfer of graphene onto other substrates difficult. Reduced graphene oxide materials also tend to contain a significant amount of oxygen and many defects in resultant graphene films[102].

### 3.2.1 Chemical Vapor Deposition

One of the most promising methods involves the chemical vapor deposition (CVD) growth of graphene whereby gaseous precursors serve as carbon sources for the formation of graphene on a substrate. High quality graphene that can be transferred onto other substrates can be synthesized as large as the catalytic substrates on which they are formed. Various metals have successfully been used as CVD catalysts for graphene growth. These include Ru[103], Ir[104], Pt[105], Pd[106], Co[107,108], Ni[109,110], and Cu[111–113].

Ni and Cu, both relatively inexpensive transition metals, have been used extensively as CVD catalysts for the synthesis of highly crystalline $sp^2$ bonded carbon in the form of nanotubes, graphite, as well as graphene. We briefly explore the formation of graphitic carbon on both metals to highlight the key differences in the catalytic mechanism. The binary phase diagrams of Ni and C as well as Cu and C are presented in Figure 3.1a and Figure 3.1b respectively[114]. The regions denoted by (Ni) or (Cu) are solid metals with the incorporation of the denoted weight percent of carbon. L denotes the metal in its liquid phase, (X) + C where X is either Ni, Cu, or L are two phase regions.

From the binary phase diagram of Ni-C in Figure 3.1a, C becomes increasing soluble in the solid metal at temperatures above 800 °C. Lowering the temperature of the solid Ni-C alloy, however, will decrease the solubility of carbon resulting in its diffusion out of Ni[110,115]. $Ni_3C$ is also metastable and serves as an intermediary phase

during precipitation of the carbon out of the Ni. Precipitation tends to occur at Ni grain boundaries, leading to the formation of thicker carbon layers above these sites[116]. Hence upon cooling the Ni-C system, carbon will form nonuniformly as layered material of varying thickness across the top surface of Ni.

#### 3.2.1.1 Copper-Catalyzed CVD

Copper, on the other hand, does not form any carbide phases, indicative of its much lower affinity for carbon[117,118]. From the binary phase diagram presented in Figure 3.1b, C has a very low solubility in Cu (~ 0.0008 weight % at ~ 1084 °C). We can compare this to Ni, for which ~0.6 weight % of C is soluble in Ni at ~1326 °C. Indeed, numerous reports indicate graphene formation on Cu catalysts is surface mediated, rather than the result of diffusion of C from bulk Cu upon cooling. For instance, by alternating between sourcing methane precursors composed of $C^{12}$ and $C^{13}$ isotopes, Li *et al.* used Raman spectroscopy to map the ordered growth of graphene islands outward from a center reflecting the dosing sequence, signifying growth via surface adsorption[119]. Later studies of in-situ monitoring of Cu surfaces via low energy electron microscopy (LEEM) with partial graphene coverage while cycling between lower and higher temperatures revealed no island growth during cooling [120].

The catalytic mechanism of transition metals has been studied extensively[121]. Metal catalysts provide low energy pathways for reactions to occur. The partially filled d-orbitals and their propensity to form intermediate compounds, such as metastable alloys, makes transition metals particularly well suited catalysts. They are also able to adopt a variety of oxidation states and hence donate or accept electrons from the reagent. The electronic configuration of Cu is given by [Ar] $4s^1 3d^{10}$ and forms the common ions $Cu^{2+}$ with configuration [Ar] $3d^9$ and $Cu^{3+}$ with configuration [Ar] $3d^8$. The incompletely filled d-shells enable Cu to facilitate the exchange of electrons, making them suitable catalysts. This is also the case for other transition metals, such as Ni with its electron configuration of [Ar]$4s^2 3d^8$. Copper, however, has the lowest affinity to carbon due to its normally filled 3d-electron shell, which gives it a more stable configuration. Hence copper does not form any carbide phases[117] and only forms soft bonds with carbon through a charge transfer between the $\pi$ electrons of the $sp^2$ hybridized carbon and the empty 4s shell of copper[121]. The very low reactivity of Cu with C but the ability of C to form stably on the metal surface via weak bonding makes Cu particularly well suited as a catalyst for graphitic carbon formation.

Cu has become the most widely used metal catalyst for graphene synthesis because of its low carbon solubility, abundance, and relatively cheap cost. The latter

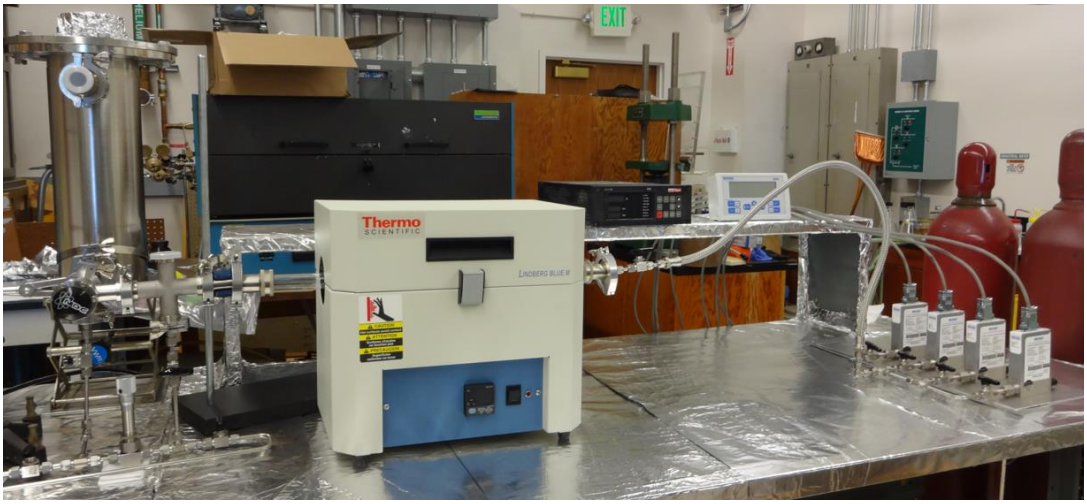


Figure 3.2: High-purity graphene CVD system. High purity precursor gas flow rates are controlled by variable set point, high purity MFCs through a quartz tube positioned in a tube furnace (max. temp. 1200 °C). Growth pressures can be varied via a high precision needle valve downstream the growth chamber which is then connected to a large liquid nitrogen trap and onto to a vacuum pumping station. The synthesis system is backfilled with high purity argon gas during venting.

two are important for scaling up production of graphene, various schemes of which have been proposed for roll-to-roll production and have been implemented in synthesizing sheets as large as 30 inches[122]. Graphene synthesis has been achieved with Cu catalysts in the form of foils of varying thicknesses[122–124], electron beam deposited onto substrates[125], molten Cu on high temperature substrates[126], and as single crystals with a known surface crystal structure[127–129]. Cu foils, in particular, are inexpensive, commercially available from a number of prominent retailers, and easily customizable in terms of dimensions. Their use also makes transfer of graphene onto other substrates relatively straightforward, as described in detail below.

### 3.2.2 Large Domain Graphene Synthesis

The copper foils typically used for the CVD synthesis of graphene are polycrystalline in nature with many grains of different shapes and sizes. Their surfaces are also rough and some, including the very commonly used 99.8% Cu foil from Alfa Aesar (25 µm, product #46365), have very prominent ridges due to the way they are rolled out in production[130]. Graphene grown on Cu foils are a patch work of varying domains stitched together at boundaries. Domain sizes and shapes as well

as the nature of the boundaries in-between them hugely influence the electrical, mechanical, and thermal properties of CVD-grown graphene. For instance, CVD-grown graphene has lower electron mobilities, typically ranging from a few hundred to 4000 $cm^2/V{\cdot}s$ at room temperature[131]. The lower mobilities of CVD grown graphene have been attributed primarily to the presence of domain boundaries. Furthermore, the mechanical strength of graphene boundaries has been reported to depend on the degree of angle mismatch between adjacent domains[132]. We thus set out to understand and ultimately optimize CVD synthesis conditions to grow graphene with large single-crystal domains and few domain boundaries. A simple optical method discussed in section 3.2.2.1 in conjunction with Raman characterization is utilized in this chapter to study and optimize the synthesis of graphene using the main graphene CVD setup in the Zettl lab. Based on the experiments and results discussed here, I went on to design and build a new, high quality graphene CVD system, pictured in Figure 3.2.

### 3.2.2.1 Visualizing Graphene

Numerous techniques are used to visualize and characterize graphene, including scanning electron microscopy (SEM)[123], transmission electron microscopy (TEM)[113], scanning tunneling microscopy (STM)[133,134], low energy electron microscopy (LEEM)[135], atomic force microscopy (AFM)[136], Raman spectroscopy[137], and electron backscatter diffraction (EBSD)[138,139]. By transferring graphene onto SiO substrates with sufficient oxide thickness, graphene domains can also be observed with optical microscopes[140]. Each method has its advantages and setbacks, and we use several of them in characterizing synthesized graphene in this chapter. One major delay, however, is that they tend to be tedious and are time consuming to perform, requiring multistep chemical treatments and complex transfer processes of the graphene from the growth medium. A more convenient and higher throughput method is required which enables quick and accurate assessment of synthesized graphene. Ideally, such a method would not require transferring the graphene onto other substrates or grids and could be done shortly after a growth run.

With this in mind, we employ a rather straightforward observation technique to optically characterize graphene grown directly on Cu foils via a simple thermal treatment process. Graphene has excellent thermal stability[141] and is virtually impermeable while being optically transparent in the visible spectrum. These unique properties as well as its ability to protect the underlying Cu surface from oxidation when subjected to certain oxidizing temperatures (< 400 °C)[142] are critical for enabling the simple optical characterization technique described herein. Cu itself is quite chemically reactive with a surface that is easily oxidized to form Cu oxides.

These oxides are considerably different in color than pure Cu, oftentimes a much darker shade of red or orange. Oxidation of a Cu foil will result in a stark contrast in color between those regions covered with graphene and the bare surface, making graphene domains easily visible by the naked eye under an optical microscope. This can be done following a CVD graphene growth run by thermally treating the Cu foils in air at 150 °C for 5 minutes. Thermal treatment was achieved by either removing Cu foils following growth from the quartz tube and placing it on a clean glass slide on a hot plate, or by exposing the Cu foil to air while still in the quartz tube by disconnecting the flange fittings from both ends of the tube. The former method was more uncontrolled due to high temperature gradients near the surface of the hot plate and inaccuracies in surface temperature. A more uniform oxidization could be achieved for foils still in the quartz tube following a run. The different grains of the polycrystalline Cu surface will oxidize at varying rates and will oftentimes result in the formation of different color surfaces as can be seen in Figure 3.7. To make visualizing the geometric form of graphene domains apparent, the growth phase of a synthesis run is stopped before full coverage of Cu foil is achieved. The reliability of this simple, oxidation-based method to visualize graphene domains can be demonstrated by comparing it to images obtained via SEM and by optical microscopy of samples transferred onto SiO substrates[143].

#### 3.2.2.1.1 Raman Characterization

We gauge the quality of graphene on Cu post-oxidation using micro-Raman spectroscopy with a 514 nm laser. In Figure 3.3a, a white nearly-hexagonal graphene covered region is seen amidst a peach-colored Cu background. These are not the "true" colors of the two regions as the wxPropView software used with the BlueFOX camera on the Olympus BX60 optical microscope will digitally alter color contrasts, but nevertheless two distinct regions are discernible. Raman spectra of the regions indicated by the purple, green, red, and blue dots were taken and are presented in Figure 3.3b. There are no clear peaks in the Raman spectrum taken at the purple spot located over the peach-colored region of the bare Cu. The distinct G and 2D peaks of graphene located at ~ 1590 $cm^{-1}$ and ~ 2660 $cm^{-1}$ respectively are present in all three Raman spectra taken over the white hexagon, indicating coverage by graphene in this region. There is a slight D band peak near 1350 $cm^{-1}$ in the center of the domain designated by the blue dot, signifying the presence of a greater degree of disorder in carbonaceous materials, likely the result of surface impurities which served as the site of graphene nucleation. The intensity ratio $I_{2D}/I_G$ is 8.2, 5.7, and 3.7 for the points indicated by the green, red, and blue dots respectively. The full-width, half-max of the point indicated by the red spot is 28 $cm^{-1}$. These ratios, sharp 2D

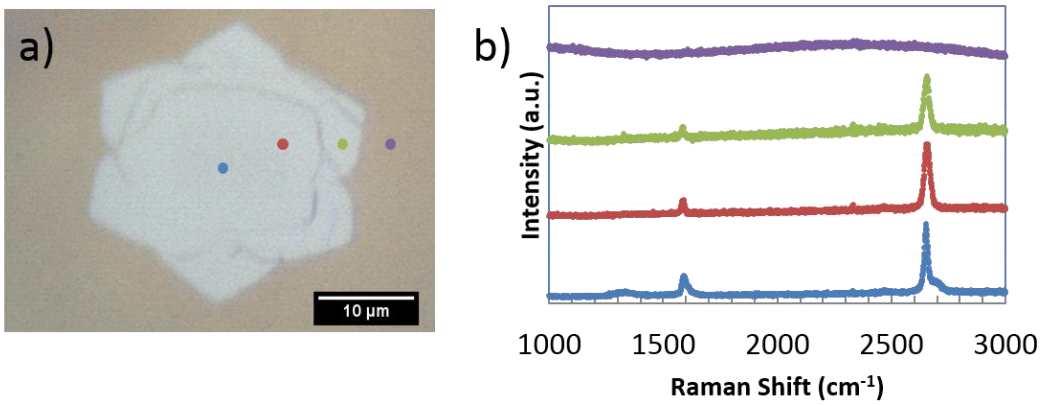


Figure 3.3: Raman spectra of graphene on Cu foil. (a) Optical image of a graphene domain seen as white amidst a darker contrast background which corresponds to the Cu foil. (b) Raman spectra taken at corresponding colored spots indicated in (a).

peaks, and the lack of D band intensity are characteristic of high-quality, single-layer graphene. Hence the previously described thermal treatment is nondestructive to the pristine graphene.

With this simple optical characterization technique based on the oxidation off non-graphene covered Cu, we have a high throughput and swift method to gauge the results of synthesis runs. Indeed, multiple runs could be accomplished back to back with a quick assessment of the results of one run allowing us to change the necessary parameters of the immediately following run with very little lost time.

### 3.2.2.2 Copper Foil Pre-Treatment

The surface structure of the Cu foils plays an important role in the formation of graphene domains. In particular, regions of Cu grain boundaries, defects, surface coarseness, and surface impurities serve as nucleation sites for graphene. Surface damage such as scratches or folds during handling of the foil can also act to seed nucleation[144]. Furthermore, the Cu foils are polycrystalline. Raman spectroscopy and electron backscatter diffraction (EBSD) have also been used to investigate the effect of Cu surface crystallographic orientation on synthesized graphene. Monolayer graphene is reported to grow preferentially on low-index Cu facets and at faster rates on Cu(111) film surfaces[145,146].

The Cu foils examined in these studies were commercially obtained from Alfa Aesar, including the 99.8% purity (25 µm, product # 46365) and the 99.999% (25 µm, product #10950). Cu foils from Sigma Alderich (99.98% purity, #349178) were briefly explored as well. Some of the as-purchased foils are produced with a thin coating covering the surface so as to prevent oxidation of the Cu. Cu foils otherwise are covered by a native oxide layer[147]. Coatings reduce the catalytic activity of the Cu foil, but also introduce impurities which serve as nucleation sites and distort graphene domain growth. Experimentally, graphene grown on as-purchased Cu foils tended to form smaller (< 10 µm) islands. The graphene islands appear as white flower-like shapes, which are known to be composed of multiple crystal domains[120]. Graphene synthesis occurs rapidly and with very little control over domain size and shape.

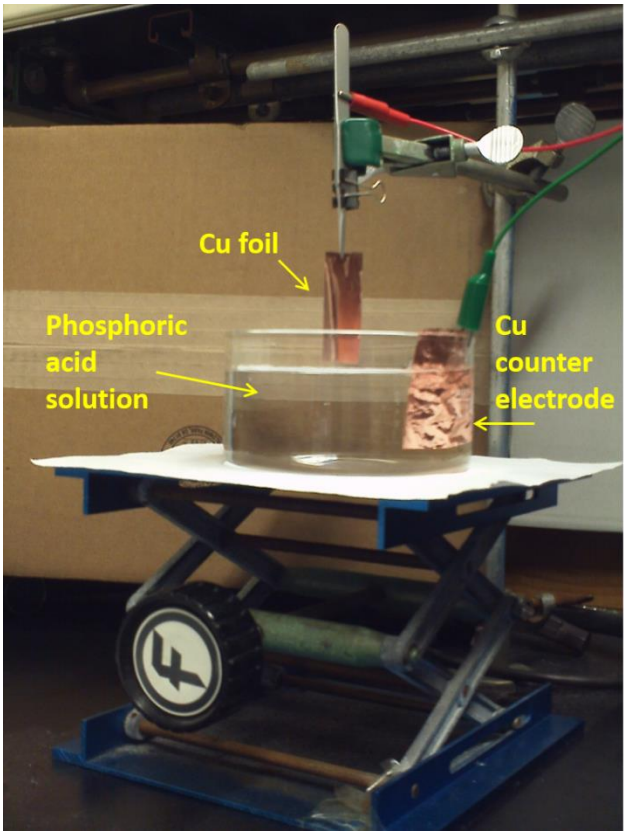


Figure 3.4: Setup for electrochemical polishing of Cu foil.

### 3.2.2.2.1 Electrochemical Polishing

In an effort to minimize nucleation sites, and hence form larger single-crystal domains, treatment of the Cu foil surface before growth steps is vital. Cu foils can be subjected to chemical treatments prior to loading in the quartz tube. For instance, $Cu_20$ can be removed from surfaces to some extent by dipping foils in acetic acid[148]. Electrochemical polishing of metal surfaces to obtain very flat morphologies has also been demonstrated as beneficial to graphene growth[149,150]. In our own experiments, electrochemical polishing was a necessary step in order to synthesize hexagonal graphene domains of larger size. We attribute this to both the smoothening of the Cu foil surface, but perhaps more importantly to the removal of any anti-oxidation coating on the as-purchased Cu foils.

Copper foils were electrochemically polished using a setup as depicted in Figure 3.4. A piece of copper foil 1" x 2" was cut from stock carefully to minimize

wrinkling. One end of the foil was fastened onto by a clean metal tweezer. The foil was then suspended above a solution bath by clamping the metal tweezers above a Petri dish containing the etching solution, which is placed on a vertical translation stage. A counter electrode metal was submerged in the solution bath with the negative electrode attached to it from a power supply. Upon connecting the positive terminal to the metal tweezers, the stage is raised to submerge the Cu foil in the etching solution. Various voltages and etching times were investigated, but a standard recipe was to maintain 5V for 60 seconds during the polishing process. Within a few seconds of submersion, small bubbles are seen to form around the counter electrode. Visual inspection of the Cu foil reveals a gradual shinier surface as etching proceeds. Etch rates will be highest at the corners and edges of the foil as well as at the meniscus at the top of the solution bath. After the surface is sufficiently etched, the stage is lowered, the Cu foil immediately dipped in two consecutive baths of deionized (DI) water followed by rinsing with copious amounts of DI water at the Millipore station, and finally blow-dried with Ar. The Cu foil is then ready to be loaded into the quartz tube, or it can be stored in ethanol to prevent oxidation for later use.

Successfully polished Cu foils of two different purities are presented in Figure 3.5a. Half of the two foils on the left, one of 99.999% purity (top) and the other 99.8% (bottom), are dipped in phosphoric acid solution and electrochemically polished at 5 V for 45 seconds. Both of these foils are then placed on a hot plate at 100 °C for a couple of minutes. Untreated Cu foils from the same stock are placed next to these for comparison. At this magnification, the polished segments look just as shinny and smooth as the unpolished areas. The heat treated, unpolished 99.8% Cu foil looks the same as the original foil, indicating the presence of an anti-oxidation coating present in the as-purchased Cu foil. Electrochemical polishing removes this coating, as evidenced by the much darker coloration in the polished regions due to oxidization upon thermal treatment for both purities of Cu foil.

A single Cu foil with three distinct regions is presented in the magnified optical image on the right of Figure 3.5b. The untreated Cu foil region on the right of the image is seen to consist of many striations, artifacts of the metal-rolling process. The center segment has been dipped in phosphoric acid, but not electrochemically etched. It is seen to contain a much rougher surface with many engraved holes and crater-like features. The electrochemically etched portion of the foil is on the left end. The ridges present in the untreated foil have receded, leaving a much smoother finish. A few cavities are also seen, likely the result of etching from residue phosphoric acid when the Cu foil is removed from the polishing bath prior to being rinsed in water. Electrochemical polishing is able to smoothen the striated surface of the foil due to the variation in current density and hence etch rate across the positively biased surface. Regions which protrude out and have higher curvature,

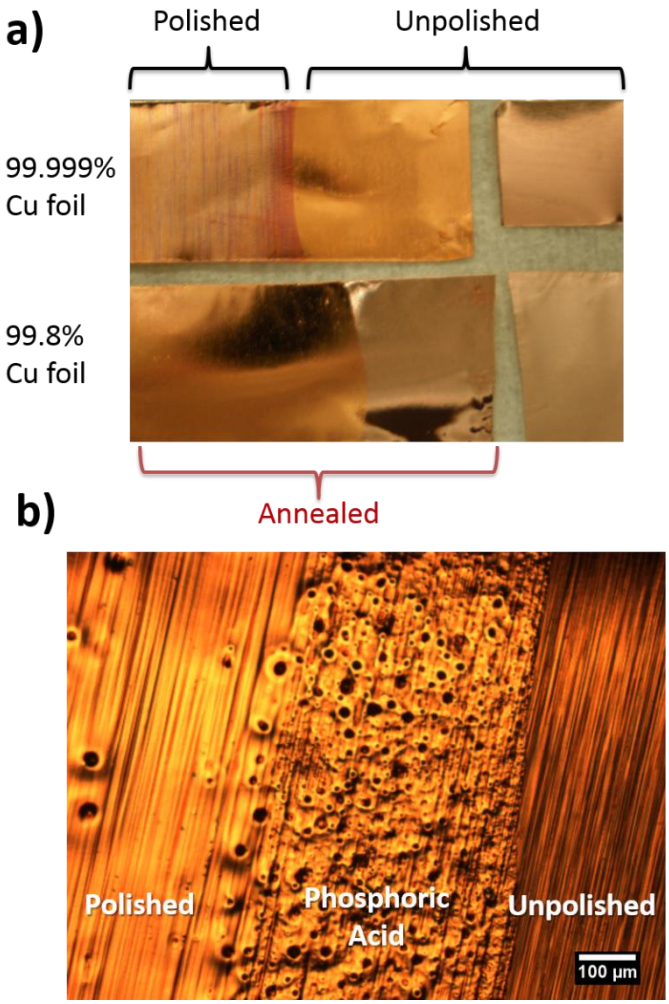


Figure 3.5: Electrochemically polished Cu foil. (a) Low magnification image of electrochemical treatment on two types of Cu foil and (b) higher magnification image of foil near solution meniscus.

such as at the peaks of surface impurities, are etched more quickly than flatter areas[149].

We explored the effect of varying several etching parameters on the final morphology of the Cu surface. The geometry of the counter electrode has a large effect on the uniformity of polishing the Cu foil surface, with geometries investigated including rings, parallel plates, and metal sheets of varying thicknesses and composition. Foil placement with respect to counter electrode also affects uniformity and rate of etching. Much work can be done here to optimize the

configuration, but for the sake of simplicity, most polishing was conducted using a Cu foil counter electrode cut to the same dimensions and from the same stock material used for graphene growth. The to-be-polished Cu foil was submerged into the solution parallel to the counter electrode surface, with the side closest to the counter electrode carefully tracked and ultimately loaded face up in the quartz tube during growth.

We also explored various phosphoric acid solutions as the etching medium. Higher concentrations of phosphoric acid provided for quicker, but also more nonuniform etching of surfaces. The best results were obtained with an electrochemical polishing solution consisting of 100 mL of DI water, 100 mL of ethanol, 50 mL of orthophosphoric acid, 15 mL of isopropyl alcohol, and 1 g of urea (we refer to this recipe as the "50 mL orthophosphoric mixture" in the remainder of the chapter).

#### 3.2.2.2.2 Annealing

Pretreatment of Cu foils prior to graphene growth oftentimes involves an annealing phase where the Cu foil is thermally reduced in a hydrogen atmosphere at some elevated temperature. In our studies, this was achieved by flowing hydrogen through the quartz tube with the Cu foil at some elevated temperature, typically above 1000 °C, for some extended period of time. The annealing and growth steps can be carried out at different pressures, although system pressure is oftentimes kept constant throughout for simplicity. Thermal treatment in hydrogen prior to growth helps to reduce oxygen present in the quartz tube and on the foil as well as remove moisture present in the system. Annealing the foil is also meant to increase Cu grain sizes and eliminate surface structural defects.


Figure 3.6: Effect of Cu annealing on graphene growth.(a) 150 sccm $H_2$ under vacuum pressure @ 1020 °C for 1 hr. (b) 500 sccm $H_2$ at 17 psia at 1020 °C for 1 hr. (c) 500 sccm $H_2$ at 17 psia at 1020 °C for 5 hrs.

The results of various annealing parameters on graphene growth are presented in Figure 3.6. In these trials, synthesis was conducted using 99.8% purity Cu foil under the same growth parameters flowing 2.5 sccm $CH_4$ and 500 sccm $H_2$ at 1020 °C for 65 min. In all of the runs, we note the presence of cavities in the Cu foil which result from residue etching solution as described above. For an anneal under vacuum conditions flowing 150 sccm $H_2$ at 1020 °C for 1 hour, as presented in Figure 3.6a, the ridges of the Cu foil have not completely disappeared, and barring the indentations, the foil is smoother than when untreated. Graphene islands of various non-distinct shapes less than 100 µm in size can be discerned. When annealing is done just above atmospheric pressure (17 psia) with 500 sccm $H_2$ at 1020 °C for 1 hour (Figure 3.6b), the Cu surface has much flatter ridges. The surface is more fluid, with less protrusions and edges. Graphene domains up to 300 µm edge-to-edge with hexagonal as well as square shaped structures are present. By increasing the annealing time to 5 hours, as depicted in Figure 3.6c, there does not appear to be any suppression in nucleation with graphene domain density and size comparable to the 1 hour anneal of Figure 3.6b. The prominent ridges of the original Cu foil, however, have completely disappeared. Instead, we note the existence of prominent step edges and height gradients across the surface. At temperatures above ~800 °C, Cu will sublimate from the foil surface. The rate of sublimation depends on factors such as temperature and system pressure. Indeed, foils annealed at 1020 °C for 5 hours under low pressures (with the rough vacuum pump on) were completely evaporated. Foil surface morphology fluidly changes during annealing and growth steps, including the formation and evolution of Cu step edges which become more pronounced for longer anneal times[120]. Increasing the annealing temperature to 1070 °C did not result in any more noticeable cleaner Cu surface or enhancement in graphene domain size for the growth parameters explored here.

Hence annealing at atmospheric pressure under a flow of $H_2$ at 1020 °C for 1 hour was sufficient for preparation of Cu foils for graphene growth. High temperature annealing of the Cu substrate reduces surface impurities, kinks, and defects as well as removes contaminants which leads to a suppression in graphene nucleation. Reducing the nucleation density is conducive to the growth of larger monocrystalline domains. Annealing may also aid in the preferential growth of Cu(111) facets, the lowest energy Cu surface[151], which have been reported to enable faster rates of high quality graphene growth when compared to other crystal surfaces[145]. If the growth step is to be conducted at low pressure, simply turning on the vacuum pump following an anneal at atmospheric pressure will result in the abrasion and roughening of the Cu foil surface due to the sudden increase in turbulent gas flow over the molten Cu surface. It is thus necessary to drop the

temperature of the system below 800 °C before radically changing pressure or gas flows.

### 3.2.2.3 Copper Foil Purity

Utilizing the pretreatment techniques described above, we investigated the influence of Cu foil purity and type as well as the effect of electrochemical polishing on graphene island growth. The results of examining untreated and polished Cu foil of both 99.8% purity (25 µm, Alfa Aesar, # 46365) and 99.999% purity (25 µm, Alfa Aesar, # 10950) are presented in Figure 3.7. For all of these runs, substrates were annealed under 150 sccm $H_2$ at 1020 °C for 1 hour at atmospheric pressure prior to the growth step conducted flowing 500 sccm $H_2$ and 2.5 sccm $CH_4$ at 1020 °C for 5 minutes at low pressure (i.e. with valve to the rough vacuum pump fully open). The surface of the as-purchased higher purity foil (Figure 3.7a) is much smoother with well-defined grain boundaries and no ridges present compared to the 99.8% purity foil (Figure 3.7b). Note also the contrast in Cu grain colors due to the oxidation of different crystal surfaces. After 5 minutes of growth, there are many isolated and some conjoined graphene islands less than 10 µm in size (Figure 3.7a and Figure 3.7b). Many of the polygonal shaped regions of growth are hexagonal with some nearby graphene domains correlated in orientation, as highlighted by the red circles in Figure 3.7a and Figure 3.7b. There are clear linear arrays of graphene islands formed on the 99.8% foil of Figure 3.7b. This is due to the preferential nucleation at defects along the Cu surface, in this case along ridges which are not present in the higher purity foil. The islands grow across grain boundaries with many preferentially nucleating at such sites as denoted by the yellow arrow in Figure 3.7a. This along with the lack of correlation in orientation of most domains grown on a single Cu grain suggests a weak influence of the Cu grain structure on graphene growth[134]. By examining larger regions of the foils beyond those imaged here, the density of graphene islands was found to be comparable for the two foil types in these runs.

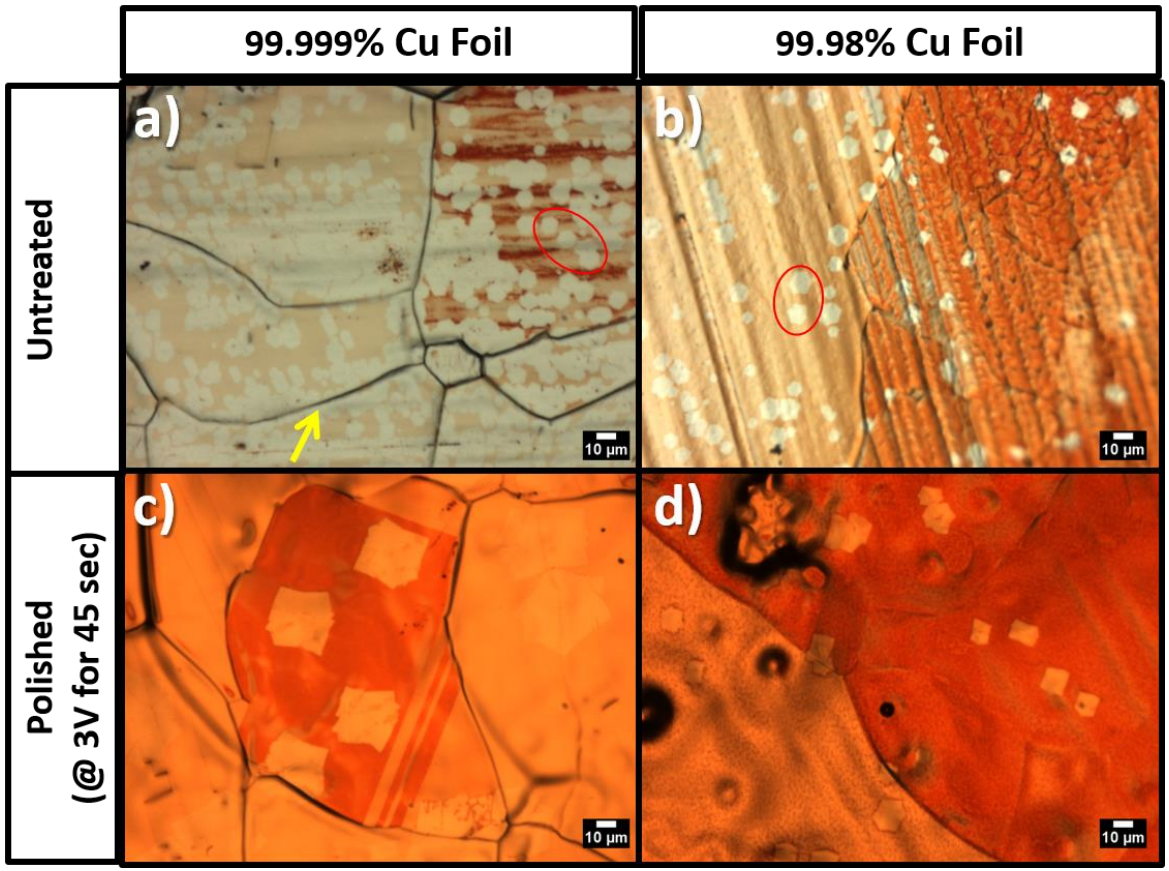


Figure 3.7: Effect of Cu foil purity and electrochemical polishing on graphene growth.(a) – (d) first annealed with 150 sccm $H_2$ at 1020 °C for 1hr followed by growth with 2.5 sccm $CH_4$ / 500 sccm $H_2$ at 1020 °C for 5 min.

Significantly different synthesis results are obtained for both foil types when they are electrochemically polished prior to growth runs. Cu foils were treated in the 50 mL orthophosphoric acid mixture described above at 3V for 45 seconds. Polishing smoothened out foil surfaces and reduced the number of nucleation sites as evidenced by the drastically lower density of graphene islands in both Figure 3.7c and Figure 3.7d. The regions of graphene growth measure roughly 10 μm for the 99.8% purity foil (Figure 3.7d), but are almost three times larger when grown on the high purity Cu (Figure 3.7c). Electrochemical treatment is vital for the suppression of nucleation sites and smoothening of Cu foil surfaces, hence fostering the growth of larger graphene domains.

#### 3.2.2.4 Role of Hydrogen & Precursor Partial Pressures

After exploring various treatments and factors involved in annealing Cu foils, we sought to understand the role of various parameters during the growth step. Different CVD setups and systems can produce different results even for the same growth recipe. This can in part be attributed to the natural variations in setup, including gas precursor purity, geometry of tubing and CVD setup, and the very important pumping mechanism and cooling trap used to bring the system under vacuum. The cleanliness of the system and its maintenance is also vitally significant. Indeed, growth recipes which produce a particular type of graphene may be difficult to reproduce on the same CVD equipment some time later. Nevertheless, understanding the roles of growth parameters and their influence on the synthesis of graphene, especially for a particular CVD setup, is critical for being able to customize growth patterns and gain ultimate control of graphene quality.

One of the most important components of any CVD recipe is hydrogen gas. It is the cornerstone of any annealing step, sometimes introduced into the foil-containing quartz tube along with a buffer gas such as argon. Hydrogen in the elevated temperature atmosphere of the tube furnace will thermally reduce oxides and remove water vapor within the quartz tube. At higher gas partial pressures, less Cu evaporates off of the foil surface, allowing for longer annealing times at higher temperatures.

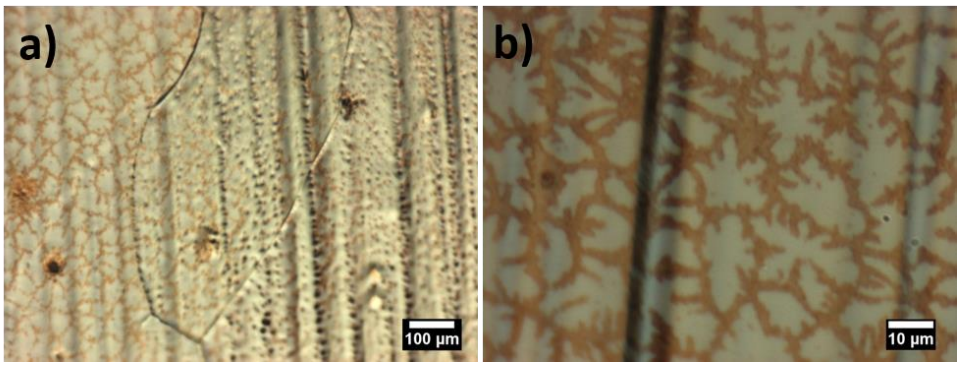


Figure 3.8: Two-step graphene growth images taken at low mag (a) and high mag (b) showing flower-patterned graphene domains. Growth phase consists of first 20 sccm $CH_4$ / 10 sccm $H_2$ for 5 min followed by 120 sccm $CH_4$ / 10 sccm $H_2$ for 5 min all at 1020 °C.

Hydrogen plays an even more vital role during the growth step. To understand its influence, the results of graphene growth as a function of hydrogen flow rate and ratio to methane precursor gas during the growth phase of graphene synthesis was investigated. A standard two-step growth recipe used often in the Zettl group[152] involved first flowing 20 sccm $CH_4$ with 10 sccm $H_2$ for 5 min followed by 120 sccm $CH_4$ with 10 sccm $H_2$ for another 5 minutes, all at 1020 °C and low pressure (i.e. with the rough vacuum pump on). With a lower flow rate of methane in the first step, fewer nuclei of graphene will be formed. After 5 minutes, increasing the partial pressure of methane while maintaining the temperature will promote faster graphene growth and full surface coverage. In the latter step, few new nuclei will be formed and the increase in available methane will preferentially promote growth from existing graphene nuclei[153]. The results of such a two-step growth process are presented in Figure 3.8. In the optical image of Figure 3.8a, portions of the Cu surface are fully covered with graphene. Oxidation of the foil makes graphene domain boundaries darker in contrast and clearly visible. In the optical image of higher magnification of Figure 3.8b, graphene islands are seen to form flower-like shapes 10 – 20 µm in size. The dendritic extensions of the islands lack any aligned structure. In both steps of this growth recipe, the ratio of $H_2$ to $CH_4$ flow rate is less than 1 with plenty of methane precursor gas available to supply carbon to the Cu foil surface. Similar flower-shaped graphene domains a few tens of µm in size were obtained for single step growths for $H_2$: $CH_4$ flow rate ratios $\leq 1$ when $CH_4$ flow rate was varied in the 2.5 - 20 sccm range.

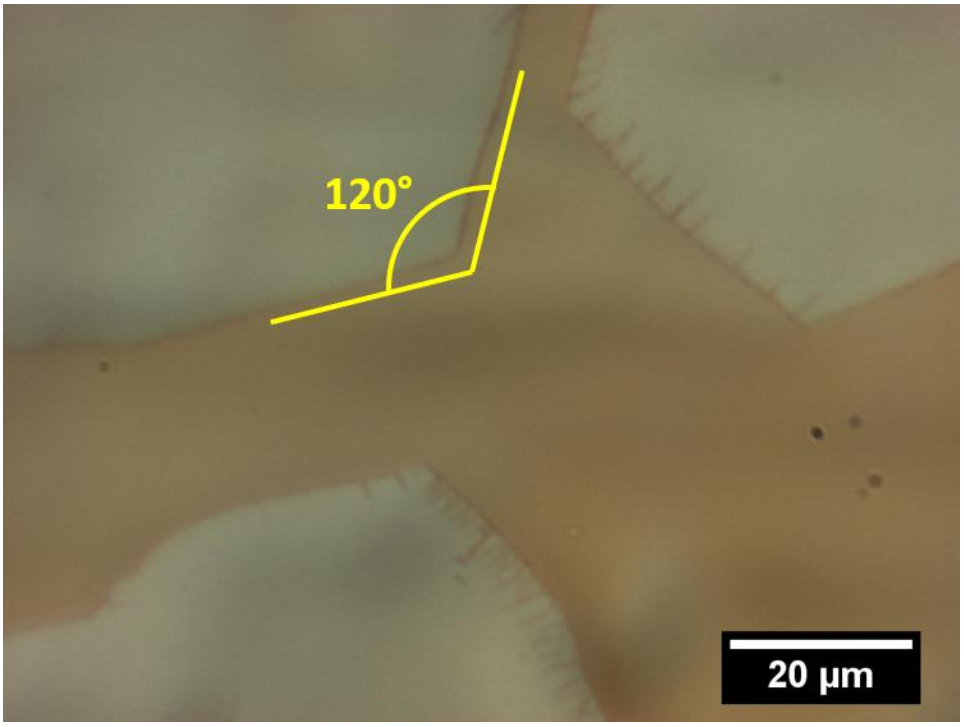


Figure 3.9: Hexagonal graphene domains exhibiting 120° angles and tears near domain edges.

When the flow rate and hence partial pressure of $H_2$ was much greater than that of $CH_4$, a different regime of graphene growth is achieved. The results of a synthesis flowing 2.5 sccm $CH_4$ and 500 sccm $H_2$ at 1020 °C at low pressure are presented in Figure 3.6 for a range of different annealing parameters, Figure 3.7 over different copper foils, and Figure 3.9. Graphene domains form distinctly polygonal shapes, most often hexagonal in nature. As highlighted in Figure 3.9, the edges of the graphene domains tend to form 120° angles. The hexagonal formation of graphene domains is important and worthy of further explanation. In particular, such domains are known to be single-crystalline[154,155]. Adjacent domains may merge together to form domain boundaries, as is the case in Figure 3.6b and Figure 3.6c. Occasionally, tears and cracks are readily observable on graphene domains as in Figure 3.9. This can be attributed to the differences in thermal expansion coefficients between graphene and copper ($\alpha_{graphene} = -6 \times 10^{-6}$ /K at 27 °C [156], $\alpha_{Cu} = 24 \times 10^{-6}$ /K [157]). Upon cooling from high temperatures following the growth step, the Cu foil will shrink and mechanically deform the graphene forming wrinkles in addition to tears[144].

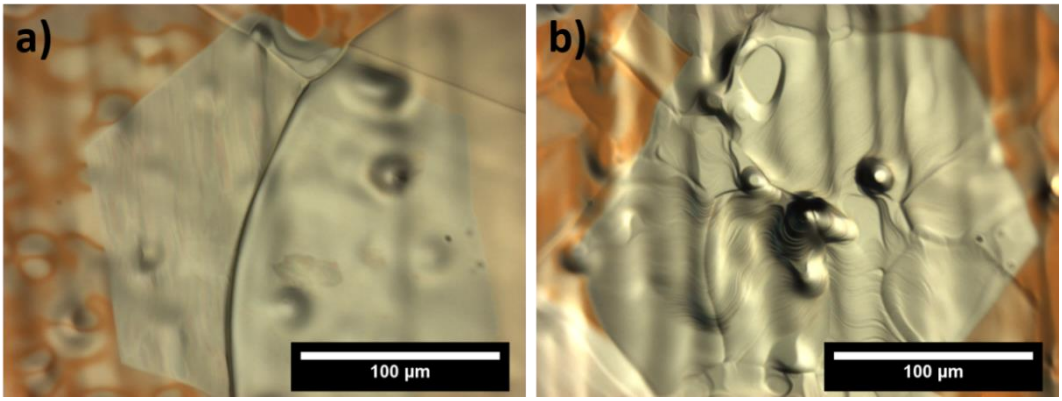


Figure 3.10: Hexagonal graphene domains (a) growing across Cu grain boundaries and (b) preferentially nucleating at Cu defect sites.

Furthermore, the singly-crystalline graphene domains tend to nucleate at defect sites and can grow across Cu grain boundaries, as evidenced in the optical images of Figure 3.10. In Figure 3.10a, a graphene domain roughly 200 µm in width with straight hexagonal edges has formed across a Cu grain boundary over two Cu grain structures. In the optical image of Figure 3.10b, the noticeably elevated defect on the Cu foil surface served as the site of nucleation. Very clear Cu steps and edges are visible in the region of graphene growth. These form due to the motion induced of Cu steps on the foil from Cu sublimation at the elevated temperatures during growth. Cu atoms beneath the graphene islands must diffuse laterally from beneath the graphene out to its edge before they can leave the surface. Hence the front of a Cu sublimation from the foil surface is decelerated upon coming across graphene domains. This results in the bunching up of step edges from various sublimation fronts underneath the graphene to form more pronounced steps. This phenomenon has been recorded by Wofford *et al*. for Cu hillock formation beneath four-lobbed graphene islands[120].

Graphene growth rate can be reduced by increasing the partial pressure of hydrogen during the growth step as indicated by the results presented in Figure 3.11. A standard polishing preparation and anneal at 1020 °C with 500 sccm $H_2$ for 1 hour at 17 psia was following by a growth flowing 2.5 sccm $CH_4$ with varying amounts of $H_2$ for two different times. After 65 minutes of growth, the edge-to-edge width of synthesized graphene domains were 73 µm, 150 µm, and 190 µm for $H_2$ flow rates of 1000 sccm, 800 sccm, and 500 sccm respectively. The greater partial pressure of $H_2$ reduces the rate of graphene domain growth. After 2 hours of growth, the domain sizes expand to 310 µm and 240 µm under flows of 800 sccm and 1000 sccm of $H_2$ respectively with full coverage attained when flowing 500 sccm $H_2$. If the growth rate

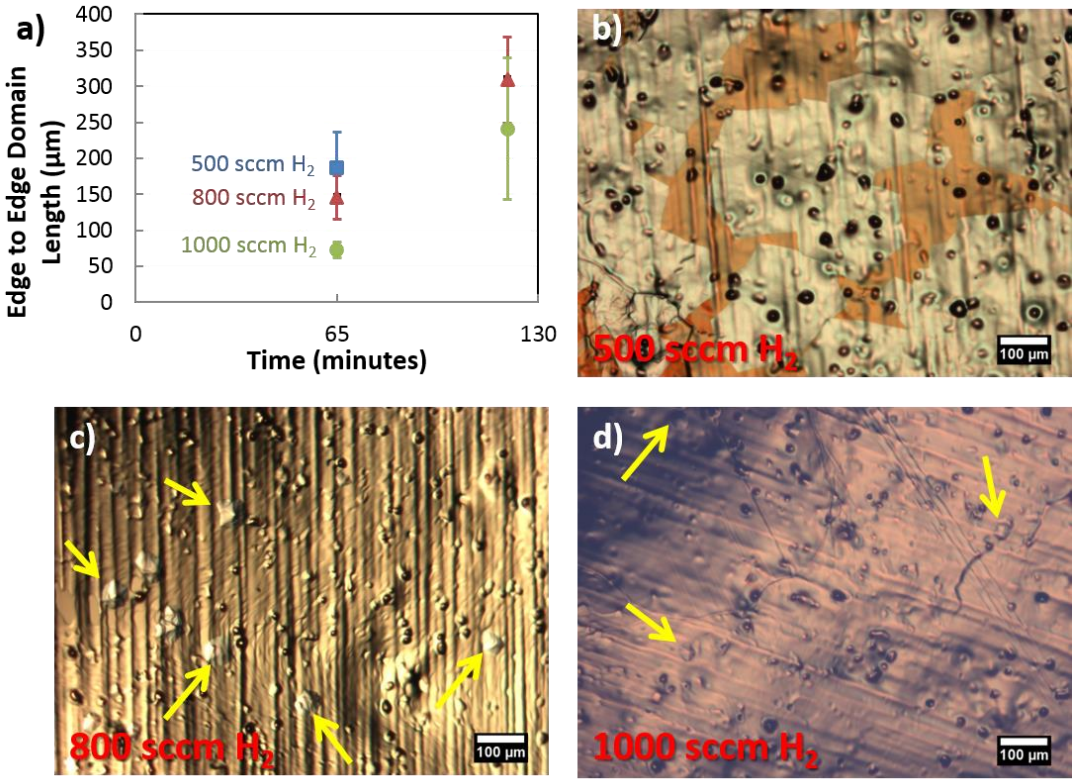


Figure 3.11: Influence of $H_2$ on graphene domains.(a) Domain size dependence on $H_2$ flow rates over time. Graphene domains, indicated by yellow arrows, on Cu foil surfaces with (b) 500 sccm $H_2$, (c) 800 sccm $H_2$, and (d) 1000 sccm $H_2$. All runs were conducted flowing 2.5 sccm $CH_4$ for 65 min.

of graphene domains is substantially reduced such as by dramatically increasing the $H_2$: $CH_4$ ratio, continued Cu sublimation from the non-covered foil surface will result in greater impedance to domain growth. This is due in part to the formation of steep Cu steps at the edges of the graphene domains to the greatly diminished Cu surface. This effect is even more pronounced at low pressures when there is greater Cu sublimation. For particularly high $H_2$: $CH_4$ ratios, as when 1000 sccm $H_2$ was used, domain sizes tended to saturate and full coverage of Cu foils were not attainable with longer growth times.

Optical images of the Cu foils following 65 min runs with various $H_2$ content are presented in Figure 3.11b, Figure 3.11c, and Figure 3.11d. Domains possess crisp straight edges and are predominantly hexagonal. The smaller graphene regions in Figure 3.11c and Figure 3.11d are indicated by yellow arrows with those of the former visibly elevated from the Cu foil surface. This effect is due to the pronounced

sublimation of Cu from the non-covered surface which, as discussed above, may limit the ultimate size of the graphene domains and prevent full coverage growth. Furthermore, there is also a reduction in the density of nucleated graphene islands as the ratio of $H_2$: $CH_4$ is increased. The higher partial pressure of $H_2$ is seen to suppress sites of graphene growth.

The maximum attainable $H_2$ flow rate using the Zettl group CVD system was 1000 sccm. Furthermore, the partial pressures of the growth gases are potentially as important as their relative ratios. We thus sought to push the limits of $H_2$: $CH_4$ by decreasing the flow rate of $CH_4$, which under the previous experimental setup could not be carried out below 2.5 sccm $CH_4$. Using a Brooks model 5850S mass flow controller with maximum flow rate of 4 sccm, $CH_4$ flow rates of 1.0, 0.5, and 0.15 sccm corresponding to experimentally measured partial pressures of 23, 12 and 4 mTorr could be attained. For a growth step involving 1.0 sccm $CH_4$ and 500 sccm $H_2$, sharp hexagonally shaped graphene domains 40 μm in width following a 75 minute run at 1020 °C were obtained. Longer growth times were not conducted to see if full surface coverage could be obtained. No graphene was synthesized when 0.5 sccm $CH_4$ was used along with 500, 250, 100, or 10 sccm $H_2$ at 1020 °C after 1 hour. These preliminary results suggest reducing methane partial pressures while keeping $H_2$:$CH_4$ flow ratios relatively large are a promising regime for the nucleation of a few isolated graphene domains which could be made to grow large.

We now elucidate the multiple roles $H_2$ plays in the synthesis of graphene. As previously mentioned, the presence of $H_2$ during annealing and the growth step helps reduce oxygen present in the system and on the Cu foil surface. Furthermore, it serves as a co-catalyst in the activation of carbon on the Cu foil surface. Without $H_2$ present during the growth step, the $CH_4$ precursor gas would have to chemisorb on the Cu surface to form the activated carbon species which could react on the surface to grow into graphene. The activated carbon species, which serve as intermediaries between the initially adsorbed $CH_4$ molecule and the final surface C atom plus four H atoms, are methyl ($CH_3$), methylene ($CH_2$), and methylidyne (CH). DFT calculations reveal that the dehydrogenization of methane as well as all three intermediaries on a Cu surface are endothermic with activation energy barriers in the 1 – 2 eV range[158]. Atomic carbon is likely energetically unfavorable on a Cu surface, required ~ 3 eV of energy to produce C + 4H from an adsorbed $CH_4$ molecule [158]. In the early phases of graphene growth, active carbon species on the surface likely contain hydrogen until they grow large enough to be stable without hydrogen. The following steps are proposed as a viable route by which hydrogen catalyzes the formation of activated carbon species on the foil surface[159]

$$Cu + H_2 \rightarrow Cu + 2H_S \quad (3\text{-}1)$$

$$(CH_4)_S + Hs \rightarrow (CH_3)_S + H_2 \quad (3\text{-}2)$$

$$(CH_x)_S + H_S \rightarrow (CH_{x-1})_S + H_2, \qquad x = 3,2,1 \quad (3\text{-}3)$$

where the subscript *s* denotes a surface adsorption. In the first step, since molecular hydrogen will dissociate on the Cu, it is able to form surface active hydrogen atoms. These could then react with surface adsorbed molecules of methane to form activated surface methyl. Subsequent dehydrogenation will produce $(CH_2)_s$ and $(CH)_s$. The activated carbon species come together in the formation of the more stable graphene, which may occur in the following series of steps:

$$(CH_3)_S + H_S + graphene \rightarrow (graphene + C) + 2H_2 \quad (3\text{-}4)$$

$$(CH_2)_S + graphene \rightarrow (graphene + C) + H_2 \quad (3\text{-}5)$$

$$(CH)_S + H_S + graphene \rightarrow (graphene + C) + H_2 \quad (3\text{-}6)$$

Hydrogen also plays a vital role in controlling the size and shape of graphene domains during growth. Following nucleation, graphene islands will continue to grow with the subsequent attachment of carbon atoms following the above described schemes. Hydrogen is capable of etching carbonaceous materials and attacks weakly bound carbon atoms at the growth front of graphene islands[159]. In the range of low $H_2$:$CH_4$ concentrations, carbonaceous species are produced and replenished onto growing graphene islands faster than the hydrogen etch rate. This results in the formation of many smaller graphene regions in a "diffusive" growth regime whereby dendritic, flower-like patterns are formed. As the hydrogen partial pressure is increased for a set methane flow, weakly bound carbon atoms are readily etched from the growth edges of graphene. The observed prevalence of hexagonally shaped domains indicates a strong bond among the carbon atoms constituting their domain edges. The most robust edge termination is in the zig-zag configuration[154]. Raman mapping and electron diffraction of hexagonal domains confirm the zig-zag nature of edges[134,154,159]. Furthermore, hexagonally shaped domains are undoubtedly regions of a single crystallinity, as has been verified in diffraction studies[150,155,160]. As domain size increases, less of the Cu foil surface is exposed to act as a catalyst for methane adsorption and carbon activation, resulting in lower graphene growth rates[153]. The ultimate size of the graphene domains will be dictated by the interplay between hydrogen etching of graphene edges and the availability of carbon atoms to replenish them in addition to the aforementioned changing Cu surface morphology. Under

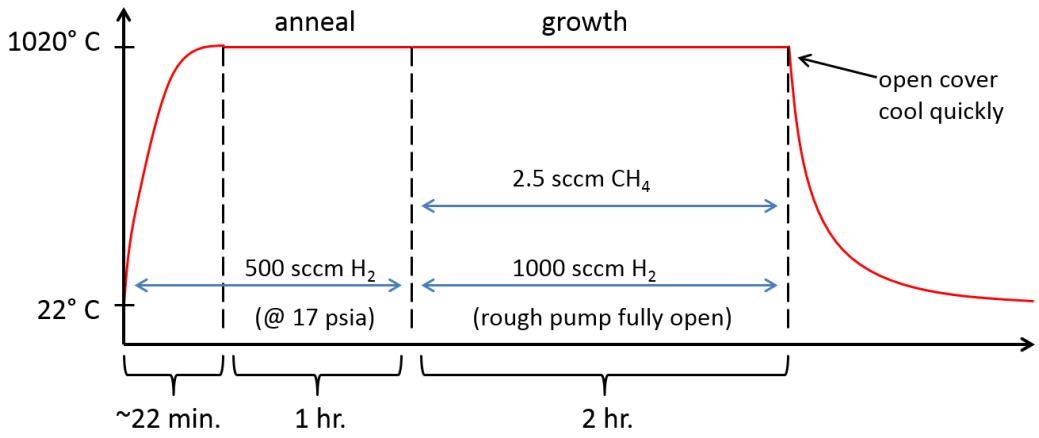


Figure 3.12: Growth recipe for large domain graphene.

certain conditions, such as for low $CH_4$ partial pressures, the graphene islands may stop growing once they reach a certain size due to the insufficient supply of active carbon species on the remaining Cu surface to attach onto graphene edges faster than the edges are etched. This will result in partial coverage by graphene no matter how long the growth phase is extended. In our experiments, no growths occurred for $CH_4$ partial pressures below 12 mTorr.

### 3.2.2.5 Large Domain Graphene

With deeper insight into the role of various parameters on the synthesis of graphene, we sought to grow large, single-crystalline domains of monolayer graphene. Using the Zettl group CVD setup for graphene synthesis, we used the growth recipe presented in Figure 3.12. The Cu foil employed here is 99.8% in purity simply because it was more readily available and cheaper than the higher grade Puratronic (99.999%) foil. A 1" x 2" piece of Cu foil is electro-polished in the 50 mL orthophosphoric mixture solution at 5 V for 60 seconds. The rinsed and blow-dried foil is then slid into a cleaned and annealed 1" quartz tube. After placing the quartz tube with Cu foil centered in the middle of the tube furnace, it is fastened tightly to the mass flow controllers (MFCs) on one end and the exhaust on the other. Prior to increasing the temperature, the system is purged multiple times with Ar and/or $H_2$ gas.

Under a flow of 500 sccm $H_2$, a needle valve between the quartz tube and an exhaust line out to the fume hood is adjusted to maintain a slight positive pressure

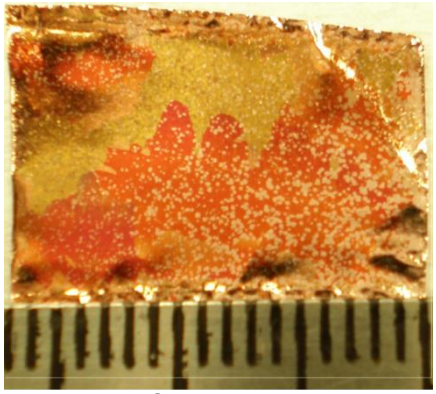


Figure 3.13: Cu foil post-synthesis. Large individual graphene domains are visible with the naked eye as lighter contrast speckles amidst a darker, oxidized Cu foil surface. Precursor gases flowed from the left to the right.

overpressurizing the system is dangerous and requires the user actively monitor the pressure. The temperature of the furnace is then ramped up to 1020 °C in approximately 26 minutes. The foil is then annealed under these conditions for 1 hour. For the subsequent growth step, the pressure inside the quartz tube must gradually and very carefully be dropped. This is accomplished by first turning on the mechanical rough pump (Alcatel Pascal 2010 SD) with the value from the quartz tube to the pump initially closed. The needle valve leading to the fume hood is then closed, followed by a gradual opening of the valve leading to the rough pump. This last step must be conducted very carefully to ensure the pressure does not build up too high in the system while at the same time avoiding a sudden rush of gas out to the pump which may coarsen the surface of the Cu foil or worse, carry the foil itself. With the valve to the rough pump fully open ensuring the highest vacuum conditions for growth, the flow of $H_2$ is gradually ramped up to 1000 sccm and $CH_4$ flow initiated at 2.5 sccm for 2 hours.

The growth phase is terminated by cooling the system very rapidly in order to quench growth dynamics. This is achieved by opening up the top of the tube furnace until the temperature drops below ~ 800 °C, followed by further cooling the region of the quartz tube with an electric fan. Other schemes by which to rapidly cool the Cu foil include removing the foil from the tube furnace altogether such as by sliding the furnace down the axis of the tube or by using magnets to pull a boat-mounted Cu foil from the furnace's hot zone [161]. Once the temperature of the system has dropped below 50 °C, the gasses can be cut off, the quartz tube vented back up to

pressure, and the Cu foil carefully removed. In the clean, high-purity setup depicted in section 3.2.2, the quartz tube is vented with Ar gas to minimize contamination.

The Cu foil is then heated to 200 °C for 4 minutes to oxidize the non-covered Cu regions making the graphene coated regions clear. An optical image of the foil post-synthesis is presented in Figure 3.13 with yellow, orange and red regions visible throughout due to Cu oxidation of different grains. There are also many light colored speckled regions dotting the entire foil which are more densely present on the right end. These are regions covered by graphene domains and large enough to be seen by the naked eye without the need for microscopes. The blue arrow indicates the direction of gas flow with the surface pictured here being the side of the Cu foil facing upward when loaded in the quartz tube.

In Figure 3.14a – f, higher magnification optical images of different regions on the Cu foil are presented. Hexagonal graphene domains with straight edges are clearly visible throughout. Multiple domains meet forming boundaries which cannot be clearly distinguished using this optical characterization technique. This 2 hour run produced partial coverage over the foil. A higher tendency to nucleate along Cu foil ridges has produced some linear arrays of domains, as in Figure 3.14a and Figure 3.14b. The domains range is size, with hexagonal shaped domains as large as 400 μm in edge-to-edge length attainable.

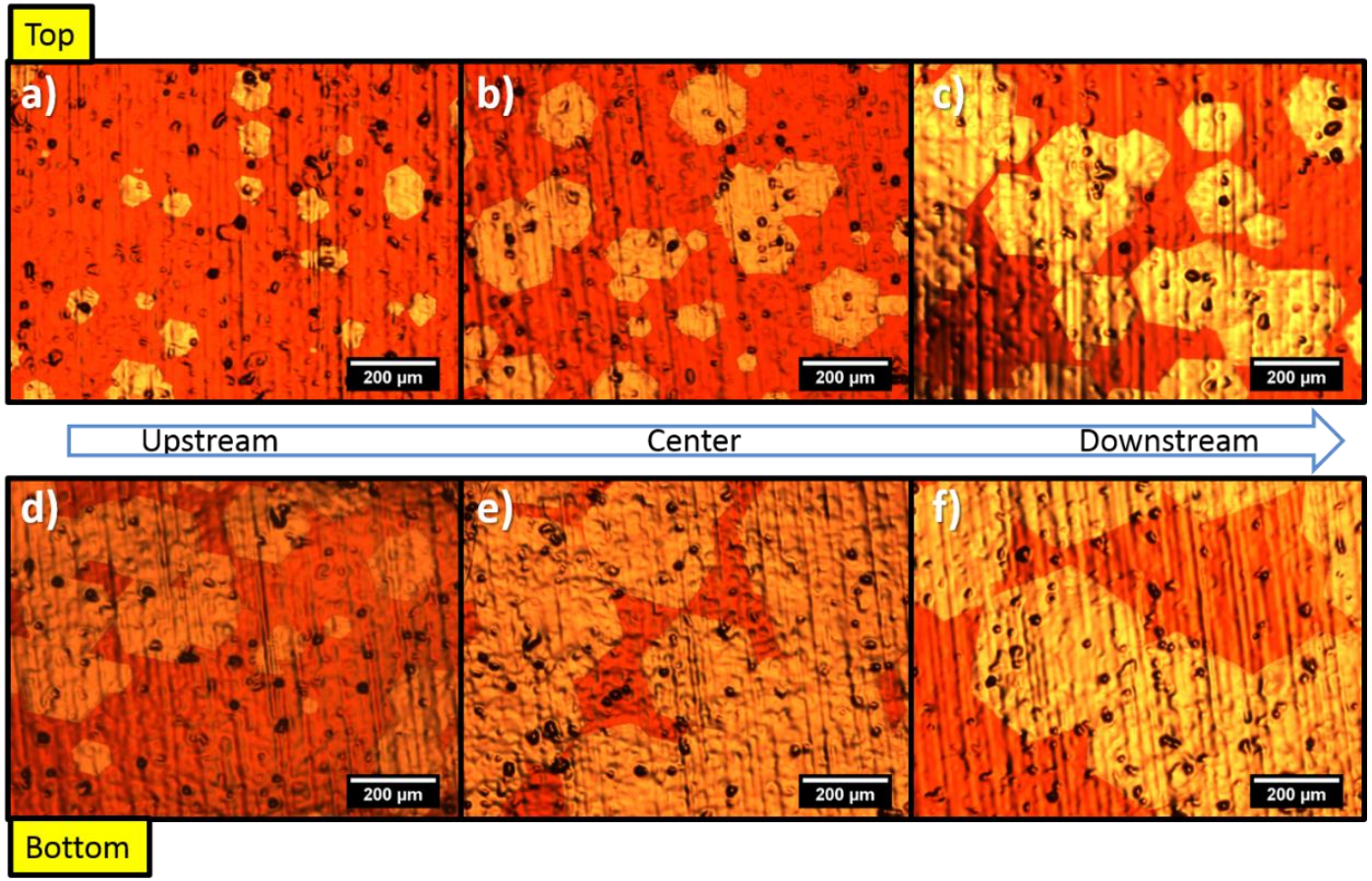


Figure 3.14: Large hexagonal domains of graphene on Cu foil. Domain sizes and shapes vary across the top and bottom (labeled) as well as horizontally across the surface of the Cu foil. Precursor gas flow direction is labeled.

The spatially inhomogeneous domains have formed throughout the top and bottom of the Cu foil. The variation in domain sizes, even within a small region, is indicative of graphene nucleation occurring at various times during the growth. Graphene domain sizes grown on the bottom side of the foil tend to be larger than those on top. In this particular run, the Cu foil was loaded directly into the quartz tube and by virtue of its dimensions, sat closer to the bottom of the tube. Hence the temperature on the underside is likely higher than the top of the foil, leading to more rapid growth dynamics and domain expansion.

A greater degree of surface coverage with larger graphene domains is achieved downstream the Cu foil as well. We note that the foil was positioned in the very center of the tube furnace. The hottest zone of the furnace should be in the center with a temperature drop moving further away towards the open ends of the furnace. The gases introduced to the system start off at room temperature as they flow into the quartz tube over the Cu foil and hence the hottest region experienced by the precursor gas will be slightly offset downstream the exact middle of the tube furnace. Any surface growth dynamics will occur more rapidly in this region downstream the foil compared to those more upstream. This spatial inhomogeneity in growth can be minimized with a more uniform temperature profile within the tube furnace, such as with the use of insulation around the quartz tubing to plug the open ends of the tube furnace.

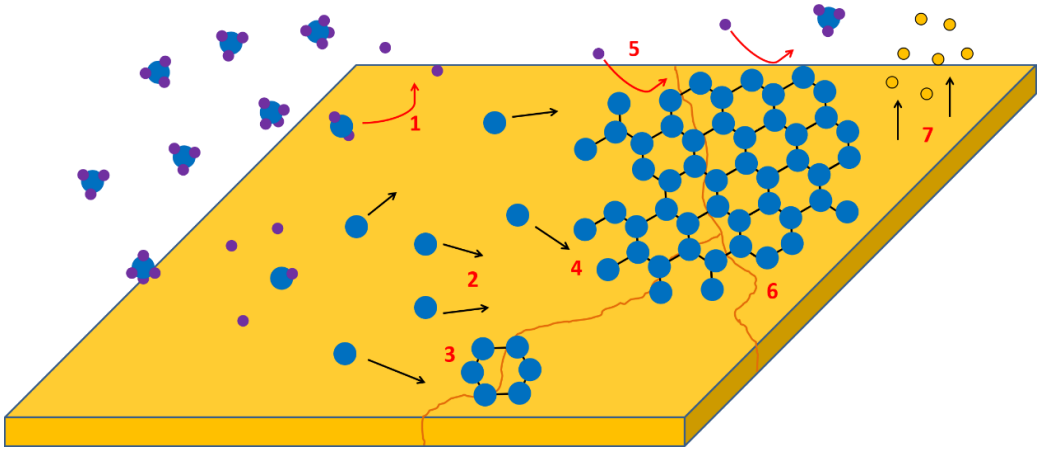


Figure 3.15: Schematic of CVD graphene synthesis on Cu foil. Carbon and activated C species are denoted by blue dots, H by purple dots, and Cu by orange dots.

### 3.2.3 Growth Mechanism

A schematic describing the growth mechanism of layered graphene over a copper surface is illustrated in Figure 3.15. The carbon containing feedstock, in our case methane, is catalytically decomposed over the copper surface (depicted by red arrow labeled 1 in Figure 3.15), providing surface adsorbed active carbon species $(CH_x)_s$, $x$ = 1,2,3. In Figure 3.15, a blue dot is used to denote any type of active carbon species, including carbon atoms (C). Driven by thermal and concentration gradients, the adsorbed carbon radicals will both diffuse along the surface as well as desorb from it (2). Nucleation of polycyclic hydrocarbon structures will occur preferentially along surface impurities, step edges, and grain boundaries (3). Graphene domains will grow with the incorporation of nearby active carbon species (4). During this growth phase, domain edges are etched by $H_2$ gas resulting in continual edge reconstruction (5). In an atmosphere with a sufficient supply of carbon, graphene regions will continue to grow, traversing surface defects and copper grain boundaries (6). Eventually separate graphene domains will join together, forming a continuous layer of graphene with domain boundaries. Formation of a continuous intact layer of graphene over the Cu surface prevents further methane molecules from dissociating into carbon radicals on the catalytic surface, preventing the formation of additional graphene layers. Because both annealing and growth steps are conducted at temperatures near the melting point of copper (1085 °C), Cu is continually evaporating from the surface throughout the process, but at a much lower rate beneath regions of graphene coverage (7).

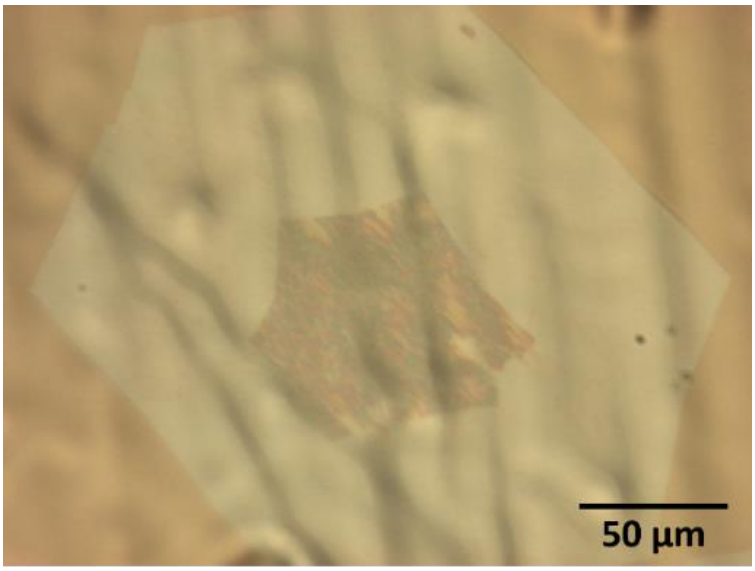


Figure 3.16: Multilayer graphene domain. Cu foil annealed under 500 sccm $H_2$ at 1020 °C for 1 hr. and grown with 2.5 sccm $CH_4$ / 800 sccm $H_2$ at 1020 °C for 65 min.

### 3.2.4 Multilayer vs. Monolayer Growth

In addition to the synthesis of large monolayers of single-crystalline graphene domains, the recipes utilized in these studies also grew a minority of multilayer regions of graphene. In particular, electrochemically polished Cu foils subjected to long anneals and subsequent growths with low $CH_4$ concentrations tended to consistently produce some hexagonal domains with smaller concentric hexagonal domains. An example of such a growth is presented in Figure 3.16 where a very high $H_2$:$CH_4$ ratio is used during the growth step. The multiple layers of graphene are visibly discernible on the Cu foil as a slight variation in contrast and streaking, and have been confirmed to be multilayer graphene by SEM characterization and Raman spectroscopy. The majority of the growths explored in these studies involved high $H_2$:$CH_4$ ratios. In this regime, as the methane partial pressure is increased, there is a greater propensity for the formation of multilayers, most of which are bilayers. The polygonal nature of the second and third graphene layers indicates their etching by hydrogen as well. Their concentric orientation with respect to the first layer, with higher layers forming in the middle of lower order layers, hint at the simultaneous seeding of multiple graphene layers together.

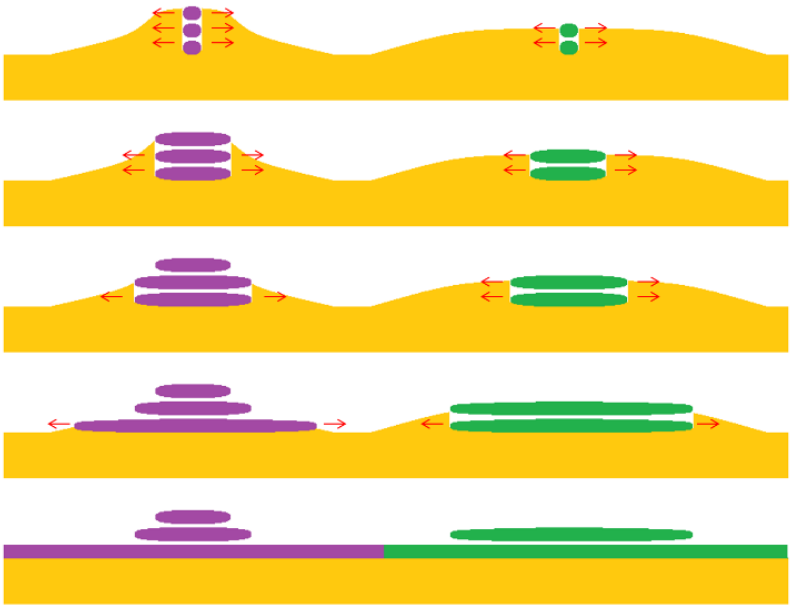

Figure 3.17: Schematic of multilayer domain nucleation and growth. Nucleation preferentially occurs at defect sites, depicted here as raised surfaces. Graphene layers (purple and green) grow at the Cu surface interface (red arrows).

Multilayer graphene growth was only observed for electrochemically polished Cu foils for growths conducted with high $H_2$:$CH_4$ partial pressure ratios. To explain this, we first note the greatly reduced number of nucleation sites present on the foil as a result of both polishing and long anneal times. In the $H_2$-rich atmosphere during the growth step, supersaturated C atoms on the Cu surface at nucleation sites are more likely to survive getting etched by $H_2$ than single-layer seeds where a few surface C atoms might serve as the initiating sites for monolayer growths. There will thus be a higher propensity for nucleation of multilayer growths.

A proposed nucleation scheme similar to that of Sun *et al*.[161] for multilayer graphene is depicted in Figure 3.17. In a growth regime with elevated levels of carbon-containing precursor gas, C atoms supersaturate a nucleation site, such as a surface impurity or Cu grain boundary. These multilayer seeds are able to grown insofar as the Cu surface is able to supply the layers of graphene with activated carbon species. The propagation of the respective layers is catalyzed at the Cu-graphene front at the edges of the graphene domains. Upon recession of the interface due to the propagation of graphene growth and the sublimation of the Cu surface, growth in higher order layers is terminated. For a flatter Cu surface

geometry, multiple layers of graphene may grow initially due to the rapid consumption of carbon nearby the nucleation site. As the first layer propagates at a more rapid rate due to its exposure to surface particles, higher order layers will eventually cease expanding with less active carbon available to them. Graphene regions with differing number of layers will grow until they meet with other domains, forming domain boundaries. Once the foil is completely covered, no additional graphene layers are grown.

# 3.3 Next-Generation Graphene Liquid Cells

## 3.3.1 Electron Microscopy of Liquid Environments

With a much greater degree of control and understanding of the role of various parameters in the synthesis of graphene, we are able to customize its growth in order to suit a desired application. In this section, we will focus on one particular and novel use of graphene to aid in the electron microscopy of liquid environments. As will become clear, our ability to controllably grow large domain and multilayer graphene is critical in this application.

A great deal of phenomena within liquid phase environments are interesting subjects worthy of detailed investigation, including the synthesis of nanoparticles in solution, the biological activity within cells, and electrochemical reactions. The high temporal and atomic-scale spatial resolution of electron microscopy makes this a uniquely capable technique for characterizing structures and processes in liquid environments. Visualizing the molecular mechanisms involved in the functioning of cells while maintain the viability of the cell with minimal intrusion to the biological system is a key challenge for cell biologists[162]. Cryo-electron microscopy has been used to image cellular structures by freezing biological specimens which are then cut into ultrathin cross sections[163,164]. This method, while allowing for "snapshots" of a cellular system to be taken, necessarily destroy the cells and do not allow for imaging in their natural liquid environments. Furthermore, reaction kinetics and mechanisms for the synthesis of nanoparticles and electrochemical reactions of electrode-containing cells filled with an electrolyte could also be probed with unprecedented spatial resolution in real time with the aid of liquid-phase electron microscopy.

In transmission electron microscopy (TEM), a beam of electrons with energy between 100 and 300 keV is incident on a thin sample. As the electron beam passes through, the sample modifies the phase and amplitude of the electrons. The transmitted electrons contain information which can be used to characterize the sample. This technique, however, must be conducted in a vacuum environment so that the electron source can emit electrons without being damaged and in order to minimize scattering of the beam from particles other than the sample itself. Samples to be characterized via TEM must thus be compatible with a vacuum environment and hence are usually solid in nature.

Thus the main challenge is the inherent incompatibility of liquid samples with the high vacuum environment necessary for electron microscopy. In order to overcome this challenge, liquids can be sealed within an enclosure that is both small enough to allow sufficient transmission of the electron beam, but also strong enough in order to prevent leakage of the encapsulated solution [165,166]. These cells have been

constructed of various materials, with silicon nitride (SiN) most commonly being implemented as the window material [167–169]. SiN is rather easy to fabricate and manipulate while robust enough to withstand the pressure differential between the inside of the liquid cell and the vacuum environment outside. These liquid cells, however, tend to result in poor image resolution and a limited field of view. SiN has a relatively high atomic number and has to be thick enough to prevent rupturing. The design of these cells produces thick liquid layers. Once inside the ultra-high vacuum TEM column, the windows tend to bow as well, leading to increased liquid thickness in the center of the window [170].

### 3.3.2 Graphene Liquid Cells

With the Zettl group in 2012, Yuk *et al*. presented a new class of liquid cells wherein the solution is trapped in-between layers of graphene, aptly referred to as the graphene liquid cell (GLC)[171], depicted in Figure 3.18. The high strength and flexibility of graphene along with its impermeability to small molecules makes it well suited for trapping materials[85]. With a thickness of one carbon atom and a low atomic number (Z=6), there is little scattering of the electron beam off of the graphene viewing window. Graphene supports allow for high contrast imaging of all types of materials, including light atoms and organic molecules[85,172]. Furthermore, electron beam induced charging and heating is minimized due to graphene's high electrical and thermal conductivities[173]. Graphene serves as a highly flexible, electron transparent material with minimal chemical and physical interference with the encapsulated liquid environment.

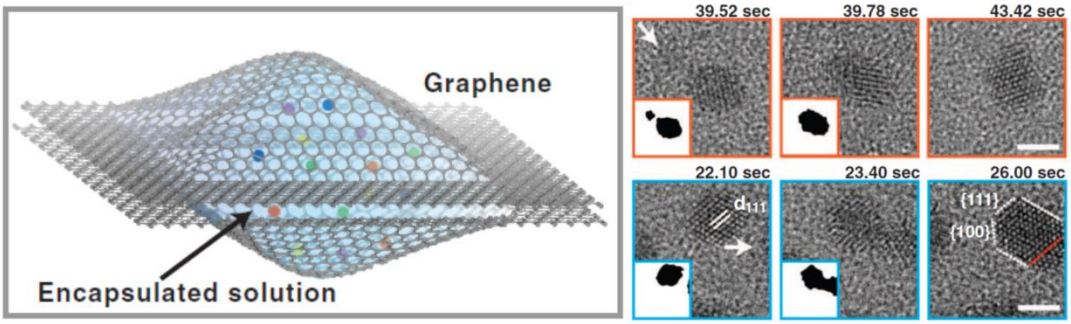


Figure 3.18: Graphene liquid cells. Illustration of solution trapped in-between graphene layers (left) and TEM images demonstrating nanocrystal growth and evolution in a GLC with atomic resolution. (Images from Yuk *et al*.[171])

Yuk *et al*. demonstrated the encapsulation of a Pt growth solution in between two layers of graphene suspended over the holes of a standard TEM grid (Quantifoil®, Ted Pella). The relatively strong van der Waals forces between the graphene layers enables the trapping and sealing of pockets of liquid. Underneath the electron beam, the solution is reduced, allowing for direct atomic resolution imaging of colloidal platinum nano crystal growth. Since then, the graphene liquid cell has been used to image three-dimensional dynamics of soft materials, namely double stranded DNA tagged at its ends with Au nanoparticles, with nanometer resolution[174]. The structures of biological specimens such as the influenza virus and whole cells have also been studied in native solutions using GLCs using low-dose TEM at room temperature[175]. More recently, the 3D structure of Pt nanocrystals has been reconstructed from high-resolution TEM images of the freely rotating particles in solution using the GLC[176].

The graphene liquid cell in its original implementation based on the trapping of liquid pockets in between two layers of graphene is not without its shortcomings. Foremost, the location of encapsulated liquid solutions cannot be controlled. In practice, this may translate into a great deal of time searching a sample in the TEM for trapped solution. The size of encapsulated drops is also uncontrollable. Most pockets are rather thin, between 6 and 200 nm[171], enhancing the effect of particle-substrate interaction. With SiN-based liquid cells, the volume of encapsulated solution is set, but cannot be varied. Furthermore, in its original design, the GLC is not amenable to investigating fluid flows or electrical biasing in solutions.

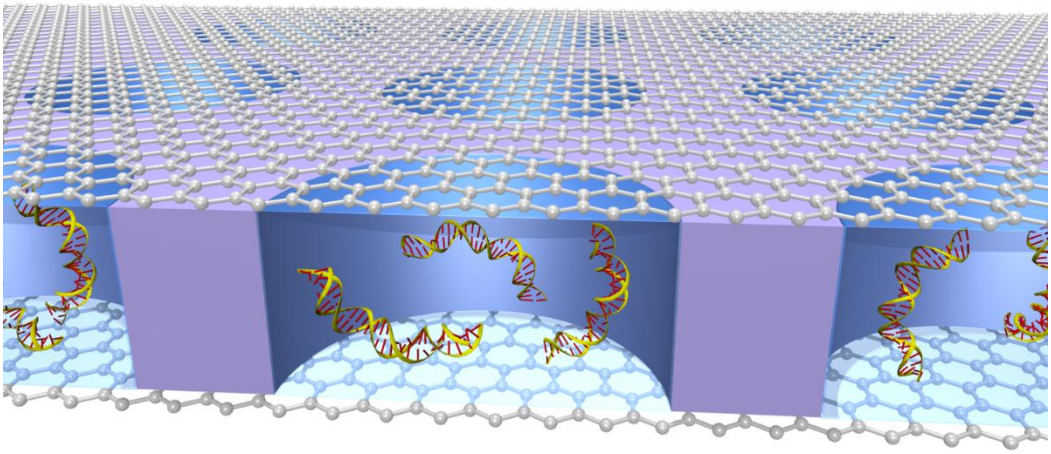

Figure 3.19: Schematic illustration of next-generation graphene liquid cells. Image depicts nanometer scale cavities containing freely diffusing DNA molecules in water capped with graphene sheets for *in-situ* TEM observations of dynamic and chemical events. (Image courtesy of H. Rasool)

### 3.3.3 Next-Generation Graphene Liquid Cells

In order to address these limitations, my colleague Haider Rasool and I set out to design and achieve an alternate liquid cell for the TEM of liquid environments utilizing the great advantages of graphene as window material. Figure 3.19 is a schematic of the next generation graphene liquid cell (NGGLC). Solution and any particles or systems contained within are encapsulated in cavities of preset size, capped on the top and bottom with layers of graphene. The cavities are made in a layer of SiN whose thickness can be varied. In this design, both the height and diameter of the cavities can be controlled as well as their location on the SiN membrane. By using standard lithographic techniques on SiN, future modifications to the simple cavity design could allow for the implementation of nanoscaled channels as well as the deposition of conducting electrodes. In this manner, fluid flow dynamics as well as chemical reactions could be monitored in-situ. With the addition of imbedded electrodes, as can be achieved with a combination of etching and then deposition onto the SiN, electrochemical phenomena can be investigated as well.

#### 3.3.3.1 Fabrication

##### 3.3.3.1.1 Graphene Transfer

Graphene is grown on both sides of the Cu foil during a CVD run. In order to transfer the layer of graphene onto another desired substrate, we proceed using either a "support-layer" method or a "direct-transfer" technique. The former method can be used to transfer graphene onto arbitrary substrates[124]. After a synthesis run, the Cu foil is laid out flat on a clean glass slide with the desired graphene side facing up. The foil can be made adequately flat by pressing down on it with another clean glass slide. The foil is then taped down to the glass slide with Kapton tape covering all four edges. A thin layer of poly(methyl methacrylate) (PMMA) (MicroChem 950 PMMA A4) is spin cast onto foil which has been taped down to the glass slide. For such a large surface, the PMMA is first drop cast until the entire foil is covered in PMMA solution and then the spin coater is ramped up to 3000 rpm and left to spin for 1 minute. The PMMA will form as a nonuniformly thick layer over the foil, developing thicker towards the foil edges. Sometimes this step is followed by baking the PMMA coated samples, such as at 100 °C for 10 min, but we usually proceeded without this bake in order to minimize residual PMMA on the final graphene layer. The foil is then removed from the glass slide, and plasma etched (Plasma Etch) flowing 50 sccm $O_2$ at 50 W for ~20 sec with the PMMA-coated side down. Raman spectroscopy can be used to gauge the degree of graphene removal as many growth recipes may grow varying degrees of multilayer films. The foil is then cut into smaller pieces, typically 1 $cm^2$, and then carefully placed on a bath of copper etchant with the PMMA-coated side face up for ~ 2 hours. The copper etchant used most often was sodium persulfate ($Na_2S_2O_2$), prepared by mixing 0.5 g/mL of $Na_2S_2O_2$ in DI water. Once the copper has been fully etched, the transparent graphene-PMMA film will be left floating in the etchant. Using a clean glass slide, this film is then carefully scooped up and transferred to float in two subsequent bathes of DI water in order to remove residual etching solution. They can then be scooped onto the desired substrate, which if too small, can be taped onto a glass slide with double-sided sticky tape for easier handling during scoopage. The PMMA can either be removed by placing the substrate in bath of acetone for 30 min followed by dipping in isopropyl alcohol or by annealing the sample at 400 °C in a for 60 min flowing hydrogen (500 sccm) and argon (250 sccm).

In a direct-transfer process, graphene can be placed on TEM grids without using PMMA or other transfer polymers which oftentimes leave residue on the final layer of graphene. Following a synthesis run, the Cu foil is laid flat with the desired graphene side face down onto a clean glass slide. It is tapped along all four of its

edges to form very tight seals. The foil is then plasma etched in 50 sccm $O_2$ at 50 W for ~ 20sec with the Cu foil face up. The coil is then cut into smaller 1 $cm^2$ pieces. A drop of isopropyl alcohol (IPA) is then placed onto one of the pieces with the graphene side face up. A TEM grid, typically a Quantifoil TEM substrate, is placed with the metal grid side facing up onto the drop of IPA. The IPA will wet both the graphene film and the carbon-coated side of the TEM grid and as it evaporates, will result in the adhesion of the two. Evaporation can be hastened by baking the foil with the TEM grid, such as by placing it on a hotplate at 100 °C for 10 min. Once dried, the foil can be placed on a bath of copper etchant solution as described above, leaving a floating TEM grid with graphene.

The transfer process will unavoidably lead to the presence of defects in the graphene and impurities on the film. Residual polymer, namely PMMA, is difficult to get rid of. Transferred graphene will also develop cracks and wrinkles once laid on the new substrate. Tearing of transferred films can be minimized by ensuring strong adhesion of the graphene to the substrate. Oftentimes, graphene is transferred onto curved and non-flat substrates with conformal coating desired. This can be achieved by using a thinner support layer in the abovementioned transfer technique by using PMMA A2 or by diluting the PMMA with anisole. The much thinner support layer will be more difficult to see floating and is much more susceptible to damage. Direct transfer of is useful in directly placing graphene on a TEM grid without the use of transfer polymers[177].

#### 3.3.3.1.2 Liquid Cell Cavities

We now discuss the fabrication of the cavity-controllable graphene liquid cells; the first step before any graphene can be transferred is to create cavities in a SiN medium. TEM chips with suspended SiN windows of varying size and thickness are readily available from a number of vendors. The chips used here had a membrane window thickness of 100 nm $Si_3N_4$ measuring 1 x 1 mm with a surrounding silicon support of 200 μm (SPI Supplies). Cavities can be created in the SiN membrane using a focused ion beam wherein high energy ions strike the SiN at a focused spot to sputter away material from the surface. In order to mill very small features on the nonconductive silicon nitride membrane, a thin coating of metal can be deposited to facilitate charge neutralization of the surface. Focused ion beam (FIB) tends to create cavities with non-vertical side walls, often tapered down the deeper a material is etched. FIB can also be tedious and time consuming as cavities are etched one at a time.

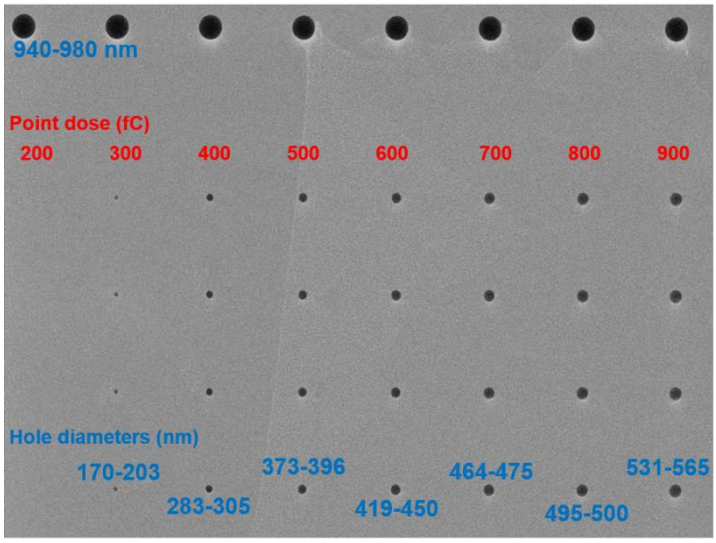


Figure 3.20: SiN etched cavities via nanolithographic processing. SEM image depicts columns of holes exposed with point doses of charge (values labeled above columns in red). After etching, hole cavities protrude through the SiN membrane (final hole diameter values are labeled below columns in blue).

A more scalable mechanism for the etching of holes through a SiN membrane may involve an ebeam lithographic process. In order to coat the top of such a small substrate with resist, the chips were mounted onto the edge of a double-sided adhesive tab placed on a small square glass slide which measured roughly 2 x 2 cm. After the chip was mounted on the spin coater with the SiN membrane side facing up, a drop of PMMA A4 was placed on the chip and wicked away with a kimwipe so that a thin layer of resist covers the surface. In order to form as thin and as homogenous layer of resist on such a small surface, the following ramp-up procedure was followed. This being coater is slowly ramped up to 1000 RPM, left for 20 seconds, then slowly ramped up to 2000 RPM where it is left for another 20 seconds and then finally ramped up to 3000 RPM, and left for 3 minutes. After carefully removing the TEM chip from the adhesive tab, it is baked at 185 °C for approximately 20 minutes on a hotplate. Following the same procedure, a second layer of PMMA A4 was spun and baked on. Experimentally, we found that two layers of PMMA A4 was necessary in order to prevent rupturing of the SiN membrane in later steps during etching.

The coated chips are then loaded in the SEM (FEI Sirion XL30) and are ready to be written on using the Nanopattern Generation System (NPGS). The best way to lithographically pattern holes of small diameters on the SiN membrane is by exposing the resist using a point dosage rather than an area dose. In doing so, the center-to-center and line-spacing distances in the NPGS file determine the distance between

adjacent holes. Multiple patterns may be written on the large surface of the SiN window using the NPGS array function. After exposure, the chips are developed in 1:3 MIBK: IPA solution for 3 min 30 sec followed by dips in two DI water baths. The chips are then plasma etched using the 'ptherm' equipment in the Marvel Nanolab using a recipe of 25 sccm $CF_4$, 75 sccm $CHF_3$, and 100 sccm He at 100 W for 3 min 30 sec. Placement of the chips in an acetone bath for an hour is sufficient to clean off the remaining resist.

An SEM image of a SiN membrane with an array of various cavity sizes is presented in Figure 3.20. By varying the point dosage of exposure during NPGS writing, the diameter of the etched cavity can be varied. In this image the point dosage in femtocoulombs (fC) for a particular column of holes is labeled in red with the final resultant range in hole diameters for the column labeled in blue. For this particular membrane, the smallest diameter hole is roughly 100 nm. We note, however, that edged holes possess a parabolic profile and complete etching through smaller diameter holes is more difficult to achieve. TEM characterization is used to gauge whether a particular cavity has been etched all the way through the silicon nitride membrane. A hard mask, as can be achieved by depositing a patterned thin metal layer on top of the silicon nitride membrane, may be used to facilitate complete etching of a hole through the SiN without the unwanted effect of widening the upper diameter of the cavity during this process.

Once the SiN medium with appropriately fashioned cavities is prepared, we proceed with the fabrication of the graphene liquid cell. We now describe the route by which solution can be encapsulated within a NGGLC. Graphene is first grown onto a Cu foil (25 μm) using a low pressure CVD technique, as previously described. Using the polymer-assisted transfer technique discussed earlier, we obtain a single film of graphene with PMMA support floating atop a bath of DI water. The PMMA support in this step should be made thin by spin coating PMMA A2 dissolved in anisole (1:1) and not baking it after it covers the foil. This is critical in order for the graphene to form conformally on the backside of the SiN chip which has a recessed indentation onto the SiN window. The PMMA-supported graphene film is then scooped up onto the backside of a SiN membrane chip. This can be achieved by placing the silicon nitride chip membrane-side-down onto the edge of a double sided adhesive tab which is stuck onto a standard glass slide. The scooped PMMA-supported graphene film must be left to dry on the chip. Using an optical microscope, one can observe as the film dries, it should gradually adhere to the chip and the film initially suspended over the 1 x 1 mm window should tear at the edges and stick to the SiN membrane. A second film of PMMA-supported graphene must be transferred onto a bath of the solution to be encapsulated. This is then scooped up onto the top side of the SiN chip which already has graphene film on the underside and left to dry. Van der Waals

forces will enable the graphene to form a seal with SiN surface, forming pockets of trapped solution. The layers of PMMA can finally be removed with acetone, followed by rinsing with IPA.

# Chapter 4

# Extended Pressure Inductively Coupled Plasma Synthesis of BNNTs

## 4.1 Boron Nitride Nanotubes

Boron nitride nanotubes (BNNTs), first synthesized in 1995 by the Zettl group and collaborators[178], are wide-bandgap structural analogs[7] to carbon nanotubes[1]. Importantly, the special chemical, optical, thermal, and radiation-absorption properties of BNNTs make them far superior to their carbon counterparts for many applications[179]. Theoretical[180] and experimental[13,19] studies demonstrate that the electronic energy bandgap is ~5eV independent of tube diameter and chirality, but can be tuned by the application of transverse electric fields[13]. A host of other BNNT properties have been considered, including tunable thermal conductivity[181], piezoelectricity[182], biocompatibility[183], hosts for silocrystal structures[184], electron field emission[16], water purification[185], and reinforcements for structural composites[186,187], to name just a few.

## 4.2 BNNT Synthesis Techniques

An unfortunate constraint that has severely limited the scientific study and industrial application of BNNTs and related BN-based nanostructures such as BN nanoribbons (BNNRs) and BN nanococoons (BNNCs) is the general lack of availability of the synthesized materials. The synthesis of boron nitride nanotubes has proven to be far more challenging than their carbon counterparts. Many of the techniques which have successfully been implemented and developed for the synthesis of carbon nanotubes do not work as well for boron nitride. In general, techniques to

grow BNNTs can be classified in one of two groupings, namely medium temperature and high temperature methods.

### 4.2.1 Medium Temperature Synthesis

In the class of methods conducted at "medium temperatures," the operating temperature during synthesis is below 2000 °C, far below the vaporization temperature of pure boron which is ~ 4000 °C.

#### 4.2.1.1 Chemical Vapor Deposition

The chemical vapor deposition (CVD) of nanotubes involves the decomposition of a gaseous precursor containing the elements of the desired nanotube composition over metal catalysts via a high energy source. The energy may be provided by the high temperature (700 °C - 1200 °C) of a furnace as in thermal CVD or the reactive ions of a plasma as in plasma enhanced CVD (PE-CVD). Carbon nanotubes are made using gaseous hydrocarbons such as methane, acetylene, or ethylene. The metal catalysts, such as Ni, Cu, Co, Fe, Pt, etc., are typically deposited on a substrate and loaded into the center of the reactor chamber which oftentimes is a quartz or alumina tube. Annealing the thin layer of metal catalyst may cause it to bead up into small nanoparticles which serve as seeds to "crack" the carbon-containing gas molecules into surface activated carbon atoms. These reactive carbon atoms may be absorbed into the metal catalyst or diffuse on its surface to come together and bond with other reactive carbon atoms forming C-C bonds that extend to produce the walls of a nanotube or the shells of a nanococoon. Nanotube diameters are determined by the size of the metal nanoparticle seeds, and tend to be an order of magnitude greater than those grown by higher temperature techniques (~40 nm versus ~4 nm).

By using a boron and nitrogen containing gaseous precursors, a CVD route for the synthesis of BNNTs is possible. For instance, when borazine ($B_3N_3H_6$) is flowed over metal catalysts such as Co, Ni, NiB, or $Ni_2B$ at temperatures near 1100 °C, a white powder forms atop the substrates which consists predominantly of multi-walled boron nitride nanotubes (MWBNNTs)[188]. An alternate CVD route where both the precursor and the catalyst are in the vapor phase is referred to as floating zone CVD. For example, in boron oxide CVD (BOCVD), ammonia gas is introduced into a reactor chamber with boron oxide, which is formed by reacting boron with an oxide, such as $SiO_2$ or $Fe_20_3$[189]. Considerable amounts of MWBNNTs were synthesized using a similar approach by loading a mixture of boron and magnesium oxide (with a molar ratio of 1:1) into a BN-custom made reaction tube and heating it to 1300 °C using a

radiofrequency (RF) induction furnace[190]. The generated boron oxide gas and Mg vapor is then transported into a reaction chamber maintained at 1100 °C where a flow of ammonia is introduced. The Mg acts as a floating zone catalyst for the reaction of $B_2O_2$ and $NH_3$ to form a white BNNT-containing material that accumulates on the chamber walls.

CVD grown tubes are relatively cheap to produce, but the process is inherently non-continuous requiring the dismantling of the reactor chamber in order to collect the limited quantity of nanotube product from the surface of the substrates. Furthermore, these tubes tend to be multiwalled, significantly shorter than BNNTs grown at high temperatures, and contain many structural defects.

#### 4.2.1.2 Ball-Milling

Ball milled nanoscale tubular and bamboo-like structures are produced by loading hard stainless steel balls with boron powder into a small vessel filled with pressurized ammonia gas. The vessel is then continuously rotated for an extended period of time. In doing so, energy is imparted onto the boron particles mechanically through constant collisions producing structural and chemical changes. After ball-milling, Chen *et al.* annealed their product material at 1200 °C in a tube furnace flowing nitrogen to complete the conversion of any remaining B into BN[191]. Although a great deal of tubular BN structures can be formed in this manner, the product suffers from very low purity and the tubes are very defective, with many curved walls, and typically bamboo-like morphology. Ball milling of powders, however, could be useful for breaking apart particles and thus decreasing the size of precursor powders which could then be used in other synthesis processes.

#### 4.2.1.3 Substitution Reaction

As CNTs are easier to synthesize in larger scales with high quality and are nearly identical in structure to BNNTs, substitution reaction is based on using CNTs as templates which can then be converted to BNNTs. The carbon atoms of CNTs are substituted by boron and nitrogen atoms via a carbothermal reduction of boron oxide using carbon sourced by the initial nanotubes in a nitrogen atmosphere at temperatures between 1000 °C and 1600 °C [192]. The proposed reaction proceeds as:

$$B_2O_3(s) + 3C(CNTs) + N_2(g) \rightarrow 2BN(BNNTs) + 3CO(g) \qquad (4\text{-}1)$$

In this manner, MWBNNTs[192,193] as well as some single wall boron nitride nanotubes (SWBNNTs) using higher synthesis temperatures of 1580 °C [194] have

successfully been produced. The converted BNNTs tend to have smaller diameters and fewer shells than the starting CNTs. By modifying the temperature of conversion and the nature of the initial CNTs, the final product may also include BCN nanotubes as well as remnant CNTs. Oxidizing this product at 650 °C will leave behind pure BNNTs.

### 4.2.2 High Temperature Synthesis

High temperature methods include those which involve the vaporization of boron or boron nitride, typically occurring at temperatures greater than 3000 °C.

#### 4.2.2.1 Arc-Discharge

Attempting to create fullerenes of carbon, Iijima *et al.* sustained an arc-discharge in-between two graphite electrodes and discovered nanoscale tubular carbon structures in the resultant soot[1]. Arc-discharge involves the striking and briefly sustaining a hot arc plasma in-between two conducting electrodes. This results in the consumption of the anode and the production of soot which accumulates throughout the chamber. The arcing occurs in an inert gas environment with the formation of a "boule" which may build up on the cathode. Modifications to the synthesis conditions, including the incorporation of metal catalysts such as Ni, Co, or Ni-Co in the pressed graphite rods, have enabled both bulk synthesis of multi-walled carbon nanotubes (MWCNTs)[195] as well as the formation of single walled carbon nanotubes (SWCNTs)[196].

Since the electrodes must be electrically conducting, adapting this method to make nanotubes of the wide bandgap boron nitride has not been so straightforward. In 1996, Chopra *et al*. in the research group of Alex Zettl overcame this impediment by inserting a pressed rod of hexagonal-BN (*h*-BN) into a hollow tungsten electrode[178]. Arcing against a water-cooled copper electrode produced grey soot which deposited on the cathode. The BN is indirectly evaporated, ultimately generating MWBNNTs. Solidified tungsten was spattered throughout the synthesis chamber, indicating anode temperatures during synthesis exceeded 3422 °C, the melting point of tungsten. Since this first successful synthesis of BNNTs, many different modifications to this technique have been carried out. One such effort involved the arcing of $HfB_2$ electrodes in a chamber filled with nitrogen[197]. The metallic $HfB_2$ has a high melting point and will react with $N_2$ at high temperatures to form BN. Arc-grown tubes are among the highest quality of any synthesis method, with very highly crystalline tube walls hundreds of microns in length. However, arc-grown material tends to produce a relatively low yield of few-walled BNNTs (2 – 10

layers) amidst many impurities and remnants of the consumed electrodes. This too is a batch synthesis process that cannot make scalable quantities of BNNTs.

#### 4.2.2.2 Laser Vaporization

Laser vaporization is another high-temperature BNNT synthesis method wherein a continuous or pulsed laser is focused on a solid target to vaporize it in a gaseous atmosphere. The target may consist of metal catalysts and its composition, as well as that of the surrounding gases, is adjusted according to the desired composition of the final nanotubes. Golberg *et al.* have laser heated a cubic-BN (*c*-BN) target in a high pressure diamond anvil cell in a hyperbaric nitrogen environment to produce MWBNNTs[198].

Larger quantities of SWBNNTs were synthesized by Arenal *et al*. by vaporizing a *h*-BN target using a continuous $CO_2$ laser under a flow of $N_2$ gas at atmospheric pressure[199]. The surface temperature of the target exceeded 2930 °C, yielding mostly bundles of 2 – 10 SWBNNTs several hundreds of nanometers in length. Laser vaporization has been implemented to create different types of heteroatomic nanotubes, including N-doped CNTs[200] as well as BCN nanotubes[201] by varying the buffer gas and solid target compositions. This technique, however, is expensive to conduct, does not lend itself to large-scale production, and cannot be operated continuously.

A noteworthy advance in BNNT synthesis occurred in 2009 using a laser ablation technique to create small-wall-number, highly crystalline, and high aspect ratio pure BNNTs[29]. This catalyst-free synthesis technique utilizes a kilowatt-power laser to ablate a boron target in a high-pressure nitrogen atmosphere. The boron vapor created by the laser is condensed on a filament where it reacts with the nitrogen gas to create BNNTs.

Unfortunately, the laser-vaporization method of Smith *et al.*[29] suffers from low energy efficiency as well as limited throughput (approximately 100 mg/hour). Nevertheless, it suggests that, given the right local high input energy flux and quenching dynamics, scaled production of BNNTs and related BN nanoparticles should be achievable. Furthermore, it elucidates two key aspects of high purity BNNT production from boron precursors: (1) high pressure nitrogen environments are effective in shifting the reaction from B and $N_2$ to BN, and (2) controllable introduction of liquid boron droplets can precipitate BNNTs without a catalyst.

#### 4.2.2.3 Arc Jet Plasma

Plasma torches have been implemented with limited success in synthesizing BNNTs. Shimizu *et al*. heated a solid target of $BC_4N$ with a DC arc plasma torch operated with Ar and $N_2$-$H_2$ as plasma and sheath gases respectively[202]. The target was heated to 4730 °C, and material was deposited on nearby water-cooled copper disks. This produced predominantly multi-walled nanotubes of both carbon and boron nitride of relatively poor crystallinity. A homogenous phase of $BC_xN$ could not be obtained. Lee *et al*. fed a mixture of *h*-BN, Ni, and Y powder into the stream of an Ar-$N_2$ DC plasma torch which is fired into a small graphitic cavity in order to extend the hot zone of the plume[203]. Material collected from the surface of the reaction cylinder contained single as well as multiwalled BNNTs with straight walls alongside many *h*-BN sheets. Nearly all of the tubes contained metal catalyst seed particles. In the following sections, we will explore DC plasmas in greater detail and highlight some of their shortcomings in the processing of nanomaterials.

These techniques demonstrated the novelty of utilizing a plasma as a high temperature energy source to heat treat BN and fabricate nanotubes, but fall short of producing high quality material in a continuous and scalable fashion. Greater efforts have been conducted towards the production of CNTs using plasma torches, including one such work using a radiofrequency (RF) inductively coupled plasma (ICP). A commercial system (TEKNA PL-50, Tekna Plasma Systems) was operated at a plate power of 40 kW using Ar as both the carrier and central gas with He or He/Ar as the sheath gas mixture[204]. A mixture of carbon black and various combinations of metal catalysts (including Ni, Co, $CeO_2$, and $Y_2O_3$) were injected axially into the plasma plume. This then flows into a larger reaction chamber with graphite inserts and thermal insulation maintained at 500 Torr. Material in the form of rubbery sheets collected of off three large porous metallic filters contained ~40 % SWCNTs with diameters ~ 1.5 nm. The quality and purity of the nanotubes were dependent on the grade of the feedstock material, the plasma gas composition, and the metal catalysts used. Indeed, this system has been commercialized to scalably produce SWCNTs (Raymor Nanotech).

## 4.3 Extended-Pressure Inductively Coupled (EPIC) Plasma Synthesis

In this chapter, we demonstrate the successful operation of a high-throughput, scalable BN nanostructures synthesis process whereby precursor materials are directly and continuously injected into a high-temperature, *Extended-*

*Pressure Inductively-Coupled* plasma system (EPIC). The EPIC synthesis system is remarkably versatile in terms of synthesis parameters and allows for the injection of fluids (gases or liquids) and solids (powders) directly into the variable-power plasma plume. In addition, the high-pressure capability of the plasma (up to 10 atm) allows for dramatic shifts in chemical reaction tipping points. The system can be operated in a near-continuous fashion and has a record output of over 35 g/hour for pure, small diameter, few wall, highly crystalline BNNTs.

### 4.3.1 Plasmas

The plasma state of matter consists of unbound electrons, ions, and neutral species which overall are electrically neutral. Unlike a standard gas, electromagnetic interactions of the charged particles in the fully or partially ionized gas lead to the plasma's unique phase properties. In general, they do not possess any distinct shape or volume unless they are confined by a container or electromagnetic fields. Plasma's have high electrical conductivities, which can be comparable to those of metals, due to the free nature of the contained charge particles.

The range of species within a plasma might vary from individual atoms, molecules, monomers, and radicals to larger particles such as atomic and molecular clusters as well as nanoscale particles and larger agglomerates. Overall charge neutrality is preserved as these species are positive, negative, or neutrally charged. The particles' motions are driven thermally and electromagnetically, leading to collisions with other particles. The rate of these collisions is important in determining whether the plasma is in thermal equilibrium or not. In particular, each species *j* has its own temperature[205]

$$T_j = \frac{2}{3k} < E_j > \tag{4-2}$$

where *k* is the Boltzmann's constant and $<E_j>$ is the average kinetic energy of the species *j*.

Plasmas initiated by an electric discharge can be divided into two distinct categories characterized by the relative temperatures of the constituent species. In "thermal" or "equilibrium" plasmas, the temperatures of electrons, ions, and neutral particles are approximately equal. The plasma is said to be in local thermodynamic equilibrium (LTE) when collisions between lighter electrons and heavier ions and neutral particles occurs frequently enough to allow for the average kinetic energy of all the species to be roughly equal. Local deviations from the state of thermodynamic

equilibrium do occur, but an overall kinetic and chemical equilibrium is maintained in the plasma as a whole. As higher pressure conditions result in greater interparticle collision rates, thermal plasmas tend to form at relatively higher pressures ranging from a few Torr to an atmosphere. Thermal plasmas thus have higher particle densities with energies in the range of 1 – 2 eV, where in plasma science particle temperatures and typically expressed in electron volts such that 1 eV ≈ 11,600 K. Such plasmas are thus hot enough to melt and evaporate solid materials. Examples of thermal plasmas include those produced using DC transferred arcs, plasma torches, and radio frequency (RF) inductively coupled plasmas (ICP).

The second type of plasmas, referred to as "cold" or "nonequilibrium" plasmas, exhibit large differences in the temperatures of heavier and lighter species, with electron temperatures typically one order of magnitude larger than those of heavier ions and neutral particles. For instance, electron energies are typically a few eV whereas those of ions and neutral particles may be closer to 0.03 eV. They are characterized by lower energy densities and a significantly lower degree of ionization when compared to thermal plasmas. Typically, they have much lower electron and particle densities, but "atmospheric pressure non-equilibrium discharges," which include corona and spark discharges, are also possible. Non-equilibrium discharges at atmospheric pressure occur with high interspecies collision rates, but the transient nature of the discharge does not allow for thermal equilibrium to be attained. Non-equilibrium plasmas include some glow discharge plasmas, low-pressure RF plasmas, and corona discharges.

Low pressure non-equilibrium plasmas are commonly used in plasma etching and material sputtering processes. They are also effective in surface treatments due to the reactivity of the chemically active species in the plasma. Thermal plasmas on the other hand have much higher energy densities and thus are used to process materials through heating, melting, and sometimes vaporization. As sources of very reactive species at high temperatures, they are also used in the plasma chemical synthesis of various materials.

#### 4.3.1.1 Thermal Plasmas

In order to effectively utilize thermal plasmas for materials processing purposes, in this section we explore their thermodynamic and transport properties. In particular, the degree of ionization and composition of a plasma will depend on the makeup of the plasma gas as well as the temperatures achieved. Argon is a standard gas used in many thermal plasmas, including in plasma cutting, spraying, and coating. Argon serves as a typical plasma gas because it is relatively easy to

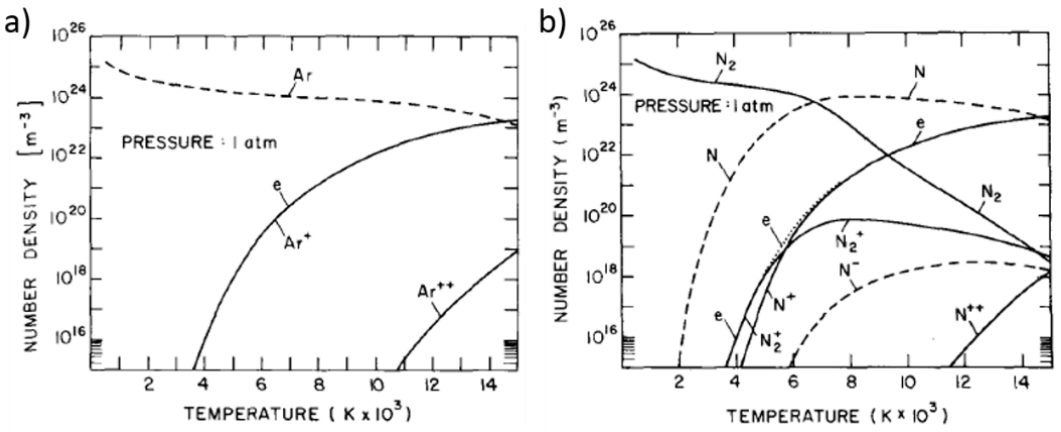


Figure 4.1: Equilibrium gas compositions of (a) argon and (b) nitrogen as a function of temperature at 1 atm. (From ref. [206])

ionize, chemically inert, and the cheapest of the noble gases. The equilibrium composition of argon at atmospheric pressure as a function of temperature is presented in Figure 4.1a[206]. The monatomic gas Ar is seen to ionize into Ar+ and electrons beginning at 4000 K and becomes doubly ionized to form Ar++ near 11,000 K. For a diatomic molecule, such as nitrogen, the equilibrium composition at various temperatures is more complicated as depicted in Figure 4.1b. The gas molecules of $N_2$ are ionized beginning around 4000 K, and at temperatures ranging from 5000 – 8000 K, the diatomic molecule is dissociated. Plasmas of diatomic molecules have higher specific enthalpies than those of monatomic gases due to their dissociation. There is also a significant increase in the specific heat and thermal conductivity of the molecular gases near the temperature of dissociation.

Figure 4.2 illustrates the specific enthalpies of some commonly used monatomic and molecular gases as a function of temperature[206]. A clear step-like increase in the specific enthalpy is observed for the diatomic gases of $H_2$, $O_2$, and $N_2$ near 4000 K, 4000 K, and 7000 K respectively. These correspond to the dissociation of these molecules. The lighter gases of $H_2$ and He have higher specific enthalpies than those of heavier molecules and hence oftentimes are mixed in with other gases in various applications of plasma processing of materials. In particular, we note the significantly higher specific enthalpy of $N_2$ compared to Ar, which will be important in the nitridation of boron particles. The high temperature profiles as well as the enhanced specific enthalpies and thermal conductivities of reactive species within thermal plasmas make them well suited for the processing of materials.

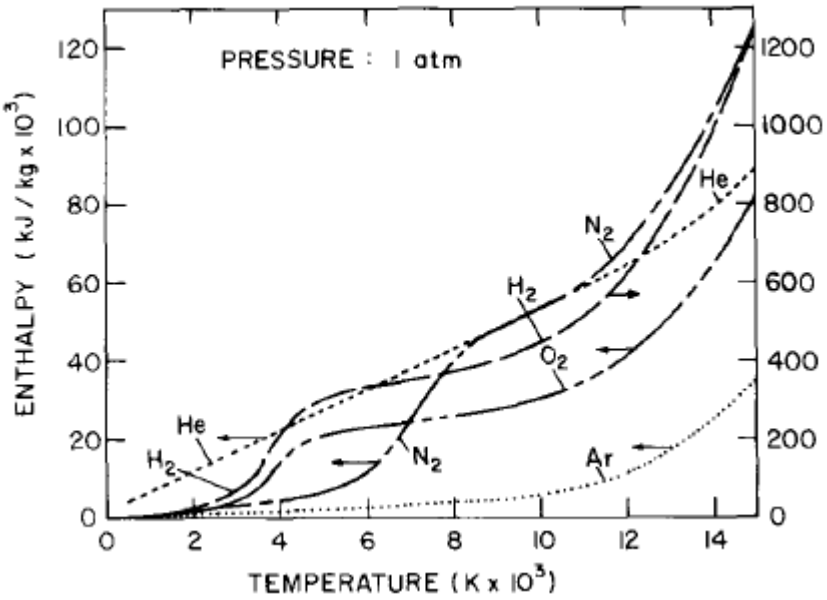


Figure 4.2: Specific enthalpies for gases of $H_2$, He, $N_2$, $O_2$, and Ar as a function of temperature at 1 atm. (From ref. [206])

#### 4.3.1.1.1 DC Plasma

There are several basic plasma generating systems, each producing different processing conditions. The most commonly used plasma devices employ a DC plasma mechanism where a plasma is generated by flowing a gas through an electric arc discharge sustained between an anode and a cathode, as illustrated in Figure 4.3a. The material to be processed may be fed into the stream of the plasma to be melted or vaporized. DC plasma torches vary in the configuration and material composition of their electrodes. For instance, inert gases may be used with a tungsten cathode and copper anode for lower power applications typically below 100 kW. Oxidizing gases cannot be used with such a system as they would damage the tungsten cathode, but can be utilized in DC plasma torches designed with two cold copper coaxial tubular electrodes wherein the plasma gas flows through the region in-between with a strong vortex motion. In the DC transferred arc plasma torch design, there is a large physical separation between the cathode and anode. Larger interelectrode distances, ranging from a few cm up to 1 m for high power industrial furnaces, permit the use of higher operating voltages and hence greater plasma power for a set arc current. The nozzle diameters of DC plasma torches are less than

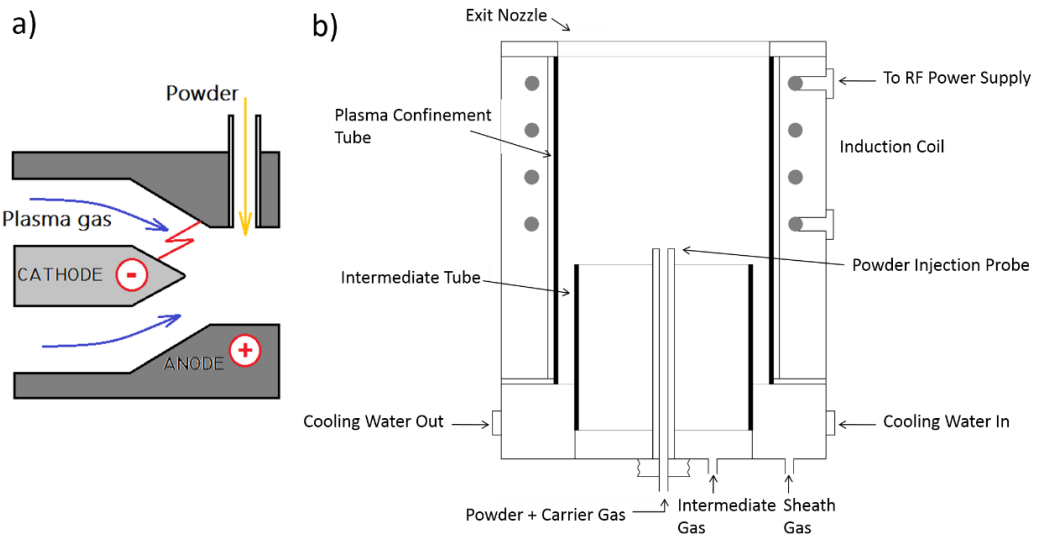


Figure 4.3: Plasma torch schematics of (a) DC plasma torch and (b) standard induction plasma torch.

10 mm with maximum plasma jet temperatures of 12,000 K and very high gas velocities of 400 – 600 m/s. The plasma volumes tend to be small and the residence time of particles injected into the plasma time relatively short, on the order of 0.5 ms.

#### 4.3.1.1.2 RF Inductively Coupled Plasma

In an inductively coupled plasma torch, energy is coupled to the plasma via the electromagnetic field generated by an induction coil[207,208]. In this manner, the plasma is never in contact with the electrodes, and thus does not gradually erode or potentially contaminate the product material. Furthermore, a wide range of gases can be used, including those which may be inert, reducing, oxidizing, or corrosive. Excitation frequencies are usually between 200 kHz and 40 MHz with most lab-scale units operating at 30 – 50 kW and larger industrial systems operated at closer to 1 MW.

A schematic of a standard induction plasma torch is presented in Figure 4.3b. A plasma is generated and sustained within a cylindrical cavity, typically made of cooled quartz or ceramic. Several gases are introduced into the tube, with injection ports located at the top of the schematic depicted in Figure 4.3b. A sheath gas flows down the walls of the torch cavity, protecting the walls from overheating and serving

as a potential medium through which the chemistry of the plasma can be slightly altered with the introduction of higher enthalpy gases, such as hydrogen. The plasma itself is maintained and stabilized with the introduction of the intermediary gas, which is usually injected into the cavity in a swirling fashion. The powder carrying gas is axially injected into the center of the plasma discharge using a water-cooled probe and serves to introduce the material to be processed into the plasma. The region of maximum plasma temperature will be located in an annular region slightly off of the center axis. This is because the eddy currents generated in the gas will be limited to the external cylindrical shell of the plasma whose thickness, referred to as the skin depth, depends on the oscillator frequency and average plasmas electrical conductivity[207]. The minimum power required to maintain a plasma depends on the oscillator frequency, gas composition, flow rate, and system pressure.

Induction plasma torches are particularly well suited for the processing of materials. In addition to eliminating the possibility of contamination from electrodes in product material, induction plasma volumes are much larger than those of DC plasma torches. This allows for a higher throughput of precursor material to be treated. High temperatures, approaching 10,000 K can be attained in induction plasmas as well. The relative low velocities of gases through the plasma, usually in the range of 10 – 20 m/s, allow for longer residence times, on the order of 10 – 20 ms in standard induction plasmas, for particles injected into the discharge. Inductively coupled plasma torches are thus well suited for in-flight melting of powders at high throughputs. In addition to functioning as a high-temperature energy source, the chemically active species within the formed plasma will play a critical role in the nitridation of boron in our efforts to synthesize nano-compounds of boron nitride. Hence both physical and chemical transformations will be involved in the processing of precursor material towards our desired product.

Furthermore, the high energy density of the thermal plasma allows for a high rate of production. The system can potentially operate in a continuous manner in contrast to the previously discussed methods for BNNT synthesis which are batch processes.

#### 4.3.1.2 Plasma Nanofabrication

We now explore the thermodynamics by which precursor materials in a powder form are thermally treated in the high-temperature zone of a plasma. Plasma torches are commonly used for spheroidization, melting and deposition, as well as plasma spray-coating primarily as a source of high-temperature and energy. Precursor material is usually solid in form, and typically in the form of a powder of nonuniform sizes and irregular shapes. If we consider a single particle injected into

the region of a plasma, energy is transferred to the particle through conduction and convection from the plasma and dissipated as radiation from the particle's surface to the proximate environment. The net energy transferred to the particle can then be written as,

$$Q_{net} = Q_{conduction\,\&\,convection} - Q_{radiation} \tag{4-3}$$

$$Q_{net} = hA(T_p - T_s) - \varepsilon\sigma A\left({T_s}^4 - {T_e}^4\right) \tag{4-4}$$

where $h$ is the heat transfer coefficient between the plasma and the particle, $A$ is the surface area of the particle, $T_p$ is the plasma temperature near the particle, $T_s$ is the particle surface temperature, $\varepsilon$ is the emissivity of the particle, $\sigma$ is the Stefan-Boltzmann constant, and $T_e$ is the temperature of the wall confining the reaction.

The total energy absorbed by the particle is obtained by integrating the net energy transferred over the residence time of the particle within the plasma, $\tau$. The particle will completely melt if this total energy is greater than the sum of the energy required to heat the particle from its initial temperature to its melting point plus the energy required to change the particle phase from solid to liquid,

$$\int_0^{\tau} Q_{net}\, dt \geq m_p C_p (T_m - T_o) + m_p H_p \tag{4-5}$$

where $m_p$ is the mass of the particle, $C_p$ is the specific heat of the particle material, $T_m$ is the melting point of the particle material, $T_o$ is the particle's initial temperature, and $H_p$ is the latent heat of fusion of the particle material.

As the particles are thermally treated from their interaction with the plasma environment, we must also consider the variation in temperature within the particle. This is particularly important in dealing with matter which is exposed to such a high temperature energy source on its surface for relatively short periods of time. The complete melting of a particle will depend on the Biot number, which is defined as the ratio of the integral average thermal conductivity of the surrounding environment of the particle, i.e. the plasma, to the thermal conductivity of the particle material,

$$B = \frac{\langle k \rangle}{k_p} = \frac{\frac{1}{T_p - T_s}\int_{T_s}^{T_p} k\, dt}{k_p} \tag{4-6}$$

where $k_p$ is the thermal conductivity of the particle material. For a Biot number less than one, the thermal resistance of the particle/plasma interface is greater than the thermal resistance within the particle. For B << 1, the temperature within the particle is approximately uniform throughout its volume and will change as heat is exchanged with the surrounding environment. If the Biot number is greater than one, thermal gradients within the particle will develop and the material will experience nonuniform heating. The temperature difference between the surface and center of a particle will depend strongly on the heat flux to the particle, the particle's material, and the composition of the plasma gas.

The feed rate of particles into a plasma will also significantly affect the degree to which each particle is melted in-flight. As more material is fed into the plasma, the temperature of the plasma will drop and hence decrease the rate at which individual particles are heated[209]. Greater particle feed rates will result in fewer molten and vaporized particles. The critical loading level depends on the thermal and physical properties of the material being treated, the plasma composition and power levels, as well as the mechanism by which power is injected into the stream of the plasma.

With the aim of synthesizing nanoscale tubular structures, simply melting or vaporizing a precursor powder would not be sufficient. The chemically active species within the plasma may serve as components in the final product material. The formation of boron nitride nanostructures may thus be achieved using boron-containing feedstock introduced into a plasma of nitrogen gas. As such, the plasma serves the dual role of providing reactants as well as heating them to high enough temperatures for the necessary chemical reactions to occur. Precursor materials may take the form of solids, liquids, or gases.

#### 4.3.1.3 Plasma Modeling

The plasma processing of materials and in particular the synthesis of nanoparticles is a complex problem. The process involves complex heat and mass transfer routes that result in rapidly occurring phase changes. Elaborate interactions between particles and the freely moving charged ions and electrons of the plasma environment involve many variables. There are various techniques for measuring certain components of the process. For instance, emission spectroscopy may be used to evaluate the intensity of emitted spectral lines and infer temperatures. Enthalpy probes, roughly 3 mm in diameter, can be used to gauge the local enthalpy of the gas[210,211]. Fauchais *et al*. present an extensive review of plasma diagnostic tools and techniques to measure desired parameters[212]. We are ultimately concerned with the resultant material and so most of our efforts are focused on characterizing these final

products. Nevertheless, we can begin to understand the complicated dynamics involved in the plasma assisted synthesis of nanomaterials using simulations and computer modeling. Several reviews exist on the modeling of thermal plasma dynamics and nanoparticle formation within[205,206,212,213].

In particular, Kim *et al.* have conducted extensive thermodynamic and thermal flow analyses in order to understand the role of various parameters and optimize their inductively coupled plasma system for the synthesis of SWCNTs[204]. Further studies of numerical models were carried out by the same group to investigate the role of the thermo-fluid field and solid-liquid-gas phase reactions on CNT growth and to predict the yield of SWCNTs using their RF inductively coupled plasma system[214–217]. The simulations incorporate several simplified models. These include a 2D model to simulate the RF inductively generated plasma. The plasma is assumed to be in a steady state where the conservation equations for mass transport, momentum, energy, and concentration of species hold. The second model takes into account the interaction of the injected particles with the plasma environment. In terms of the injected particles, the major force affecting particle trajectories is the viscous drag force from the plasma medium with relevant equations describing heat and mass transferred between the plasma environment and the particles. The third model computes the thermo-flow field in the reactor and the last simulates the growth of CNTs based on the supersaturation of metal catalyst nanoparticles.

Another report presents a hybrid plasma equipment model (HPEM) to describe the plasma chemistry in an inductively coupled plasma used to synthesis CNTs[218,219]. HPEM is based on three sub-models describing (1) the electric and magnetic fields in the reactor, (2) the transport of electron energy simulating the behavior of electrons by a Monte Carlo process or the Boltzmann equation, and (3) a kinetics of the fluid dynamics using conservation equations to treat the other plasma species.

### 4.3.2 EPIC Synthesis System

Inductively coupled thermal plasma systems typically operate at reduced pressure (1 atmosphere and below), and no commercial system exists that is capable of operating within our desired parameter range (including high pressure, pure nitrogen operation). Therefore, we have designed and custom-built a suitable EPIC synthesis system from the ground up, the details of which are presented here.

Figure 4.4 shows a schematic of the EPIC system. A plasma-generating torch, driven by a 60 kW, 7 MHz power supply and suitable impedance matching network, is mounted atop a 15 cm inner diameter, 112 cm long synthesis chamber. The entire system, including synthesis chambers, exhaust system, filters, and torch body, has

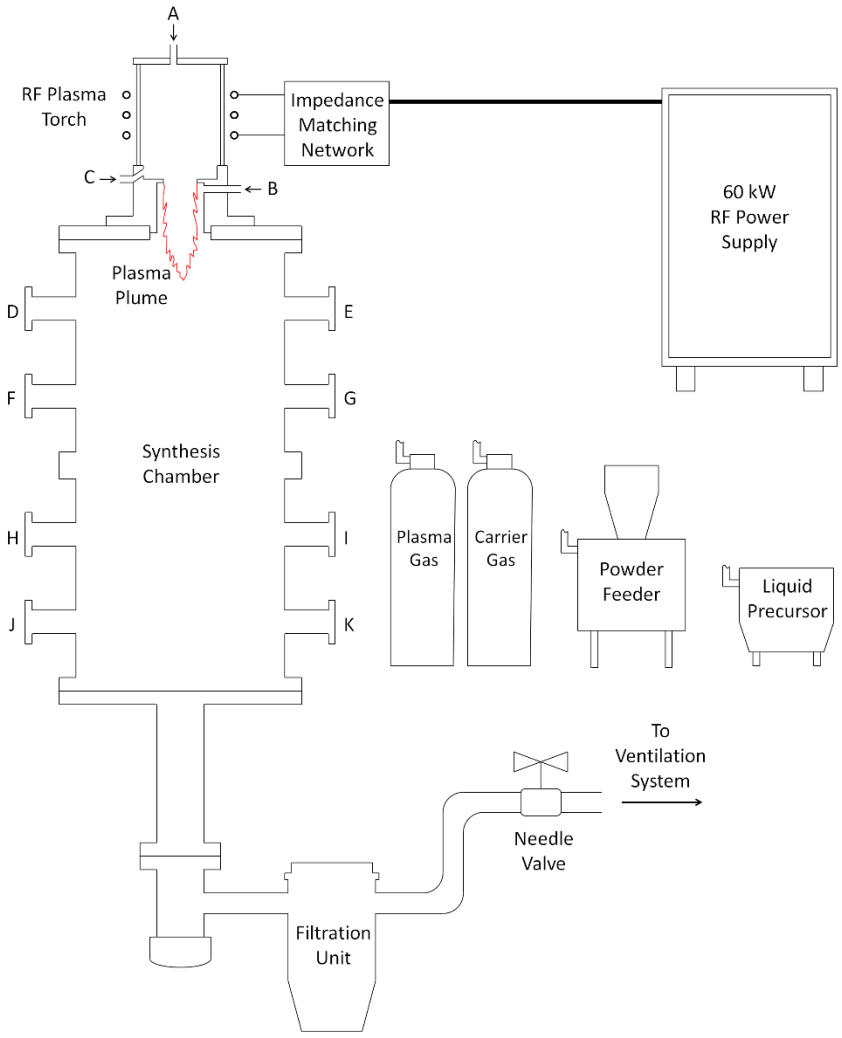


Figure 4.4: Schematic of a custom-built extended pressure inductively coupled (EPIC) thermal plasma system. Ports A, B, and C are for injection of plasma gas and/or feedstock near the plasma plume, while ports D – K are for diagnostics (such as optical monitoring of the reaction) and/or for insertion of quench modifiers or pressure-assisted purging of synthesized material.

been designed to withstand up to 10 atm of internal pressure. Pictures of the actual EPIC setup with the various components appropriately labeled are presented in Figure 4.5.

The RF plasma torch is shown in Figure 4.5, (for greater detail, see Appendix B), and consists of three water cooled copper coils wrapped around a ceramic cylinder. The unique plasma gas flow trajectories of this custom built torch are

presented in Figure 4.6. A single gas is sufficient for both plasma formation as well as torch cooling and can be introduced from one of two different ports. In the reverse vortex configuration, the plasma gas can be injected from an inlet near the bottom of the torch (labeled C in Figure 4.4), swirl upward along the inner wall of the torch body and then reverse to flow back down the center. In the direct vortex configuration, it can be introduced from the top (labeled A in Figure 4.4), swirl down through the torch body and out the exit nozzle.

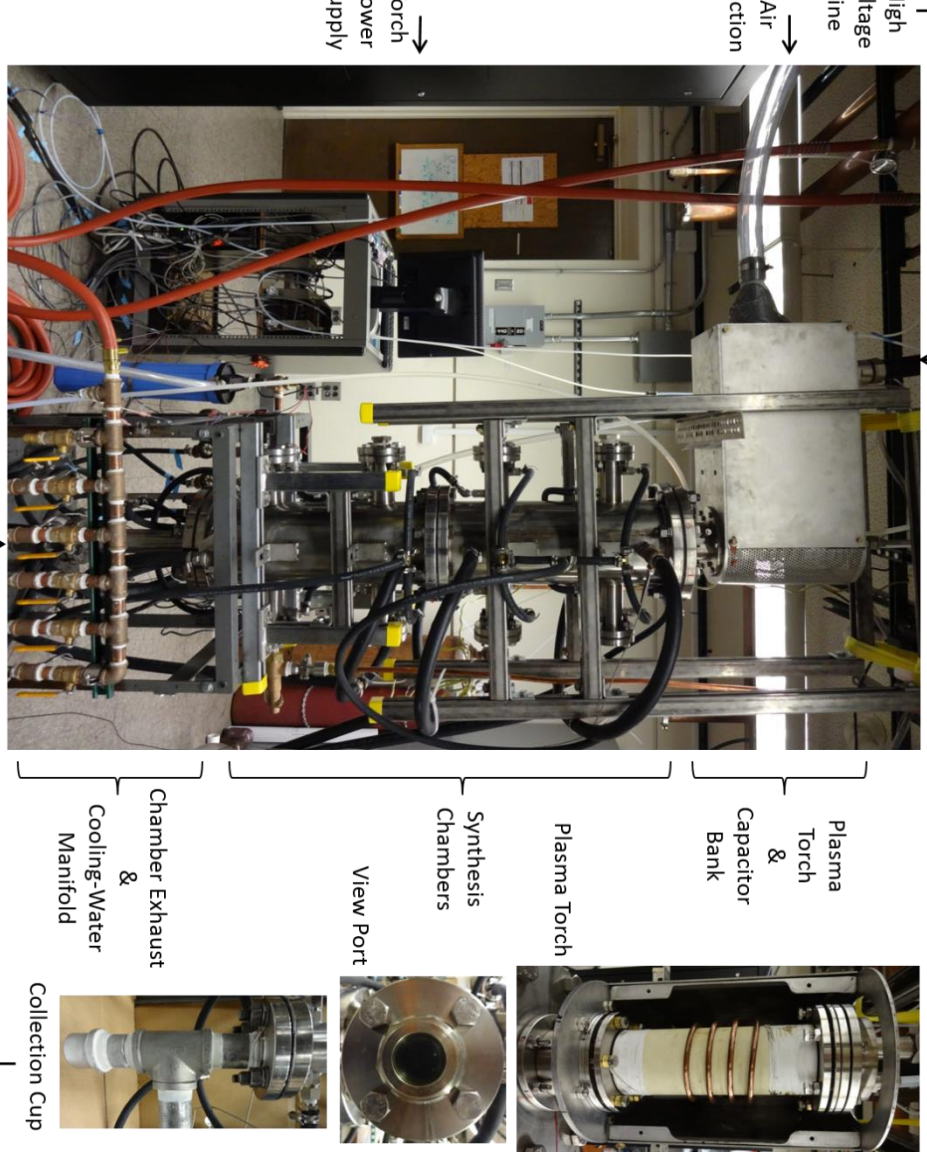


Figure 4.5: Picture of extended pressure inductively coupled (EPIC) thermal plasma system.

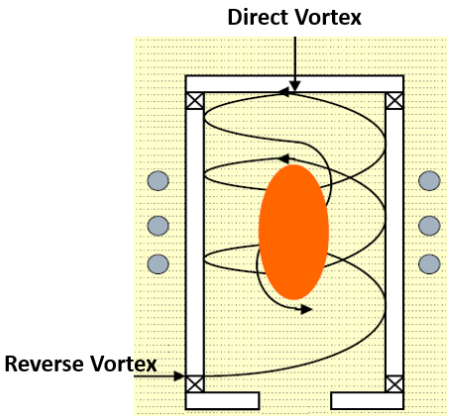


Figure 4.6: EPIC plasma torch gas flow trajectories.

Several access ports in the torch and synthesis chamber provide for materials injection/extraction and diagnostics, or for introducing quench-enhancers (such as wires or meshes). For example, the plasma gas (nitrogen) can be introduced at port A (direct vortex configuration), and boron feedstock (e.g. pure boron powder) can be injected directly into the plasma plume via port B. In this mode, the injected gas serves both as the plasma gas and sheath gas. Other modes of operation are possible, such as co-injection of the plasma gas and boron feedstock through port A, or introducing the plasma gas through port C (reverse vortex configuration) where the gas first swirls upward along the inner wall of the torch body and then back down the center. After passing through the chambers, the gases flow through a water-cooled exhaust pipe and a subsequent filtration system. A 3D rendering of the cross-section of the torch, synthesis chamber, and exhaust system, showing water-cooling jackets are presented in Appendix B. A needle valve located after the filter is used to fine tune the chamber pressure before the gases are exhausted to a ventilation system. For powder injection, a commercial powder feeder (Powder Feed Dynamics, Mark XV) is employed. The entire system (power supply, torch, adapter flanges, synthesis chamber, exhaust system) is water-cooled to allow for continuous operation and to ensure suitable thermal quench gradients within the synthesis chamber. Synthesized material can be collected manually from the opened synthesis chamber, or, more practically, via an *in-situ* pressure-purge extraction cycle which affords near-continuous (rather than batch) operation.

This versatile thermal plasma system is uniquely capable of operating under a broad range of parameters. ICPs typically operate at low pressures but never above atmospheric pressure. Ours is the first ICP to be capable of operating in a hyperbaric environment, designed for up to 10 atm, a condition which is conducive for the

synthesis of high purity BNNTs and other novel nanostructures. Furthermore, argon and/or nitrogen can serve as the plasma gas, the latter being notoriously difficult for the maintenance of a stable plasma, but critical for the synthesis of nitride nanostructures. Thus far, a stable plasma has successfully been attained with both pure argon and pure nitrogen at up to 75 psi (~5 atm) and variable plasma powers. Plasma plumes have been sustained using plasma gas flows in the 20 to 85 liters per minute (lpm) range, but could be taken beyond this range. The carrier gas can be tuned to modify the rate of introduction of reactants into the system. Details regarding the diagnostics of the EPIC system operating under various conditions are presented in Appendix C.

Understanding the function and adjusting relevant parameters are critical to optimizing processing conditions. There are several plasma parameters of significance including the plasma temperature, the velocity of plasma gas which determines the residence time of reactants in the plasma, and the plasma composition. The power density and volume of the plasma plume, which have direct bearing on these parameters as well as quench rates in the reaction zone, can be modified at any given pressure by varying the input power, gas flow rates, and makeup of primary plasma gas. In dealing with solid precursors, the important factors to consider are the particle size, chemical composition, and crystallographic structure. When injected into the plasma, a precursor's injection velocity and feeding density must be carefully considered, whether the feedstock is solid, liquid, or gas.

The quenching of vaporized or molten particles into small droplets is vital for the formation of seeded particles from which nanoscale tubular and other structures may nucleate. In the current implementation of the EPIC system, plasma-treated precursors experience a steep temperature gradient upon streaming from the high temperature region of plasma discharge into the water-cooled synthesis chamber. Quench rates can further be tuned by varying the cooling water flow rate to the synthesis chamber, lining the interior wall of the synthesis chamber with thermal blankets, or by injecting cold gases into the mix, perhaps through chamber side ports. Meshes, wires, cold fingers, and other solid materials may also be introduced downstream the plasma to serve as quenching surfaces, although they are not necessary.

#### 4.3.2.1 Temperature Profile Modeling

In the course of designing and building the EPIC synthesis system, simulations modeling various temperature profiles were conducted. Using SolidWorks Flow Simulation software, the system consisting of the two body synthesis chambers, the

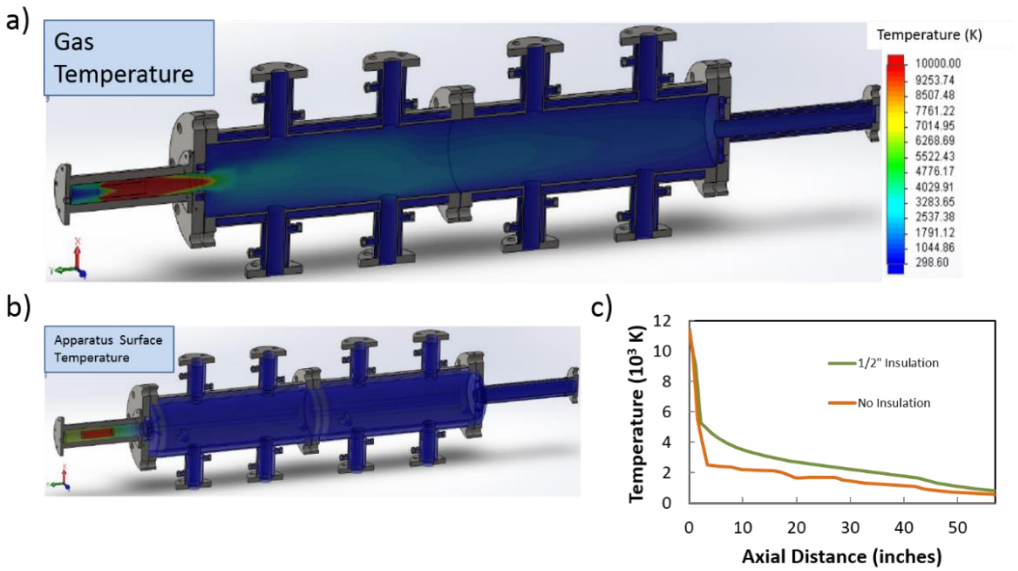


Figure 4.7: Temperature profile modeling of (a) gas flow through torch, synthesis chamber, and exhaust system and (b) inner chamber wall surfaces. (c) Gas temperature down central axis of EPIC system model. (Simulations courtesy of G. Leyva)

bottom flange and exhaust system, the top flange, and the torch were replicated. The complex inductively coupled plasma was simulated by a cylindrical heat source in the region of the torch, which could be set to any desired power output. The flow rates of cooling water through all of the ports and jackets of the EPIC system were also varied.

A typical temperature profile of nitrogen gas flowing through the torch, where it is heated by the variable power heat source, and on through the synthesis chamber is presented in Figure 4.7a. For this particular model, the gas flow rate is set at 10 L/min, the cooling water flow is 0.07 kg/s, the pressure in the chamber is set to 1 atm, and there is no insulation placed inside the chamber. The power level of the heat source is set so as to produce a core temperature close to that expected of our RF inductively coupled plasma (~10,000 K). From this simulation, we note that the synthesis chamber, ports, and most importantly the top adapter flange are sufficiently cooled. Their surface temperatures, depicted in Figure 4.7b, do not approach that of molten steel (~1400 °C). The hot zone of the gas, which experimentally may translate into the plasma plume, is seen to extend from the core of the torch, through the adapter flange, and a few inches into the synthesis chamber. This revelation is promising as one of the main sites for injecting precursor

material in our system is via a small chamber located between the exit nozzle of the torch and the top adapter flange, indicating that injected material from this site ought to adequately interact with the plasma. Furthermore, the nitrogen gas is sufficiently cooled upon exiting the exhaust system downstream the synthesis chamber.

Simulations were also conducted on the system for insertion of a thermal insulating layer of variable thickness inside the synthesis chamber. This may be necessary in practice in order to extend the hot zone of the plasma plume, and hence the residence time of the precursor material. Indeed, a thermally insulating layer of up to ¼" in thickness resulted in the hottest gas temperatures exiting the chamber. Although this does not indicate this particular thickness of insulation is optimal, it does illustrate that some thermal insulation does extent the hot zone of the plasma and too much insulation will produce higher temperatures near the exit nozzle of the torch, but at an overall reduced volume of the hot zone.

Figure 4.7c presents the gas temperature along the center axis of the system from the torch exit down through the chamber when no insulation is used and when ½" insulation is inserted. In the absence of insulation, a temperature gradient as high as ~2500 K/inch is attainable. The plasma gas and its constituents are rapidly cooled upon entering the synthesis chamber and after a few inches down the chamber, continue to cool down but at a much lower rate. The presence of a sharp inflection point separating the two regions of drastic and more gradual cooling is also present when the chamber is thermally insulated, with gas temperatures in this later case unsurprisingly higher throughout the body of the chamber.

### 4.3.3 EPIC Experimental Conditions

Although we have explored only a small fraction of the large parameter space afforded by the EPIC system, we find that with this approach the synthesis of BNNTs is remarkably effective and robust, producing high quality materials at record production rates of 35 g/hour. In the discussion below, we limit ourselves to synthesis runs in which no special quench wires or screens are used. The plasma gas is pure nitrogen injected via port A, but runs with hydrogen-nitrogen mixtures have also been explored. The boron feedstocks thus-far implemented are powders of hexagonal-BN (*h*-BN) (Alfa Aesar #11078, -325 mesh, 99.5%), amorphous boron (Alfa Aesar #11338, -325 mesh, 90%), ball-milled amorphous boron, a mixture of crystalline and amorphous boron (Alfa Aesar #11337, -325 mesh, 99%), boron carbide (Alfa Aesar #10922, 99+%), or ammonia borane (Sigma Alderich #287717, 90%). In no case is a catalyst used. All types of boron feedstock successfully produce BNNTs (and with suitable parameter adjustments, other BN nanomaterials as discussed

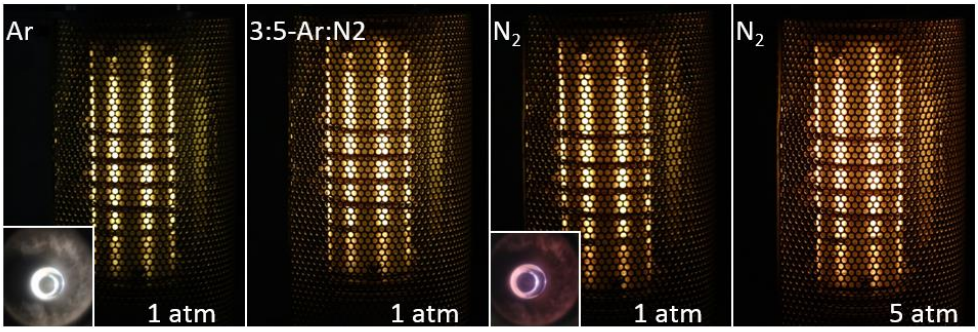


Figure 4.8: Light emanating from plasma torch for various plasma gas compositions at indicated pressures. Insets are images taken from top viewport showing a white and purple glow for pure Ar and $N_2$ plasmas respectively.

below), but the best conversion rates to date have been achieved with as-sourced amorphous boron powder (Alfa Aesar #11338). Nitrogen as the carrier gas (0.2 – 5 liters/min) is used to propel the powder radially into the plasma plume via port B near the torch nozzle at pressures varying from 14.7 – 75 psia (psi absolute), with boron injection rates between 100 and 1700 mg/min. Nitrogen flowing at 50 liters/min serves as the plasma gas with plasma power maintained at 40 – 50 kW, usually at 45 kW. Exploratory runs are typically of duration ten minutes to an hour.

Fibrils and sheets rapidly accumulated over the side port during these runs as observed live via a digital camera placed on the top side port nearest the torch. In order to prevent oversaturation of the camera from the intense plasma light, a shade 10 welding filter lens is used. Typically, very bright flashes of light are emitted from a viewing glass on the top side port opposite that of the digital camera. The periodic flashes correspond to the pulses of powder being fed into the plasma by the powder feeder, which unfortunately is noncontinuous. This is due to the tendency of boron to agglomerate, which makes feeding boron powder steadily and constantly at such low feed rates very difficult. As more material amassed throughout the chamber, the flashes of light from the viewports turned a reddish hue. Eventually the view from the camera also goes completely dark, at which point a run can be stopped.

The plasma itself will take on various colors during a run, as depicted in Figure 4.8. A plasma of Ar gas, which is used to initially ignite the plasma, illuminates white light as seen from the viewport, whereas a $N_2$ plasma gas will appear purple. In transitioning from Ar to $N_2$, the plasma plume itself becomes hotter and appears brighter. As previously discussed, $N_2$ plasmas have higher specific enthalpies than those formed of Ar. For elevated synthesis chamber pressures, the temperature of the plasma further increases and radiates even more light and heat. During certain

runs, a green glow was observed from the viewport which we suspect is due to a problematic condition where copper is melted from within the plasma torch. This and other issues encountered with the RF plasma torch are considered in Appendix E.

### 4.3.4 EPIC Product Material

Under the above conditions, the EPIC system immediately generates fibrous, light-colored, cotton-candy web-like material which soon occupies the entire cross-sectional area of the synthesis chamber, as shown in Figure 4.9a. The material initially accumulates near the upper part of the chamber (near the torch hot zone), and, as the run is continued, the synthesis chamber gets successively packed, filling a volume of 10 liters (half the total chamber volume) in approximately 20 minutes. In the 15 minute run whose resultant material is pictured in Figure 4.9a, 2.9 grams of product material was collected from the top synthesis chamber alone after feeding ~3.7 grams of boron precursor powder with a synthesis chamber pressurized to 30 psia (~2 atm). In conjunction with fibrils packing the interior volume of the synthesis chamber, the chamber walls typically also become coated in a similarly light colored material, which can be easily peeled off as a continuous felt-like film (Figure 4.9b). Often the fibril and felt materials have an overall light grayish color, which on closer inspection reveals itself as pure-white cottony patches dispersed among grayish material.

We have characterized both the fibril cotton-candy-like and felt-like sheet material and find that, over a broad range of synthesis conditions, both are composed predominantly of pure BNNTs (up to 80% yield) with wall number ranging from two to six, with the most common being double–wall tubes of outer diameter 4 nm similar to those observed using other BNNT synthesis techniques[220]. The grayish color originates from dark specks of unreacted boron (typically 20% of product) not incorporated into the pure-white (or rather transparent) tubes, and is easily removed by treatment in a nitric acid solution. In Chapter 5, we explore various routes to purify the as-synthesized BNNT material.

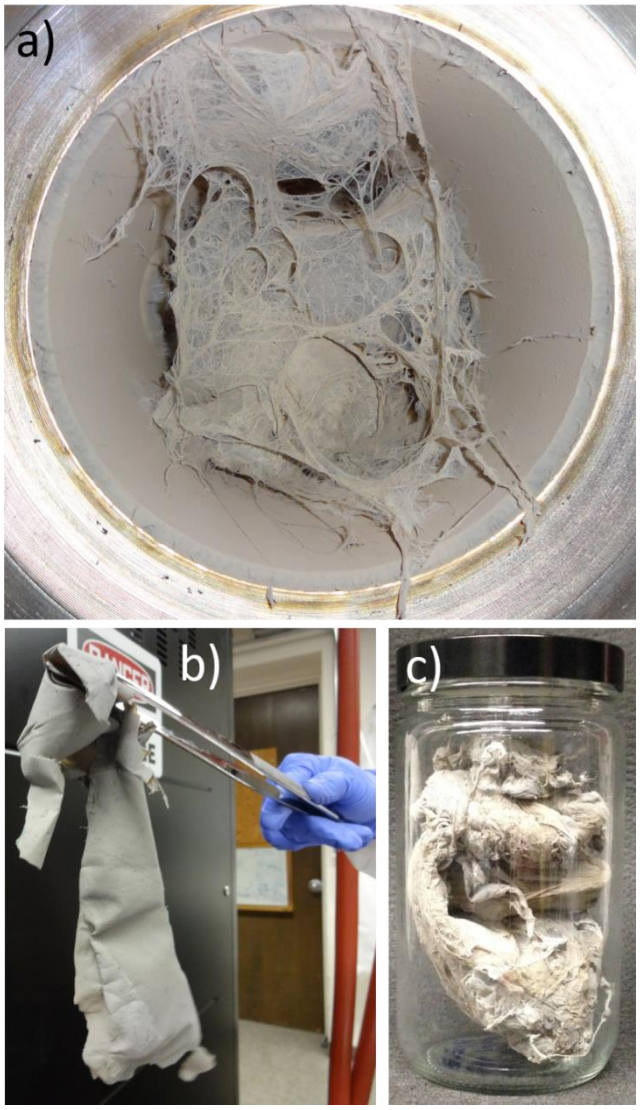


Figure 4.9: Photographs of BNNT material produced via the EPIC method. (a) As-synthesized BNNT fibril material accumulated within the 15 cm diameter synthesis chamber, as seen from below. After a few minutes of run time, the fibril mass completely fills the cross-sectional upper area of the chamber. As the reaction proceeds, the synthesized BNNTs fill more and more of the chamber volume. (b) BNNT felt-like sheet peeled intact from the walls of the reaction chamber. (c) Compressed BNNT fibril material (from a 15 min synthesis run) fills a one-liter glass jar. For (a), (b), and (c) the material is composed largely of double-wall BNNTs. Synthesis conditions: amorphous boron @ 246 mg/min; carrier gas $N_2$ @ 2.5 L/min; plasma gas $N_2$ @ 50 L/min; 40 kW plasma @ 30 psia.

#### 4.3.4.1 Characterization

The nanoscopic morphology and purity of the BNNT-containing material are elucidated using scanning electron microscopy (SEM) (FEI Sirion XL 300) with energy dispersive X-ray analysis (EDAX) capability and transmission electron microscopy (TEM) (JEOL JEM 2010 operating at 80 kV). Element-sensitive electron energy loss spectroscopy (EELS) is performed using a Phillips CM-200 TEM and a FEI Tecnai G2 TEM both operated at 200 kV. EELS characterization was conducted at the National Center for Electron Microscopy at the Lawrence Berkeley National Laboratory. Raman spectra are collected on a Renishaw inVia spectrometer using a 514 nm excitation laser.

Figure 4.10 shows characteristic SEM images of the fibril-like material removed from the center of the synthesis chamber. The low-density spongy material consists of millimeter to centimeter (or longer) whispy fiber bundles, with rough macroscopic alignment of the fibrils (Figure 4.10a). At higher magnification (Figure 4.10b, Figure 4.10c) the fibrils are seen to be composed of individual nanotubes, which are confirmed to be pure BNNTs by EELS measurements. From these images, we see that nanotube lengths exceed tens of microns. At a zoomed-in scale (Figure 4.10c), the origin of the grayish patches of the bulk material is clearly revealed as unreacted nanoscale particles of solid boron (identified by EDAX) interspersed among the pure tubes and fibrils.

TEM characterization of the fibrils reveal they are composed of many BNNTs, as presented in Figure 4.11. Networks of BNNTs, which tend to agglomerate into bundles of multiple tubes, are observed. Impurities consisting predominantly of boron particles are visible as spherical and irregularly shaped regions of dark contrast. The thicker strands, such as the one indicated by a red arrow, are composed of multiple individual BNNTs bundled together. These bundles have lengths of 10s of μm.

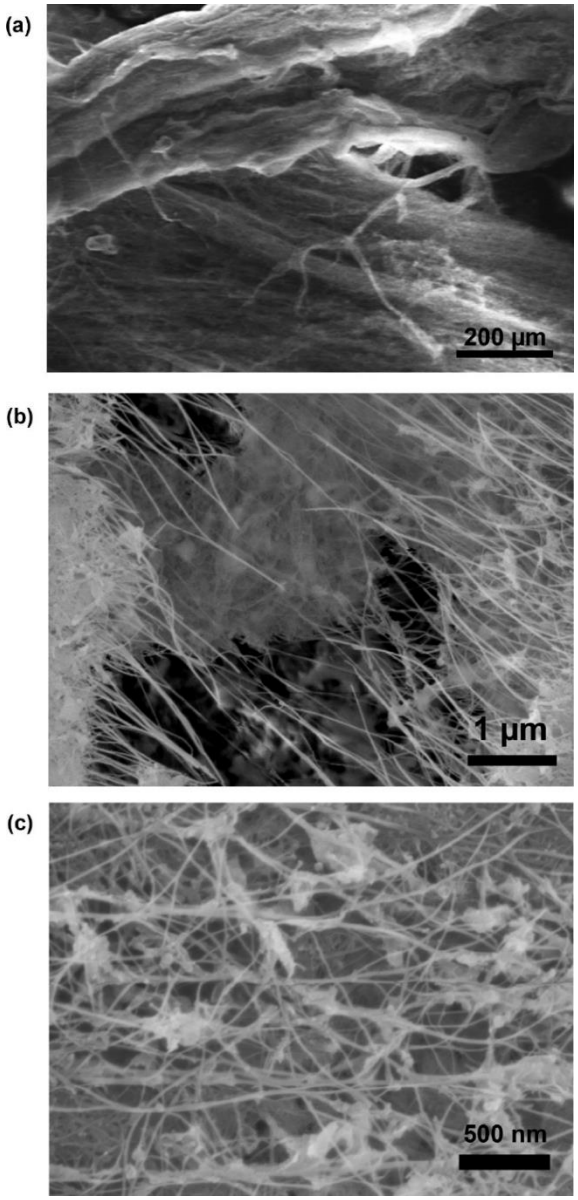


Figure 4.10: SEM images of as-synthesized BNNTs obtained from fibril-like material near the center of the synthesis chamber. (a) Low magnification image of long fibrils. (b) Higher magnification image showing BNNT bundles. (c) Zoomed-in image of BNNT bundles and tubes. High-contrast spots are solidified unreacted boron droplets. To aid in high-resolution SEM imaging, a conventional thin gold film has been sputtered onto the specimens in (b) and (c). Synthesis conditions: amorphous boron @ 150 mg/min; carrier gas $N_2$ @ 2.5 L/min; plasma gas $N_2$ @ 50 L/min; 40 kW plasma @ 45 psia.

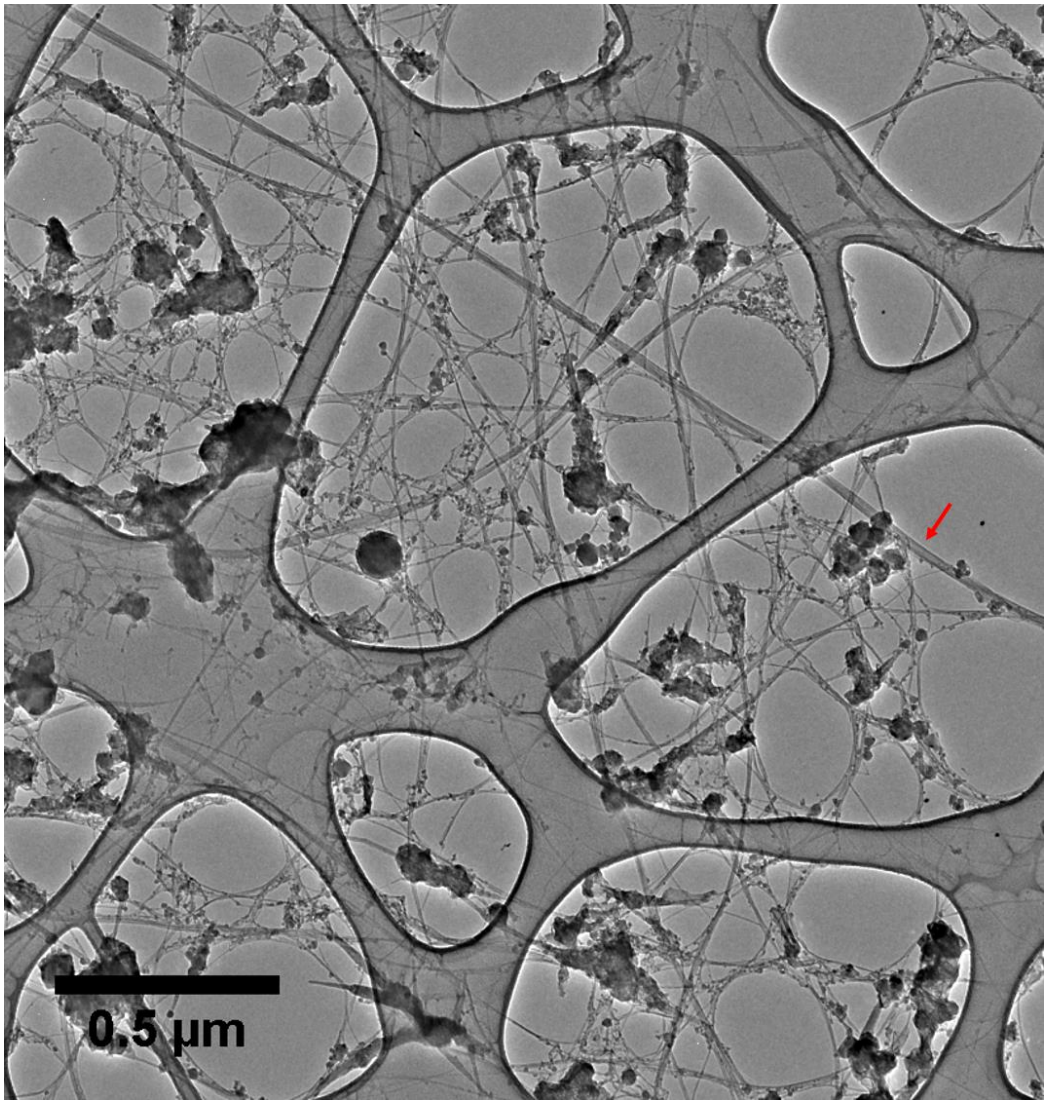


Figure 4.11: Low magnification TEM image of BNNTs produced by EPIC synthesis. Well dispersed network of BNNTs many microns long are seen amidst impurities, including unprocessed boron. The red arrow denotes a bundle of double-wall BNNTs which spans over 10 µm in length.

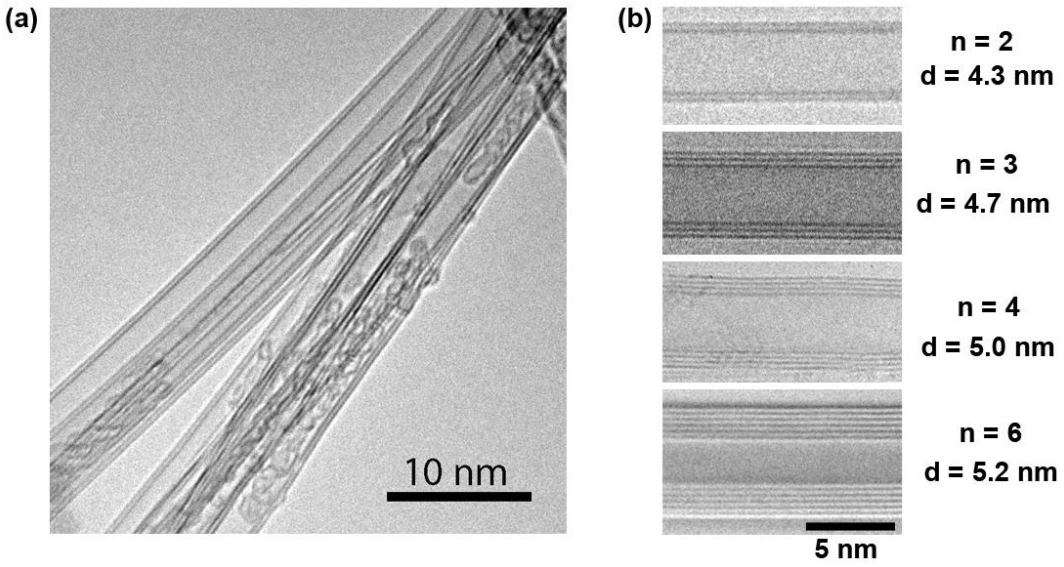


Figure 4.12: High-resolution TEM images of BNNTs produced by EPIC synthesis. (a) A bundle of double-wall BNNTs; (b) individual BNNTs with different number of walls indicated by *n* and outer tube diameter indicated by *d*. High crystallinity is apparent. Under these synthesis conditions, 70% of the BNNTs are double-wall, n=2. Synthesis conditions same as for Figure 4.10.

High resolution TEM images of individual BNNTs within the fibrils are presented in Figure 4.12. Figure 4.12a shows a typical BNNT bundle, consisting exclusively of double-walled tubes. Tube walls are perfectly straight with no discernible defects. Figure 4.12b shows details of several individual tubes. Tubes with wall number, *n*, ranging from two to six are shown, with outer diameters spanning 4 – 6 nm. The distance between tube walls is ~ 0.34nm, which matches the inlayer spacing of *h*-BN. Our TEM analysis verifies the hollow, tubular nature of the BNNTs. Counting tubes in multiple TEM sessions shows that the majority of the BNNTs are double walled (70%) with the next most predominant being triple walled (20%); 90% of the distribution has diameters ranging from 2 – 6 nm. The majority of the remaining 10% of the BNNTs are multiwall nanotubes with wall number $n \geq 3$, with only a very sparing amount of $n=1$ nanotubes, which are typically short and defective. This is discussed further below. The multiwall BNNTs are generally highly crystalline with straight walls with no "bamboo" or "Dixie-cup" like defects. The high crystallinity of the as-synthesized BNNTs is reconfirmed by selected area electron diffraction. The structural quality of the tubes is significantly higher than that seen for most other BNNT synthesis techniques and is comparable to that for BNNTs produced by the laser vaporization method[29].

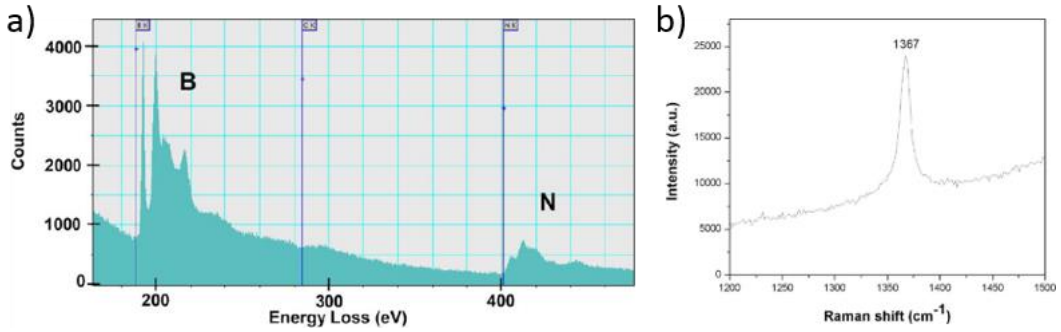


Figure 4.13: Electron energy loss spectroscopy (EELS) and Raman spectrum for BNNTs produced by EPIC method. (a) Boron and nitrogen peaks are clearly evident in the EELS spectrum and indicate an atomic ratio B/N of 1:1, as expected for pure BN nanotubes. A very small carbon peak near 285 eV arises from contamination from the carbon support grid during measurement; the as-synthesized BNNTs contain no carbon. (b) The peak position in the Raman spectrum at 1367 $cm^{-1}$ is characteristic of $sp^2$-bonded BN and the sharpness of the peak is characteristic of highly crystalline BN. Synthesis conditions: same as for Figure 4.10.

The elemental composition of the nanotubes is confirmed by electron energy loss spectroscopy (EELS). Figure 4.13a shows a typical EELS spectrum from a BNNT collected from the fibril region. Prominent boron and nitrogen peaks corresponding to the K-shell ionization edges of the two elements are clearly observed at 189 eV and 401 eV respectively. Quantifying these results yields an atomic B/N ratio of 1.0/0.8, in agreement with the expected 1/1 atomic ratio for pure BNNTs. Furthermore, these K-shell signals clearly exhibit fine structures which are attributed to the $\pi^*$ and $\sigma^*$ peaks. This confirms the $sp^2$ hybridized nature of the BN in the tubular structure. A very small carbon peak arises due to contamination from the carbon TEM support grid during measurement. Figure 4.13b shows a Raman spectrum for a BNNT, again collected from the fibril, chamber-center region. The peak at 1367 $cm^{-1}$ is attributable to the $E_{2g}$ vibration mode of $sp^2$-bonded BNNTs[17]. The FWHM is 11 $cm^{-1}$, which indicates highly crystalline "graphitic" BN[221].

### 4.3.4.2 Single wall BNNTs

The preponderance of double-wall BNNTs in our EPIC synthesis method is consistent with the ionic nature of the B-N bond and the tendency for inter-plane B-N bonding (hence the stable *A*-*A*' stacking structure of *h*-BN). An interesting question concerns the stability of single-wall BNNTs (SWBNNTs). For carbon systems, single wall nanotubes are straightforward to synthesize en mass[222], but for BN this has not

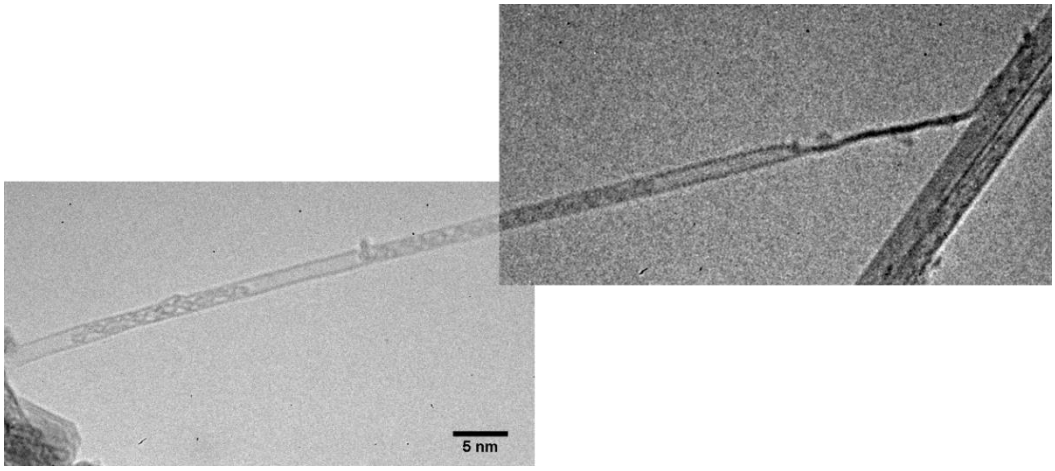


Figure 4.14: Single wall BNNT produced by EPIC synthesis whose end is structurally deformed. Synthesis conditions: amorphous boron @ 150 mg/min; carrier gas $N_2$ @ 2 L/min; plasma gas $N_2$ @ 50 L/min; 40 kW plasma @ 35 psia.

been the case[179,197]. Within the (admittedly limited) parameter range we have explored for EPIC, we find some, but not many, SWBNNTs. One such SWBNNT in a run conducted using amorphous boron powder as precursor is presented in Figure 4.14. The diameter of the tube is ~ 1.5 nm and spans a length of 75 nm before its end becomes malformed. In general, the SWBNNTs we do observe are not great in length, and at their ends they often morph into other lower symmetry, structurally tortured BN units. TEM images of SWBNNTs produced using the EPIC synthesis system using ball milled boron and boron carbide powder as precursors are presented in Figure 4.24 and Figure 4.25 respectively.

### 4.3.4.3 Collapsed BNNTs

Under appropriate synthesis conditions the EPIC system can also form a large fraction of collapsed BNNTs. For carbon nanotubes, it has been shown that for some types of nanotubes (few enough wall number and large enough diameter), the more stable configuration for a nanotube is not the conventional "inflated" tube of circular cross-section, but rather a "collapsed" or flattened tube where the tube now resembles more a ribbon. Collapsed carbon nanotube ribbons have been experimentally observed[26]. Previous efforts have examined deformed BN nanostructures by high temperature metal-catalyzed reactions of BNNTs[223], and alkali-driven "unzipping" of BNNTs has yielded BN-based ribbons[224], but edge-free

flattened-BN ribbons derived from unadulterated collapsed BNNTs have not been previously reported.

These structures are of special interest as the flattening is predicted to dramatically alter the electronic structure of the tube, allowing band gap engineering, and mechanically modulated optoelectronic devices. Using first-principles pseudopotential density-functional calculations, Kim *et al.* predict radial deformations applied transversely to a BNNT corresponding to pressures ~10 GPa would decrease the bandgap from 5 to 2 eV[11]. Such collapsed tubes could be utilized in optical applications in the visible spectrum. The bandgap of armchair BN tubes, however, is hardly affected by mechanical deformations. Bandgap modulation is a result of charge transfer from the flattened layers to the curved regions. For zigzag tubes, the closer proximity of same atomic species, namely boron atoms, along the circumference of the tube results in the overlap of charge densities in the highly curved regions[11]. Local deformations of zigzag BNNTs, wherein a flattened portion of a nanotube is located in-between two non-collapsed regions of the tube, would act as heterostructures with regions of different bandgaps adjacent to one another.

Figure 4.15a shows a high-resolution TEM image of a collapsed BNNT, flattened into a twisted ribbon, produced by the EPIC method. The flattened regions measure 6.5 nm in width, corresponding to a non-collapsed tube radius of ~2 nm which matches the size range of many double walled nanotubes in the resultant product. To date, these structures have been only produced as minority phases in the synthesis of BNNTs, but it is possible that for some set of parameters within EPIC they can be the dominant (or only) synthesis product. Flattened nanotubes with as many as 3 walls longer than several microns were observed, with most observed collapsed tubes being double-walled. Collapsed tubes oftentimes exhibit twists, as in Figure 4.15a, but straight flat regions were also observed, as in Figure 4.15b.

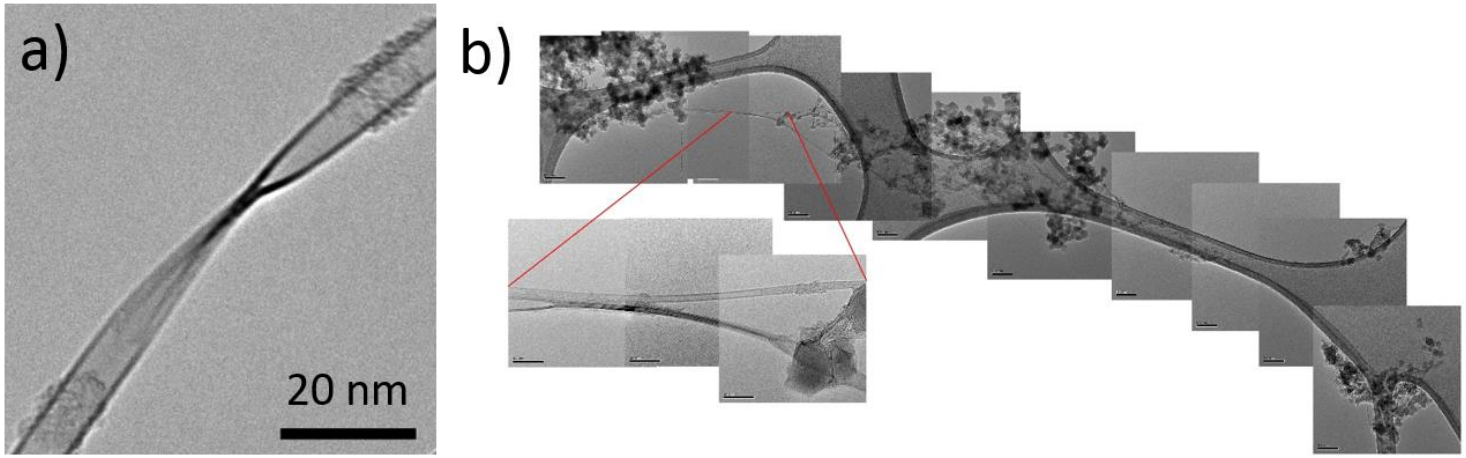


Figure 4.15: Collapsed BNNTs produced by EPIC synthesis. (a) Flattened, twisted BN nanoribbon derived from flattened BNNT. (b) Collapsed 3-walled nanotube greater than several hundred nm in length. Zoomed-in region on left is a high resolution TEM image showing nanotube region of flattening without twisting. (Image (b) courtesy of W. Mickelson)

### 4.3.5 Growth Mechanism

The EPIC system displays great versatility for tuning synthesis conditions. Variable pressure, carrier gas and feedstock type and injection rate all provide for a unique environment to grow not only high quality high aspect ratio BNNTs, but also other BN-based nanostructures. The experimental conditions under which various BN nanomaterials are synthesized can also elucidate the ways in which the nanostructures are formed. By tuning the reaction parameters, various forms of BN nanostructures can be targeted. In order to explain this distinctive capability, we present a model for the growth mechanism involved in the processing and synthesis of BN nanostructures in the EPIC plasma system.

Precursor material introduced into the plasma stream is either vaporized or molten to varying extents. The material vapor and/or molten particles are carried downstream towards the tail end of the plasma plume where the temperature will dramatically decrease. As the plume extends into the region of the water-cooled synthesis chamber, the temperature gradient will be steep. The vaporized precursor material becomes supersaturated upon quenching and will nucleate into nanoscale particles which may then coagulate with other particles. Drastic temperature gradients will enable the seeding of smaller molten and solidified particles upon exiting the plasma plume. However, precise control over the size of condensed particles is difficult to attain.

In order to elucidate the growth mechanism for the various nanostructures of BN, we first note the binary phase diagram of BN presented in Figure 4.16[225]. At temperatures below the melting point of boron near 2075 °C, two separate phases will coexist as solid *h*-BN will form alongside solid boron or gaseous nitrogen. An *h*-BN compound heated above 2400 °C will decompose into liquid boron and gaseous nitrogen. Elemental boron will remain in its liquid phase at temperatures as high as its boiling point near 3930 °C, above which it is vaporized. Both BN and B are in contrast to graphite which sublimates near 3600 °C at atmospheric pressure.

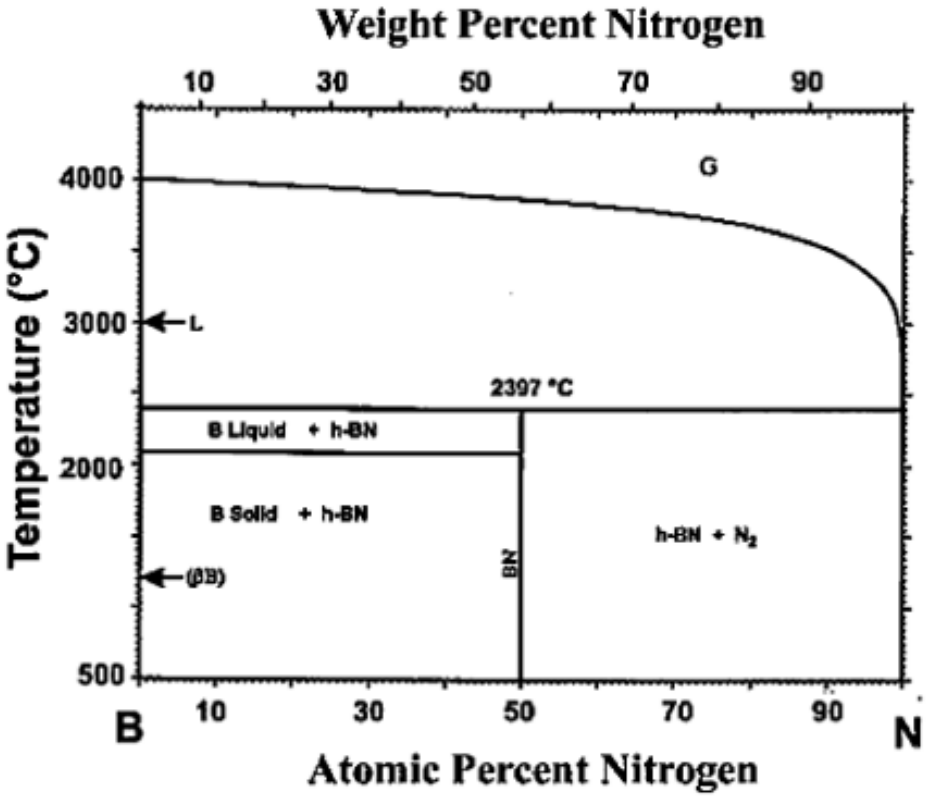


Figure 4.16: Binary phase diagram of BN. (From ref. [225])

Considering the high temperatures, which reach well above 4000 °C, and energetic species attainable within an induced thermal plasma, it is likely that boron vapor is present as the boron-containing precursor material is treated by the plasma. Indeed, in-situ UV-induced fluorescence measurements indicated the presence of boron vapor in a region a few millimeters above a BN target heated by a $CO_2$ laser wherein a surface temperature of ~3500 °C was measured by optical pyrometery[19]. Whether solid boron-containing precursor is vaporized in a plasma depends on several parameters, including the size, crystallinity and composition of the precursor particles as well as its residence time in the hot zone of the plasma. Molten boron droplets form after plasma processing. These molten droplets may form as the boron vapor condenses upon encountering the steep temperature gradient at the tail end of the plasma plume which expands into a water-cooled synthesis chamber. Droplets will also arise from the liquification of the initially solid precursor particles.

Molten boron is among the most chemically reactive substances[226]. It is known to react with any container and is even very chemically active as a high

temperature solid. In the process of melting, boron exhibits an insulator to metal transition and becomes electrically conducting[227]. Indeed, the structure of liquid boron has been studied by levitating boron particles in a stream of gas and liquefying them by a $CO_2$ laser[226,228].

As such, the liquid boron surface of the droplets is able to decompose the inert and otherwise very stable molecules of nitrogen encountered in the synthesis chamber. Ionized and dissociated $N_2$ is also provided by the plasma which interacts with the boron droplets as well. In general, nitrogen is sourced by the plasma gas, the carrier gas, and potentially during decomposition of the precursor material if it too contains N atoms, as in the case of *h*-BN or ammonia borane powders. From the phase diagram of BN, we note that as the temperature of the boron droplets fall below 2400 °C, the liquid surface reacts with nitrogen gas and activated nitrogen species to form BN structures.

The formation of nanotubes and nanococoons can be described by a root-growth, vapor-liquid-solid process[199]. In this scheme, a boron droplet serves as a seed for nucleation and growth as both a support structure off of which nanoparticles form and as the source of boron. The rapid quenching of boron vapors in the EPIC plasma process augments the nucleation of smaller boron droplets. In this manner, small-diameter BNNTs are produced without the need for metal catalysts or supplementary condenser mechanisms. As the chemical reactions between B and N progress, a $sp^2$ bonded BN layer(s) forms on the droplet surface. A continued supply of N from the environment reacting on the surface of the seed particle will perpetuate the formation of evermore B-N off of the active bonds of the BN layer. Eventually the BN cap will lift off of the droplet surface as B-N continues to be supplied to the end of the structure. The diameter of the cap and growing nanotube must necessarily be less than that of the seed particle in order that the tube continue to grow. Boron and nitrogen are integrated into the BN framework of the extending nanotube from the end of it which is interfaced with the surface of the boron droplet in an aptly named “root-growth” process. There is no need for a metal catalyst in such a route as chemical reactions are initiated at the liquid boron surface. Furthermore, by increasing the pressure of nitrogen gas in the synthesis chamber, BN forms at a faster rate since the collision rate of nitrogen with boron droplets will be proportional to the chamber pressure. Thus for even short residence times, this enhanced rate of interaction at elevated synthesis pressures enables the rapid growth of B-N networks which grow off of the boron seed particles in the form of nanotubes.

The nanotube will continue to grow as long as the surface of the boron droplet remains liquid, which from the phase diagram of BN necessitates its temperature remains above 2100 °C. Tube growth will also be terminated when the seed particles

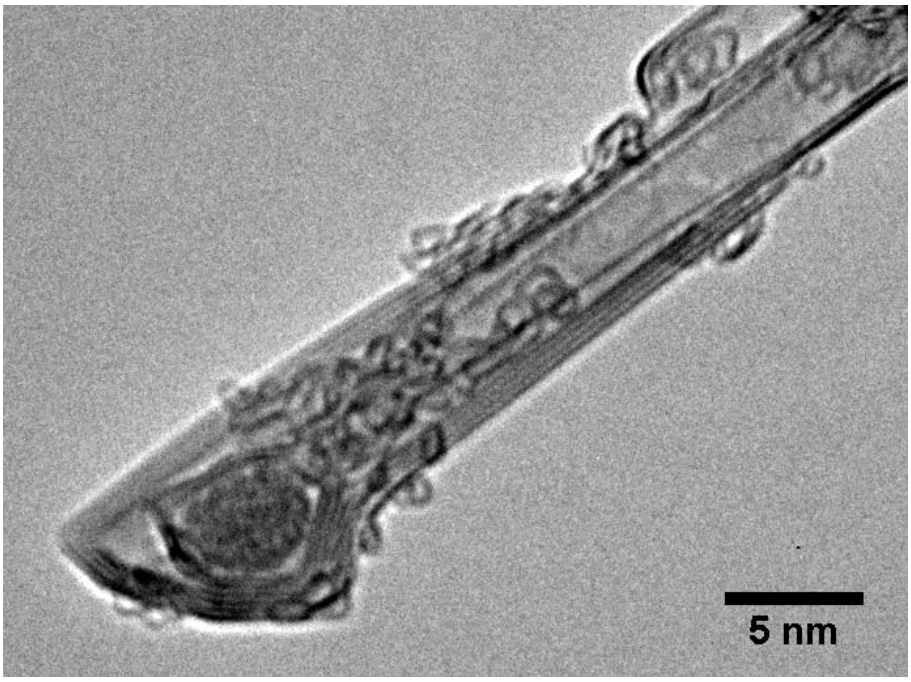


Figure 4.17: Boron particle encapsulated at nanotube end.

are diminished. Based on the relatively long nature of BNNTs synthesized via the EPIC plasma process, the residence time of seed particles is long enough to ensure an extended period of suitable growth conditions. Typical ICP processes have residence times of 10 – 25 ms. Once the boron droplet solidifies, the remaining nitrogen atoms present within and on the droplet's surface will precipitate and react with surface boron atoms to form a BN shell encapsulating the boron particle. Figure 4.17 is an image of a boron particle contained within BN layers at the end of a BNNT. It is difficult to assert the percentage of nanotubes with encapsulated boron particles in the EPIC plasma synthesis process due to the very long nature of the nanotubes. For a sufficiently long residence time, nanotube growth may terminate upon complete depletion of the boron seed particle resulting in very long nanotubes.

The formation of shells of BN around boron particles, referred to as "nanococoons" or "nanocages," follows a similar route to that of BNNTs. Initially the liquid surface of the boron droplets reacts with nitrogen to form $sp^2$ bonded BN. In the case of nanocage formation, however, the layers of BN do not form a cap which peels off of the seed particle's surface. The BN layers form around the boron particle until it is fully encapsulated, thus cutting off nitrogen access to the reactive boron surface and stopping the addition of subsequent B-N.

By tuning reaction parameters in the EPIC plasma system, particular morphologies of BN nanostructures can be attained in higher yields. For BNNT synthesis from pure boron and nitrogen, the overall reaction is

$$2B + N_2 \rightarrow 2BN \qquad (4\text{-}7)$$

This reaction rate should increase under high pressure of nitrogen, and indeed that is what is observed. At 1 atm pressure, while some BNNTs are formed, there is also a considerable amount of boron that has not completely reacted with nitrogen to form BN. In this case, there can be only a shell, or nanococoon, of BN around the boron particles. Figure 4.18 shows examples of boron-filled BN nanococoons so produced. At pressures above 2 atm, the concentration of these nanococoons begins to decrease and, at 3 atm and above, they are only a small fraction of the resulting product (<10%). While this indicates that, as previously suggested[29], high pressure nitrogen environments can assist high purity BNNT synthesis, it also corroborates the proposed mechanism of BNNT formation described above. Namely, as boron is injected into the plasma plume, it becomes a molten droplet. The surface of this droplet reacts with the nitrogen while within and as it exits the plasma plume. The higher pressure of nitrogen increases the energy density of the plasma plume and the collision rate of nitrogen atoms with the boron droplet and thereby shifts the reaction toward BN in equation (4-7). When the nitrogen pressure is relatively low, the boron does not react completely thus enabling BN nanococoons. As the nitrogen pressure increases, the boron droplet completely reacts forming mostly BNNTs. Hence, the EPIC system allows tailoring of BN-based nanoparticle growth, and thereby various forms of non-nanotube BN nanostructures can be produced in significant quantities (though in our preliminary studies not yet exclusively).

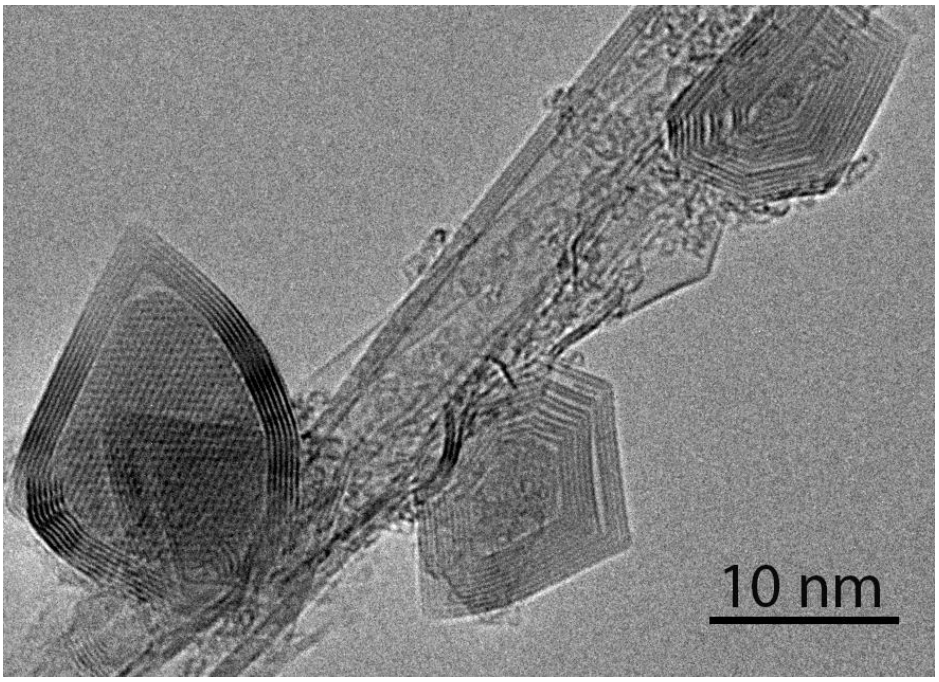


Figure 4.18: TEM image of BN nanococoons filled with boron. Encapsulated crystalline boron (left-most nanococoon) and amorphous boron (center nanococoon) are present. Synthesis conditions: amorphous boron @ 150 mg/min; carrier gas $N_2$ @ 2.5 L/min; plasma gas $N_2$ @ 50 L/min; 40 kW plasma @ 25psia.

Once created downstream the plasma, nanotubes will cluster together to form bundles, which when intertwined with other nanotubes and bundles form larger fibrils. As these and other resultant nanostructures continue to flow down the synthesis chamber, many will collect on the inner chamber walls. The presence of boron impurities makes these macroscopic films sticky and subsequently formed fibrils will adhere to these deposited layers, typically producing transparent sheets which grow across side port openings and web-like fluffy material that traverses the entire inner diameter of the synthesis chamber.

Challenges in the selective synthesis of BNNTs or other BN nanostructures persist. For instance, reports of oxygen present in particles trapped in nanocages but absent in those found at the ends of nanotubes suggest that oxygen plays a role in inhibiting the reaction of boron with nitrogen[199]. Oxygen might appear in the EPIC plasma process via the precursor material which may become oxidized or absorb water vapor when left for extended periods of time in the powder feeder. Hence maintaining precursor material in the feeding hopper under inert gas, and frequently changing the powder between runs may aid in ridding oxygen contamination and thus enhance the tailored synthesis of BNNTs. Furthermore, the presence of boron

in the product material indicates that some of the precursor feedstock is not converted into BN. Much of the solid precursors, in the form of boron or boron nitride powder, may not be sufficiently thermally treated in the plasma to liquefy or dissociate them using the current implementation of EPIC. Molten boron may also solidify before reacting with nitrogen, as evidenced by the presence of boron particles in the resultant product for runs conducted using BN powder as a precursor. Future efforts to increase BN yields include varying parameters to maintain lengthy residence times while increasing the synthesis chamber pressure, using liquid or gaseous precursors which are more easily vaporized than solids, and feeding precursors further upstream the plasma, for instance from port A in Figure 4.4.

## 4.4 Synthesis Parameters

The EPIC synthesis system has been designed and built to allow for maximum flexibility with operating parameters. For instance, the plasma can be composed of pure argon, pure nitrogen, or a combination of these and potentially other gases. Varying the plasma gas composition allows for altering the fundamental properties of the plasma, such as its specific enthalpy, as well as introducing or eliminating certain chemical compounds. For instance, in an attempt to synthesize boron nanotubes, a pure Ar plasma was used, but with little promising results. Furthermore, the power of the plasma is easily adjusted by the user. The plasma gas can be fed in through the direct or reverse vortex injection points detailed above in section 4.3.2.

Various precursors, including a number of different solid powders, can also be fed into the plasma plume at a controllable carrier gas feed rate. The vibration amplitude and powder feeding screw rate of rotation are changeable. The carrier gas itself may also be changed, for instance to $CH_4$ if we want to attempt $B_xC_yN_z$ nanoparticle synthesis, from its standard $N_2$ composition. The synthesis chamber itself can also be equipped with various condensers, collector plates or meshes, and thermal inserts.

Perhaps the most unique feature of the EPIC system is the ability to maintain an inductively coupled plasma at hyperbaric pressures up to 10 atm. As discussed above in section 4.3.5, the higher pressure capability of EPIC is critical for the high yield synthesis of BNNTs.

With such great versatility, we have only begun to explore the wide parameter space capable with the EPIC synthesis system. In the sections to follow, we describe the results of various runs conducting several operating parameters, including plasma gas composition, precursor feedstock, and using thermally insulating inserts.

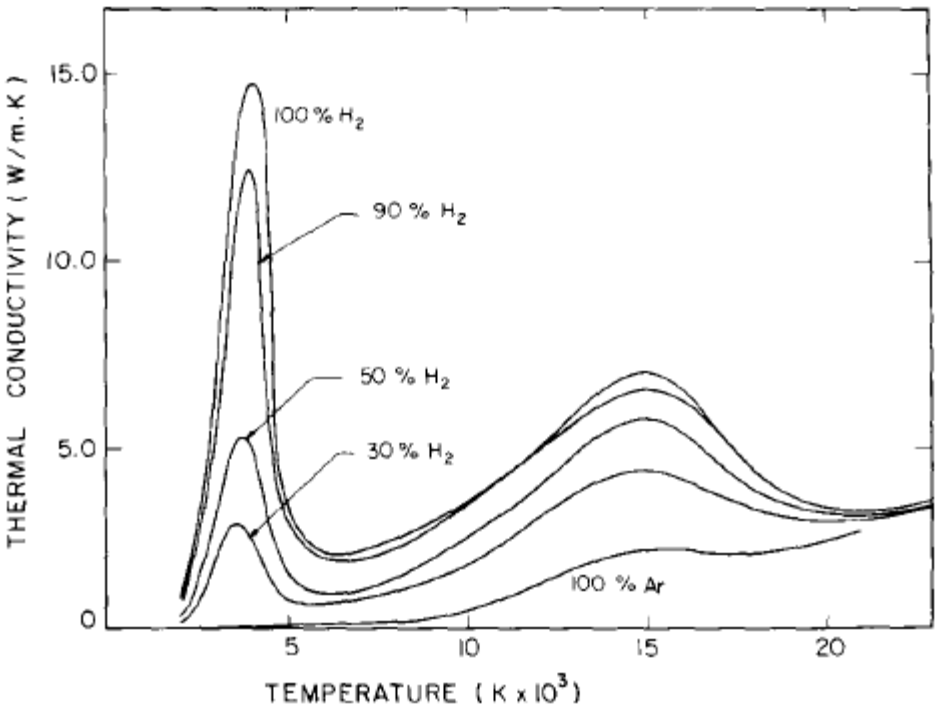


Figure 4.19: Thermal conductivity of $Ar/H_2$ mixtures as a function of temperature at atmospheric pressure. (From ref. [206])

## 4.4.1 Hydrogen Mixture Plasma Gas

As illustrated in Figure 4.2, $H_2$ has a relatively high specific enthalpy. It dissociates between 3000 – 5000 K, resulting in an enhancement of specific heat and thermal conductivity. As shown in Figure 4.19, a small concentration of $H_2$ mixed in Ar can substantially increase the gas mixture's thermal conductivity[206]. The sharp peaks observed near 4000 K correspond to the dissociation of $H_2$.

In order to investigate the effect of hydrogen on the plasma processing of BN materials, several runs were conducted using a mixture of hydrogen and nitrogen as the plasma gas. An amorphous boron powder (Alfa Aesar, -325 mesh 90%) was fed into a plasma composed of a 50 lpm flow of (a) 2% $H_2$ in $N_2$ balance and (b) 4% $H_2$ in $N_2$ balance. The synthesis chamber was pressurized to 41 psia (~2.8 atm). Greater vacuum tube anode voltages, up to 10.8 V, were required to maintain this power level relative to pure $N_2$ plasma runs. The addition of $H_2$ produced a visibly brighter plume and radiated more heat. The return cooling-water temperatures increased with greater $H_2$ concentration. Indeed, the plasma power was set at 45 kW for the

Figure 4.20: Photo of as-synthesized material produced using $N_2/H_2$ plasma gas mixtures. 50 lpm $N_2$ gas is mixed with (left) 0% $H_2$, (center) 2% $H_2$, and (right) 4% $H_2$.

2% $H_2$ run, but was only taken up to 40 kW for the 4% $H_2$ run in order to prevent overheating.

Following a 13 min run, white fibrils and sheets had accumulated along the inner walls and through the center of the synthesis chamber. As depicted in Figure 4.20, the collected material for both the 2% and 4% $H_2$ gas mixture runs were the most uniformly white material produced by the EPIC synthesis system, with greater $H_2$ concentrations creating visibly whiter material. Markedly white fluffy balls of very low density a few cm in size were also deposited on the chamber walls.

Based on the macroscopic whiter nature of resultant material produced, increased levels of $H_2$ in the composition of the plasma gas are conducive to BN synthesis. TEM characterization, as presented in Figure 4.21, reveals a great propensity for the creation of BN sheets alongside nanotubes. Runs conducted with 2% and 4 % $H_2$ mixtures contain a significantly larger amount of sheet-like material, often times appearing crumbled up and mixed with networks of nanotubes. These are labeled with red arrows in Figure 4.21b and Figure 4.21c. Long bundles of nanotubes with very clean, straight walls are also present, as depicted in Figure 4.21a. The nanotubes are mostly double-walled, with some containing 3 – 5 walls. No change in the diameter distribution of nanotubes was noticeable when compared to runs conducted without $H_2$, as most tubes were between 3 – 6 nm.

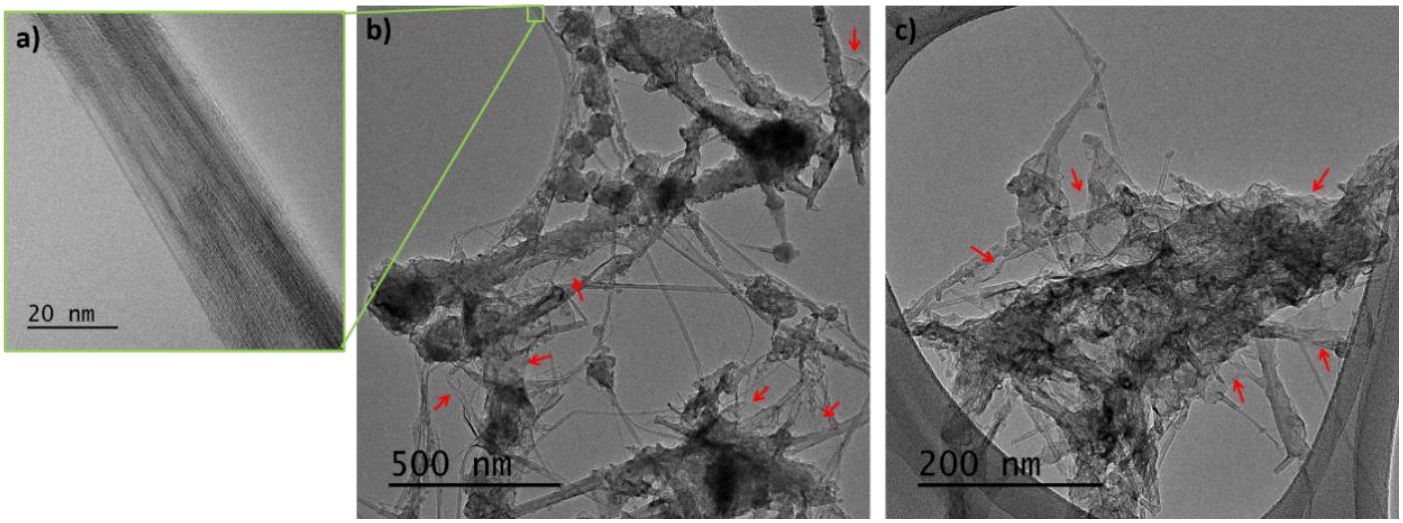


Figure 4.21: TEM images of resultant product using $N_2/H_2$ plasma gas mixtures. $N_2$ as plasma gas is mixed with (a) and (b) 2% $H_2$ and (c) 4% $H_2$. Red arrows indicate *h*-BN sheets.

As previously noted and evidenced by Figure 4.2, the incorporation of $H_2$ produces a higher enthalpy plasma which can then more readily dissociate $N_2$ and vaporize the injected boron powders. The greater thermal conductivity of the $H_2$-$N_2$ plasma will also result in more uniform heating and greater heat transfer to solid precursor particles in accordance with equation (4-6). Hence with more of the precursor material being processed, less of it will remain as an impurity leaving the final product to take on a lighter color.

After the successful implementation and investigation of various parameters in utilizing the EPIC system for the synthesis of BNNTs, a related plasma synthesis of BNNTs effort was reported[30]. In the study of Kim *et al.*, *h*-BN powder is injected into a slightly reduced- (i.e. slightly below atmospheric) pressure inductively coupled plasma, with an impressive BNNT production rate close to those reported here. Interestingly, the method of Kim *et al.* necessitates hydrogen gas, as well as pre-formed *h*-BN precursor feedstock, for meaningful yield. Using a commercial TEKNA PS-50 Torch (Tekna Plasma Systems, Inc.), the authors found it essential to include $H_2$ in their sheath gas mixture in order to produce BNNTs. In the extended-pressure EPIC method, neither hydrogen nor *h*-BN are necessary. Indeed, it appears that the "catalytic" activity of hydrogen in the Kim *et al*. method is obviated by a higher pressure nitrogen environment; similarly, the EPIC method reported here is tolerant of a wider range of boron-containing feedstock (for example pure boron powder injection yields excellent results using higher-pressure plasma, but is unsuccessful in the hydrogen catalyzed ICP study).

Nevertheless, their results highlight a key mechanism at play with the incorporation of $H_2$. The presence of H radicals in the mix is projected to slow down the recombination of free nitrogen atoms back into $N_2$, forming N-H, B-H, and B-N-H intermediate species. The B-N-H intermediate species may contribute to the growth of BNNTs, but many will form as solid by-products as the system continues to cool. These byproducts take the form of BN sheets as well as solid borazine-like polymers[30]. This likely accounts for the greater abundance of BN and other sheet material present in our runs conducted with $H_2$ gas mixtures.

### 4.4.2 Thermal Insulation

In the EPIC synthesis system, we have the ability to control the volume of the synthesis chamber and the boundaries of cooling experienced by the plasma plume upon exiting the torch. This can be achieved with the use of various inserts. As the inner chamber walls as well as the surfaces of the top and bottom adaptor flanges are directly cooled with water, these cold surfaces are very conducive to condensation of material. More importantly, they set the boundary conditions for

the temperature profile of the synthesis chamber environment experienced by processed material exiting the high temperature plasma plume. These boundary conditions can be altered. For instance, the insertion of a thin 316 SS foil (0.002" thick) thermally decoupled from the inner chamber wall allowed us to create an environment with a reduced temperature gradient exiting the plasma while maintaining the volume of the synthesis chamber. No significant difference in the yield or quality of resultant material was observed between runs conducted with and without the foil. This may have been due to insufficient thermal isolation of the foil from the chamber walls. Material collection, however, was much easier, simply requiring we pull out the foil lining from the inside of the chamber.

Volume and temperature profile control was also achieved with the use of thermal blankets as inserts. Based on our simulations, described in section 4.3.2.1, thermally insulating inserts of varying thicknesses will alter the temperature profile inside the synthesis chamber. For instance, our models predict that increasing the thickness of the thermal insulation layer up to 1" will extend the length of the plasma plume and decrease the gas temperature gradient. The temperature of the region in the vicinity of the chamber immediately after the torch exit (up to 8" after the nozzle) also increases with thicker insulation up to 1". The temperature of the gas upon exiting the bottom plate was found to be maximized when the insulation layer thickness was 1/4". Although precise quantifiable results cannot be concluded with our simulations, they do suggest that the hot zone experienced by precursor material can be extended and temperature gradients altered with the use of thermal inserts.

Experimentally, this was tested by rolling a sheet of carbon insulating fiber 4-5 times and positioning it inside the top synthesis chamber, creating a final layer ~0.5" thick. Runs with standard parameters were then conducted, feeding amorphous boron powder into a $N_2$ plasma with a synthesis chamber pressure of 48 psia (~3.2 atm) for 10 min. As depicted in Figure 4.22a, a low density ball of fibrous material collected on the inside of the carbon insert. The rolled sheet of carbon can easily be removed and unrolled, maintaining the general structure of the bulbous deposition, as imaged in Figure 4.22b for a 30 min run. The entire inner surface of the exposed carbon sheet was coated with white residue which formed as films that could be peeled off in multiple layers. A low density orb of webs and sheets which had formed across the center of the synthesis chamber is white and yellow due to the presence of boron impurities. Overall, similar yields of raw BNNT material was produced with and without the use of thermal inserts.

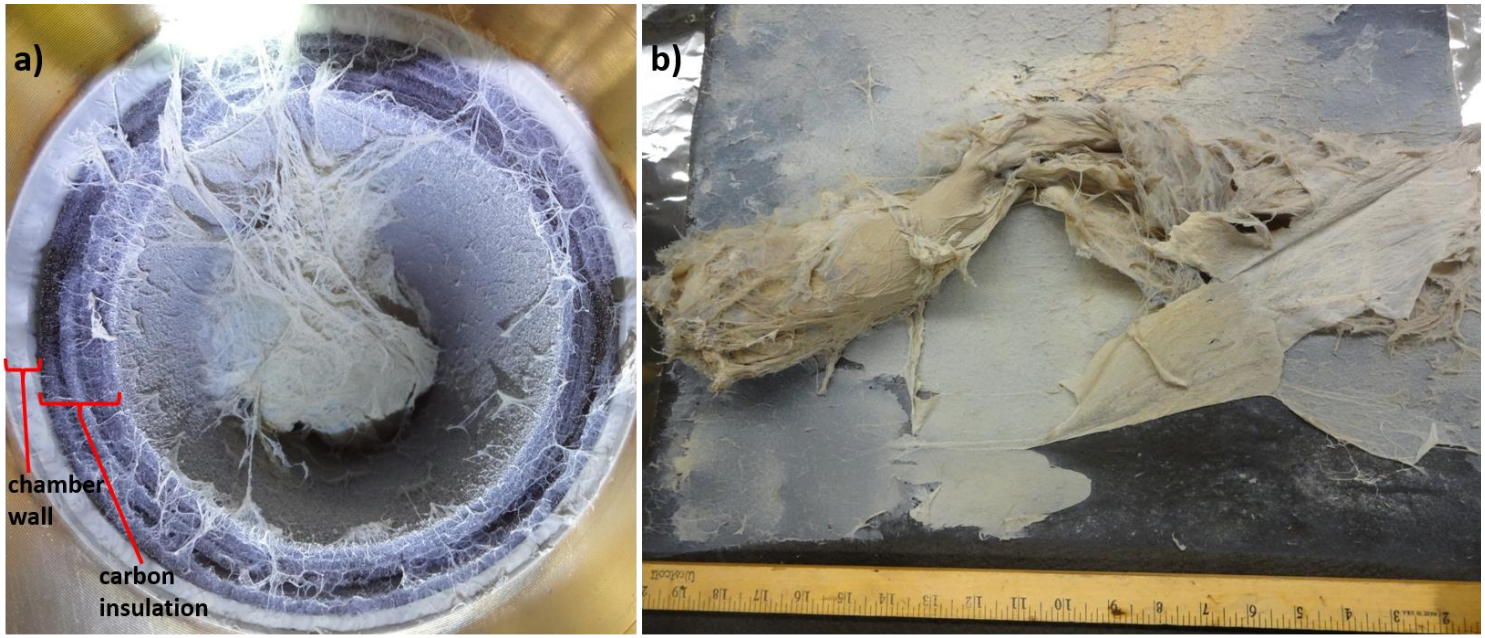


Figure 4.22: Optical images of resultant product material using thermal inserts in synthesis chamber.(a) Top chamber (as seen looking upward) following a run with BNNT material accumulated throughout the inside and wrapped thermal inserts visible. (b) As-synthesized BNNT material present on the unwrapped thermal blanket after removal from the synthesis chamber.

Based on TEM and Raman characterization, material synthesized with the thermal inserts does not qualitatively differ very much compared to those obtained without. It is composed of multiwalled nanotubes with mostly 2 – 4 walls alongside nanococoons and various impurities. The nanotubes cluster into bundles which extend beyond the several micron viewing range of this image. Sheets as well as a relatively large number of thick beaded objects which most likely are formed from amorphous boron are observed.

Longer runs did not produce a larger volume of core material, but rather increased its density. From these results, we get some insight into the growth mechanism of the resultant product. BNNTs and other material produced from the plasma process first accumulate on the chamber walls (or insulation). Eventually fibrils form which adhere to the coated walls. Subsequent fibrils interlock and form longer strands which traverse the inner diameter of the synthesis chamber. This occurs in the region of our top chamber. These long webs and threads will be forced downstream by gas flow, but also with the accumulation of evermore material. Eventually the network of webs crossing the chamber will no longer be stretched further downstream. Any subsequent material can then only deposit atop previously existing webs. Indeed, for runs conducted as long as 30 minutes, the region of the deposited material closest to the torch was predominantly hardened boron powder which could not flow through the hot zone in the nitrogen rich chamber long enough to form BN.

### 4.4.3 Solid Precursors

#### 4.4.3.1 Boron Powders

Various modifications on using boron powder as precursor material were explored. A combination of amorphous and crystalline powder (Alfa Aesar, -325 mesh, 99%) as precursor feedstock yielded less material volumetrically, and was visibly darker for similar run conditions conducted with amorphous boron powder (Alfa Aesar, 90%). Crystalline boron is a hard, brittle shiny black semimetal whereas amorphous boron is a brown powder. From the TEM image of Figure 4.23a, many more boron impurities pass through the plasma without conversion to BN. Nanotubes are similar in character to those described above possessing similar diameters, number of tube walls, and are predominantly defect-free. Notably, a greater number of boron nitride nanococoons (BNNCs) encapsulated crystalline boron. In Figure 4.23b, a double-shelled 15 nm nanocage is seen to surround a crystalline particle of boron. A smaller BNNC with three shells at the bottom of the

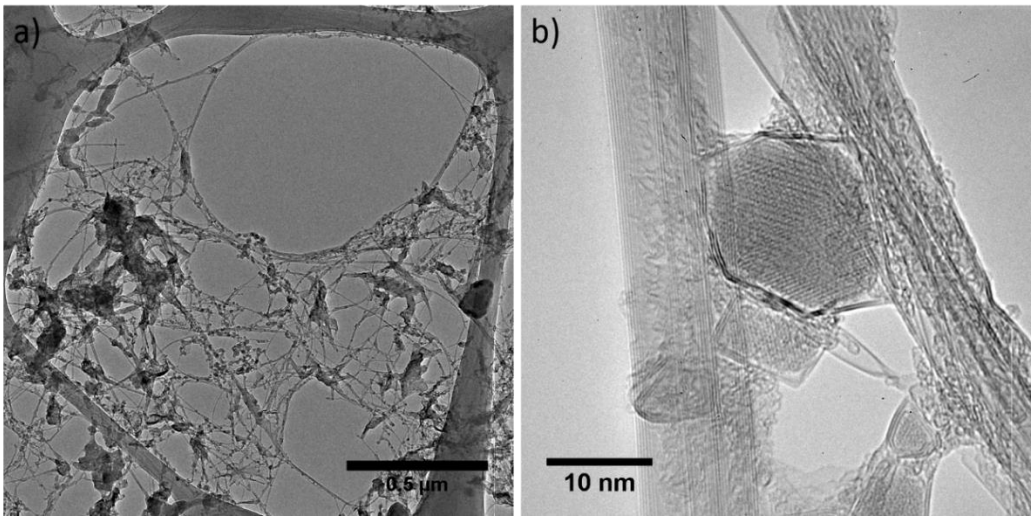


Figure 4.23: TEM images of runs conducted using crystalline and amorphous boron powder precursor. (a) Low magnification TEM image of BNNTs dispersed alongside solid particle and larger sheet-like materials. (b) High resolution TEM image of BNNT bundles and BN nanococoons encapsulating solid crystalline boron particles.

image is pictured covering an amorphous phase of boron. A bundle of nanotubes is seen on the left which contains a 5-walled and 6-walled nanotube.

The higher yield of BNNTs obtained using amorphous boron as feedstock maybe due to the presence of ~ 5% Mg impurities in that material. No metal particles were observed at the end of nanotubes in resultant material. Although the Mg does not serve as a catalyst for BNNT growth, the presence of metal in the plasma may affect the thermodynamic equilibrium compositions which foster conditions more conducive for the growth of nanotubes. Furthermore, amorphous boron is composed of agglomerates of smaller particles. The resulting larger specific surface area of the amorphous boron than the crystalline allotrope enables greater surface reactions and energy transfer to these particles from the plasma environment. Indeed, several studies report a more rapid thermal ignition of amorphous versus crystalline boron which is primarily attributed to morphological differences[229,230].

### 4.4.3.2 Ball Milled Boron

The amorphous boron powder which produced the highest yield results as feedstock material was sourced by Alfa Aesar (product # 11338, 90%). This particular powder has been filtered through a -325 grade mesh, which corresponds to a sieve

opening of 44 μm. In order to break apart agglomerates and reduce the size of boron particles even further, the powder was ball milled. Approximately 25 hard AlO balls 1 cm in diameter were loaded into a container with ~400 g of amorphous boron. The container was then loaded into a laboratory size tumbler (Thumler's Tumber, No. 140-B) and left to rotate for ~ 4 days. The constant impact of the harder AlO balls on the boron particles will grind them into smaller particles with greater surface areas, making them more reactive. The ball-milled powder was then loaded into a powder feeder (Powder Feed Dynamics, Mark XV) and used as feedstock in the EPIC system operating at a standard set of parameters (50 lpm $N_2$ plasma @ 45 kW, 15 rpm feed rate of powder via $N_2$ carrier gas, chamber pressure of 40 psia (~2.7 atm).

A network of sheets and strands collected along the chamber walls as well as across its center. Notably less material was produced compared to runs conducted with precursor powder not ball-milled. A lower magnification TEM micrograph of the resultant material following a typical run using the ball-milled precursor is presented in Figure 4.24a. Strands of nanotube bundles extended several microns in length are visible alongside larger fragments of darker contrast. There is a much higher degree of contamination in these samples relative to non-ball milled precursors. As evidenced by the higher magnification TEM image of Figure 4.24b, the bundles are made up of predominantly multiwalled nanotubes having mostly 2 – 4 walls with diameters between 2 – 4 nm. Larger MWBNNTs were also observed, but rarer, including an 8-walled BNNT 7 nm in diameter. Interestingly, SWBNNTs were more abundant as well, some with outer diameters as small as 1 nm. A single-walled, double-walled, and triple-walled nanotube are labeled 1w, 2w, and 3w in the region of Figure 4.24b. Tube walls are very straight with no defects in contrast to those typically synthesized using ball-milling techniques which produce "bamboo-like" and curved tubular structures.

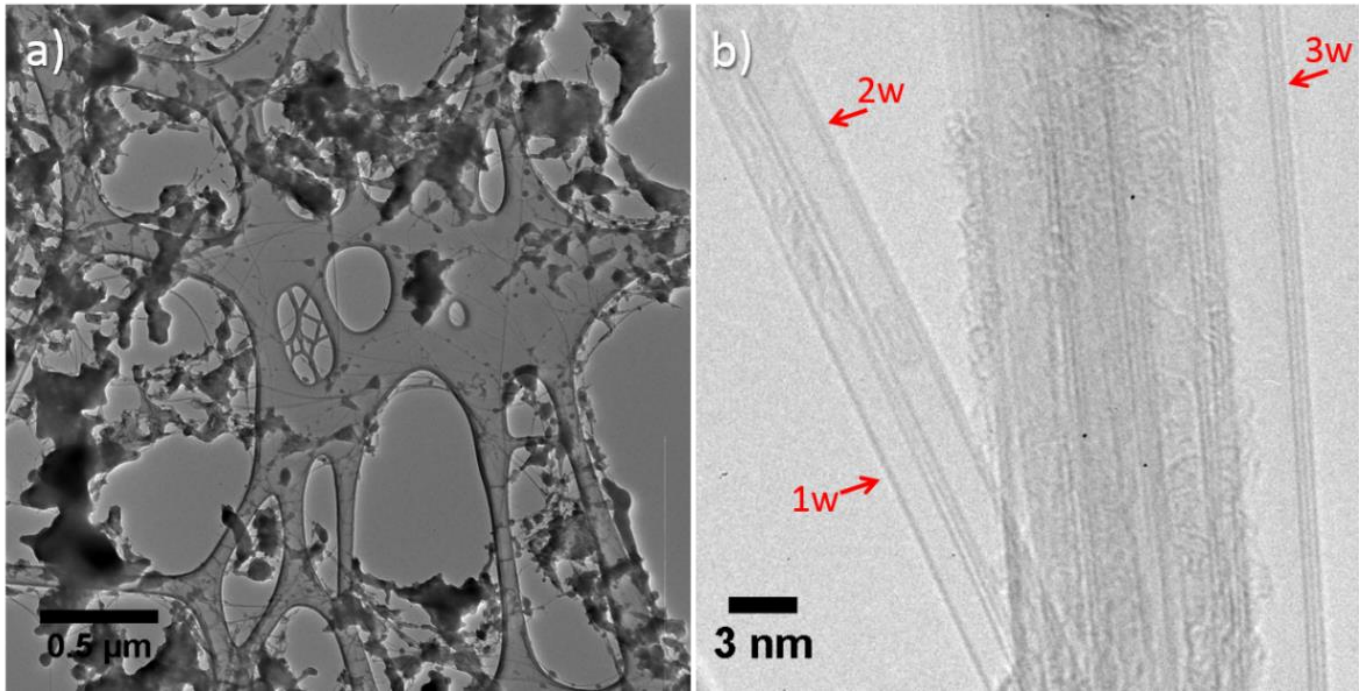


Figure 4.24: TEM images of material produced using ball milled boron powder as precursor. (a) Low magnification TEM image of BNNTs distributed amidst a lot of darker contrast impurities. (b) High resolution TEM image of bundle of highly crystalline BNNTs revealing the presence of a single wall, double walled, and triple walled BNNT (labeled in red).

The lower yield of BNNTs and greater contamination of product material observed here is due to the ball-milling procedure employed. We note that the powder was ball-milled in its plastic (likely polycarbonate) storage container. It is possible that the process of tumbling will introduce plastic contaminants from the container into the powder. Furthermore, ball-milling was conducted in air without purging or filling the vessel with inert gas. As the boron particles are broken apart, they become more reactive and in the presence of air will oxidize. Boron oxide particles introduced into the plasma require more energy to dissociate as the bond dissociation energy of B – O is 806 kJ/mol, more than 2.5 times that of B – B[231,232]. The release of reactive oxygen radicals in the plasma may also inhibit the growth of pristine nanotubes. The uptake of oxygen by boron droplets has been reported to correlate with the formation of nanocages rather than nanotubes, suggesting oxygen impedes the decomposition of nitrogen at the surface of boron droplets and thus hinders the extended reaction of boron with nitrogen[199].

#### 4.4.3.3 Boron Carbide

The bulk of our efforts have been geared towards the establishment of a scalable method to produce BNNTs. The EPIC synthesis system has also successfully created CNTs. $B_xC_yN_z$ nanotubes, however, have traditionally been difficult to synthesize controllably. With properties dependent on their exact stoichiometric makeup, $B_xC_yN_z$ make up a very rich and understudied class of nanotubes. For instance, certain compositions of BCN nanotubes are theoretically predicted to possess a bandgap in-between those of CNTs and the ~5.5 eV bandgap of BNNTs, making them potentially suitable for optoelectronic applications without the need for further functionalization[8].

A number of potential routes towards the large-scale and controllable production of BCN nanotubes can be explored with the EPIC synthesis system. The standard recipe would be to feed both boron and carbon containing precursors into a $N_2$ plasma. This could be accomplished by using a carbon-containing carrier gas, such as methane, to feed amorphous boron powder. Alternatively, a precursor mixture of amorphous boron and graphite or some other carbonaceous powder could be used.

Here we present the results of injecting boron carbide, $B_4C$ (Alfa Aesar, 99%), into a 50 lpm $N_2$ plasma. The coarser powder was less prone to agglomerating than amorphous boron and thus feed at an increased screw rate of 30 rpm. Flashes of light with a bluish hue were observed which were not as bright as those obtained when using pure boron as feedstock material. Following runs with the synthesis chamber pressurized to 40 psia (~2.7 atm), no web-like strands could be found and

the inner chamber walls were covered in a very thin layer of shiny black powder. For runs conducted at 1 atm, in addition to the shiny coating on the inner walls, several small fluffy nuggets had accumulated at the bottom of the chamber.

TEM images confirm that these low density downy balls contained nanotubes. Figure 4.25a is a low magnification TEM image illustrating a well dispersed network of few-walled nanotubes. Shells containing boron particles in the form of nanocages are also plentiful. The tubes are very long with highly oriented walls. In the higher magnification image of Figure 4.25b, a single wall, double-walled, triple-walled, and 6-walled nanotube are labeled 1w, 2w, 3w, and 6w respectively. The single-wall and doubled walled tubes are kinked at their ends. There is a wide range in the number of tube walls, with most possessing 1-3 walls. Tube lengths are typically between 2 and 6 nm, with lengths longer than several μm. A large sheet denoted with an S is also present and contains many defects. Some of the tubes seem to be damaged as well and have unraveled to produce nanoscale ribbons. A great deal of residue is present throughout these samples, likely the result of carbon contamination from the dissociation of the $B_4C$.

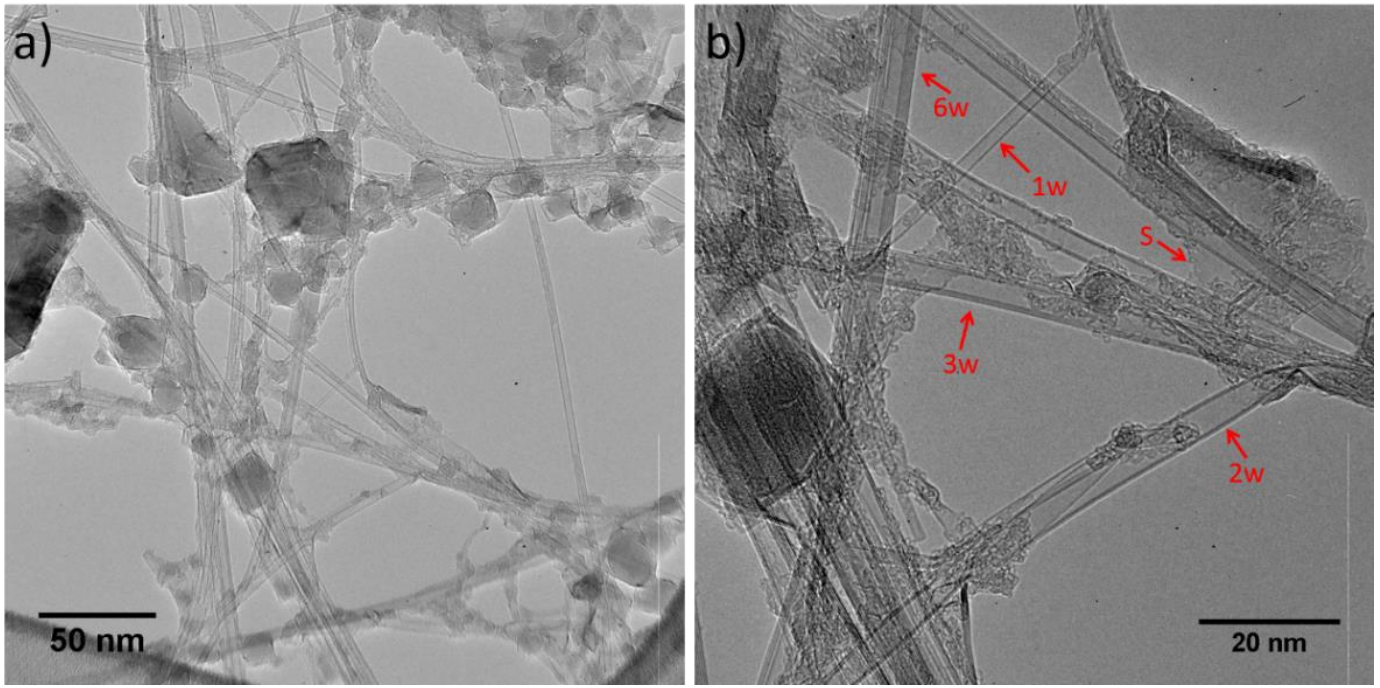


Figure 4.25: TEM images of material produced using boron carbide powder as precursor. (a) Product material consists of network of nanotubes alongside nanococoons and solid impurities. (b) Higher magnification TEM image showing a single wall, double wall, and triple wall nanotube alongside a filled nanococoon and sheets (labeled in red).

Preliminary EELS measurements conducted on these samples reveal the presence of both BNNTs as well as CNTs. EEL spectra taken from some nanotubes have both the k-shell ionization peaks of B at 189 eV and N at 401 eV in additional to distinct C peaks near 284 eV. However, unlike the B and N peaks, the C peaks exhibited a weak $\pi^*$ signal in its finer structure. This may be the result of amorphous carbon residue on the BNNTs. More extensive elemental characterization is needed, such as elemental mapping, to discern the spatial distribution of the elements in question. If $B_xC_yN_z$ nanotubes are being formed, they are likely a minority phase and thus a more thorough and extensive search for these materials amidst an assortment of nanotubes is needed.

We attribute the notably low yield of nanotubes created from the $B_4C$ precursor to a number of factors. Perhaps most importantly, the $B_4C$ powder used here was much larger than any other solid precursor we've tested, with particles in the 22-59 μm range. Furthermore, B-C has a particularly high bond dissociation energy of 448 kJ/mol. $B_4C$ also has a higher melting point near 2450 °C when compared to that of elemental boron at 2075 °C. Significantly more energy will need to be imparted on these $B_4C$ particles in order to melt them and create the molten droplets that act as seeds for nanotube nucleation. Examining the binary phase diagram of B-C, carbon solubility within liquid boron is as high as 30% at the melting point of $B_4C$. The significant drop in carbon solubility as the temperature of liquid boron drops below the melting point of $B_4C$ results in the diffusion of C to the surface at which point it is more likely to be incorporated into a $sp^2$ bonded network. Because C-C and B-N bonds are more energetically stable than C-B or C-N bonds[233], it is likely that nanotubes will be heterogeneous with segregated domains of C and BN.

### 4.4.3.4 Boron Nitride

The 1:1 stoichiometric ratio of B:N in powders of *h*-BN make this a promising precursor material for the synthesis of BNNTs with a similar elemental composition. Hence all initial trials on the EPIC synthesis system were conducted with *h*-BN powder (Alfa Aesar #11078, -325 mesh, 99.5%) as feedstock material. With 50 lpm of $N_2$ for the plasma gas, various chamber pressures were explored with the aim of generating BNNTs. When BN powder was fed into the plasma, feeble sparkles of light could be observed from the top viewport which at times appeared white or purple.

The flickers of light appear brighter when the chamber pressure was maintained at 1 atm compared to when it was at 75 psia (~ 5 atm). Based on many runs with brighter and more frequent flashes of light visible from the top viewport

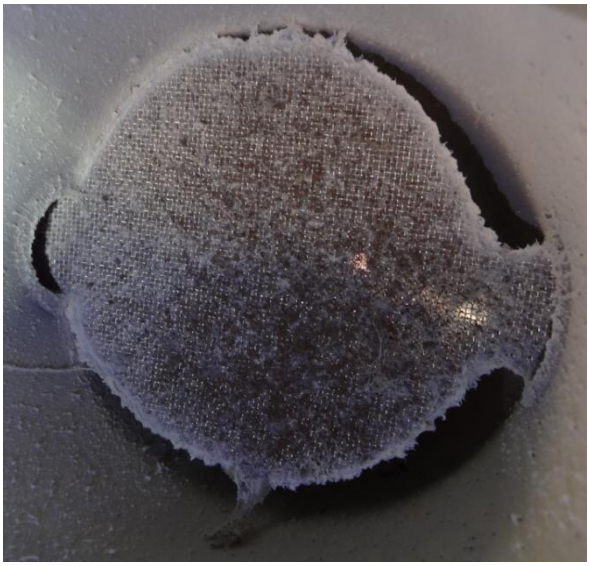

Figure 4.26: Copper mesh collector plate placed downstream plasma torch inside synthesis chamber.

using a multitude of precursor materials, the occurrence of such illumination tends to correspond to the production of fibril-like deposits. Hence it seems that such sparkles indicate the processing of precursor material. Because brighter flickers of light were observed when the BN powder was fed into a 1 atm pressure chamber versus when it was pressurized maintaining a constant carrier gas flow, we posit that pressurizing the synthesis chamber reduces both the length and volume of the plasma plume. Consequently, for a 1 atm chamber pressure, the BN powder has a longer residence time in the plasma during which it is processed, generating the vivid bursts of light. It is important to note, however, that a larger plasma volume and longer plume length, both of which occur for lower pressure environments, do not experimentally correspond to the production of the highest yield of BNNTs. As discussed above, although pressurizing the synthesis chamber shrinks the size of the plasma plume, it also increases the partial pressure of $N_2$ which allows for higher collision rates with molten boron droplets and thus promotes the transition of B + N into BN. This suggests the existence of an optimal pressure of the synthesis chamber to generate the highest yield of BNNT material, which according to our studies depends on a number of other variables including precursor material.

Following a 10 min run, various white fibrils accumulated at a number of spots in the chamber. They most notably formed as webs over the viewports and Cu collector meshes as well as strands on the collector plate at the bottom of the chamber as depicted in Figure 4.26. Distinct macroscopic threads were not present in runs conducted with a 75 psia (~5 atm) pressurized chamber. A thin layer of white

powder coated the inside of the chamber, which was predominantly *h*-BN residue. Overall, the yield of fibril-like material was very low.

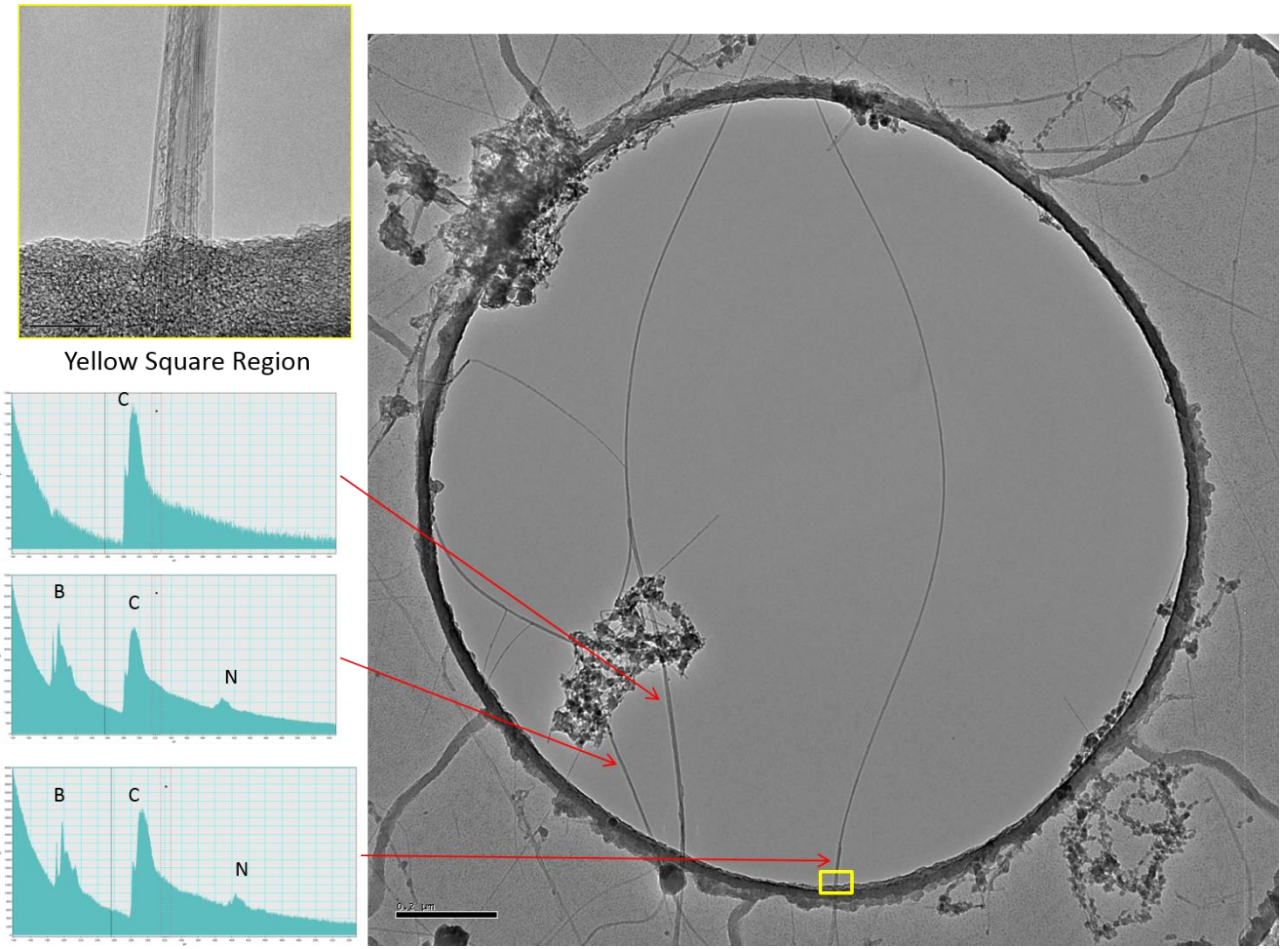


Figure 4.27: TEM images and EELS spectra of material produced using boron nitride powder as precursor. Sample was collected from exhaust system.

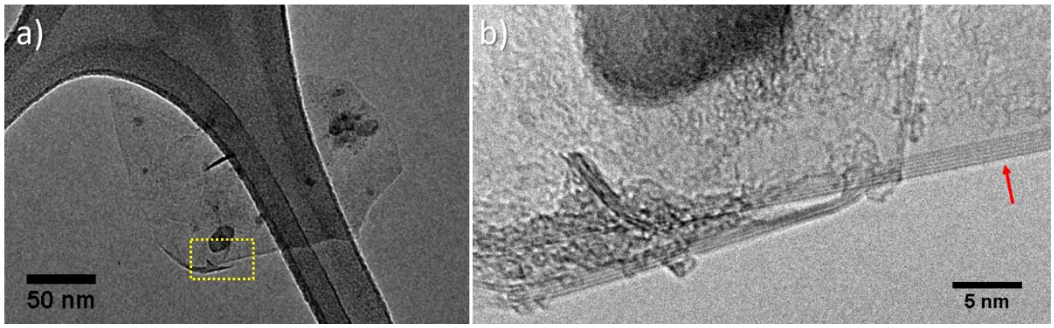


Figure 4.28: *h*-BN sheets present in resultant product material using BN powder precursor. (a) Low magnification TEM image of sheet impurities. (b) High magnification image of the yellow boxed region from (a) revealing the edges of stacked *h*-BN sheets. Red arrow indicates the edge of 6 stacked sheets.

TEM characterization of the web structures reveal they are composed of nanotubes in addition to many other impurities. The TEM image of Figure 4.27 shows numerous bundles of nanotubes greater than a few μm in length in addition to amorphous contaminants. The long strand traversing the center of the Quantifoil TEM grid hole consists of several nanotubes, as highlighted by the yellow region and illustrated in the inset, one of which is double-walled and another contains 3 walls. An amorphous layer of material is clearly visible over this nanotube bundle which originates from the Quantifoil TEM grid. The nanotubes are highly crystalline with few defects in the walls. Most tubes have 2 or 3 walls with some single-walled nanotubes present as well. Virtually no tubes with greater than 5 walls were observed. Outer tube diameters were mostly 2 – 4 nm, with some as large at 6 nm. Overall, the nanotubes here were on the smaller end in terms of diameter and number of tube walls when compared to nanotubes synthesized using amorphous boron powder as a precursor. As displayed in Figure 4.28, many sheets which are likely *h*-BN were also found in the resultant material. In Figure 4.28a, several impurities are visible in this low magnification TEM image, include a larger sheet-like structure. A zoomed-in image of the yellow boxed region is presented in Figure 4.28b revealing the edges of the sheets. The red arrow indicates the sheet consists of 6 stacked layers.

The elemental composition of the nanotubes was gauged using EELS. The EELS spectra of two nanotube bundles are displayed in Figure 4.27. Prominent peaks corresponding to the k-shell ionization edge of B and N are present at 189 eV and 401 eV respectively. The fine structures of these k-edge peaks are consistent with the $\pi^*$ and $\sigma^*$ peaks, confirming the presence of $sp^2$ bonded BN in these structures. The carbon peak at 284 eV is also clearly discernible. Amorphous carbon is certainly a

contaminant considering the carbonaceous nature of the Quantifoil TEM grid and the visible layer of amorphous material present over the bundle of nanotubes in the yellow inset. Nevertheless, the $\pi^*$ structure in the C peak does indicate the formation of a $sp^2$-hybridized structure. An extensive EELS examination of this particular sample reveal CNTs, lacking any B or N EELS peaks, are indeed present. A more detailed investigation and finer spatial resolution on individual tubes would be necessary in order to determine whether $B_xC_yN_z$ nanotubes were synthesized in the process.

The most likely source of carbon in these nanotube structures is the graphite rod located at the top of the torch. An electric arc between the rod and the copper torch is used to ignite the plasma, a process which is known to form CNTs[1]. The sample imaged in Figure 4.27 was obtained from a metal mesh located in the exhaust line which would collect these arc-grown CNTs alongside the low yield of BNNTs.

Overall, BN powder as a precursor feedstock did not yield a high rate of BNNTs under the synthesis parameters examined thus far. Unlike the abundance of sheets and fluffy material synthesized using amorphous boron powder, the fibrils produced here were isolated and limited to a few strands collected on the viewport or on the chamber bottom. BNNTs were also found in the powder accumulated on the chamber walls, but at nowhere near the levels obtained with other feedstock powders. This can be attributed to the higher bond dissociation energy of B-N, which is 389 kJ/mol, compared to that of B-B, which is 297 kJ/mol. Furthermore, BN does not have a molten phase and begins to decompose at 2400 °C, whereas solid boron liquefies at 2075 °C. Nevertheless, the operating parameters of the EPIC synthesis system were never fully explored using BN powder as the feedstock. It is highly likely that a high plasma power, perhaps in conjunction with incorporating $H_2$ into the plasma gas mixture to increase its enthalpy, at some intermediary synthesis chamber pressure, i.e. between 1 and 5 atm, would produce higher yields of BNNTs with BN powder as precursor.

#### 4.4.3.5 Ammonia Borane

The hydrogen dense ammonia borane ($H_3NBH_3$) is another promising precursor candidate. 30 grams of $H_3NBH_3$ (Sigma Alderich, 90%) were loaded into the hopper and fed at a reduced vibration amplitude of 60 and screw feed rate of 15 rpm into a pure 50 lpm $N_2$ gas plasma operated at 50 kW. Runs for which the synthesis chamber was pressurized to 45 psia (~3 atm) produced a thick layer of material which coated the entire inner walls of the chamber. No significant web-like structures were produced except a few strands near the top adapter flange. The coating material was among the thickest and most cohesive to deposit on the walls and could easily be peeled off into large sheets, as depicted in Figure 4.29a. This

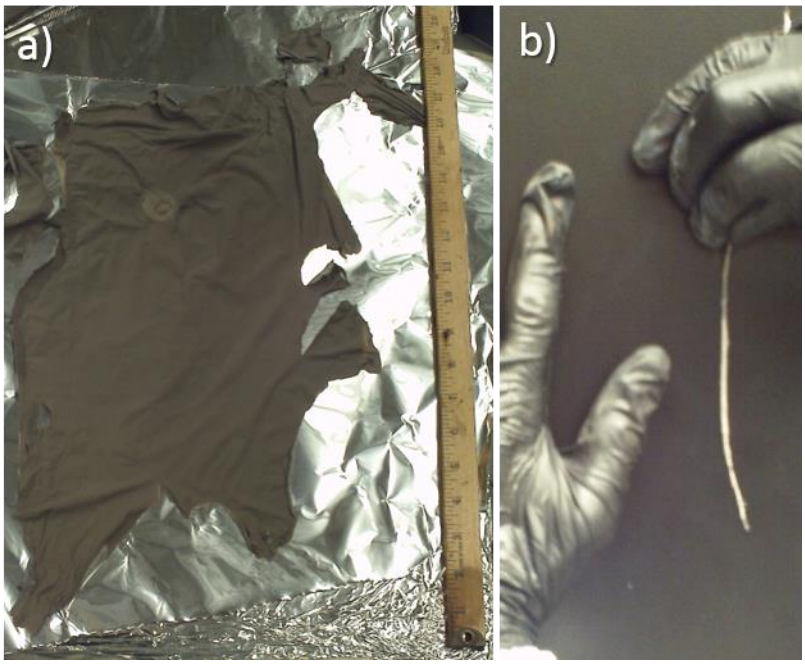


Figure 4.29: Raw material produced using ammonia borane powder precursor. (a) Sheet peeled off of chamber walls. (b) Yarn of as-synthesized BNNT material twisted by hand.

sheet nearly 18” in length was peeled off of the top chamber, with the region of lighter contrast near the center corresponding to the location of the side port. The felt-like structures are very flexible, but mechanically strong enough to withstand tearing when transported through the air. As is the case with other deposited material collected off of surfaces, the sheets are composed of multiple layers. These layers can carefully be peeled apart from each other in order to obtain transparent films. Longer synthesis runs will produce thicker depositions and more sheet layers.

This higher density cloth-like substance could be twisted into strands of yarn several inches long, as illustrated in Figure 4.29b. This indicates the material is composed of long fibrils which fasten around one another. Thinner, weaker regions in the spun thread were weak points for breakage when small masses were hung to test its mechanical strength. Yarns of BNNT have been reported[29,30] which are similarly finger spun to strengthen the structural integrity of the resultant material and support a small load. Purification of the as-synthesized material is expected to eliminate coarse impurities and enable greater interaction between nanotube bundles and hence fibrils, allowing for the spinning of stronger yarns. In combination with well-established textile processing techniques, BNNTs can be spun into threads and fibers for use in fabrics and clothes.

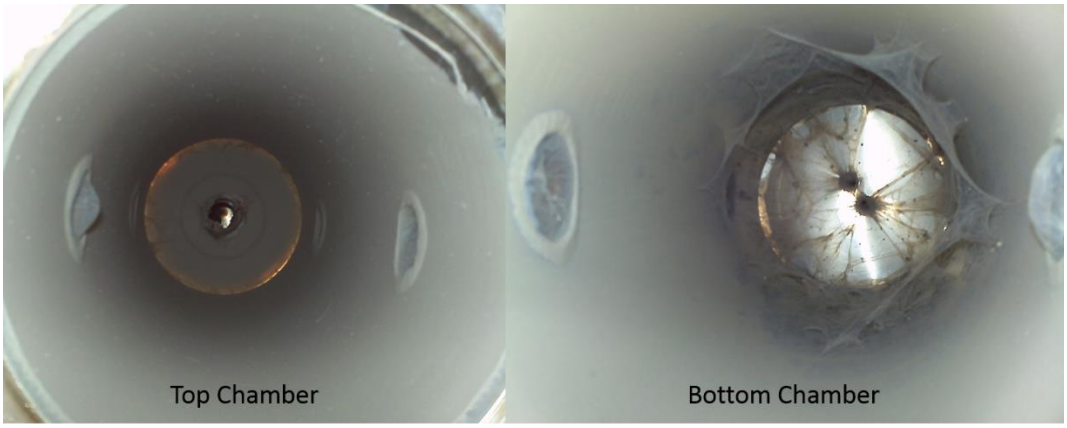


Figure 4.30: Synthesis chambers following a run using ammonia borane powder precursor showing more fibrils formed on the bottom chamber. Both chambers are pictured as seen looking up (left) and down (right) into the top and bottom chambers respectively.

Ammonia borane was also injected into a variable flow rate $N_2$ plasma with synthesis chamber pressure maintained at 1 atm. For a plasma gas flow rate of 50 lpm, hardly any bright flashes were observed from the viewport at the top chamber. As it was reduced to 25 lpm, we noticed a much brighter illumination emanating from the top chamber view port, but also flashes of light from the two viewports of the bottom synthesis chamber. Note that as the $N_2$ plasma gas flow drops, the torch and inductor cooling water temperatures did not significantly increase, which could have been a concern as the higher plasma gas flow rates help keep the torch cooler. The plasma itself also becomes dimmer with the plasma plume shrinking in volume.

The typical results of feeding $H_3NBH_3$ into a low flow rate $N_2$ plasma gas (25 lpm) with the synthesis chamber maintained at 1 atm are presented in Figure 4.30. The walls of the entire synthesis chamber are coated in a relatively thicker layer of material. Interestingly, quite a few fibrils have formed at the bottom synthesis chamber and indeed more so than in the top chamber. This corresponds to the observed flashes of light from the bottom chamber viewports indicating a shift in flow dynamics enabling a greater degree of material to accumulate further downstream.

## 4.5 Conclusion

Here we have presented a versatile, scalable, high-throughput synthesis method for the production of highly-crystalline, low-wall-number, high aspect ratio BNNTs. The direct-injection, extended pressure EPIC system allows for a wide range of synthesis parameters, including catalyst-free BNNT production at a rate of 35 g/hour, nearly 300 times the production rate of the laser vaporization method[29]. The high pressure compatibility of a pure nitrogen plasma in the exclusively capable EPIC plasma system is particularly well suited for the nitridation of other materials and the formation of nanoscale nitrides such as silicon nitride, indium nitride, and gallium nitride. Indeed, the process described here is adaptable to an exceptionally large variety of feedstock material of differing elemental compositions and phases. With the especially unique hyperbaric compatibility and variability of an induction thermal plasma, the wide parameter space accessible with the EPIC plasma method makes it promising for other synthesis challenges, for example alloy $B_xC_yN_z$ nanotubes[8,11,234], and likely other nanostructures containing elements in addition to or other than boron and nitrogen.

# Chapter 5

# Purification of Boron Nitride Nanotubes

## 5.1 Sample Impurities

In order to fully take advantage of the extraordinary properties of BNNTs and continue to investigate their fundamental physical and chemical characteristics, processing material in order to obtain the purest, high quality nanotubes is critical. As-synthesized BNNTs contain various impurities that must be removed in order to achieve their full potential. For instance, in order to transfer the high mechanical strength of BNNTs into a polymer matrix, a clean tube surface is required to form a strong interfacial bond with the polymer and any impurities in the composite serve as weak points from which fractures can originate.

A low magnification TEM image of the as-synthesized material gathered from the center of the EPIC synthesis chamber drop cast onto a lacey carbon TEM grid is presented in Figure 5.1a. Numerous long bundles of nanotubes are visible throughout the sample. Many prominent spherical and globular regions of dark contrast are also visible. Much of these are amorphous and crystalline boron particles, some of which are encapsulated within BN shells. Some of the boron powder fed into the plasma during synthesis will simply reform as boron nanoparticles predominantly spherical in shape or may not be vaporized. Boron particles exhibit various morphologies, but are predominantly spheroids ranging in size from a few nanometers to tens of microns.

Molten boron droplets also serve as seeds for tube and shell growth and hence may end up enveloped in BN. Figure 5.1b depicts several BN 'nanococoons' wherein boron nanoparticles have been encapsulated within 2 – 3 layers of hBN. The nanococoons are polyhedral in shape with different numbers of faceted surfaces. Sometimes labeled 'nano-onions', they range in size from 4 to several hundred nm in diameter. The clear lattice fringes attest to the crystalline nature of the filling

material, although an amorphous phase of boron is just as prevalent in most synthesis runs. The elemental composition of these particles has been confirmed by EELS to be that of boron.

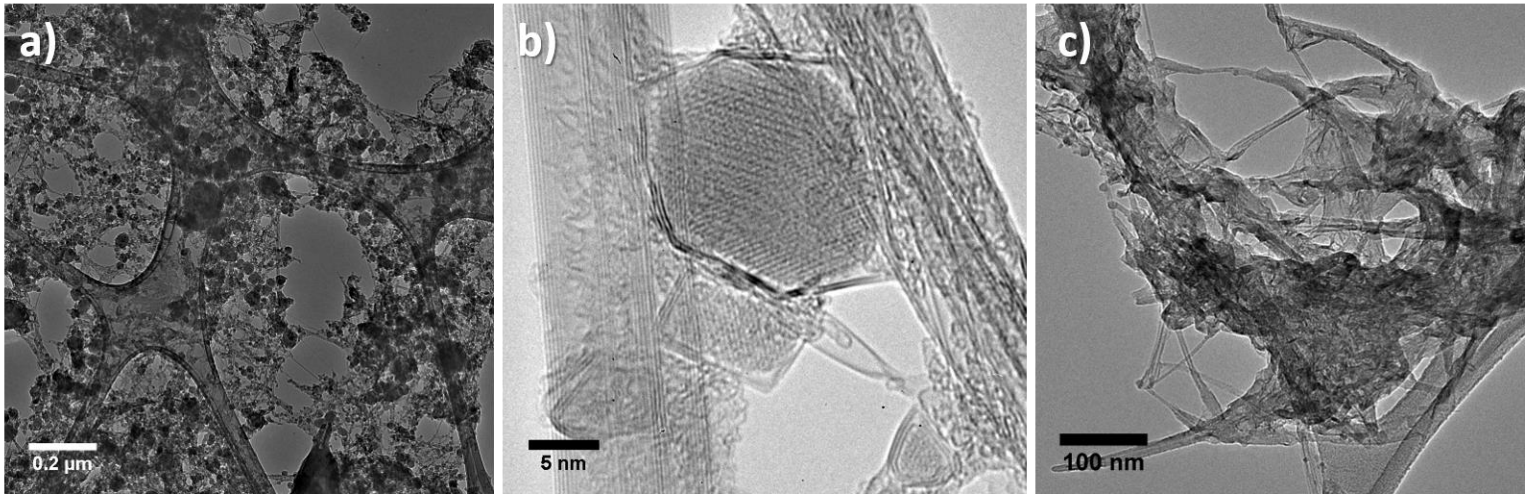


Figure 5.1: Resultant material impurities.TEM images of (a) as-synthesized BNNT material, (b) crystalline boron encapsulated within BN cages, and (b) BN sheet-like material.

Other non-tubular BN impurities are also present in the raw material. BN particles and fibers, sometimes with diameters on the order of a few microns, are produced. Figure 5.1c shows a cluttered BN sheet amidst nanotubes. Such sheets can be microns in scale and when folded over on itself, appear as regions of varying contrast depending on the number of overlaying layers. Due to the similar chemical composition of these impurities with BNNTs, separating the two is particularly challenging. Unlike many other synthesis techniques, there are no metal impurities present in the product of the EPIC plasma method.

Various techniques have been developed for the purification of carbon nanotubes (CNTs)[235,236]. Many of these methods cannot be employed on their BN analogues or do not work as well because of the different chemical nature of the two. For instance, amorphous carbon particles and layers can be burned off of CNTs by heating them in air, but a high-temperature oxidation of boron produces $B_2O_3$ which remains in the sample. Impurities composed of BN are particularly difficult to remove due to the high oxidation resistance of BN. Indeed, there are only a few reports on the purification of BNNTs[237–242]. In this chapter, the results of numerous BNNT purification attempts with varying degrees of success are presented. The techniques are assessed and evaluated for their effectiveness via transmission electron microscopy (JEOL TEM 2010), scanning electron microscopy (FEI Sirion XL30) equipped with energy dispersive X-ray analysis (EDAX), Raman spectroscopy (Renishaw inVia), Fourier transform infrared spectroscopy (Nicolet 6700), and thermogravimetric analysis (Perkin Elmer TGA7).

## 5.2 Purification Techniques

Purification methods fall into two basic categories, namely chemical or physical. Chemical methods employ the principle of selective oxidation wherein certain impurities are oxidized at a faster rate than the more resistant BNNTs. Physical techniques use differences in physical sizes, aspect ratios, and densities to separate BNNTs from impurities. Combinations of physical and chemical techniques are likely to be required in order to eliminate the complete spectrum of impurities present in a sample while maintaining the structural integrity of BNNTs.

## 5.3 Chemical Oxidation

Boron makes up the largest percentage of impurities by weight in the product material of the EPIC plasma method. It is most often amorphous and sometimes crystalline in nature. The particles vary in size from a few nanometers to tens of

microns with varying morphologies, but are predominantly spherical. The presence of many dangling bonds and structural defects in these boron particles results in a greater oxidation activity than BNNTs. BN nanococoons and other polyhedral structures made of BN are also more susceptible to oxidation than the straight walls of BNNTs. The presence of non-six membered rings and greater strain due to their larger curvature make these structures more chemically reactive. In an oxidizing environment, these sites will be attacked first. Chemical purification methods are based on the idea of selective oxidation etching wherein boron, BN nanococoons, and other less stable BN impurities are oxidized at a faster rate than BNNTs. Chemical purification methods include both gas phase oxidation, using air or $O_2$, and liquid phase oxidation, using acid treatments and refluxing.

Defects present on BNNT walls are also very chemically active. A major disadvantage of oxidative techniques is that it tends to damage tube walls, oftentimes opening up tube caps and sometimes tearing them apart. Furthermore, oxygenated functional groups may also be introduced onto BNNTs, modifying the chemical and physical nature of the material. Subsequent nanotube surface chemistry can be performed with such tubes. The chemistry of BN based nanomaterials and in particular their functionalization is the subject of ongoing research conducted by Sally Turner in the Zettl group.

### 5.3.1 Gas Phase Oxidation

A gas phase oxidative purification of BNNTs was attempted by heating as-synthesized material in air at 800 °C for 1 hour. Material collected from the center of the EPIC plasma synthesis chamber was placed in an alumina boat inside a quartz tube with both ends open and heated in a tube furnace. The heating resulted in a grey colored product with white outer coating, lighter in shading than the material prior to heating. Figure 5.2 presents typical EDX spectra taken from the as-synthesized and oxidized BNNTs clearly indicating the presence of oxygen in the later. Fine and amorphous BN particles in addition to boron nanoparticles are more chemically reactive than the crystalline BNNTs. These impurities will thus oxidize more readily. In one run, the mass of the thermally treated material increased by 44% from 41 to 59 mg due to the formation of $B_2O_3$. The possible oxidation reaction for the conversion of fine and amorphous BN structures is:

$$BN + O_2 \rightarrow B_2O_3 + NO(g) + NO_2(g) \quad (5\text{-}1)$$

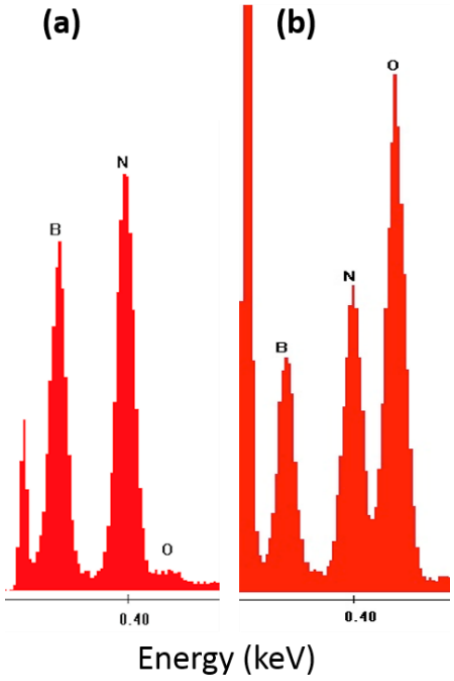


Figure 5.2: Representative EDX spectra of BNNT material (a) as-synthesized and (b) after thermal oxidation.

Following thermal oxidation, the BNNT material was then periodically sonicated in a bath of water at 90° C for 1 hour to dissolve the boron oxide and subsequently vacuum filtered (0.4 µm polycarbonate). $B_2O_3$ has a high solubility in hot water at 98 °C [243]. After drying, the filter paper with thin BNNT layer is sonicated in IPA for 5 min to disperse the material prior to being drop cast onto 300 mesh lacey carbon grids.

A low magnification TEM image of the thermally treated and washed material is presented in Figure 5.3a. Many tube bundles of varying thickness are visible to a greater degree as compared to the raw material indicating the removal of many larger impurities. However, the sample is far from pure. Numerous large dark contrast fragments several microns in length are likely boron nitride sheets which were not burned off. Although many boron particles are not clearly visible in this image, optical microscopy reveals their continued presence in thermally treated material.

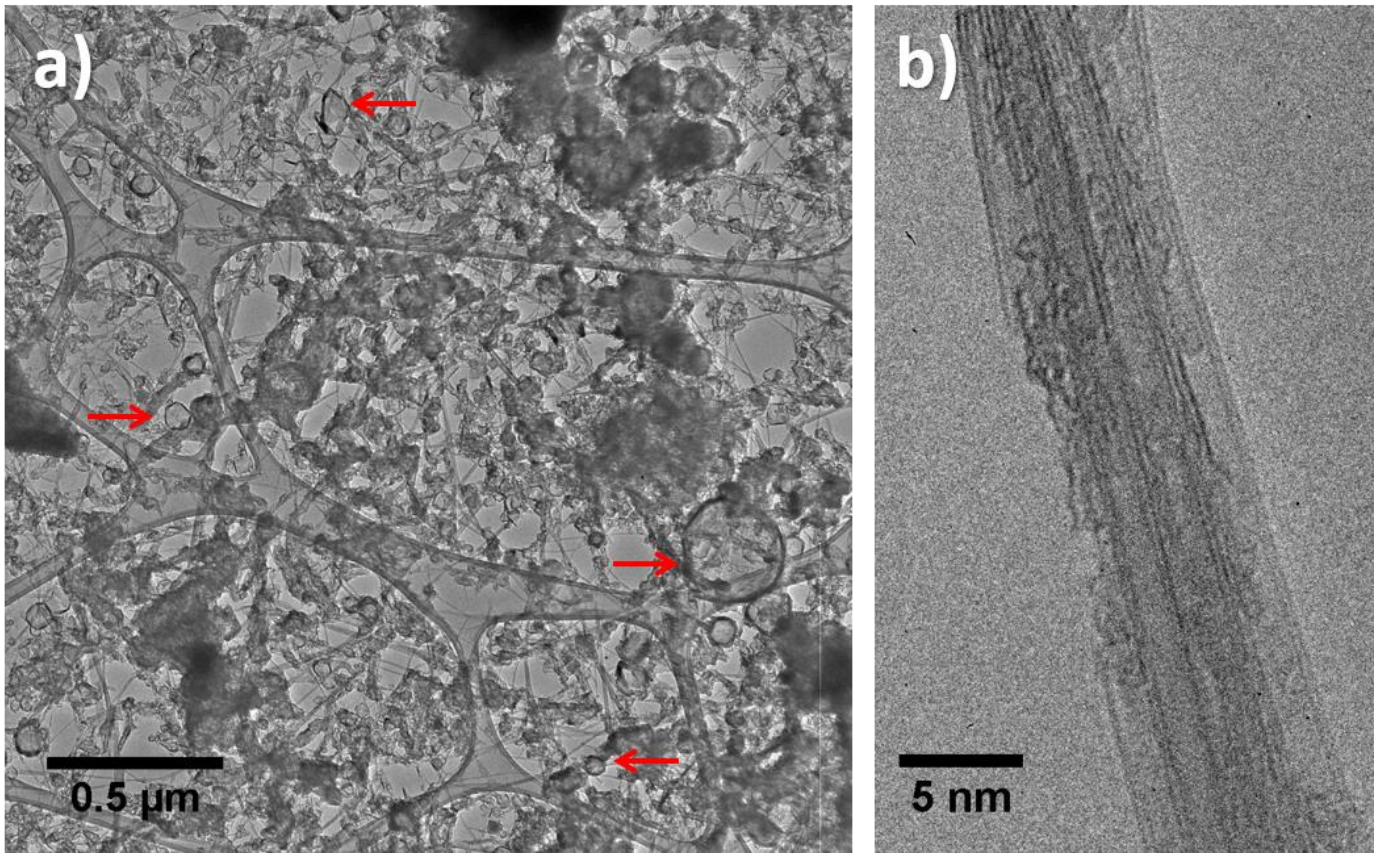


Figure 5.3: Thermally oxidized BNNT material. (a) TEM image of resultant material after thermal oxidation and washing in water. Red arrows indicated hollow nanococoons. (b) Bundle of double-wall BNNTs with some tube wall damage.

The oxidation of particles contained within layers of *h*-BN was also observed. The red arrows of Figure 5.3a highlight empty nanococoons. Encapsulated boron is oxidized and then dissolved in the hot water treatment. During heating, the highly curved edges of the faceted shells must have been attacked and etched away, allowing for the penetration of oxygen into the nanococoons. Empty nanococoons are very rarely present in as-synthesized material but do occasionally appear in the gas-phase oxidized material.

Some tube walls are also damaged during treatment, as highlighted in Figure 5.3b. The sidewall of a double-walled nanotube has been split open in a bundle of otherwise pristine double-walled tubes. Damaged nanotubes are present, although not very prevalent. Previous studies have found thermal oxidation may reduce the number of nanotube layers[28,244]. Chen *et al.* attribute this to the formation of $B_2O_3$ layers on the external surfaces of BNNTs which forms a non-uniform coating on the outside of tubes[28]. The formed oxides either fall off or are dissolved in solution, leaving behind holes in the tube. However, as evident in Figure 5.3b, most of the tubes are not damaged, due in great part to their high degree of crystallinity. This may indicate that the thermal treatment ought to have been conducted at a temperature lower than 800 °C in order to maintain the structure of more thin nanotubes.

The poor results of purification are in part due to the nonuniform exposure of BNNTs to oxygen during thermal treatment. Fibrils present on the outside of the BNNT material are readily oxidized, shielding those which are located further inside from equal exposure to the air. A higher purification yield may be achieved by crushing up the initial material to increase surface area exposure or by directly placing material in a rotating quartz tube[245]. Heating the sample in a flow of pure oxygen will also result in a much greater degree of oxidization.

### 5.3.2 Liquid Phase Oxidation

Liquid phase oxidative techniques facilitate a more even oxidation of product material. Oxidative ions and acid ions dissolved in a solution uniformly etch raw samples which can be disbursed quite homogeneously in a bath of solution with sonication or a stirring spin bar. Liquid phase methods allow for greater control over treatment conditions and oxidant type. This method, however, also tends to attack tube wall defect sites and thus damage BNNTs, sometimes opening or splitting them apart depending on etching conditions. Chemical modification of nanotube surface is another consequence. The two oxidants explored for BNNT purification and presented in this chapter are nitric acid and hydrogen peroxide.

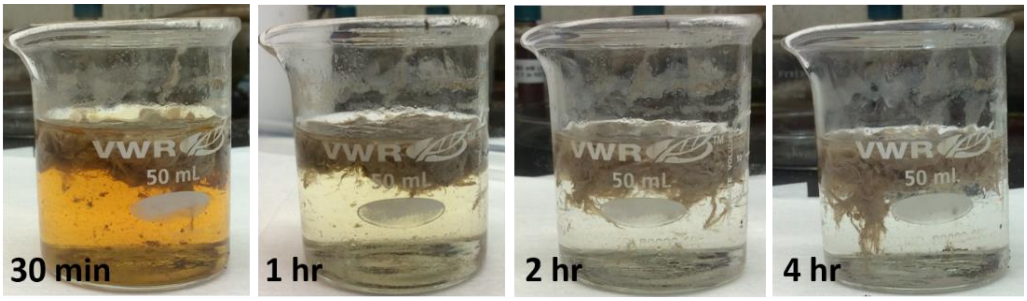


Figure 5.4: Nitric acid etching of as-synthesized material over a 4-hour period.

### 5.3.2.1 Nitric Acid

The mild oxidant nitric acid can selectively etch boron particles as well as open up most nanococoons. It is inexpensive and able to remove metal particles without introducing further impurities. Raw material is placed in a beaker with ~ 40 ml $HNO_3$ (70%, Sigma-Alderich) heated to 90 – 120 °C for 1 – 4 hours. Sometimes the beaker is periodically sonicated or contains a stirring spin bar to disburse material in solution. As evident in Figure 5.4, upon introducing the as-synthesized material into the nitric acid bath, red fumes are emitted and the solution turns yellow as the majority of boron impurities are etched. The material becomes lighter in color the longer it is etched. With time, the material becomes more soluble and further submerges into the nitric acid, in part due to the surface chemical modification of BNNT material. Indeed, as-synthesized BNNT material is highly hydrophobic whereas chemically treated tubes disburse more readily when sonicated in water. After refluxing, the etched material is washed in multiple baths of deionized (DI) water until a pH of ~ 7 is attained. As pictured in Figure 5.5, nitric acid etched material is visibly much whiter than the as-synthesized BNNT material, which has a slightly grey tinge due to the presence of impurities.

Figure 5.5: Picture of as-synthesized and nitric acid treated material. Chemically treated material (right) can be made much whiter than material collected following a run (left) due to the removal of impurities such as boron.

Typical SEM images of the nitric acid treated material alongside the raw sample is shown in Figure 5.6. Due to its insulating nature, BN materials tend to charge up when probed with an electron beam. It was thus necessary to sputter a very thin layer of gold over both the raw material collected directly from the synthesis chamber as well as the nitric acid treated material, which has been critical point dried. Much of the boron particles visible in Figure 5.6a have been removed in the chemically etched sample of Figure 5.6b. In addition to fibrils, globule-like structures are also visible in the latter.

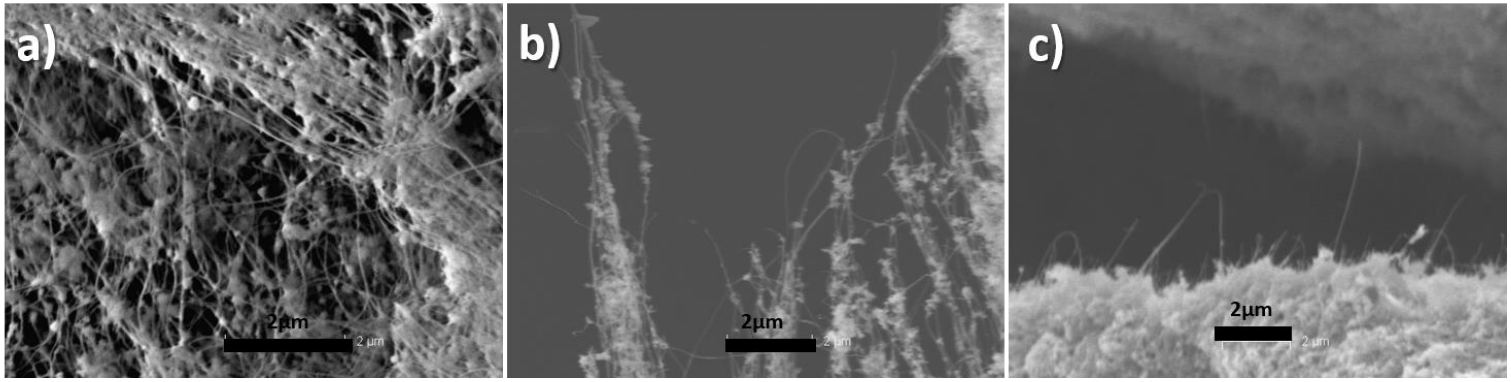


Figure 5.6: SEM images of BNNTs (a) as-synthesized, (b) post-$HNO_3$ treatment, (c) post-$H_2O_2$ treatment.

TEM characterization of the chemically treated material is presented in Figure 5.7. From the low magnification TEM image of Figure 5.7a, it is clear that nearly all boron particles have been removed. Most of the nanococoons are also empty, indicating the successful etching of the encapsulated boron. However, some boron particles within BN shells survived, as indicated by the green arrows. Isolated and bundles of nanotubes are seen amidst other impurities. In the TEM image of Figure 5.7b, a bundle of BNNTs is depicted, a result of the tendency of BNNTs to agglomerate. The difficulty of achieving isolation and dispersion of BNNTs and impurities of the resultant material means that not all particles are equally exposed to the chemical environment. Boron particles shielded by BN materials, as seen in Figure 5.7, are less likely to get etched. Longer etch times have produced material with nearly all nanococoons empty and no visible boron. Some of the cluttered regions of darker contrast in Figure 5.7a and Figure 5.7b are sheets of BN, which nitric acid treatment alone cannot remove. Furthermore, from Figure 5.7c, it is clear that smaller particles such as nanococoons stuck to the sides of tubes cannot be separated with high efficiency using this method alone.

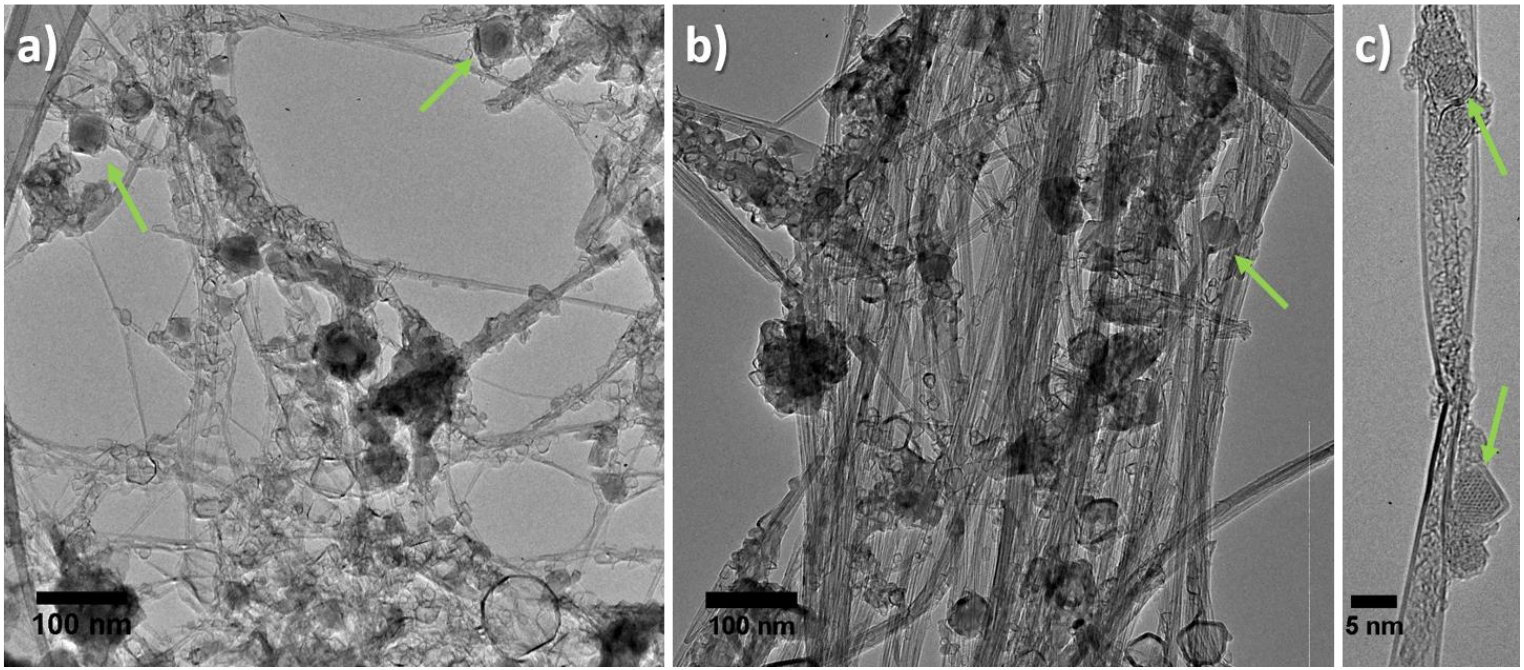


Figure 5.7: TEM images of nitric acid treated BNNTs. (a) Low magnification image of BNNT network with many hollow nanococoons. (b) BNNT bundle with interspersed emptied nanococoons. (c) Kinked double-wall BNNT with very small nanococoons containing encapsulated crystalline boron. Green arrows indicate nanococoons containing boron.

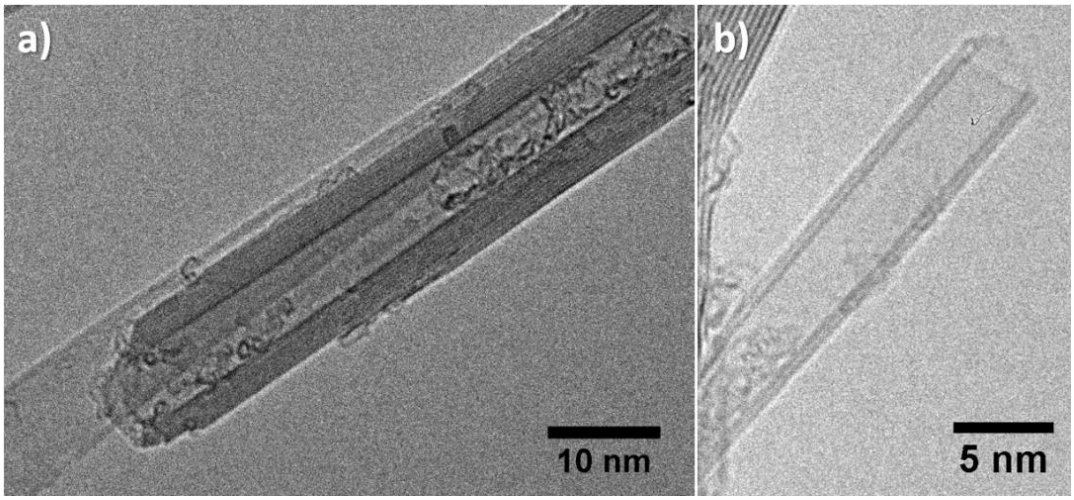


Figure 5.8: Open ended-MWBNNTs. (a) TEM image of MWBNNT with highly curved cap etched open. (b) Pristine double-wall BNNT with opened end.

Acid refluxing is also seen to damage the nanotubes, sometimes significantly. As previously mentioned, regions of highest strain are more chemically active, such as at the capped end of nanotubes where there are non-six member rings present in the lattice of *h*-BN. These sites will be selectively attacked, oftentimes opening up the end of a nanotube as demonstrated in Figure 5.8. In Figure 5.8a, the highly curved end of a multiwalled BNNT is selectively etched with some damage to outer tube walls. In Figure 5.8b, the capped end of a double-walled nanotube has been removed without damaging the highly crystalline tube walls.

Defect sites present in tube walls are also more susceptible to chemical damage. In the image of Figure 5.9a, several nanotubes within a bundle have been completely damaged and torn open, as indicated by the red arrows. Orange arrows point to outer tube wall damage, which is more common, where the tube is not completely severed. The outer walls of the MWBNNT of Figure 5.8a are also seen to peel back off of the nanotube. From Figure 5.9b, a double-walled BNNT has unraveled in the middle following a reflux treatment in nitric acid, leaving small fragments and sheets of BN. Indeed, there are notably more sheets and fragmented impurities following chemical treatment than before, most likely due to the damaging and tearing open of some nanotubes and nanococoons.

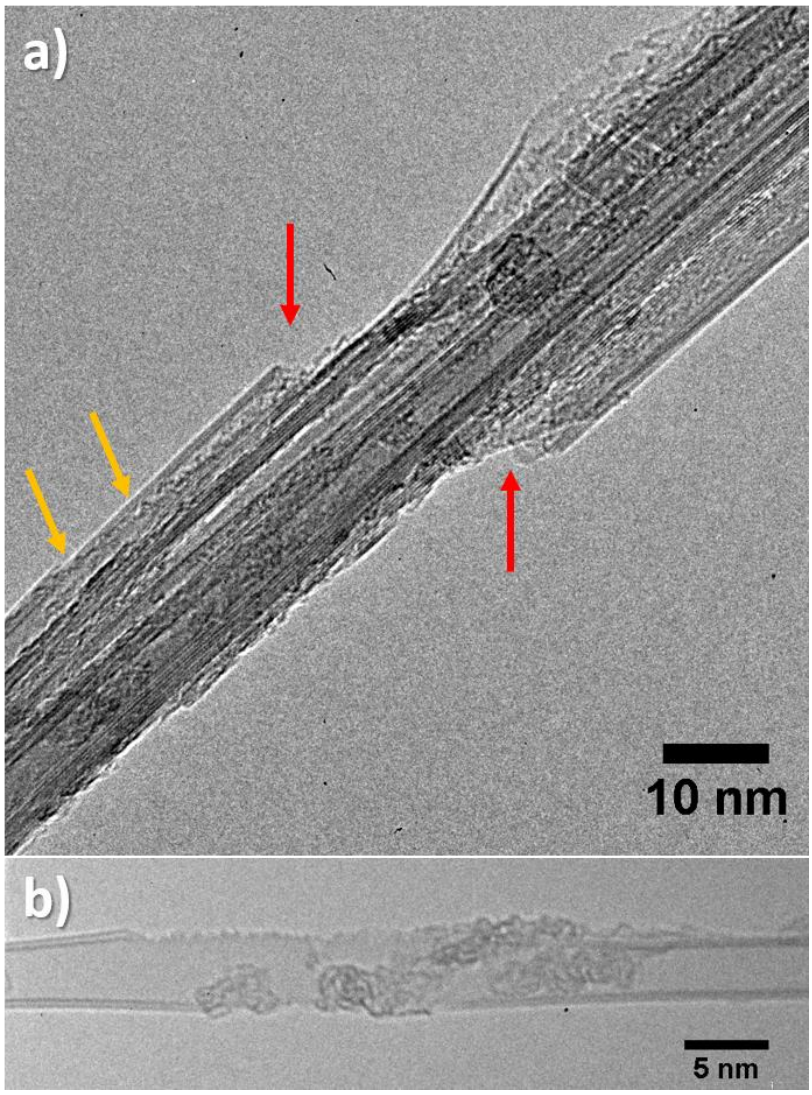


Figure 5.9: BNNT etching damage. (a) Bundle of MWBNNTs with damage to several nanotubes indicated by arrows. (b) Double-wall BNNT exhibiting tube unraveling near center.

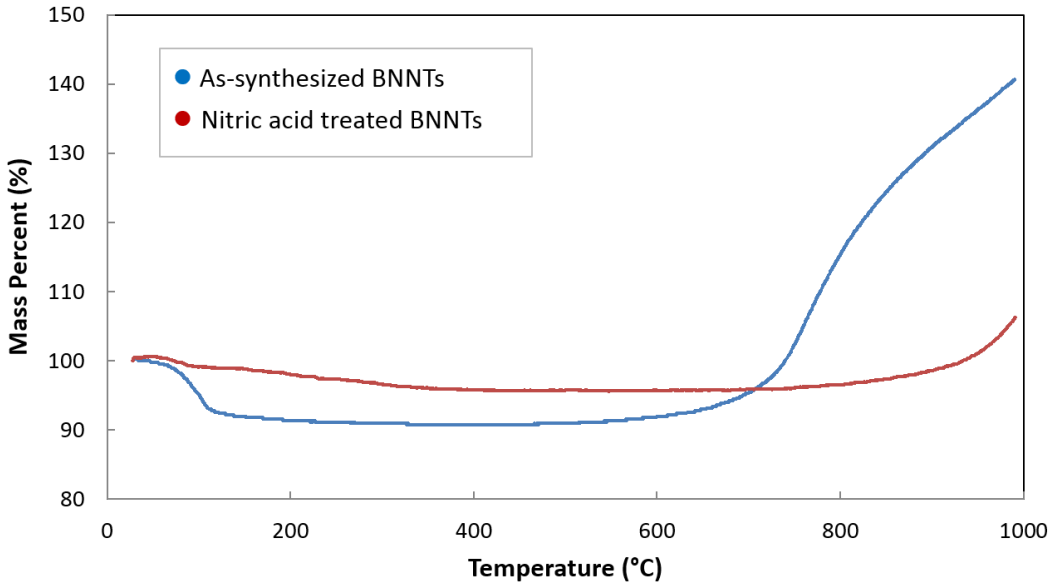


Figure 5.10: TGA of BNNT material. As-synthesized (blue) and nitric acid treated (red) BNNT material are heated at a rate of 10 °C/min.

Sample purity can be gauged by thermogravimetric analysis (TGA). The results of TGA conducted on as-synthesized and nitric acid treated samples showing the change in sample weight as a function of temperature are presented in Figure 5.10. 100 mg of each sample was heated up to 990 °C at a rate of 10 °C/min in air. For the raw material, a sharp weight increase (55 wt%) is observed starting at 650 °C. This is due to the oxidation of mostly boron, but also some BN particles, and the formation of $B_2O_3$. The nitric acid treated tubes don't exhibit the steep increase in weight until 900°C and then only by 11 wt. %. Impurities such as boron, amorphous BN, and polyhedral BN structures including nanococoons are more reactive than nanotubes and will oxidize more readily. The lower onset of temperature rise in the as-synthesized material indicates a greater degree of oxidation, originating from a greater quantity of impurities in this sample. The lower weight increase in the nitric acid treated material also indicates a higher degree of crystallinity in this material, suggestive of a larger ratio of hexagonal BN. A drop in the weight at the beginning of heating is observed and can be attributed to the vaporization of moisture and desorption of gases[246,247].

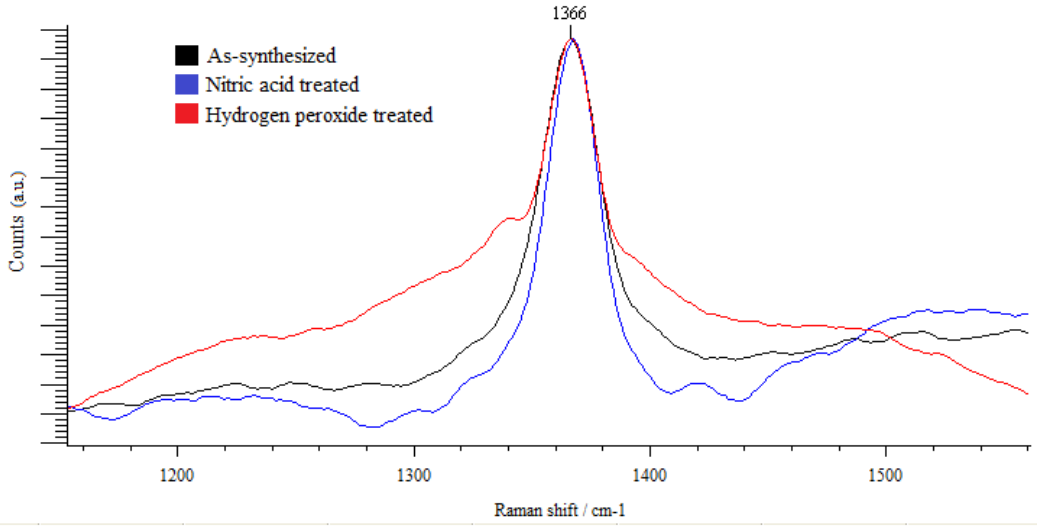


Figure 5.11: Raman spectroscopy of BNNT material. The spectra of as-synthesized, nitric acid treated, and hydrogen peroxide treated material are presented.

The Raman spectra of nitric acid treated material is presented alongside that of as-synthesized material in Figure 5.11. Both spectra display a prominent peak at 1366 $cm^{-1}$ which originates from the $E_{2g}$ vibrational mode of $sp^2$-bonded BNNTs[17]. The full-width, half-maximum (FWHM) of these peaks are 33 $cm^{-1}$ and 26 $cm^{-1}$ for the as-synthesized and nitric acid treated materials respectively. The sharper Raman peak of the latter is an indication of higher crystallinity in this sample[221]. This indicates a higher degree of pure hexagonal BN following nitric acid treatment of the original resultant product.

Despite sonicating and stirring during chemical etching, these samples also suffered from nonuniform etching to an extent. BNNTs tended to bundle together, hindering equal exposure of solution to all tubes and nanoparticles. This is evidenced with the existence of some nanococoons still filled with boron while most were empty. The biggest disadvantage is the clear damage to and sometimes destruction of nanotubes. Double walled nanotubes (DWNTs), which make up greater than 60% of the tubes in as-synthesized material, made up a much smaller percentage of the etched NTs. Under certain etching conditions, for instance at 120 °C for 4 hours, DWNTs are difficult to find. These and other few walled nanotubes are more susceptible to being completely torn or unraveled apart, leaving behind thicker multiwalled nanotubes (MWNTs). Damaged or split-apart nanotubes will leave behind other BN impurities, such as sheets or nanoribbons. In order to improve upon the purity of chemically etched BNNTs, a subsequent process for the removal of remnant BN impurities, such as sheets or hollowed nanococoons, should be

implemented. Furthermore, as in the case of CNTS, the purity and yield of BNNTs subject to a nitric acid etch will depend on the concentration of the nitric acid and time period of reflux. Further studies on nitric acid treatment of BNNTs would elucidate the most efficient conditions.

#### 5.3.2.2 Hydrogen Peroxide

Hydrogen peroxide is another inexpensive oxidant which can remove boron impurities. A high temperature and pressure environment will facilitate the oxidation of impurities. As-synthesized BNNTs (50 mg) are added to 30 mL of isopropanol and sonicated for 30 minutes. The solution is then transferred to the PTFE beaker of an acid digestion bomb (Parr, 125 mL capacity). The isopropanol is evaporated from the Teflon beaker overnight in a vacuum oven at 60 °C to allow the dispersion to stick to the walls. To the dry beaker, 40 mL of hydrogen peroxide (30 % wt.) is added with no further sonication. The effect of sonication is the subject of further investigations. The beaker is placed in the bomb, sealed, and placed in an oven at 120 °C for 24hr. When a different size acid digestion bomb or different amount or concentration of $H_2O_2$ is used, the pressure buildup in the vessel must be calculated to ensure it does not exceed the beaker's limit. Pressure buildup is due to the conversion of $H_2O_2$ into water and $O_2$ as well as water above its atmospheric boiling point. Once removed from the oven and allowed to cool, the peroxide treated material is vacuum filtered on an anodized aluminum membrane (Whatman, 0.2um pore size) and washed with DI water and isopropanol.

The $H_2O_2$ treated tubes are chemically modified, as noted by their solubility in water, as seen in Figure 5.12. The initially very hydrophobic material is now dispersible in water due to the attachment of hydrophilic groups to nanotube surfaces[248]. Indeed, further moieties can be attached to the functionalized nanotubes. The hydrogen peroxide treatment of BNNTs could be a first step in the functionalization and ultimate incorporation of BNNTs into composite materials.

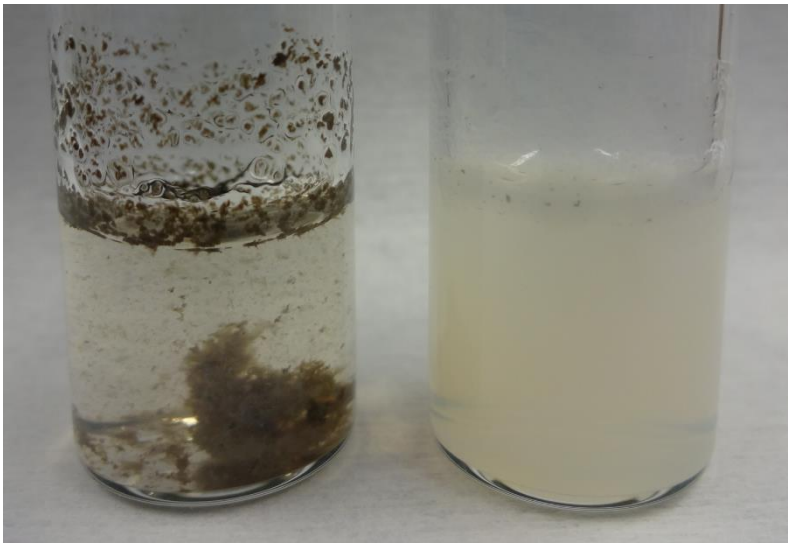

Figure 5.12: Hydroxylated BNNTs in water demonstrating (left) separation for as-synthesized BNNTs and (right) solubility for $H_2O_2$ treated BNNTs.

An SEM image of $H_2O_2$ treated material is shown in Figure 5.6c. The material was peeled off of the filter paper after the solution containing BNNTs in $H_2O_2$ was vacuum filtered. Compared to the raw material, there are fewer macroscopic particles present, signifying the removal of these impurities. Numerous fibril bundles are visible throughout the sample as well. Notably, more debris is visible when $H_2O_2$ is used than when refluxed in $HNO_3$. Unlike the $HNO_3$ etched samples, those treated with $H_2O_2$ were not critical point dried and hence appear much denser.

Further TEM characterization in presented in Figure 5.13, revealing the presence of many BN sheets alongside isolated nanotube bundles. Although no boron particles are seen, the sample contains much debris and non-tubular structures. Boron is readily removed in the highly oxidative environment of the pressurized $H_2O_2$ solution which suggests remnant fragments are composed of the more chemically inert BN. These are mostly in the form of flakes and clusters of sheets. As highlighted by the green arrows, virtually all of the nanococoons present are empty. This is repeatedly observed for material subjected to the $H_2O_2$ treatment described above and illustrates the chemical treatment conditions here are highly oxidative, more so than when a heated bath of $HNO_3$ was used.

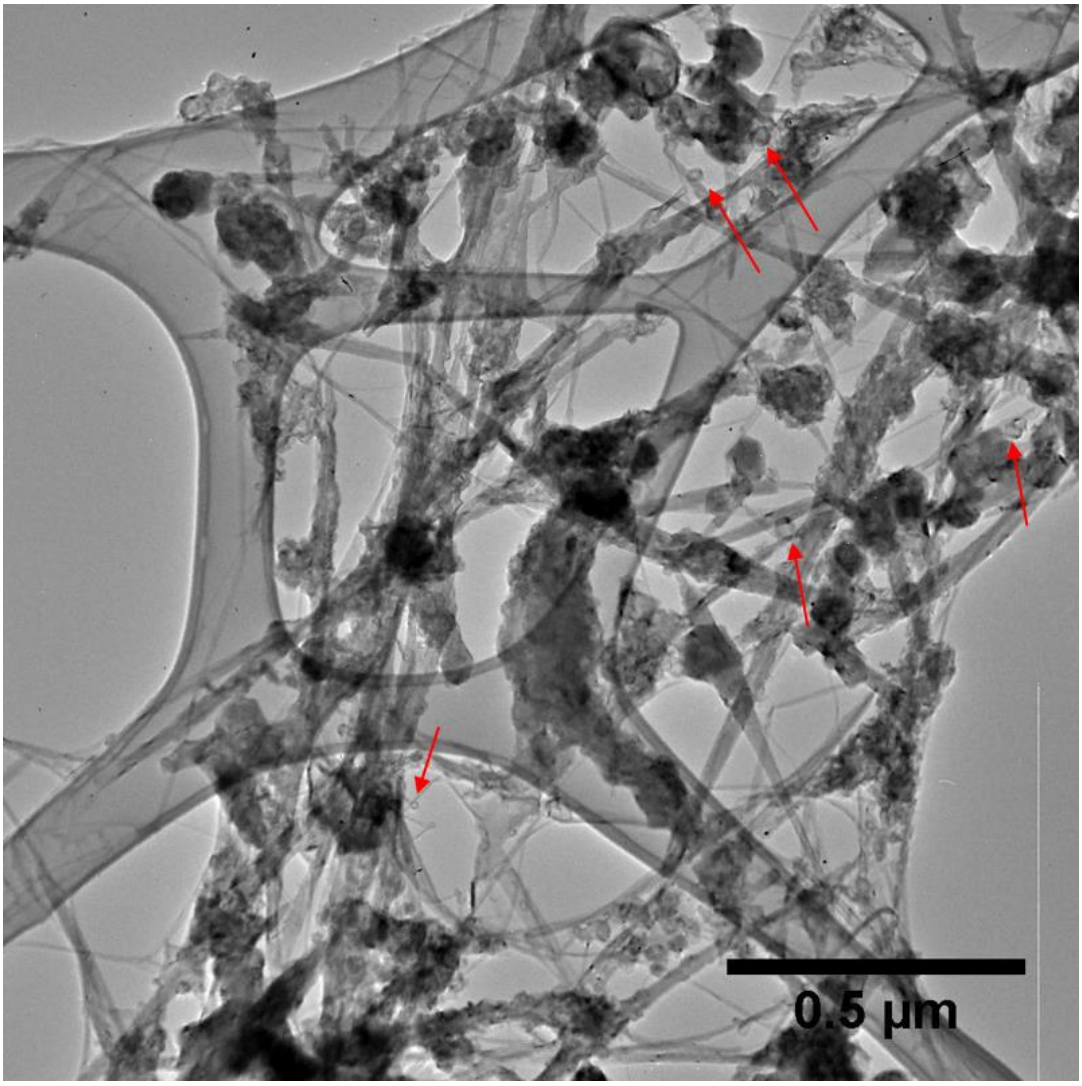


Figure 5.13: Network of BNNTs post-$H_2O_2$ treatment. Arrows indicate emptied nanococoons.

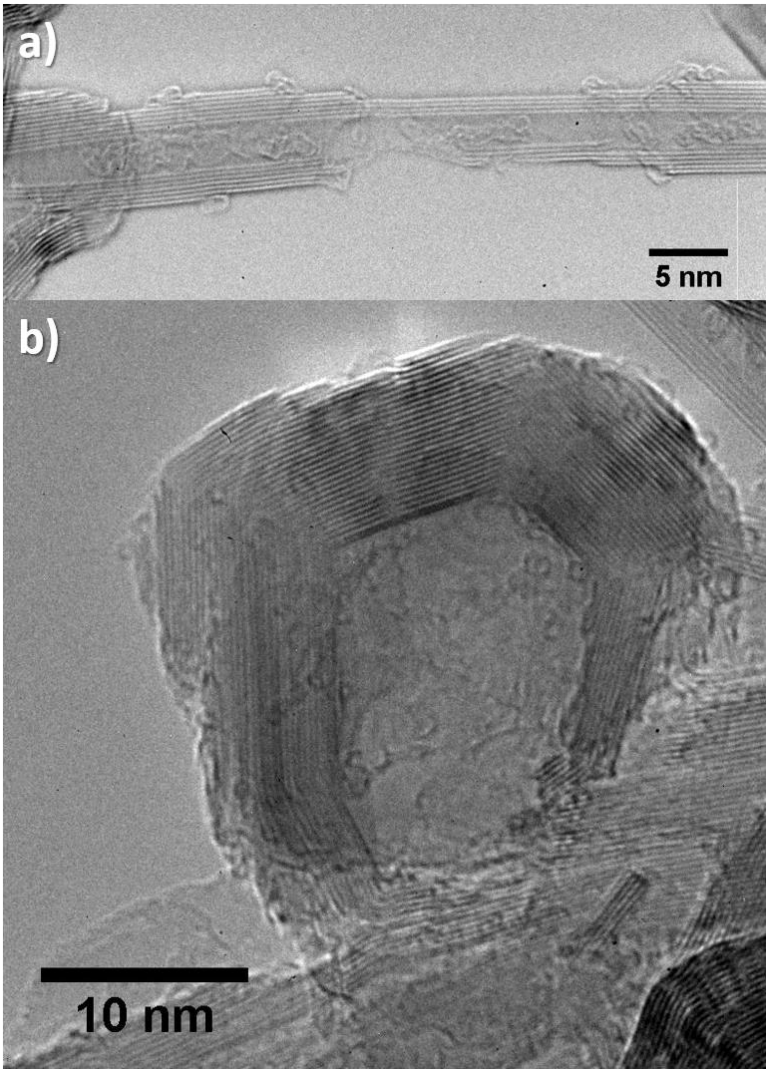


Figure 5.14: $H_2O_2$ treatment damage to (a) MWBNNT walls and (b) BN nanococoon.

Furthermore, the increased chemical reactivity here also results in a greater degree of damage to both nanotubes and other graphitic BN structures. In Figure 5.14a, a nanotube with as many as 13 walls visible to the left is very damaged, revealing multiple layers of tube walls peeled back leaving a large hole which penetrates through all walls to the inner tube cavity. In Figure 5.14b, the outer layers of a very thick nanococoon have been etched away. $H_2O_2$ treated material exhibits more nanotube damage than in any other purification technique presented in this chapter.

The Raman spectrum of product material subjected to a hydrogen peroxide treatment is presented in Figure 5.11. A peak at 1366 $cm^{-1}$ is once again visible indicating the presence of *h*-BN. This peak, however, is wider than those obtained from as-synthesized and nitric acid treated materials. Note that both chemical treatments were conducted using material from the same run, which is presented here as the as-synthesized sample. In particular, the FWHM following $H_2O_2$ etching is 48 $cm^{-1}$. The broader peak may be due to the greater degree of damage to *h*-BN networks as substantiated by TEM observation.

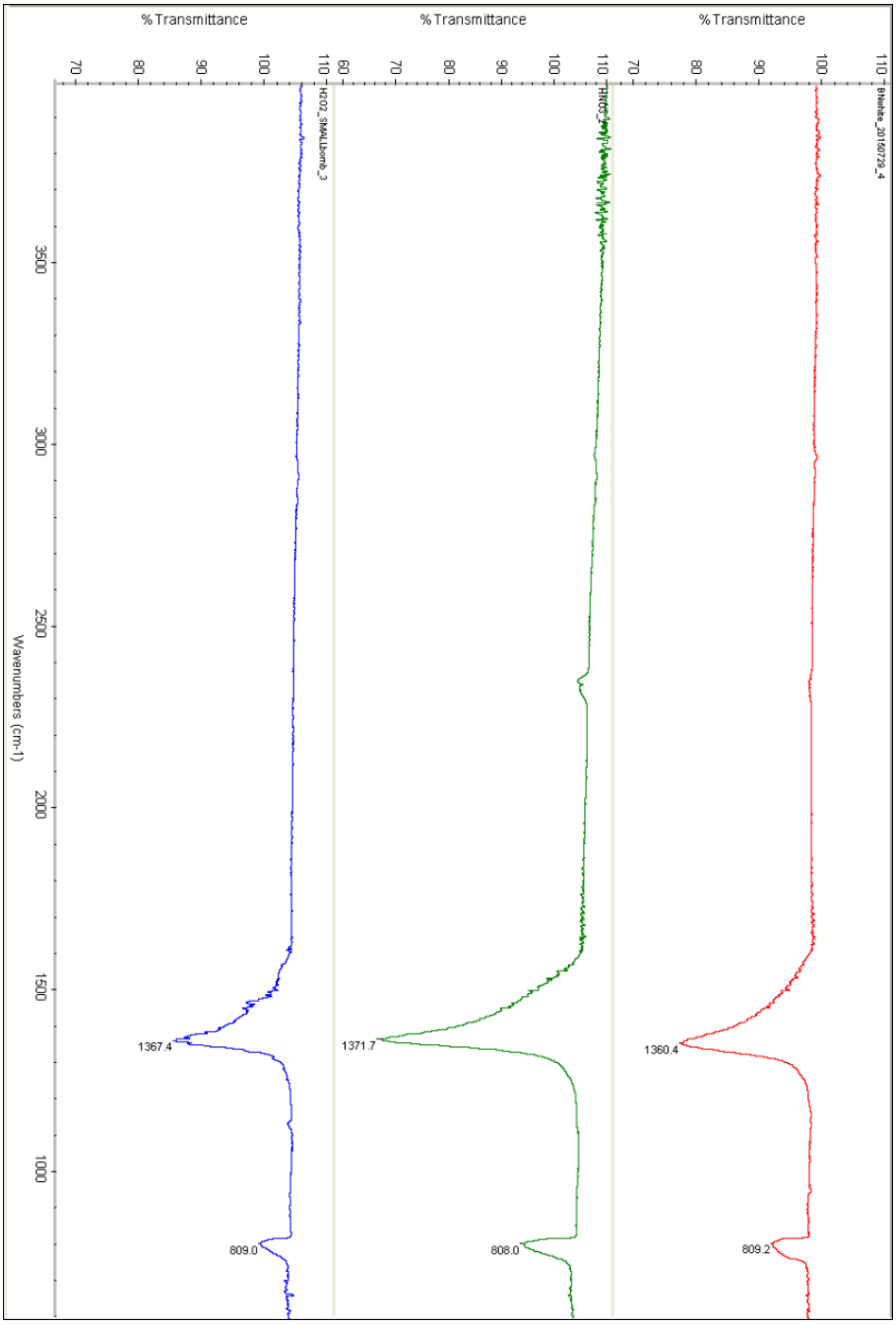


Figure 5.15: FTIR spectroscopy of BNNT material. The FTIR spectra presented are those of the (red) as-synthesized product, (green) following nitric acid treatment, and (blue) following hydrogen peroxide treatment.

Fourier transform infrared spectroscopy (FTIR) was conducted on several samples including the as-synthesized BNNT material collected directly from the synthesis chamber, BNNT product material subjected to nitric acid treatment, and BNNT product material subjected to $H_2O_2$ treatment in the chemical bomb (Figure 5.15). In the spectrum of the unprocessed material, there are two prominent peaks at 1360.4 $cm^{-1}$ and 809.2 $cm^{-1}$ which originate from the BNNTs. These two peaks correspond to the $E_{1u}$ B-N transverse optical vibration and the $A_{2u}$ B-N vibration perpendicular to the tube axis[249]. Following acid etching in $HNO_3$, these peaks are narrower and slightly shifted to 1371.7 $cm^{-1}$ and 808.0 $cm^{-1}$ respectively. The sharpening of these signature peaks indicates a higher purity of $sp^2$-bonded BN material. When the raw material is treated with $H_2O_2$, signal peaks are observed at 1367.4 $cm^{-1}$ and 809.0 $cm^{-1}$, both of which have greater FWHM than those obtained for the as-synthesized BNNTs. A slight peak is observed near 1514 $cm^{-1}$ which is due to the $E_{1u}$ longitudinal optical B-N vibration parallel to the tube axis. The splitting of the $E_{1u}$ peaks in the FTIR spectra has been reported as indicative of purified BNNTs[249].

Liquid phase oxidation using nitric acid or hydrogen peroxide are viable routes for the large scale purification of BNNTs. Chemically treated BNNT will also be functionalized, increasing their chemical activity and solubility in many organic and aqueous solvents. The chemical modification of nanotube surfaces enables the subsequent bonding of moieties, making them suitable for the attachment of additional nanoparticles[250] or to enhance their interaction with matrix material to form mechanically reinforced composites with superior thermal and chemically resistance. Nevertheless, liquid phase oxidative techniques also suffer from shortcomings, in particular tube damage and the inability to remove non-tubular BN impurities.

## 5.4 Physical-Based Purification

Chemical treatment of BNNTs results in structural damage to tube walls as well as chemical modification of their surfaces. In order to maintain the innate physical and chemical properties of the synthesized nanotubes, alternate purification methods not based on oxidation are desirable. To this end, the physical differences between pristine tubes and impurities in the collected material can be used to separate them out. These include size, aspect ratio, density, and solubility. Physical methods, such as filtration or centrifugation, can thus provide non-destructive and non-oxidizing approaches to purify BNNTs from impurities. Since these techniques are executed in solution, the as-synthesized material must have good dispersability in the solutions. This is facilitated with the use of surfactants and sonication.

### 5.4.1 PmPV Wrapping

BNNTs can be made soluble in a solution by wrapping them with the conjugated organic polymer poly(m-phenylene-co-2,5-dioctoxy-*p*-phenylenevinylen) (PmPV)[251]. A chain of PmPV tends to coil, forming a helical structure. Through intermolecular proximity and π-π interactions, the coiled polymer will readily wrap around nanotubes[252–255]. Cathodoluminescence experiments suggest a better adhesion of PmPV with BNNTs than CNTs[251]. Indeed, the PmPV wrapping of BNNTs synthesized using chemical vapor deposition with boron oxide as a reactant (BOCVD) have been demonstrated as an effective step in the their purification[237].

Well dispersed, PmPV wrapped BNNTs would subsequently be centrifuged in order to separate them from the more massive, denser impurities present in the collected material. Centrifugation, particularly at higher speeds (~20000 g's), could also be used to separate polymer wrapped BN nano-sheets and nanoribbons from BNNTs based on differences in density and fluid flow resistance[256].

Briefly, cotton-candy like material traversing the center of the synthesis chamber of the EPIC plasma system is first collected. The material is mixed with PmPV in a vial of chloroform, 1,2-dichloroethane (DCE), or *N*,*N*-Dimethylformamide (DMF). The BNNTs are made soluble with a mild sonication. The solution is then centrifuged at 2000, 5000, and 10000 rpm in a centrifuge (Beckman Coulter Optima XL-100k Ultracentrifuge) for 45 min. The resulting supernatant is collected and drop cast onto 300 mesh lacey carbon Cu TEM grids. Alternately, the collected supernatant can be filtered, rinsed with DCE, sonicated in IPA and then drop cast onto TEM grids in order to wash off small particles adhered onto tube bundles and yield a cleaner final product.

In order to remove PmPV and recover pristine BNNTs, the solution containing the PmPV-BNNTs was heated to 60 °C to evaporate the solvent and then at 500 °C for 20 min to fully burn off the PmPV. The initially yellow sample turns white during heating. As shown in Figure 5.16a, PmPV coats and adheres to nanotube bundles after the two are sonicated in solvent together. From Figure 5.16b, PmPV is seen to coat the outside of individual BNNTs within this bundle of a few nanotubes. A helical wrapping of the polymer is observed around the right-most nanotube. Following the thermal treatment, the surface of the BNNT is clean with little to no residue left behind and shown in Figure 5.16c. The red arrows indicate regions inside the BNNT bundle shielded from the outside in which PmPV may be retained. The BNNTs are not damaged in the process and retain their highly crystalline configuration since the PmPV wrapping is a noncovalent bonding.

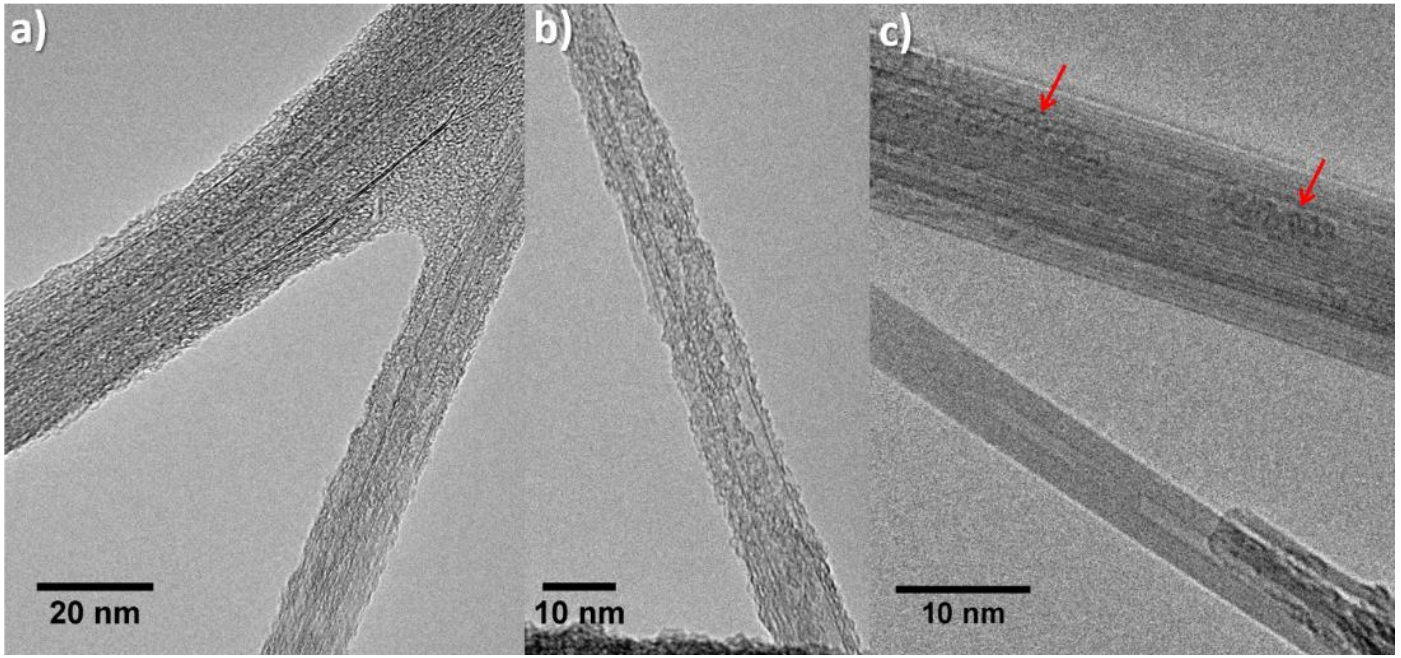


Figure 5.16: PmPV wrapping of BNNTs. (a) Bundle of BNNTs coated in PmPV. (b) Individual BNNTs wrapped by PmPV. (c) BNNTs recovered following heating of PmPV-BNNT composite. Red arrows indicate potential remnant PmPV.

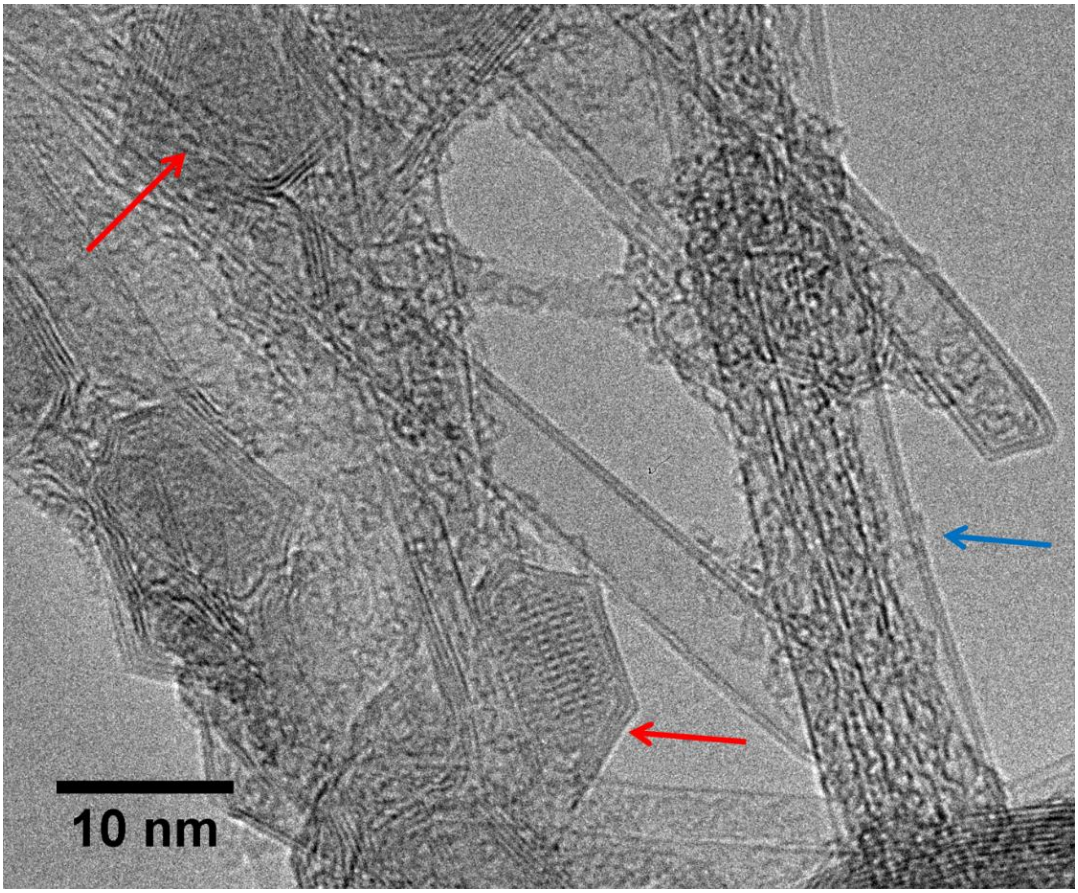


Figure 5.17: BNNTs post-PmPV wrapping and centrifuging. BN nanococoons (red arrows), BN sheets, amorphous B particles are present in addition to BNNTs. BNNTs are found isolated as well as in bundles (blue arrow).

There are a number of shortcomings with purifying tubes physically using the PmPV wrapping method. As noted in Figure 5.17, impurities with similar densities and sizes as nanotubes, such nanococoons and segmented sheets, continue to remain in the sample. Boron particles encapsulated by BN layers are also present, some of which are indicated by red arrows. Small amorphous particles stuck to nanotubes are particularly difficult to remove. A more vigorous sonication may detach them, but this may come at the expense of physically damaging nanotubes. Furthermore, physical purification methods rely on the BNNT samples being highly dispersible. Even with the wrapping of PmPV, boron particles and BNNTs have a high propensity for agglomerating. Centrifugation will result in many tube clusters sedimenting out alongside impurities, as depicted in Figure 5.17. A bundle of BNNTs consisting of double walled as well as single wall tubes are designated in Figure 5.17

by a blue arrow. To minimize this, centrifuging should follow sonication of BNNTs with PmPV in solvent as soon as possible. Furthermore, physical separation of BNNTs from impurities is time consuming and only possible on a small amount of material at a time. Considering the low yield of purified BNNTs, this technique is inefficient on its own.

## 5.5 Multistep Methods

The techniques of purifying the resultant BN product material of the EPIC synthesis process have their advantages and shortcomings. The gas phase oxidation explored here is a straightforward means by which to get rid of amorphous carbon, in the process oxidizing boron impurities which can then be dissolved in water. However, it is not as effective at removing boron as liquid phase techniques due to the limited access of oxygen to more deeply impended impurity particles in agglomerates of the BN material. Liquid phase oxidative techniques, including both nitric acid and hydrogen peroxide treatments, are more effective at etching away boron impurities, including those within BN nanocages. These methods are also more scalable. Nevertheless, oxidative purification techniques tend to damage and to some extent chemically modify the surface of BNNTs. They are also unable to adequately remove non-tubular BN impurities present in the as-synthesized material, such as nanococoons and *h*-BN sheets. Physical separation methods, such as PmPV wrapping and centrifuging, are able to segregate nanotubes from denser particles, including some nanococoons, but at the cost of ultimately yielding few nanotubes.

In order to achieve a high yield of high purity BNNTs, a multiple step purification method will likely need to be employed using a combination of both chemical and physical purification techniques. Smaller particles such as boron attached to nanotubes or small nanococoons are particularly difficult to remove. Effective sonication will be key to getting rid of these impurities adhered to the walls of BNNTs using appropriate solvents which enable sufficient dispersion. A number of multi-step purification methods have been reported for CNTs[257–262]. No longer limited by the quantity of BNNT material available, similar routes may prove suitable for BNNTs.

# Chapter 6

# Metal-Filled Boron Nitride Nanotubes

In this chapter, we present a simple and universal wet-chemistry route to fill the hollow inner cores of boron nitride nanotubes (BNNTs) efficiently with metals. The fillers conform to the cross-section of the tube cavity, and extend in length from a few nm to hundreds of nm. The methodology is robust and is demonstrated for noble metals (Au, Pt, Pd and Ag), transition metals (Co, Ni, Fe, Cr, Cu), and post-transition elements (In). Up to 60% of BNNTs of a given preparation batch have some degree of metal encapsulation, and individual tubes can have up to 15% of their core volume filled during initial loading. Encapsulated materials of various morphologies are formed within BNNTs of different lengths, diameters, and number of tube walls. High resolution transmission electron microscopy (HRTEM) and scanning transmission electron microscopy (STEM) accompanied by electron energy loss (EELS) and energy dispersion X-ray spectroscopy (EDS) were used to study their nanostructures and chemical compositions. The growth, movement, and fusing of metal nanoparticles within the BNNTs are also examined.

## 6.1 Filling Nanotubes

In 1992, Broughton and Pederson[263] predicted that capillary forces would be sufficient to drive a liquid into the inner cavity of a carbon nanotube (CNT). The following year, CNTs annealed in an evacuated ampule with lead powder where successfully filled with molten Pb[264]. Over the last couple of decades, the filling of CNTs with metals, oxides, halides and even biomolecules has been reported[265–270]. The filler/CNT systems have been studied both theoretically and experimentally, demonstrating intriguing physical and chemical properties and potential applications in optoelectronics, nanothermometry, and catalysis[271–279]. However, the conducting or semiconducting nature of a CNT, as well as its chemical reactivity, can induce a

undesirable interactions between the filler and the host, hindering the ability to investigate intrinsic properties (optical, electrical and catalytic) of fillers[280–283], such as metal nanoparticles or nanorods and limiting their application.

As discussed in chapters 4 and 5, boron nitride nanotubes (BNNTs) are wide-bandgap structural analogues to CNTs[7,178]. Recall that they are electrically insulating, chemically inert, with excellent thermal oxidation resistance and high mechanical strength[179]. This makes them attractive for studying the intrinsic properties of encapsulated materials. Notably, by filling BNNTs with metal nanowires or nanorods, electrically conducting nanocables shielded by insulating layers can be constructed. Despite these advantages, there are few reports of filling BNNTs with fullerenes, oxides, carbines, halides and metals [184,284–287]. In the cases reported, filling either occurs *in–situ* during the synthesis of BNNTs[288] or ex–situ (post-synthesis) using a vapor phase transport method[286]. There has also been a report on the electrochemical deposition of Cu into BN tubes with relatively large diameters (~300nm)[289]. However, these methods are not universal and have only worked for a limited number of materials, such as those which serve as catalysts for BNNT growth or materials with a low vaporizing temperature. Additionally, low filling efficiencies makes these methods far from ideal. A new method is needed which can work for a variety of filler materials at mild conditions with high filling yields and at lower costs, such as a solution-based approach. However, capillarity-induced filling of BNNTs using solution-based methods has not been reported; this is likely attributable to the greater difficulty in wetting a the hexagonal BN surface compared to C[290].

In this chapter, we present and explore a successful wet-chemistry post-tube-synthesis route to the encapsulation of metallic nanostructures (including short nanocrystals, rods, and long wires) within BNNTs. As many as 60% of the BNNTs in the preparation batch have some degree of filling, with individual tubes having as much as 15 % of their interior volume occupied by metal. We also explore the movement of metallic nanoparticles within the BNNT, as well as the fragmenting and fusing of nanoparticles.

## 6.2 Methods of Filling Nanotubes

Nanotubes can be filled *in-situ* during their synthesis as precursor material can be enveloped within formed tubular cavities[291,292]. Efforts to fill BNNTs have predominantly been carried out in this vein[285,288,293–296]. Materials can be filled that have surface tensions too high for other methods (see discussion below) and the enclosed material is protected from a post-synthesis environment. However, the possible filling material is limited to those which serve as catalysts during nanotube growth. NT crystallinity may also be comprised as walls form to conform around

molten particles[293,295]. Low filling efficiencies and a lack of control make filling NTs *in-situ* during synthesis far from ideal.

Recent high-yield synthesis methods producing highly crystalline BNNTs make it more practical to separate synthesis and filling procedures[297]. One post-synthesis route to fill nanotubes is based on the physical flow of molten material into a nanotube via capillarity. In this method, nanotubes are mixed with metal precursors such that when the system is sufficiently heated, the caps of the nanotubes are opened, and capillary forces drive the surrounding molten material into the tube cavity. Subsequent thermal treatment or electron irradiation can be used to alter the nature of the filling material.

The work presented here is the first successful filling of boron nitride nanotubes utilizing a wet chemistry method[268]. In this method, the tips of the BNNTs are first opened by refluxing in a nitric acid bath or thermal annealing in air. The non-capped tubes are then mixed in a metal-salt solvent bath resulting in the filling of tube cavities with the solution. Once vacuum filtered, metal nanoparticles are then formed following thermal reduction. *In-situ* filling of the BNNTs can be obtained when as-synthesized BNNTs are refluxed in a metal-salt containing nitric acid bath and subsequently annealed.

A wet chemistry approach provides more versatility in terms of potential filling material as well as an additional degree of control over the formed nanoparticle structures. In the physical method, encapsulated materials tend to form as nanowires, oftentimes originating from a tube end[264,267,298]. Only molten materials with suitable wettability are able to fill tube cavities, hence limiting the types of enclosed matter attainable. As highlighted below, the low surface energy of BNNTs result in their poor wettability by liquid metals. Indeed, the physical filling of BNNTs with metals have only been demonstrated via a carbothermal substitution method wherein initially open-tipped CNTs are filled with molten metal in parallel with the concurrent process of tubular shell compositional modification from C to BN[285]. Chemical filling simply requires the metal-salt precursor be sufficiently soluble in a solvent capable of wetting the BNNTs. Various morphologies from spheres, to short rods, to longer wires can be observed throughout a nanotube using this method.

## 6.3 Opening Nanotube Tip Ends

Many of the BNNTs synthesized via the EPIC plasma method have closed nanotube ends. These caps tend to be polyhedral and must be opened in order to facilitate filling the inside cavity of the tube via capillarity. The closed ends of a nanotube are necessarily formed by the inclusion of non-six membered rings or other defects in the hexagonal lattice structure, producing curved regions which culminate

in the closure of the tip ends. The regions of high curvature experience the largest strains and are the sites of highest chemical reactivity[269,270,299]. When treated in a hot nitric acid bath or annealed in the presence of oxygen, the capped ends of the nanotube will be the first sites comprised by the chemical reaction. This is clearly evident in Figure 5.8 where the nanotubes have been selectively damaged at the regions of highest curvature.

### 6.3.1 Thermal Oxidation

Ajayan *et al.* have shown that thermal oxidation can open capped nanotube ends, providing a route for liquids to flow in[265]. As an alternative to treating the tubes in nitric acid, as-synthesized BNNTs could be heated in the presence of oxygen at 800 °C for several hours to open tip ends[28]. The capped ends and any tube defects are the first to become damaged and open up. Prolonged exposure to oxygen at such high temperatures will gradually attack the dangling bonds of a nanotube, damaging walls near defect sites and shortening the tube overall. Amorphous boron present in the synthesized material collected from the EPIC plasma system is also oxidized forming boron oxide, which subsequently can be dissolved in water thus purifying the resultant BNNT product.

However, thermal oxidation chiefly affects the nanotubes readily exposed to the air, namely those present on the outside of a fibril. Ideally, the as-synthesized material should be uniformly exposed to oxygen during annealing, by such means as crushing it up and spreading it over a large surface. In practice, thermally oxidizing nanotubes produces a low yield of open tipped tubes, oftentimes much shorter and more damaged, alongside longer capped NTs.

### 6.3.2 Chemical Treatment

Chemically treating the as-synthesized nanotube material proved to be a more effective method to remove cap ends. Sonicating or stirring the nanotube material in a hot nitric acid bath facilitated the uniform dispersion and exposure of tube ends to be opened. Amorphous boron impurities present in as-synthesized material were also chemically etched and removed in this step, resulting in a visibly whiter product. Nitric acid also damages tube walls so prolonged treatment will tend to destroy and unravel few walled NTs, as illustrated in Figure 5.9 and Figure 6.1a. This leaves mostly nanotubes with larger number of walls, as well as *h*-BN sheets.

Figure 6.1b show a TEM image of MWBNNTs after nitric acid treatment, including a five-walled BNNT with etched open tip end. The ending caps of many

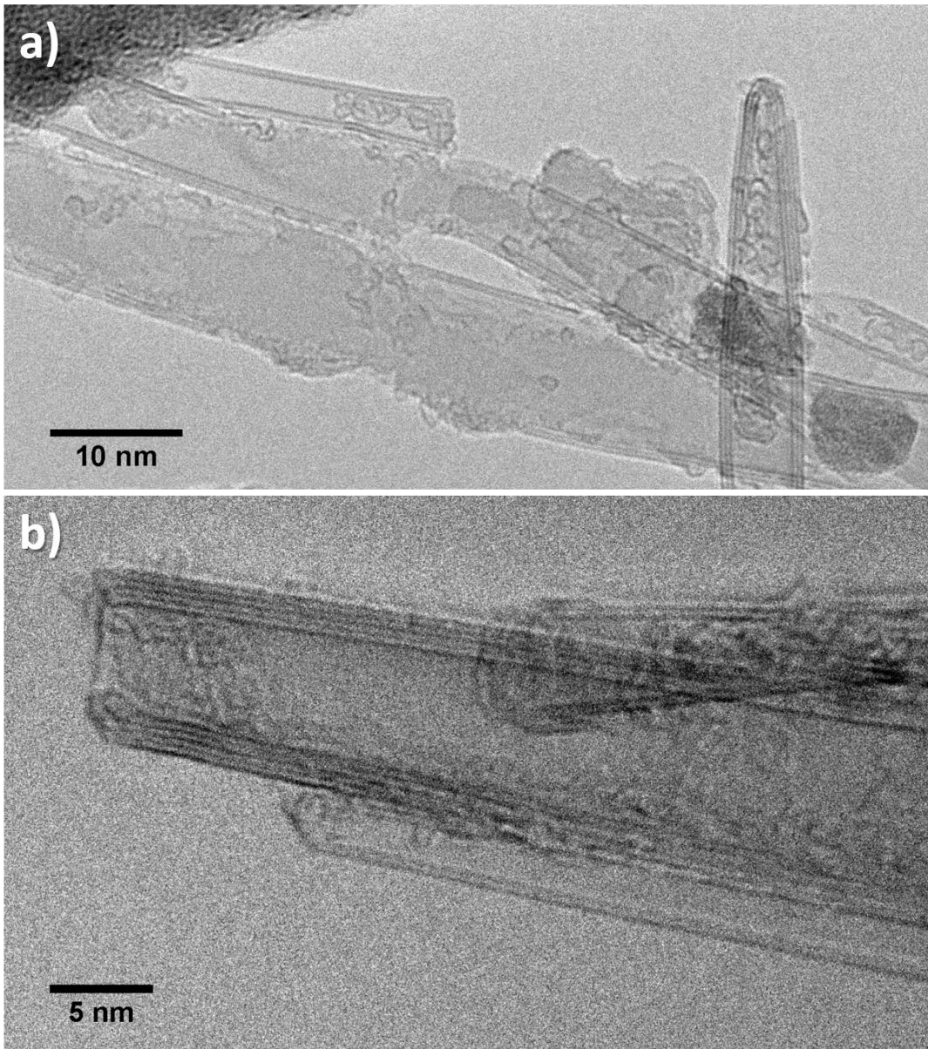


Figure 6.1: Nitric acid treated BNNTs. (a) Damaged and unraveled few-walled BNNTs and BN sheets. (b) MWBNNT with end etched open.

tubes are removed, which allows for the filling of the metal precursor solution. Sometimes nanotube walls were damaged and peeled off.

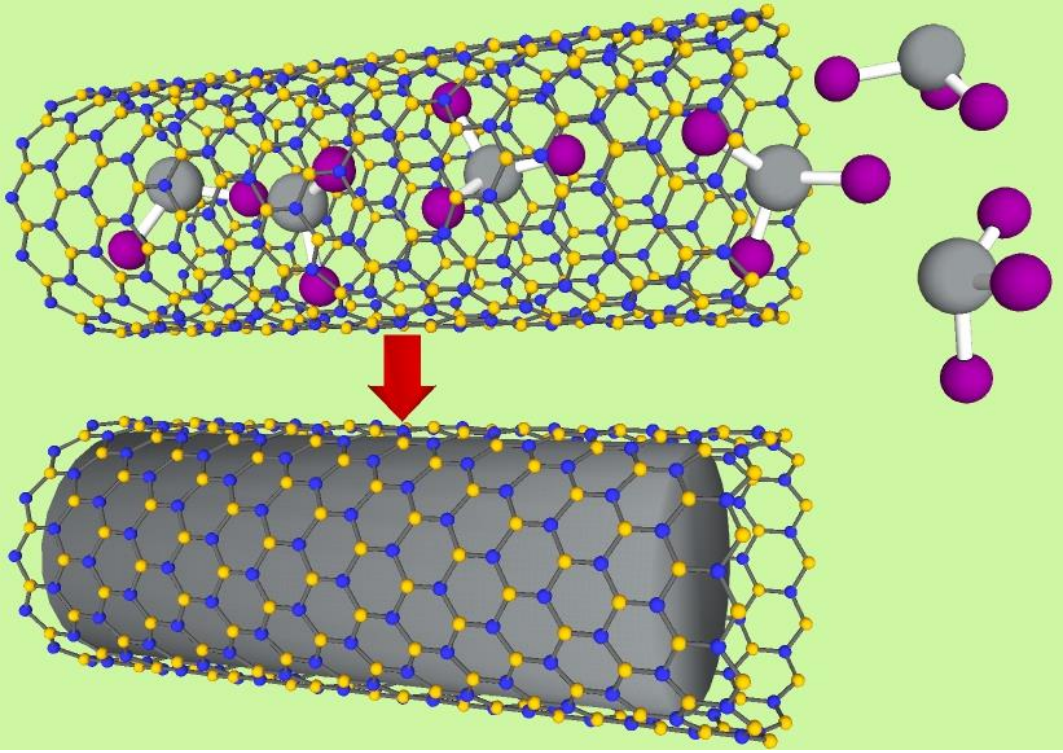

Figure 6.2: Capillarity driven metal filling of BNNTs.

## 6.4 Wet-Chemistry Route to Fill BNNTs

### 6.4.1 Experimental Conditions

BNNTs used for the encapsulation are synthesized using the Extended Pressure Inductively Coupled (EPIC) plasma method[297]. Briefly, amorphous boron powder (Alfa Aesar, - 325 mesh) is fed into a pure nitrogen plasma at elevated pressure. Energetic species and high collision rates promote the effective growth of BNNTs. The BNNTs are usually double-walled with high crystallinity and lengths up to several microns. The small inner diameters (~ 2–6 nm) of EPIC plasma synthesized BNNTs make them especially conducive to drawing in liquids via capillarity[300].

Fibril-like material collected from the center of the synthesis chamber, confirmed by TEM to predominantly consists of BNNTs, is refluxed in a nitric acid bath at 120 °C for 3 hours, to open NT tip ends. After rinsing in deionized water, the BNNTs

are left overnight in a bath of 0.5 mol/L of metal-salt precursor dissolved in ethanol. An illustration of the filling process is presented in Figure 6.2. The salts enter the tube interior via capillary action. Alternatively, following an *in-situ* filling approach, the metal-salt precursor can be dissolved in the hot nitric acid bath within which the as-synthesized BNNTs are refluxed for several hours. The products are then vacuum filtered and subsequently thermally treated in a 200 sccm flow of $H_2$ at 600 – 800 °C for 1 – 4 hours to reduce the metal salts yielding dense metal nanoparticles within the core of the BNNTs. The experiments described here are for a single-shot process (where only one filling step is performed), but the process can be repeated to enhance the overall filling factor of the tubes.

The metal-filled BNNTs are sonicated in isopropyl alcohol and drop cast onto 300 mesh lacey carbon Cu or Au grids for characterization by high resolution transmission electron microscopy (HRTEM) (JEOL JEM 2010 operating at 80 kV) and scanning transmission electron microscopy (STEM) (FEI TitanX operating at 300 kV). The composition of the product is evaluated with sub-nm resolution by a combination of energy dispersive X–ray (EDS) and an electron energy loss (EELS) spectroscopies. STEM, EDS, and EELS characterizations were conducted at the National Center for Electron Microscopy at the Lawrence Berkeley National Laboratory.

### 6.4.2 Metal-Filled BNNTs

The straightforward and versatile wet chemistry method described of immersing nanotubes in a metal-salt solution following the opening of cap ends described above, and a subsequent thermal reduction filled the inner cavities of the nanotubes with metal. Figure 6.3a shows a representative result of the capillary force induced filling of an opened BNNT encapsulating Pt nanoparticles and nanorods (denoted as Pt@BNNTs). The particle lengths range from 1 nm to hundreds of nanometers with a width normally defined by the inner diameter of the BNNTs (mostly 2 – 4 nm as reported). During sample preparation, a small amount of precursor material remained on the nanotubes, resulting in extra particles/rods outside of the nanotubes. The facets of filled nanorods conform nicely to the inner cavity of the tubes. The positions of filling nanoparticles/nanorods as being within the tubes were confirmed by tilting the TEM stage (see Figure 6.5) and by using STEM as discussed later.

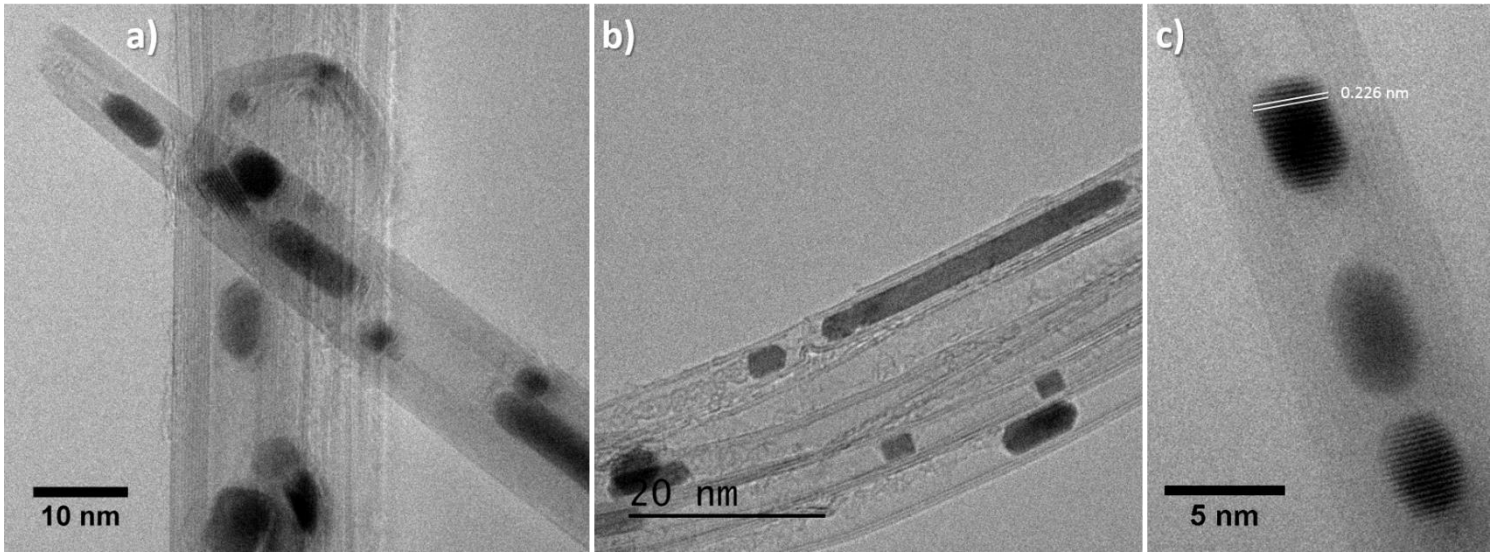


Figure 6.3: Platinum-filled BNNTs (Pt@BNNTs). HRTEM images of (a) BNNT with opened tip end filled with Pt nanoparticles. (b) Encapsulted Pt nanostructures within BNNTs. (c) Pt nanoparticles with lattice fringes corresponding to (111) planes.

### 6.4.2.1 Pt@BNNTs

Figure 6.3 shows representative HRTEM images of a Pt@BNNT sample prepared from $H_2PtCl_6$ dissolved in ethanol. There are several small particles (less than 5 nm long) with different facets and shapes, and a long rod (~50 nm long). Their widths are defined by the inner diameter of the BNNTs (<10 nm). A closer look at the dent near the left end of the rod (Figure 6.3b) reveals that the rod itself may be formed by fusion of a small particle and a long rod during the annealing process. Even a nanotube with a narrow constrictions in the middle (Figure 6.3b) can be filled with Pt rods/particles from both sides of the kink. Traces of residual precursor solution are visible next to the particle left of the kink due to incomplete thermal reduction. In some cases, arrays of nanoparticles were formed instead of long rods (Figure 6.3c). The distance between lattice fringes of those particles is 0.226 nm, which corresponds to the (111) interplanar spacing of FCC Pt. The facets of some particles form clear 120° angles and reveal clear fringes due to the Pt's crystal lattice structure.

Interestingly, filled BNNTs with oxides and metals prepared by other methods (e.g. in–situ during synthesis of BNNTs) do not exhibit definite atomic boundaries between innermost shells of the tubes and filling materials. This may result from the spontaneous phase separation of nanotubes and nanowires during growth. In our case the annealing is mild, which does not alter the structures of BNNTs and the usage of ethanol or nitric acid as a solvent helps to wet the walls. The filling metals almost always conform to the inner cross-sectional area of the BNNTs, forming a leak-tight plug. As we demonstrate below, however, under the right circumstances the plugs can be physically translated along the axis of the BNNT. Detailed TEM studies show that the percentage of BNNTs with some Pt filling is ~ 40%.

### 6.4.2.2 Au@BNNTs

Similar results are obtained for other metal-salt precursors. Figure 6.4a – c are TEM images of Au@BNNTs prepared from $AuCl_3$. Interestingly, gold nanostructures tend to form long nanorods with curved caps instead of nanoparticles with distinct facets. These nanorods also conform perfectly to the innermost walls of nanotubes. Au nanorod lengths range from 50 to 350 nm, with small diameters of 2 – 6 nm. Lattice fringes in the Au nanorod of Figure 6.4c are spaced at 0.204 nm, corresponding to the (002) interplanar spacing of Au. The nanotube confinement creates very high aspect ratio nanorods without the need for any surface stabilizing ligands as prepared by other solution methods[301,302]. These pure, nanoscaled, gold rods encapsulated by electronically and chemically inert BNNT are ideal subjects for studying nanoplasmonics. The favorable formation of Au rod–shaped nanostructures can be attributed to several factors. For example, the surface energy difference between gold and its hexagonal BN container, as well as the volume change during the thermal reduction from liquid to solid phase.

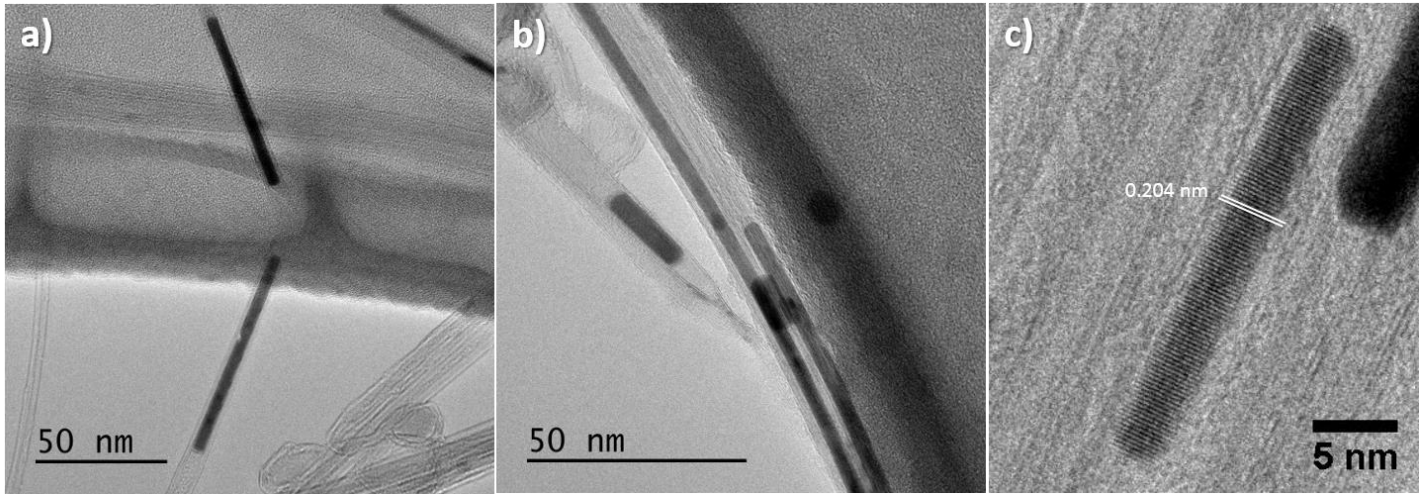


Figure 6.4: Gold-filled BNNTs (Au@BNNTs). TEM images of (a) gold nanorod structures within a bent BNNNT and (b) gold particles formed almost exclusively as long nanowires. (c) HRTEM of a single-crystallite Au nanorod with clear lattice fringes corresponding to (002) planes.

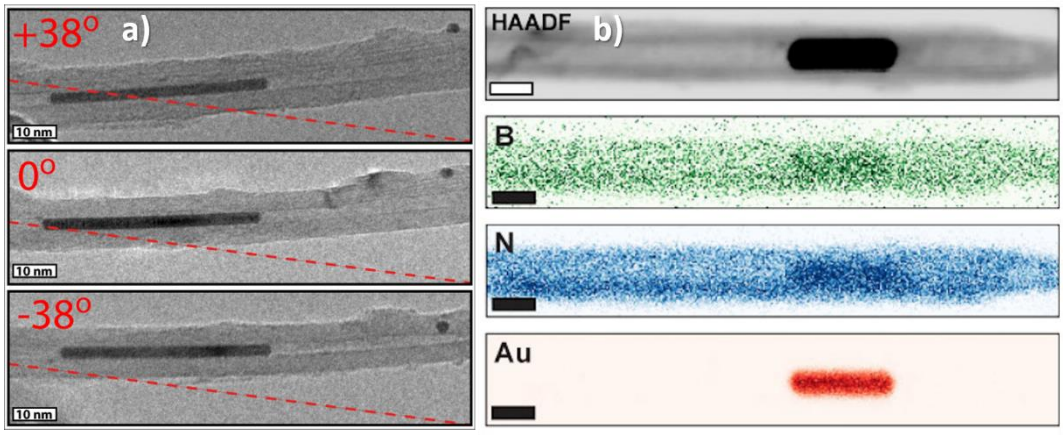


Figure 6.5: Position confirmation and chemical composition of filling material. (a) Series of TEM images of a sample tilted about the dashed red line confirming encapsulation of Au nanorods inside the BNNT cavity. (b) STEM high angle annular dark field image (contrast inverted for easier viewing) and EDS maps show chemical composition of filling material. (Courtesy of B. Shevitski)

### 6.4.2.3 Chemical Composition and Encapsulation Confirmation

In order to confirm the chemical composition of resultant materials and circular cross-section of formed metal nanostructures, a series of TEM images are taken at various sample tilts. Figure 6.5a shows results for Au@BNNT sample. The TEM stage (and therefore the nanotube) is titled clockwise and counterclockwise 38° along the red dotted line. While a small particle located on the outer surface of the tube (in the right corner of the images) changes its position upon tilting, the nanorod does not move with respect to the tube walls or change its diameter. This confirms that the metal nanorod is tightly encapsulated by the boron nitride nanotube. Additional evidence for tight metal nanorod confinement is provided by high–angle annular dark field (HAADF) STEM imaging, as shown in Figure 6.5b.

EDS and EELS were performed to confirm the chemical composition of encapsulated materials. Similar experiments were done on other metal-filled BNNTs, giving similar results in terms of particle/rod position and purity of metallic substances. Representative results are shown in Figure 6.5b for Au@BNNT. The contrast of the dark field image clearly shows the nanorod inside of the nanotube, and elemental mapping using EDS highlights the distribution of elements (B, N and Au) along the nanotube. As shown, elemental gold nanorods are confined inside the cavity of the BNNT.

The EDS spectrum of Figure 6.6 confirms the purity of the metallic rod by showing only a strong Au K edge at in addition to prominent peaks corresponding to the B K and N K edges. There is no trace of other elements such as O or Cl. The apparent increase in the B and N signals corresponding to the Au nanoparticle as seen in Figure 6.5b is due to the increased Bremsstrahlung background in the spectral region of the B and N K shell edges. EELS spectrum on non-filled regions indicate a B/N ratio of ~ 1.0.

The elemental composition of platinum particles within a BNNT is also presented in Figure 6.7. Elemental mapping reveals the uniform presence of B and N along the tube axis and clear Pt signals corresponding to the location of Pt particles. The EDS spectrum shows peaks originating from B, N, Pt, and Cu with no peaks due to Cl or O. Cu peaks are from the Cu TEM grids.

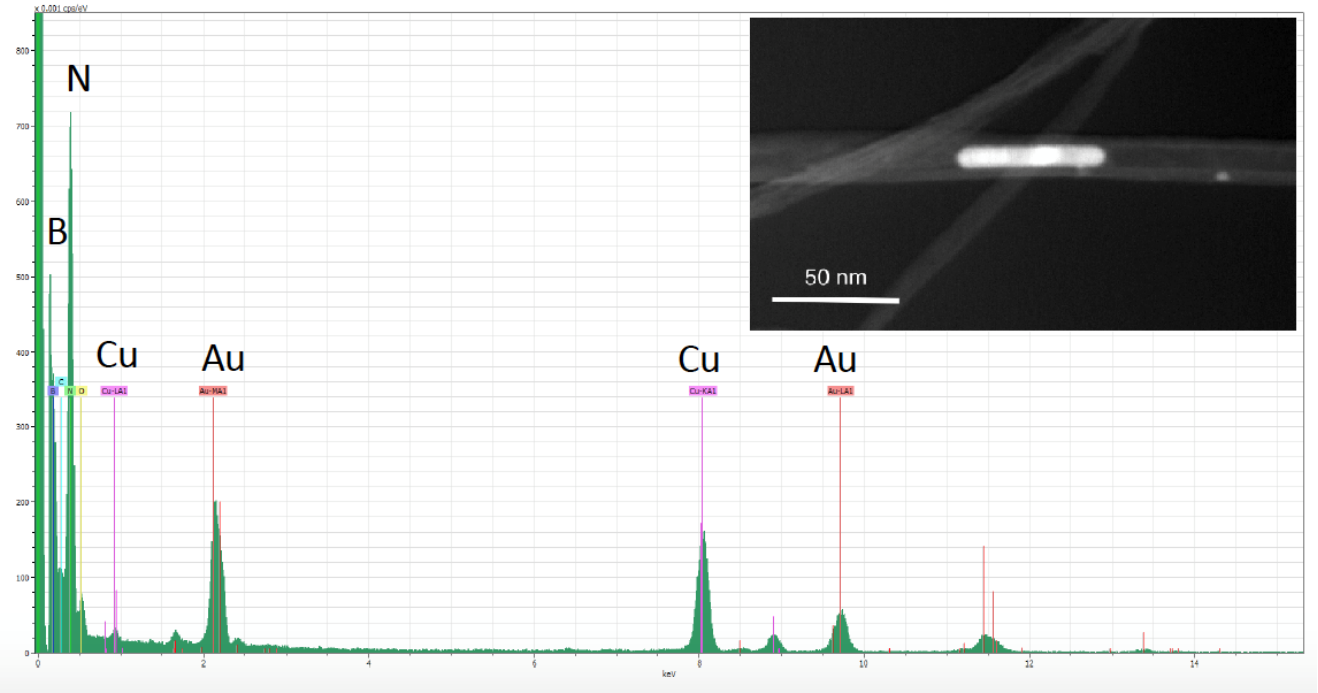


Figure 6.6: Elemental composition and position of Au@BNNTs. HAADF image (inset) and EDS spectrum of a Au nanorod within a BNNT showing only Au signals with negligible traces of O and Cl. Cu peaks in the spectrum are from the copper TEM grid. (Courtesy of B. Shevitski)

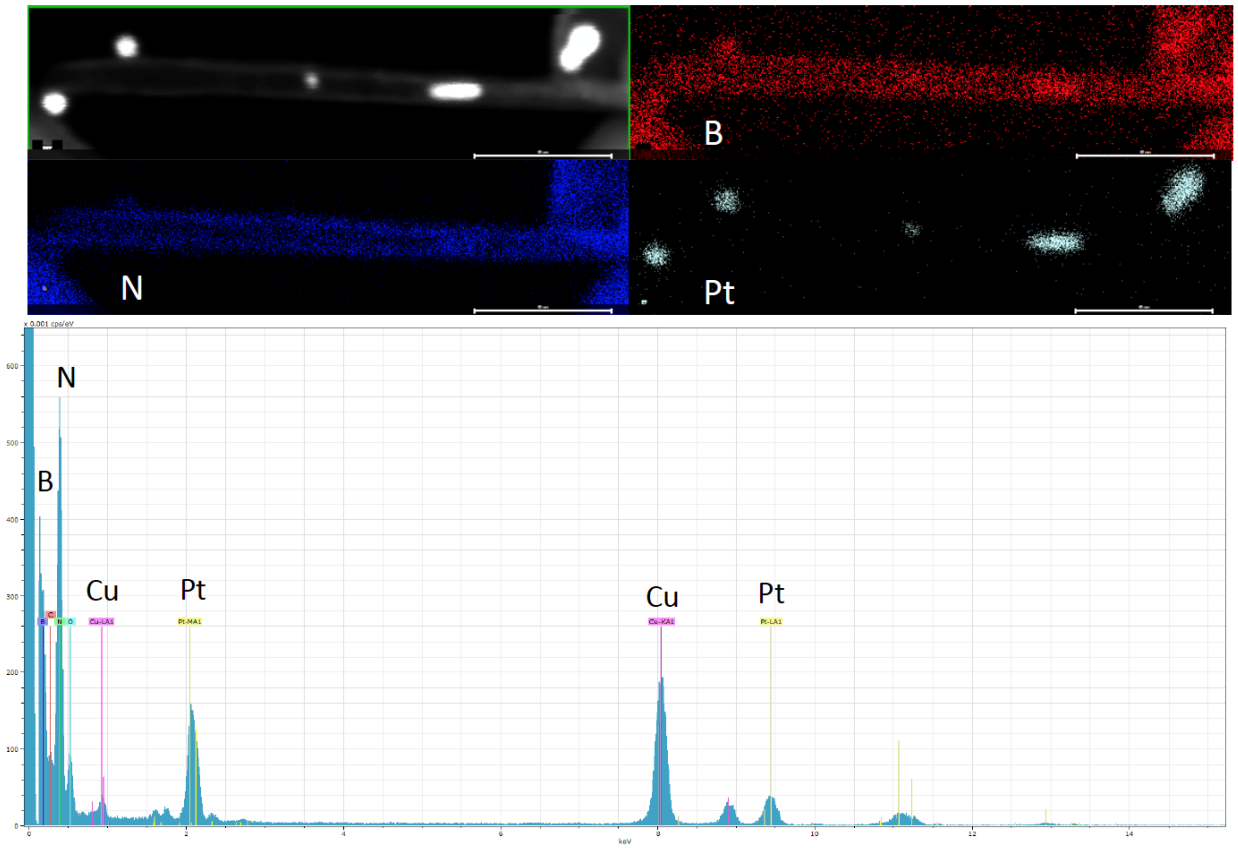


Figure 6.7: Elemental composition and position of Pt@BNNTs. HAADF image, EDS mapping and spectrum of Pt nanoparticles within a BNNT. Cu peaks in the EDS spectrum are from the copper TEM grid. (Courtesy of B. Shevitksi)

### 6.4.2.4 M@BNNTs; M = Pd, Ag, In, Ni, Co

A similar method was applied to prepare other metal-filled BNNTs, including Pd@BNNT from $PdCl_2$, Ag@BNNT from $AgNO_3$, In@BNNT from $In(NO_3)_2$, Ni@BNNT from $Ni(NO_3)_2$, Co@BNNT from $Co(NO_3)_2$. Figure 6.8a – h are representative TEM images of these samples. The identity of filling materials is confirmed by high resolution TEM and electron spectroscopy of the crystals. Figure 6.8a is Pd@BNNT, which clearly shows Pd particles following the distortion of the BNNT structure. The encapsulated particle imaged in the inset has sharp 120° facets with lattice fringes of 0.225 nm corresponding to the (111) interplanar spacing of FCC Pd. Figure 6.8b is HRTEM of In@BNNT showing intriguing crystalline In nanorods (35 nm long and 8 nm diameter) forming a clear atomic interface with the innermost tubular shells. The spacing between lattice fringes is measured to be 0.278 nm, which corresponds to the (224) lattice spacing of tetragonal In. Similarly, Figure 6.8c shows TEM images of encapsulated Co particles inside BNNTs. The particles conform nicely with the contour of BNNT innermost walls. The measured regular spacing of the observed planes of the lattice is 0.210 nm, which is consistent with the interplanar spacing of (100) HCP Co. Figure 6.8d of Ni@BNNT displays a BNNT bundle, some of which are filled. The inset reveals an encapsulated Ni particle with lattice fringes indicative of a crystalline structure. Occasionally metal fillings displayed regions of varying contrast and / or lattice fringes along the tube axis, such as the Cu nanorod within a BNNT of Figure 6.8e, which stem from the presence of multiple crystal domains. Several lattice spacings corresponding to different zone axis are clearly displayed in Figure 6.9a for Cr@BNNT. Much like Au, Ag filling forms almost exclusively nanorods as in Figure 6.8h. The 30 nm long by 5 nm wide Ag rod in Figure 6.8h exhibits lattice fringes spaced at 0.230 nm which matches the distance between (111) planes in Ag. These metal@BNNT systems are potential objects for study of nanoscaled plasmonic (Ag), sensors (Pd)[303], thermometer (In)[304] and magnetism (Co)[305].

Many of the metals display faceted structures, such as the Co@BNNT of Figure 6.8c as well as Ag@BNNTs whose crystals form clear 120° and 140° angles respectively. The latter is 73 nm long, 9 nm in diameter, representative of the almost exclusive nanorod structure formed by Ag fillings. Other fillings were more unstructured, bound simply by the inner tube cavity, such as the Cr@BNNTs and Fe@BNNTs of Figure 6.8f and Figure 6.8g respectively. Some of the enclosed nanoparticles do not display clear lattice fringes, which may be due to weak scattering intensity or a structure resembling amorphous materials.

The observed contact angles of > 90° for some of the filling metals, such as those of Pt and Au in Figure 6.3 and Figure 6.4, suggest they wet the BN surface poorly. As evidenced in Figure 6.9b, indium metal nanoparticles conform more

readily to inner tube cavities, likely a result of its greater wettability due to its significantly lower surface tension (see discussion below). Comprehensive TEM studies reveal a large variance in the filling efficiencies for the various metals, from Pd@BNNTs with ~20 % of tubes observed with some metal filling to those of Cr@BNNTs with < 5 %.

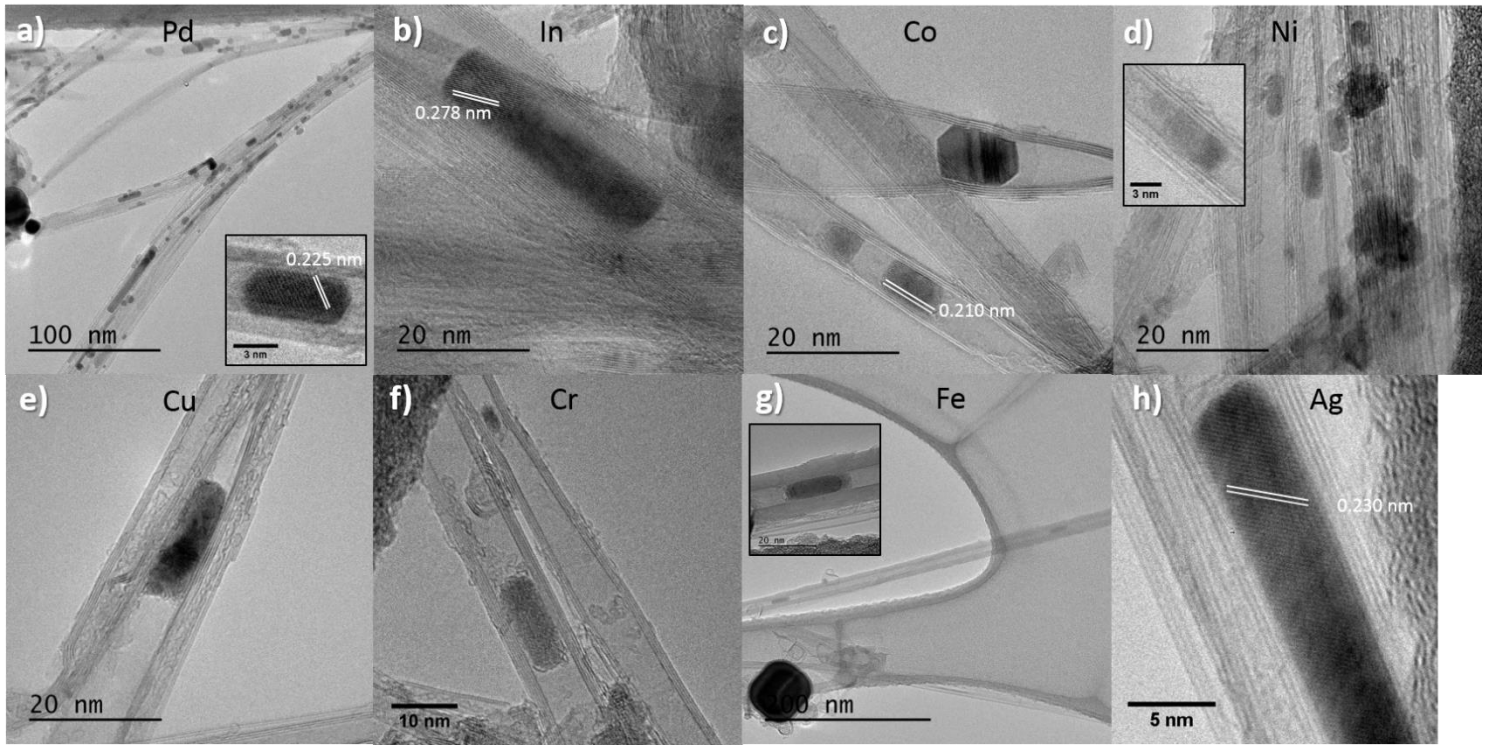


Figure 6.8: TEM images of various metal-filled BNNTs (M@BNNTs)including (a)Pd, (b) In, (c) Co, (d) Ni, (e) Cu, (f) Cr, (g) Fe, (h) Ag. The insets of (a), (d), and (g) are higher magnification images of encapsulated materials. Lattice spacings are denoted in relevant images.

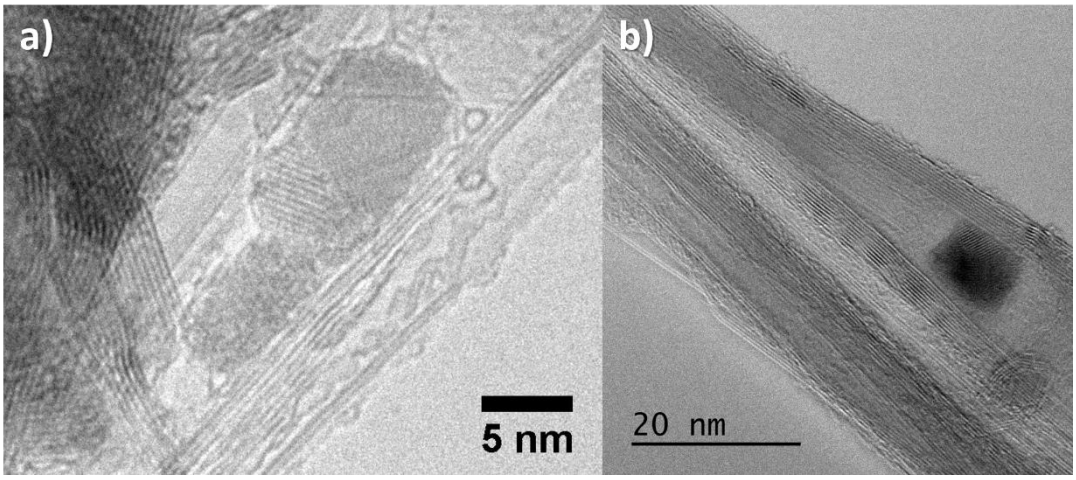


Figure 6.9: Cr@BNNTs and In@BNNTs. (a) Multiple crystal lattice domains are visible in Cr particles within BNNTs. (b) In nanoparticles conforming to the nonuniform inner cavity of a BNNT.

The effect of thermal treatment temperature and time on metal crystal morphology and size was also investigated. For several metals, thermal treatments were conducted at 600, 700, 800 and 900 °C for 1, 2 and 4 hours maintaining the same $H_2$ flow rate. We did not observe any striking variations in metal structures and dimensions for different treatment temperatures and run times. This is likely due to metals being sufficiently reduced as all treatment temperatures are well above the reduction temperatures of the metal salts, but still below the melting points of the pure metals (with the exception of In), disallowing further coalescence with increased treatment time. The metal structures and dimensions do, however, depend on the metals themselves as discussed above. Recall that Pt, for instance, tends to form particles, and long rods while Au tends to form very long nanowires.

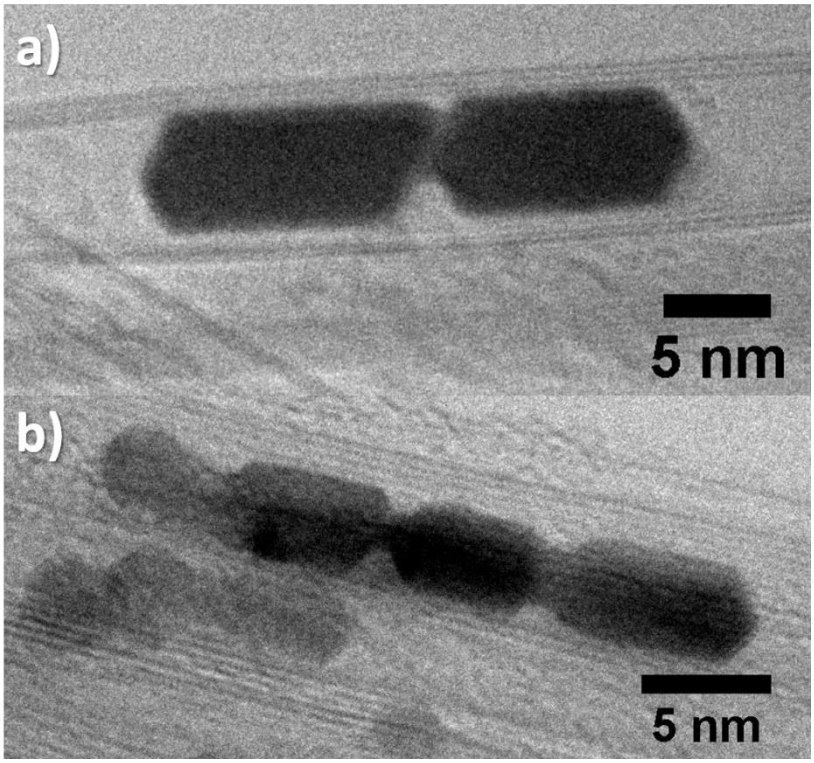


Figure 6.10: Nanosausages formed by sintering of Pt nanoparticles.

### 6.4.2.5 Nano-Sausages

Other interesting structures are observed for metals formed within the BNNTs. Occasionally we observed sausage-shaped structures formed by two nanoparticles or even arrays of particles (Figure 6.10) that are different particles/short rods connected at their ends, which we have dubbed "nano-sausages". These nano-sausages were most prominent with Pt rods which exhibited multiple neckings, conceivably the result of simultaneous growth of closely spaced Pt particles/rods during the reduction from proximate solutions. Another possibility for their formation is transport and subsequent end-to-end fusing of formerly separated particles, as suggested by Fan *et al.*[306–309]. The intriguing shapes of these marginally – coupled, segmented nano-sausages and their relationship to plasmonic and catalytic properties are subjects for further investigation.

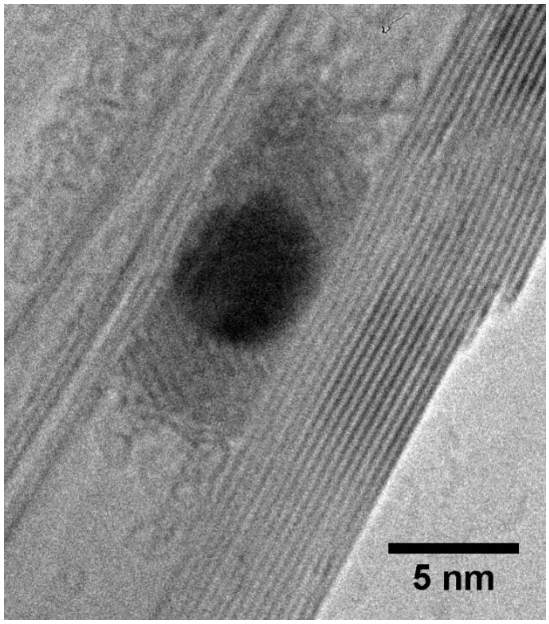


Figure 6.11: Core-shell filling of BNNTs. Nanosphere formed within BNNT exhibiting 2 distinct phases in a core-shell geometry, likely Fe – FeO.

### 6.4.3 Metal Oxide Filled BNNTs

Occasionally within the BNNTs we observe oxides of notably reactive metal particles, for example $In_2O_3$, as evidenced by the presence of O signals in EDS spectra. The oxidation occurs only at two ends of metal rods/particles (Figure 6.12). This indicates that a full conversion to an elemental metal has already taken place and that the oxidation of the nanowire ends is a result of interaction with ambient oxygen, or less likely from products of the salt reduction confined in the BNNT following the $H_2$ reduction step.

The Fe@BNNTs of Figure 6.11 reveal a structure with two distinct phases. A dark contrast particle is flanked on two sides by regions of lighter contrast which display lattice fringes. This core-shell geometry may be formed of Fe and FeO as these fillings were conducted using iron chloride metal-salt precursor.

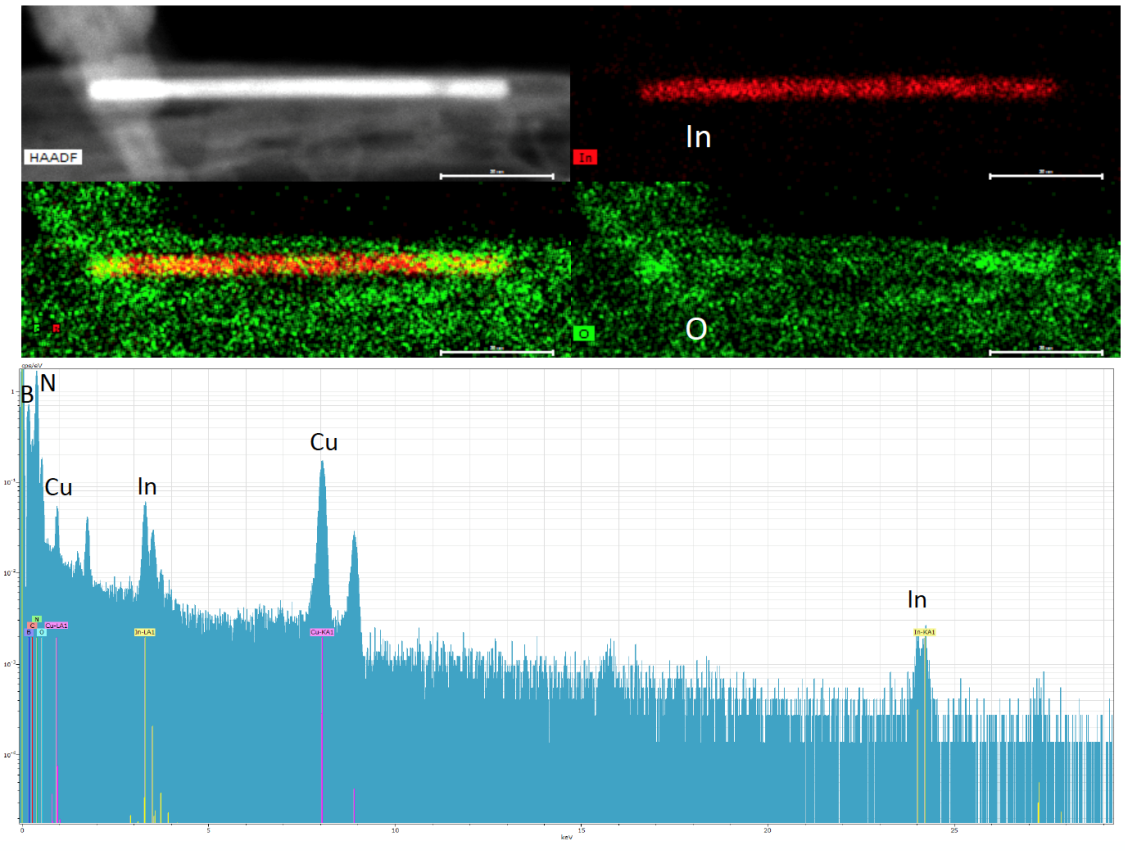


Figure 6.12: Position confirmation and elemental composition of In@BNNTs. HAADF image, EDS mappings and EELS spectrum of indium within BNNTs. Indium oxide is indicated at the two ends of In nanorods. Cu peaks in EELS spectrum originate from the copper TEM grid. (Courtesy of B. Shevitki)

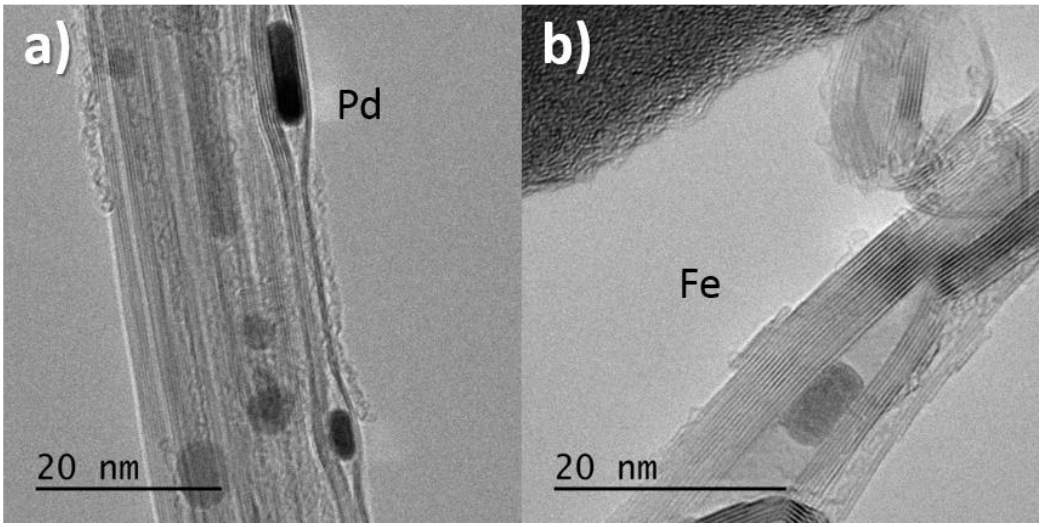


Figure 6.13: Metal filling material within collapsed nanotubes and in-between *h*-BN layers with (a) Pd and (b) Fe or FeO.

### 6.4.4 Inter BN-Layer Metal Filling

Nanoparticles and nanorods were also observed in otherwise collapsed BNNTs as well as in the regions between *h*-BN sheets. In Figure 6.13a, a Pd nanorod and nanosphere fill the inner cavity of a collapsed tube. A Fe (or FeO) nanoparticle in Figure 6.13b occupies a region in-between several layers of *h*-BN sheets with a small gap between it and the closest sheets. Intercalating *h*-BN sheets with a metal salt-solvent solution to then reduce into a metal particle is energetically very demanding, hinting at the collapsing of tubes or the enshrouding by *h*-BN sheets following nanoparticle formation. These inter *h*-BN layer fillings were observed in various samples for multiple metals.

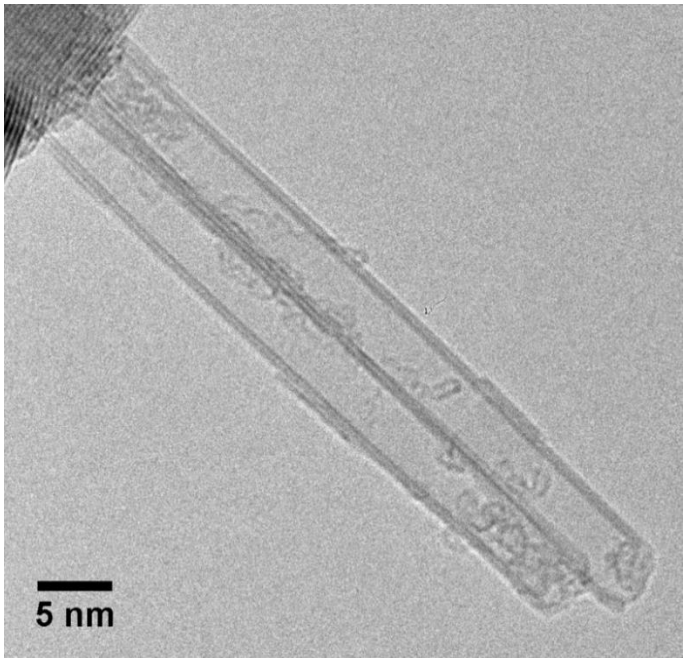


Figure 6.14: Chemically treated BNNTs revealing etched, but plugged tube ends.

### 6.4.5 *In-Situ* vs. 2-Step Filling

The *in-situ* filling method, wherein metals salts were dissolved in the nitric acid bath used to etch open nanotube ends, yielded a lower filing efficiency than when a two-step approach was implemented. Figure 6.15 is a representative illustration of Pt and Au encapsulating nanotubes filled in two steps (Figure 6.15a and c) and *in-situ* (Figure 6.15b and d), where the volume of tubes filled is clearly greater using the former method. This may be the result of amorphous residue left on or over the opened tip of a nanotube during the nitric acid etch causing it to be plugged up and hence preventing metal-salt solution from filling the inner cavity[300]. Two such BNNTs whose capped ends have been etched, but have tip ends plugged following chemical treatment are presented in Figure 6.14. When the tubes etched in nitric acid are removed and subsequently put in the metal-salt ethanol solution, they are sonicated. This may facilitate the removal of these plugged ends. Furthermore, ethanol's surface tension (22 mN/m) is lower than that of nitric acid (41 mN/m), and lower than the reported value of the surface tension of BNNTs (27 mN/M)[310]. Ethanol thus wets the nanotubes to a greater degree, resulting in an enhanced filling, as discussed below.

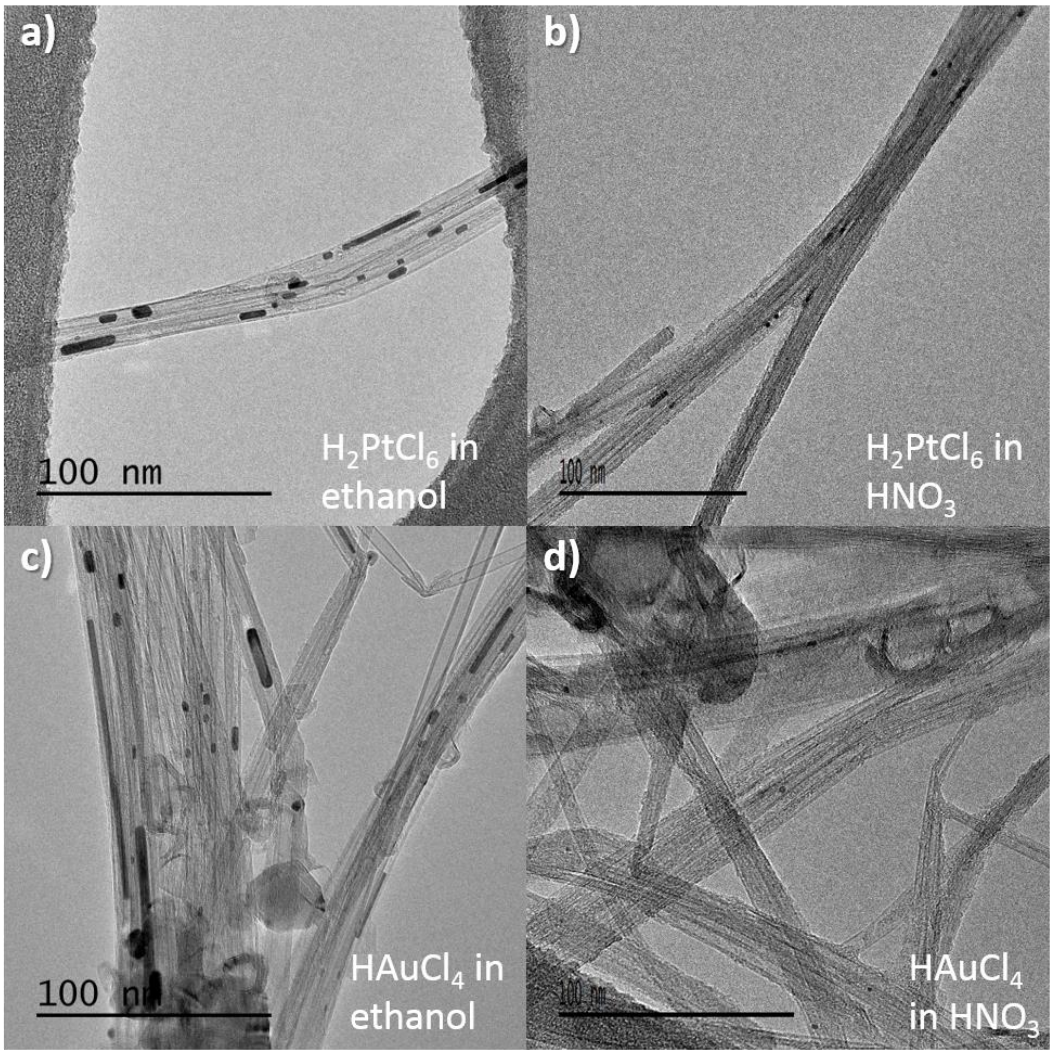


Figure 6.15: *In-situ* vs. 2-step filling. TEM images of BNNTs following filling procedure of (a) 2-step to produce Pt@BNNTs using $H_2PtCl_6$ dissolved in ethanol, (b) *in-situ* to produce Pt@BNNTs using $H_2PtCl_6$ dissolved in $HNO_3$, (c) 2-step to produce Au@BNNTs using $AuCl_4$ dissolved in ethanol, (b) *in-situ* to produce Au@BNNTs using $AuCl_4$ dissolved in $HNO_3$.

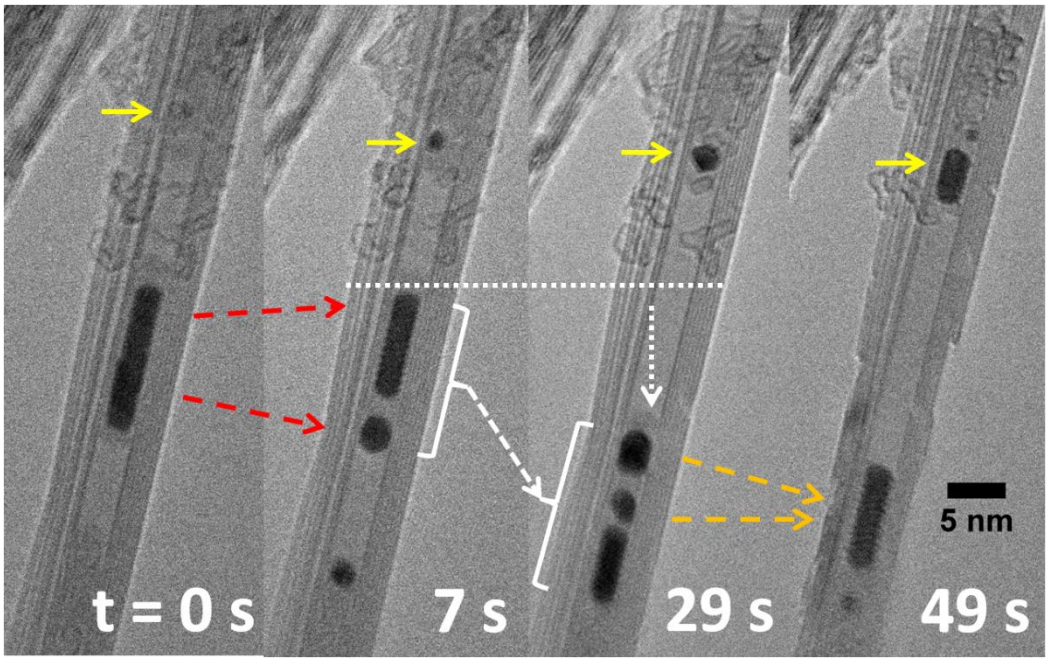


Figure 6.16: Nano-test tube environment revealing electron beam irradiation induced evolution of Au@BNNTs demonstrating nucleation and growth (solid yellow arrows near top of nanotube); splitting (dashed red arrows from t = 0s to 7s); agglomeration (dashed orange arrows from t = 29s to 49s); and splitting, agglomeration and translation (white brackets connected by a dashed arrow from t = 7s to t = 29s) of nanoscale Au particles.

## 6.4.6 Nanoscale Test Tube

In the series of TEM images of Figure 6.16, a BNNT serves as an inert nanoscale test tube within which chemical and mechanical interactions can be studied. The inside of the nanotube acts as a mold within which electron beam irradiation induced phenomena can be observed. Particle nucleation can be seen at t = 7s, indicated by solid yellow arrows, with nanorod growth occurring near the top of the nanotube from t = 0s to t = 49s. Restricted to the low dimensional environment, nanoparticles are seen to split apart (dashed red arrows from t = 0s to 7s) and agglomerate (dashed orange arrows from t = 29s to 49s). From t = 7s to 29s, the nanoparticles and nanorods near the center translate down the tube axis, indicated by the dotted white arrow. In the process of shifting, the nanoparticles exhibit splitting and agglomeration as well (white brackets connected by a dashed arrow from t = 7s to t = 29s).

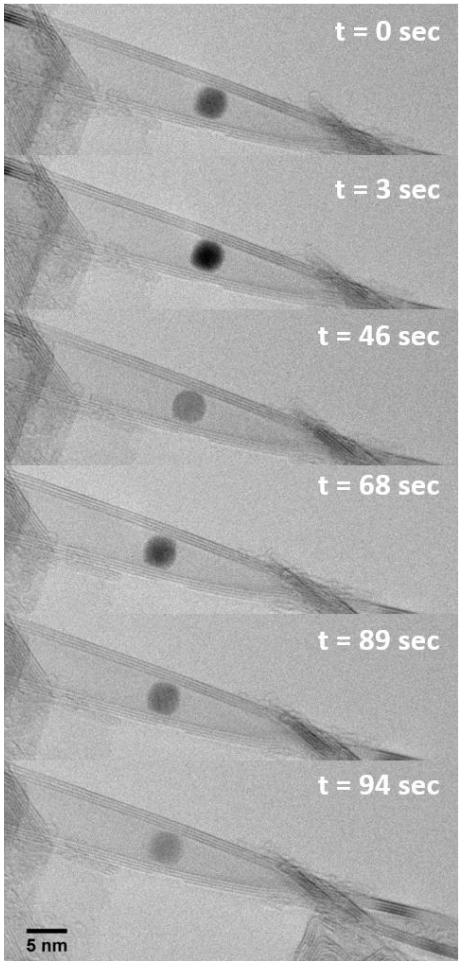


Figure 6.17: Rotating Fe nanosphere within a kinked BNNT.

This occurs without any damage to the inner tube wall, indicating a low degree of friction between filler material and the inner cavity. We note that the fluid-like motion of entrapped Au despite its high melting point of 1064 °C. This phenomenon is possible in light of the Gibbs-Thompson effect which predicts that particles with sizes below 100 nm will melt at considerably lower temperatures than those in the bulk phase[295]. The low degree of friction between the BN cavity and filler material is further evidenced in Figure 6.17 where a Fe nanosphere freely rotates within a tapered BNNT. The particle's contrast changes over time as its zone axis parallel to the electron beam varies. A slight fringe pattern attesting to the solid nature of the filling is also observable at t = 89 s that disappears upon continued rotation.

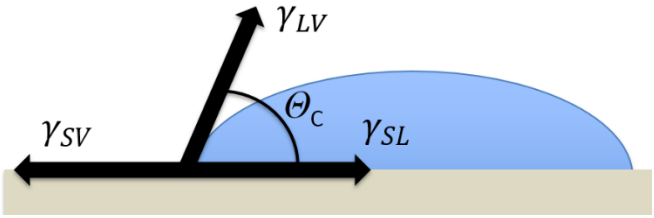


Figure 6.18: Wetting contact angle.

## 6.5 Capillary Filling of Nanotubes

The type and structure of encapsulated materials are determined by the interaction between the solid surface of the BNNT and the liquid state of the filling material. A solution which is able to sufficiently wet the graphitic BN tubular surface will be drawn into it by capillary force. Wetting occurs when the contact angle, $\Theta_C$, formed by the solid-liquid interface and the liquid-vapor interface measured from the side of the liquid, as denoted in Figure 6.18, is less than 90°. In the nonwetting regime when $\Theta_C > 90°$, pressure must be applied to cause the liquid to enter the tube. The contact angle is determined by the interfacial tensions via Young's equation:

$$\cos\Theta_C = \frac{\gamma_{SV} - \gamma_{SL}}{\gamma_{LV}} \tag{6-1}$$

where $\gamma_{SV}, \gamma_{SL}, \gamma_{LV}$ are the tensions at the solid-vapor, solid-liquid, and liquid-vapor interfaces respectively. This expression suggests that liquids with sufficiently low surface tension will wet the nanotube surface and should also be drawn into the inner cavity when then the tube ends are opened. Here we assume that the small dimensions of a nanotube cavity adhere to the Young-Laplace equation:

$$\Delta P_{LV} = 2\gamma_{LV}\cos\Theta_C{}^{-1} \tag{6-2}$$

where $\Delta P_{LV}$ is the pressure difference across the liquid-vapor interface and $r$ the radius of curvature of the meniscus. When $\Theta_C < 90°$, $\Delta P_{LV}$ will be positive and the liquid will be pulled into a capillary as there is an energy gain in the process.

In the case of CNTs, wetting occurred for elements with a surface tension less than 100 – 200 mN/m[267]. The surface tensions of BNNTs were measured to

comparable to those of their carbon counterparts[310]. A nanoscale version of the Wilhelmy method with a BNNT based force sensor has measured the surface tension of a BNNT to be 27 mN/m[310]. Those nanotubes with much larger diameters will have wetting properties approaching that of *h*-BN sheets. From Table 6-1, the surface tension γ of liquid metals explored in this study are significantly greater (570 – 1900 mN/m), suggesting the inability of the molten metals to physically flow into BNNTs without an applied pressure, i.e. via the physical method discussed above[311].

A wet chemistry approach overcomes these limits as metal-salt precursors dissolved in low surface tension solvents, such as ethanol (γ = 22 mN/m) or nitric acid (γ = 41 mN/m), can be introduced to the inside cavity of a BNNT by capillarity. The somewhat successful use of the latter solvent during *in-situ* filling attempts suggests a distribution in the cut off surface tension, likely due to the presence of a range of nanotube diameters[300]. Following the formation of metal nanoparticles and rods during a thermal anneal, TEM images of the filling material reveal a majority of convex ends of the metals inside the tubes. Such menisci are expected of nonwetting materials. Furthermore, sometimes a visible gap in-between a metal fillings and the innermost tube wall is observed, as in the Pt@BNNTs of Figure 6.3. The trapped particle or rod is equidistantly spaced from the BN structure by a distance of ~ 0.34 nm corresponding to the Van der Waals spacing of a graphitic tube. The levitated particle within the nanochannel is another manifestation of the poor wetting of BN to metals.

Table 6-1: Surface tension of metals in their liquid state.

| Element | γ (mN/m) |
|---|---|
| **Au** | 1211 |
| **Pt** | 1896 |
| **Ag** | 925 |
| **Pd** | 1467 |
| **Co** | 1779 |
| **Ni** | 1810 |
| **In** | 570 |
| **Cu** | 1352 |
| **Fe** | 1650 |
| **Cr** | 1582 |

This work is the first successful capillary filling of BNNTs using wet chemistry techniques. The small inner diameters (< 10 nm) and highly crystalline nature of BNNTs synthesized by the EPIC plasma method enhance their wettability and hence ability to draw in liquids via capillarity[300]. We find that BNNTs synthesized by other methods[190,312] cannot easily be filled with metals using wet-chemistry methods, likely due to their large inner diameters (> 50 – 80 nm) and often curvy or bamboo-like structures.[313] Ultimately, nanoparticles and nanorods form molded to the inside of the EPIC synthesized BNNT cavity with radial dimensions corresponding to the inner diameter of the nanotube. This is contrast to the smaller, segmented clusters of fillings obtained in some previous techniques[314].

### 6.5.1 Thermal decomposition of metal salts

Metal-salt precursors are dissolved in 3 ml of ethanol at a concentration of 0.5 mol/L. For *in-situ* filling attempts, metal salts were dissolved in a 4 ml nitric acid bath at a concentration of 0.5 mol/L. The metal-salt bath treated material was then vacuum filtered and placed in an alumina boat to be thermally annealed in a 1" quartz tube under a flow of 200 sccm $H_2$ at a set temperature in the range 600 – 800 °C, typically 600 °C, for 1 – 4 hrs., usually 1 hr. Encapsulated metal nitrates are likely decomposed to metal oxides and then activated to pure metal during thermal reduction as[315],

$$MO_x + xH_2 \rightarrow M + xH_2O(g) \qquad (6\text{-}3)$$

Table 6-2 lists the experimental reduction temperatures of tested metal nitrates. With the exception of In, the bulk melting points of the filler metals were never exceeded. EELS on some encapsulated nanoparticles of In, Co, Ni, Fe, Cr, and Cu reveal an oxygen peak, indicating incomplete thermal reduction to pure metals. Further reduction in the $H_2$ environment may convert these metal oxides into their elemental form, even within the confines of the nanotube cavity[268].

Table 6-2: Temperature of thermal decomposition / reduction for metal salt precursors.

| Element | T (°C) |
|---|---|
| **$HAuCl_4 \cdot xH_2O$** | 345[316] |
| **$H_2PtCl_6 \cdot 6H_2O$** | 510[317] |
| **$AgNO_3$** | 327[315] |
| **$PdCl_2$** | 679[318] |
| **$Co(NO_3)_2 \cdot 6H_2O$** | 241[315] |
| **$Ni(NO_3)_2 \cdot 6H_2O$** | 312[315] |
| **$In(NO_3)_2 \cdot xH_2O$** | 250[315] |
| **$Cu(NO_3)_2 \cdot xH_2O$** | 277[315] |
| **$Fe(NO_3)_3 \cdot 9H_2O$** | 192[315] |
| **$Cr(NO_3)_3 \cdot 9H_2O$** | 260[319] |

## 6.5.2 Size-Dependence

Size dependent filling behavior for different metals may also occur. For example, BN cavities filled by Ag are notably larger (~ 4 – 9 nm) than those containing Co fillings (~ 2 – 6 nm) (Figure 6.19). Similar size-dependence has been observed for CNTs as well, where a theshold diameter is proposed for cappillary filling of different materials based on a polarizability description of the wetting conditions.[300] Our measurements for diameter dependence of filled BNNTs is presented in Figure 6.19 for selected encapsulated metals.

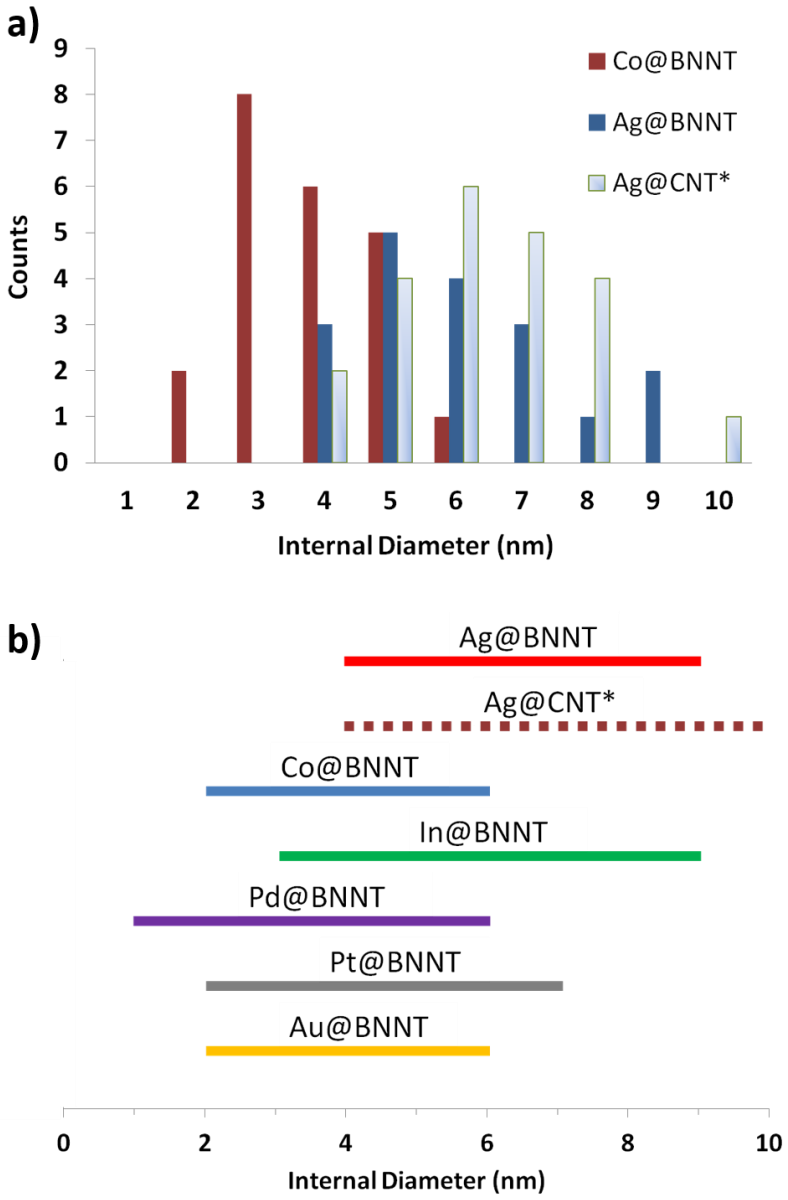


Figure 6.19: Diameter dependence of filled BNNTs. (a) Histogram of the diameter dependence of the internal cavity of BNNTs encapsulating Co and Ag. (b) Typical ranges of internal cavity diameters of BNNTs containing various filling metals. For comparison the distribution and diameter ranges for Ag within CNTs (denoted Ag@CNT*) is taken from ref. [300].

Table 6-3: Calculated maximum filling factor of an individual nanotube

| Metals | Maximum filling factor (volume %) |
|---|---|
| **Pt** | 5.4 |
| **Au** | 16 |
| **Pd** | 20 |
| **Ag** | 26 |
| **In** | 6.7 |
| **Co** | 9.0 |

### 6.5.3 Filling Efficiency

The incomplete filling of the nanotubes can in part be understood when the conditions for capillarity are considered. The capillary forces drawing a liquid into the tube cavity are strongest when the inside cavity is initially empty. Nanotubes filled with an air or gas will oppose the entry of liquids, even if they have low surface tensions. Liquids can still be drawn into the inner tube cavity, but the process will be much slower and the gas must have a route to escape, such as via a tube end or by being dissolved in the liquid. The BNNTs filled *in-situ* presumably contain nitrogen gas within inner tube cavities as a result of the synthesis process. Material transferred to a metal-salt ethanol bath is most likely filled with nitric acid following the reflux step. Sonicating or leaving nanotubes in the filling solvent for an extended period of time may facilitate a higher filling yield.

Discrete nanorods or arrays of nanoparticles are formed throughout a tube cavity during thermal reduction as the contained metal-salt precursor's volume reduces to form the denser metal fillings. Careful TEM investigation reveal that the metal nanoparticles have a propensity to form randomly along the tube and can be found near the middle as well as towards the openings of the tubes. Calculations of the reduction in volume from precursor to pure elemental metal indicate filling efficiencies obtained are close to their expected maximum value for some fillers (Table 6-3). For instance, some individual BNNTs were filled up to 10 volume % with Au, compared to their calculated maximum filling factor of 15 volume %. The very high aspect ratio and tendency of the BNNTs to cluster into bundles makes precise filling efficiencies difficult to determine. The tube lengths may also influence the filling factor of individual tubes. Theoretical maximum filling yields utilizing wet-chemistry techniques have also been reported in the case of CNTs. During the

solution-based filling procedure described above, solvent molecules will be encapsulated together with the metal salt precursors within BNNTs. Non-metal filled regions will be left behind following thermal treatment due to the removal of these solvents and other resultant products formed during the thermal reduction of the metal-salt precursor.[320] The loading procedure may be repeated to enhance filling yields. It should also be possible to separate filled tubes from empty ones using techniques which depend on density, such via centrifugation.

## 6.6 Advantages and Prospects

In this chapter, we have demonstrated a simple, but effective route to encapsulate various metal nanoparticles and nanorods (Pt, Au, Pd, Ag, In, Co, Ni, Fe, Cr, Cu) within BNNTs by a post-synthesis wet–chemistry method for the first time. TEM, STEM, EDS and EELS data confirm the successful filling of metals with regular crystalline structures and definite atomic boundaries within the nanotube shells. The previous few methods have demonstrated some degree of success in the filling of BNNTs with only a limited number of materials, in particular only those which could be used as catalysts for the growth of BNNTs (Fe, Co) or fillers with low vaporizing temperature (KCl). The approach presented here is versatile and applicable for a wide range of materials with various vaporizing temperatures. Moreover, the previously reported methods have very limited filling yields (less than 30 % versus 60 % as in our report). They are also more expensive and time consuming, for instance required the tedious creation of ampoules. Furthermore, they are inherently small batch processes, producing only a small amount of final sample (few mg) at a time. This makes all previous techniques not suitable for large scale application, such would be required for incorporation of these filled BNNTs for thermal management and composites. Our solution – based filling approach together with our large scale method of producing BNNTs using the new EPIC synthesis system creates an opportunity to make gram – scale quantities of pure metal-filled BNNTs at low costs. For application such as electromagnetic shielding composites, large amounts of materials would be required with high mechanical strength and thermal resistance yet conducting to dissipate the electromagnetic radiation. Metal-filled BNNTs prepared by the current method perfectly match these requirements. Moreover, the large quantity of metal filled BNNTs also finds promising applications in catalysis (Pt@BNNTs), hydrogen storage (Pd@BNNTs), plasmonics (Au@BNNTs), thermal management (Ag@BNNTs), and memory devices (Co@BNNTs).

Furthermore, the previous methods require high temperatures (600 – 1000 °C), making them incompatible for the filling of chemical and bio-molecules. On the other hand, our method is based on the solution filling conducted at room

temperature, which is suitable for biochemical molecules such as water, proteins, DNA. The filling of the inner cavity of BNNTs with biochemical molecules could be the first step to open up a new field of nanopore science based on BNNTs.

BNNTs not only spatially confine the metal crystals, but also serve as an electrically and chemically inert shell to protect and enhance the stability of metal nanostructures. Therefore, these metal@BNNTs create an opportunity to study the intrinsic optical, electrical, magnetic, and catalytic properties of nanoscaled metals. The filling of BNNTs with magnetic materials, such as Co, Ni, and Fe, could be particularly useful in magnetic storage and nanoelectronic devices. Finally, the reported filling method can be applied for the study of electron beam induced chemical reactions and physical dynamics in confined spaces in which BNNTs can act as a truly nanoscale test tubes.

# Bibliography


1. Iijima, S. Helical microtubules of graphitic carbon. *Nature* **354,** 56–58 (1991).
2. Guo, T. *et al.* Self-Assembly of Tubular Fullerenes. *J. Phys. Chem. Lett.* **99,** 10694–10697 (1995).
3. Peigney, A., Laurent, C., Dobigeon, F. & Rousset, A. Carbon nanotubes grown in situ by a novel catalytic method. *J. Mater. Res.* **12,** 613–615 (1997).
4. Dai, H. *et al.* Single-wall nanotubes produced by metal-catalyzed disproportionation of carbon monoxide. *Chem. Phys. Lett.* **260,** 471–475 (1996).
5. Medlin, D. L., Friedmann, T. A., Mirkarimi, P. B., Mills, M. J. & McCarty, K. F. Evidence for rhombohedral boron nitride in cubic boron nitride films grown by ion-assisted deposition. *Phys. Rev. B* **50,** 7884–7887 (1994).
6. Lee, R. *et al.* Catalyst-free synthesis of boron nitride single-wall nanotubes with a preferred zig-zag configuration. *Phys. Rev. B* **64,** 6–9 (2001).
7. Rubio, A., Corkill, J. L. & Cohen, M. L. Theory of graphitic boron nitride nanotubes. *Phys. Rev. B* **49,** 5081–5084 (1994).
8. Miyamoto, Y., Rubio, A., Cohen, M. L. & Louie, S. G. Chiral tubules of hexagonal BC2N. *Phys. Rev. B* **50,** 4976–4979 (1994).
9. Golberg, D., Bando, Y. & Dorozhkin, P. Synthesis, Analysis, and Electrical Property Measurements of Compound Nanotubes in the B-C-N Ceramic System. *Mrs Bull.* **88,** 38–42 (2004).
10. Tang, C. *et al.* Fluorination and electrical conductivity of BN nanotubes. *J. Am. Chem. Soc.* **127,** 6552–6553 (2005).
11. Kim, Y. H., Chang, K. J. & Louie, S. G. Electronic structure of radially deformed BN and BC nanotubes. *Phys. Rev. B* **63,** 205408 (2001).
12. Khoo, K. H., Mazzoni, M. S. C. & Louie, S. G. Tuning the electronic properties of boron nitride nanotubes with transverse electric fields: A giant dc Stark effect. *Phys. Rev. B* **69,** 201401 (2004).
13. Ishigami, M., Sau, J. D., Aloni, S., Cohen, M. L. & Zettl, A. Observation of the Giant Stark Effect in Boron-Nitride Nanotubes. *Phys. Rev. Lett.* **94,** 056804 (2005).

14. Nakhmanson, S. M., Calzolari, A., Meunier, V., Bernholc, J. & Buongiorno Nardelli, M. Spontaneous polarization and piezoelectricity in boron nitride nanotubes. *Phys. Rev. B* **67,** 235406 (2003).
15. Bai, X., Golberg, D., Bando, Y., Zhi, C. & Tang, C. Deformation Driven Electrical Transport of Individual Boron Nitride Nanotubes. *Nano Lett.* **7,** 632–637 (2007).
16. Cumings, J. & Zettl, A. Field emission and current-voltage properties of boron nitride nanotubes. *Solid State Commun.* **129,** 661–664 (2004).
17. Wu, J. *et al.* Raman Spectroscopy and Time-Resolved Photoluminescence of BN and B x C y N z Nanotubes. *Nano Lett.* **4,** 647–650 (2004).
18. Lauret, J. S. *et al.* Optical transitions in single-wall boron nitride nanotubes. *Phys. Rev. Lett.* **94,** 4–7 (2005).
19. Jaffrennou, P. *et al.* Optical properties of multiwall boron nitride nanotubes. *Phys. Status Solidi* **244,** 4147–4151 (2007).
20. Lebedkin, S. *et al.* FTIR-luminescence mapping of dispersed single-walled carbon nanotubes. *New J. Phys.* **5,** 1–11 (2003).
21. Harutyunyan, H. *et al.* Defect-Induced Photoluminescence from Dark Excitonic States in Individual Single-Walled Carbon Nanotubes. *Nano Lett.* **9,** 2010–2014 (2009).
22. Murakami, Y. *et al.* Photoluminescence sidebands of carbon nanotubes below the bright singlet excitonic levels. *Phys. Rev. B* **79,** 195407 (2009).
23. Dresselhaus, M. S. & Eklund, P. C. Phonons in carbon nanotubes. *Adv. Phys.* **49,** 705–814 (2000).
24. Hernández, E., Goze, C., Bernier, P. & Rubio, A. Elastic properties of C and BxCyNz composite nanotubes. *Phys. Rev. Lett.* **80,** 4502–4505 (1998).
25. Bellucci, S. Carbon nanotubes: physics and applications. *Phys. Status Solidi* **2,** 34–47 (2005).
26. Chopra, N. G. & Zettl, A. Measurement of the elastic modulus of a multi-wall boron nitride nanotube. *Solid State Commun.* **105,** 297–300 (1998).
27. Bai, X. *et al.* Direct Force Measurements and Kinking under Elastic Deformation of Individual Multiwalled Boron Nitride Nanotubes. *Nano Lett.* **7,** 2146–2151 (2007).
28. Chen, Y., Zou, J., Campbell, S. J. & Caer, G. L. Boron nitride nanotubes: Pronounced resistance to oxidation. *Appl. Phys. Lett.* **84,** 2430–2432 (2004).
29. Smith, M. W. *et al.* Very long single- and few-walled boron nitride nanotubes via the pressurized vapor/condenser method. *Nanotechnology* **20,** 505604 (2009).
30. Kim, K. S. *et al.* Hydrogen-catalyzed, pilot-scale production of small-diameter boron nitride nanotubes and their macroscopic assemblies. *ACS Nano* **8,** 6211–

6220 (2014).
31. Berber, S., Kwon, Y. & Tomanek, D. Unusually high thermal conductivity of carbon nanotubes. *Phys. Rev. Lett.* **84,** 4613–4616 (2000).
32. Pop, E., Mann, D., Wang, Q., Goodson, K. & Dai, H. Thermal Conductance of an Individual Single-Wall Carbon Nanotube above Room Temperature. *Nano Lett.* **6,** 96–100 (2006).
33. Xiao, Y. *et al.* Specific heat and quantized thermal conductance of single-walled boron nitride nanotubes. *Phys. Rev. B* **69,** 205415 (2004).
34. Chang, C. W., Okawa, D., Garcia, H., Majumdar, A. & Zettl, A. Breakdown of Fourier's Law in Nanotube Thermal Conductors. *Phys. Rev. Lett.* **101,** 075903 (2008).
35. Savić, I., Stewart, D. a. & Mingo, N. Thermal conduction mechanisms in boron nitride nanotubes: Few-shell versus all-shell conduction. *Phys. Rev. B - Condens. Matter Mater. Phys.* **78,** 1–5 (2008).
36. Will, G. & Ploog, K. Crystal structure of I-tetragonal boron. *Nature* **251,** 406–408 (1974).
37. Teter, D. M. & Hemley, R. J. Low-Compressibility Carbon Nitrides. *Science* **271,** 53–55 (1996).
38. Li, D. *et al.* Structure and hardness studies of CNx/TiN nanocomposite coatings. *Appl. Phys. Lett.* **68,** 1211 (1996).
39. Mu, T. *et al.* Synthesis and characterization of polyether structure carbon nitride. *J. Mater. Res.* **19,** 1736–1741 (2004).
40. Li, H. Y., Shi, Y. C. & Feng, P. X. Growth and control of microscale to nanoscale carbon nitride particles. *Appl. Phys. Lett.* **89,** 142901 (2006).
41. de Heer, W. a., Chatelain, A. & Ugarte, D. A Carbon Nanotube Field-Emission Electron Source. *Science* **270,** 1179–1180 (1995).
42. Collins, P. G. & Zettl, A. A simple and robust electron beam source from carbon nanotubes. *Appl. Phys. Lett.* **69,** 1969 (1996).
43. Fursey, G. *Field Emission in Vacuum Microelectronics*. (Kluwer Academic/Plenum Publishers, 2005).
44. Fowler, R. H. & Nordheim, L. Electron Emission in Intense Electric Fields. *Proc. R. Soc. London Ser. A.* **119,** 173–181 (1928).
45. Wang, X. Q., Wang, M., He, P. M., Xu, Y. B. & Li, Z. H. Model calculation for the field enhancement factor of carbon nanotube. *J. Appl. Phys.* **96,** 6752–6755 (2004).
46. Chen, X. Q., Saito, T., Yamada, H. & Matsushige, K. Aligning single-wall carbon nanotubes with an alternating-current electric field. *Appl. Phys. Lett.* **78,** 3714 (2001).
47. Fennimore, A. Experimental Studies of the Nanomechanical Properties of

Nanotubes. (University of California, Berkeley, 2005).
48. Gadzuk, J. W. & Plummer, E. W. Field emission energy distribution (FEED). *Rev. Mod. Phys.* **45,** 487–548 (1973).
49. Shiraishi, M. & Ata, M. Work function of carbon nanotubes. *Carbon N. Y.* **39,** 1913–1917 (2001).
50. Bonard, J., Salvetat, J., Stöckli, T. & Forr, L. Field emission from carbon nanotubes : perspectives for applications. *Appl. Phys. A* **69,** 245–254 (1999).
51. Rinzler, A. G. *et al.* Unraveling nanotubes: field emission from an atomic wire. *Science* **269,** 1550–1553 (1995).
52. Ibe, J. P. *et al.* On the electrochemical etching of tips for scanning tunneling microscopy. *J. Vac. Sci. Technol. A* **8,** 3570 (1990).
53. Albrektsen, O. Reliable tip preparation for high-resolution scanning tunneling microscopy. *J. Vac. Sci. Technol. B* **12,** 3187 (1994).
54. Cricenti, A., Paparazzo, E., Scarselli, M. A., Moretto, L. & Selci, S. Preparation and characterization of tungsten tips for scanning tunneling microscopy. *Rev. Sci. Instrum.* **65,** 1558 (1994).
55. Fotino, M. Tip sharpening by normal and reverse electrochemical etching. *Rev. Sci. Instrum.* **64,** 159–167 (1993).
56. Meyer, J. A., Stranick, S. J., Wang, J. B. & Weiss, P. S. Field emission current-voltage curves as a diagnostic for scanning tunneling microscope tips. *Ultramicroscopy* **42-44,** 1538–1541 (1992).
57. Loeb, G. E., Bak, M. J., Salcman, M. & Schmidt, E. M. Parylene as a chronically stable, reproducible microelectrode insulator. *IEEE Trans. Biomed. Eng.* **24,** 121–128 (1977).
58. Verhagen, J. V., Gabbott, P. L. & Rolls, E. T. A simple method for reconditioning epoxy-coated microelectrodes for extracellular single neuron recording. *J. Neurosci. Methods* **123,** 215–217 (2003).
59. Begtrup, G. E. Silicon Nitride Membranes for Electrical and Thermal Transport Studies of Nanotubes. (University of California, Berkeley, 2008).
60. Oldham, D. J., Bleay, J. A. & Blackburn, D. A. Electromigration and Deformation in Pure Gold. *Acta Metall.* **25,** 1345–1354 (1977).
61. Jensen, K., Weldon, J., Garcia, H. & Zettl, A. Nanotube radio. *Nano Lett.* **7,** 3508–3511 (2007).
62. Jensen, K., Kim, K. & Zettl, A. An atomic-resolution nanomechanical mass sensor. *Nat. Nanotechnol.* **3,** 533–537 (2008).
63. Weldon, J. A., Alemán, B., Sussman, A., Gannett, W. & Zettl, A. Sustained mechanical self-oscillations in carbon nanotubes. *Nano Lett.* **10,** 1728–1733 (2010).
64. Alemán, B. J., Sussman, A., Mickelson, W. & Zettl, A. A Carbon Nanotube-based

NEMS Parametric Amplifier for Enhanced Radio Wave Detection and Electronic Signal Amplification. *J. Phys. Conf. Ser.* **302,** 012001 (2011).
65. Paudler, W. *Nuclear Magnetic Resonance*. (Wiley, 1987).
66. Hahn, E. L. Nuclear induction due to free larmor precession. *Phys. Rev.* **77,** 297–298 (1950).
67. Grannell, P. K., Orchard, M. J., Mansfield, P., Garroway, A. N. & Stalker, D. C. A FET analogue switch for pulsed NMR receivers. *J. Phys. E.* **6,** 1202–1204 (1973).
68. Griffin, D. D., Kleinberg, R. L. & Fukuhara, M. Low-frequency NMR spectrometer. *Meas. Sci. Technol.* **4,** 968–975 (1993).
69. Sidles, J. A. Noninductive detection of single-proton magnetic resonance. *Appl. Phys. Lett.* **58,** 2854–2856 (1991).
70. Rugar, D., Budakian, R., Mamin, H. J. & Chui, B. W. Single spin detection by magnetic resonance force microscopy. *Nature* **430,** 329–332 (2004).
71. Degen, C. L., Poggio, M., Mamin, H. J., Rettner, C. T. & Rugar, D. Nanoscale magnetic resonance imaging. *Proc. Natl. Acad. Sci. U. S. A.* **106,** 1313–1317 (2009).
72. Nichol, J., Hemesath, E., Lauhon, L. & Budakian, R. Nanomechanical detection of nuclear magnetic resonance using a silicon nanowire oscillator. *Phys. Rev. B* **85,** 1–6 (2012).
73. Prance, R. J. & Aydin, A. Acquisition of a nuclear magnetic resonance signal using an electric field detection technique. *Appl. Phys. Lett.* **91,** 2–4 (2007).
74. Purcell, S. T., Vincent, P., Journet, C. & Binh, V. T. Tuning of Nanotube Mechanical Resonances by Electric Field Pulling. *Phys. Rev. Lett.* **89,** 276103 (2002).
75. Bonard, J. M., Klinke, C., Dean, K. A. & Coll, B. F. Degradation and failure of carbon nanotube field emitters. *Phys. Rev. B* **67,** 115406 (2003).
76. Cleland, A. N. & Roukes, M. L. Noise processes in nanomechanical resonators. *J. Appl. Phys.* **92,** 2758–2769 (2002).
77. Meirovitch, L. *Elements of Vibration Analysis*. (McGraw-Hill, 1986).
78. Cleland, A. N. *Foundations of Nanomechanics: from Solid-State Theory to Device Applications*. (Springer, 2003).
79. Cleland, A. N. & Roukes, M. L. Fabrication of high frequency nanometer scale mechanical resonators from bulk Si crystals. *Appl. Phys. Lett.* **69,** 2653–2655 (1996).
80. Jensen, K., Peng, H. B. & Zettl, A. Limits of nanomechanical resonators. *Proc. 2006 Int. Conf. Nanosci. Nanotechnology, ICONN* 68–71 (2006).
81. Bruland, K. J., Garbini, J. L., Dougherty, W. M. & Sidles, J. A. Optimal control of force microscope cantilevers. I. Controller design. *J. Appl. Phys.* **80,** 1951–1958 (1996).

82. K.S. Novoselov, A.K. Geim, S.V. Morozov, D. Jiang, Y. Zhang, S.V. Dubonos, I.V.Grigorieva, A. A. F. Electric Field Effect in Atomically Thin Carbon Films. *Science* **306,** 666–669 (2004).
83. Geim, A. K. & Grigorieva, I. V. Van der Waals heterostructures. *Nature* **499,** 419–25 (2013).
84. Lee, C., Wei, X., Kysar, J. W. & Hone, J. Measurement of the Elastic Properties and Intrinsic Strength of Monolayer Graphene. *Science* **321,** 385–388 (2008).
85. Yuk, J. M. *et al.* Graphene veils and sandwiches. *Nano Lett.* **11,** 3290–3294 (2011).
86. Sharma, B. K. & Ahn, J. H. Graphene based field effect transistors: Efforts made towards flexible electronics. *Solid. State. Electron.* **89,** 177–188 (2013).
87. Aboutalebi, S. H. *et al.* High-performance multifunctional Graphene yarns: Toward wearable all-carbon energy storage textiles. *ACS Nano* **8,** 2456–2466 (2014).
88. Wallace, P. R. The band theory of graphite. *Phys. Rev.* **71,** 622–634 (1947).
89. Bolotin, K. I. *et al.* Ultrahigh electron mobility in suspended graphene. *Solid State Commun.* **146,** 351–355 (2008).
90. Castro Neto, A. H. . *et al.* The electronic properties of graphene. *Rev. Mod. Phys.* **81,** 109–162 (2009).
91. Das Sarma, S., Adam, S., Hwang, E. H. & Rossi, E. Electronic transport in two-dimensional graphene. *Rev. Mod. Phys.* **83,** 407–470 (2011).
92. Weiss, N. O. *et al.* Graphene: An Emerging Electronic Material. *Adv. Mater.* **24,** 5782–5825 (2012).
93. Balandin, A. a. *et al.* Superior thermal conductivity of single-layer graphene. *Nano Lett.* **8,** 902–907 (2008).
94. Balandin, A. Thermal properties of graphene and nanostructured carbon materials. *Nat. Mater.* **10,** 569–581 (2011).
95. Pop, E., Varshney, V. & Roy, A. K. A. K. Thermal properties of graphene: Fundamentals and applications. *MRS Bull.* **37,** 1273–1281 (2012).
96. Stankovich, S. *et al.* Graphene-based composite materials. *Nature* **442,** 282–286 (2006).
97. Hernandez, Y., Lotya, M., Rickard, D., Bergin, S. D. & Coleman, J. N. Measurement of multicomponent solubility parameters for graphene facilitates solvent discovery. *Langmuir* **26,** 3208–3213 (2010).
98. Berger, C. *et al.* Electronic Confinement and Coherence in Patterned Epitaxial Graphene. *Science* **312,** 1191–1196 (2006).
99. Emtsev, K. V *et al.* Towards wafer-size graphene layers by atmospheric pressure graphitization of silicon carbide. *Nat. Mater.* **8,** 203–207 (2009).
100. Bogomolov, V. N. Liquids in ultrathin channels (Filament and cluster crystals).

*Sov. Phys. Uspekhi* **21,** 77–83 (2007).

101. Tung, V. C., Allen, M. J., Yang, Y. & Kaner, R. B. High-throughput solution processing of large-scale graphene. *Nat. Nanotechnol.* **4,** 25–29 (2009).
102. Park, S. & Ruoff, R. S. Chemical methods for the production of graphenes. *Nat. Nanotechnol.* **4,** 217–224 (2009).
103. Sutter, P. W., Flege, J. I. & Sutter, E. a. Epitaxial graphene on ruthenium. *Nat. Mater.* **7,** 406–411 (2008).
104. Seah, C. M., Chai, S. P. & Mohamed, A. R. Mechanisms of graphene growth by chemical vapour deposition on transition metals. *Carbon N. Y.* **70,** 1–21 (2014).
105. Sutter, P., Sadowski, J. T. & Sutter, E. Graphene on Pt(111): Growth and substrate interaction. *Phys. Rev. B - Condens. Matter Mater. Phys.* **80,** 1–10 (2009).
106. Murata, Y. *et al.* Orientation-dependent work function of graphene on Pd(111). *Appl. Phys. Lett.* **97,** 143114 (2010).
107. Orofeo, C. M., Ago, H., Hu, B. & Tsuji, M. Synthesis of large area, homogeneous, single layer graphene films by annealing amorphous carbon on Co and Ni. *Nano Res.* **4,** 531–540 (2011).
108. Ago, H. *et al.* Epitaxial chemical vapor deposition growth of single-layer graphene over cobalt film crystallized on sapphire. *ACS Nano* **4,** 7407–7414 (2010).
109. Yu, Q. *et al.* Graphene segregated on Ni surfaces and transferred to insulators. *Appl. Phys. Lett.* **93,** 113103 (2008).
110. Reina, A. *et al.* Growth of large-area single- and Bi-layer graphene by controlled carbon precipitation on polycrystalline Ni surfaces. *Nano Res.* **2,** 509–516 (2009).
111. Lee, Y. *et al.* supporting infro Wafer-Scale Synthesis and Transfer of graphene films. *Nano Lett.* **10,** 490–3 (2010).
112. Mattevi, C., Kim, H. & Chhowalla, M. A review of chemical vapour deposition of graphene on copper. *J. Mater. Chem.* **21,** 3324 (2011).
113. Bhaviripudi, S., Jia, X., Dresselhaus, M. S. & Kong, J. Role of kinetic factors in chemical vapor deposition synthesis of uniform large area graphene using copper catalyst. *Nano Lett.* **10,** 4128–4133 (2010).
114. Massalski, T. B., Okamoto, H., Subramanian, P. R. & Kacprzak, L. *ASM Handbook: Alloy Phase Diagrams*. (ASM International, 2002).
115. Kim, K. S. *et al.* Large-scale pattern growth of graphene films for stretchable transparent electrodes. *Nature* **457,** 706–710 (2009).
116. Obraztsov, A. N., Obraztsova, E. A., Tyurnina, A. V. & Zolotukhin, A. A. Chemical vapor deposition of thin graphite films of nanometer thickness. *Carbon N. Y.* **45,** 2017–2021 (2007).

117. McLellan, R. B. The Solubility of Carbon in Solid Gold, Copper, and Silver. *Scr. Metall.* **3,** 389–391 (1969).
118. López, G. A. & Mittemeijer, E. J. The solubility of C in solid Cu. *Scr. Mater.* **51,** 1–5 (2004).
119. Li, X., Cai, W., Colombo, L. & Ruoff, R. S. Evolution of graphene growth on Ni and Cu by carbon isotope labeling. *Nano Lett.* **9,** 4268–4272 (2009).
120. Wofford, J. M., Nie, S., McCarty, K. F., Bartelt, N. C. & Dubon, O. D. Graphene islands on Cu foils: The interplay between shape, orientation, and defects. *Nano Lett.* **10,** 4890–4896 (2010).
121. Earnshaw, A. & Harrington, T. J. *The Chemistry of the Transition Elements*. (Oxford University Press, 1972).
122. Bae, S. *et al.* Roll-to-roll production of 30-inch graphene films for transparent electrodes. *Nat. Nanotechnol.* **5,** 574–578 (2010).
123. Li, X. *et al.* Large-area synthesis of high-quality and uniform graphene films on copper foils. *Science* **324,** 1312–1314 (2009).
124. Lee, Y. *et al.* Wafer-Scale Synthesis and Transfer of Graphene Films. *Nano Lett.* **10,** 490–493 (2010).
125. Ismach, A. *et al.* Direct Chemical Vapor Deposition of Graphene on Dielectric Surfaces. *Nano Lett.* **10,** 1542–1548 (2010).
126. Wu, Y. a *et al.* Large single crystals of graphene on melted copper using chemical vapor deposition. *ACS Nano* **6,** 5010–5017 (2012).
127. Gao, L., Guest, J. R. & Guisinger, N. P. Epitaxial Graphene on Cu ( 111 ). *Nano Lett.* **10,** 3512–3516 (2010).
128. Rasool, H. I. *et al.* Atomic-scale characterization of graphene grown on copper (100) Single Crystals. *J. Am. Chem. Soc.* **133,** 12536–12543 (2011).
129. Zhao, L. *et al.* Influence of copper crystal surface on the CVD growth of large area monolayer graphene. *Solid State Commun.* **151,** 509–513 (2011).
130. Hirsch, J. & Lücke, K. Overview no. 76. *Acta Metall.* **36,** 2863–2882 (1988).
131. Song, H. S. *et al.* Origin of the relatively low transport mobility of graphene grown through chemical vapor deposition. *Sci. Rep.* **2,** 1–6 (2012).
132. Rasool, H. I., Ophus, C., Klug, W. S., Zettl, A. & Gimzewski, J. K. Measurement of the intrinsic strength of crystalline and polycrystalline graphene. *Nat. Commun.* **4,** 2811 (2013).
133. Pan, Y. *et al.* Highly ordered, millimeter-scale, continuous,single-crystalline graphene monolayer formed on Ru (0001). *Adv. Mater.* **21,** 2777–2780 (2009).
134. Yu, Q. *et al.* Control and characterization of individual grains and grain boundaries in graphene grown by chemical vapour deposition. *Nat. Mater.* **10,** 443–449 (2011).
135. Orofeo, C. M. *et al.* Influence of Cu metal on the domain structure and carrier

mobility in single-layer graphene. *Carbon N. Y.* **50,** 2189–2196 (2012).
136. Wang, H. *et al.* Controllable synthesis of submillimeter single-crystal monolayer graphene domains on copper foils by suppressing nucleation. *J. Am. Chem. Soc.* **134,** 3627–3630 (2012).
137. Ferrari, a. C. *et al.* Raman spectrum of graphene and graphene layers. *Phys. Rev. Lett.* **97,** 1–4 (2006).
138. Lu, A. Y. *et al.* Decoupling of CVD graphene by controlled oxidation of recrystallized Cu. *RSC Adv.* **2,** 3008 (2012).
139. Tao, L. *et al.* Synthesis of high quality monolayer graphene at reduced temperature on hydrogen-enriched evaporated copper (111) films. *ACS Nano* **6,** 2319–25 (2012).
140. Blake, P. *et al.* Making graphene visible. *Appl. Phys. Lett.* **91,** 18–21 (2007).
141. Liu, L. *et al.* Graphene oxidation: Thickness-dependent etching and strong chemical doping. *Nano Lett.* **8,** 1965–1970 (2008).
142. Chen, S. *et al.* Oxidation resistance of graphene-coated Cu and Cu/Ni alloy. *ACS Nano* **5,** 1321–1327 (2011).
143. Jia, C., Jiang, J., Gan, L. & Guo, X. Direct Optical Characterization of Graphene Growth and Domains on Growth Substrates. *Sci. Rep.* **2,** 1–6 (2012).
144. Han, G. H. *et al.* Influence of copper morphology in forming nucleation seeds for graphene growth. *Nano Lett.* **11,** 4144–4148 (2011).
145. Wood, J. D., Schmucker, S. W., Lyons, A. S., Pop, E. & Lyding, J. W. Effects of polycrystalline Cu substrate on graphene growth by chemical vapor deposition. *Nano Lett.* **11,** 4547–4554 (2011).
146. Ishihara, M., Koga, Y., Kim, J., Tsugawa, K. & Hasegawa, M. Direct evidence of advantage of Cu(111) for graphene synthesis by using Raman mapping and electron backscatter diffraction. *Mater. Lett.* **65,** 2864–2867 (2011).
147. Butt, M. Z. Effect of hydrogen attack on the strength of high purity copper. *J. Mater. Sci. Lett.* **2,** 1–2 (1983).
148. Chavez, K. L. & Hess, D. W. A Novel Method of Etching Copper Oxide Using Acetic Acid. *J. Electrochem. Soc.* **148,** G640–G643 (2001).
149. Luo, Z. *et al.* Effect of substrate roughness and feedstock concentration on growth of wafer-scale graphene at atmospheric pressure. *Chem. Mater.* **23,** 1441–1447 (2011).
150. Yan, Z. *et al.* Toward the Synthesis of Wafer-Scale Single-Crystal Graphene on Copper Foils. *ACS Nano* **6,** 9110–9117 (2012).
151. Chatain, D., Ghetta, V. & Wynblatt, P. Equilibrium Shape of Copper Crystals Grown on Sapphire. *Interface Sci.* **12,** 7–18 (2004).
152. Regan, W. R. Screening-engineered Field-effect Photovoltaics and Synthesis, Characterization, and Applications of Carbon-based and Related

Nanomaterials. (University of California, Berkeley, 2012).
153. Li, X. *et al.* Graphene films with large domain size by a two-step chemical vapor deposition process. *Nano Lett.* **10,** 4328–4334 (2010).
154. Luo, Z., Kim, S., Kawamoto, N., Rappe, A. M. & Johnson, a T. C. Growth Mechanism of Hexagonal Shape Graphene Flakes with Zigzag Edges. *ACS Nano* **5,** 9154–9160 (2011).
155. Robertson, A. W. & Warner, J. H. Hexagonal single crystal domains of few-layer graphene on copper foils. *Nano Lett.* **11,** 1182–9 (2011).
156. Bao, W. *et al.* Controlled ripple texturing of suspended graphene and ultrathin graphite membranes. *Nat. Nanotechnol.* **4,** 562–566 (2009).
157. Nelson, J. B. & Riley, D. P. The thermal expansion of graphite from 15C to 800C: part I. Experimental. *Proc. Phys. Soc.* **57,** 477 (1945).
158. Zhang, W., Wu, P., Li, Z. & Yang, J. First-principles thermodynamics of graphene growth on Cu surfaces. *J. Phys. Chem. C* **115,** 17782–17787 (2011).
159. Vlassiouk, I. *et al.* Role of Hydrogen in Chemical Vapor Deposition Growth of Large Single-. *ACS Nano* **7,** 6069–6076 (2011).
160. Wu, B. *et al.* Equiangular Hexagon-Shape-Controlled Synthesis of Graphene on Copper Surface. *Adv. Mater.* **23,** 3522–3525 (2011).
161. Sun, Z. *et al.* Large-Area Bernal-Stacked Bi-, Tri-, and Tetralayer Graphene. **6,** 9790–9796 (2012).
162. Sali, A., Glaeser, R., Earnest, T. & Baumeister, W. From words to literature in structural proteomics. *Nature* **422,** 216–225 (2003).
163. Adrian, M., Dubochet, J., Lepault, J. & McDowall, A. W. Cryo-electron microscopy of viruses. *Nature* **308,** 32–36 (1984).
164. Dubochet, J. *et al.* Cryo-electron microscopy of vitrified specimens. *Q. Rev. Biophys.* **21,** 129–228 (1988).
165. Abrams, I. M. & McBain, J. W. A Closed Cell for Electron Microscopy. *Science* **100,** 273–274 (1944).
166. Parsons, D. F., Matricardi, V. R., Moretz, R. C. & Turner, J. N. Electron microscopy and diffraction of wet unstained and unfixed biological objects. *Adv. Biol. Med. Physi.* **15,** 161–270 (1974).
167. Williamson, M. J., Tromp, R. M., Vereecken, P. M., Hull, R. & Ross, F. M. Dynamic microscopy of nanoscale cluster growth at the solid–liquid interface. *Nat. Mater.* **2,** 532–536 (2003).
168. Liao, H.-G., Cui, L., Whitelam, S. & Zheng, H. Real-Time Imaging of Pt3Fe Nanorod Growth in Solution. *Science* **336,** 1011–1014 (2012).
169. Li, D. *et al.* Direction-Specific Interactions Control Crystal Growth by Oriented Attachment. *Science* **336,** 1014–1018 (2012).
170. Peckys, D. B., Veith, G. M., Joy, D. C. & de Jonge, N. Nanoscale Imaging of

Whole Cells Using a Liquid Enclosure and a Scanning Transmission Electron Microscope. *PLoS One* **4,** e8214 (2009).

171. Yuk, J. M. *et al.* High-Resolution EM of Colloidal Nanocrystal Growth Using Graphene Liquid Cells. *Science* **336,** 61–64 (2012).
172. Erni, R. *et al.* Stability and dynamics of small molecules trapped on graphene. *Phys. Rev. B* **82,** 165443 (2010).
173. Nair, R. R. *et al.* Graphene as a transparent conductive support for studying biological molecules by transmission electron microscopy. *Appl. Phys. Lett.* **97,** 153102 (2010).
174. Chen, Q. *et al.* 3D motion of DNA-Au nanoconjugates in graphene liquid cell electron microscopy. *Nano Lett.* **13,** 4556–4561 (2013).
175. Park, J. *et al.* Direct Observation of Wet Biological Samples by Graphene Liquid Cell Transmission Electron Microscopy. *Nano Lett.* **15,** 4737–4744 (2015).
176. Park, J. *et al.* 3D structure of individual nanocrystals in solution by electron microscopy. *Science* **349,** 290–295 (2015).
177. Regan, W. *et al.* A direct transfer of layer-area graphene. *Appl. Phys. Lett.* **96,** 113102 (2010).
178. Chopra, N. G. *et al.* Boron nitride nanotubes. *Science* **269,** 966–967 (1995).
179. Cohen, M. L. & Zettl, A. The physics of boron nitride nanotubes. *Phys. Today* **63,** 34–38 (2010).
180. Blase, X., Rubio, A., Louie, S. G. & Cohen, M. L. Stability and Band Gap Constancy of Boron Nitride Nanotubes. *Europhys. Lett.* **28,** 335–340 (1994).
181. Chang, C. W., Han, W. Q. & Zettl, A. Thermal conductivity of B-C-N and BN nanotubes. *Appl. Phys. Lett.* **86,** 1–3 (2005).
182. Mele, E. & Král, P. Electric Polarization of Heteropolar Nanotubes as a Geometric Phase. *Phys. Rev. Lett.* **88,** 056803 (2002).
183. Chen, X. *et al.* Boron nitride nanotubes are noncytotoxic and can be functionalized for interaction with proteins and cells. *J. Am. Chem. Soc.* **131,** 890–891 (2009).
184. Mickelson, W., Aloni, S., Han, W. Q., Cumings, J. & Zettl, A. Packing C60 in boron nitride nanotubes. *Science* **300,** 467–9 (2003).
185. Hilder, T. A., Gordon, D. & Chung, S.-H. Salt Rejection and Water Transport Through Boron Nitride Nanotubes. *Small* **5,** 2183–2190 (2009).
186. Zhi, C. *et al.* Boron nitride nanotubes/polystyrene composites. *J. Mater. Res.* **21,** 2794–2800 (2006).
187. Lahiri, D. *et al.* Boron nitride nanotubes reinforced aluminum composites prepared by spark plasma sintering: Microstructure, mechanical properties and deformation behavior. *Mater. Sci. Eng. A* **574,** 149–156 (2013).
188. Lourie, O. R. *et al.* CVD growth of boron nitride nanotubes. *Chem. Mater.* **12,**

1808–1810 (2000).
189. Tang, C. C. *et al.* Effective growth of boron nitride nanotubes. *Chem. Phys. Lett.* **356,** 254–258 (2002).
190. Tang, C., Bando, Y., Sato, T. & Kurashima, K. A novel precursor for synthesis of pure boron nitride nanotubes. *Chem. Commun. (Camb).* **2,** 1290–1291 (2002).
191. Chen, Y., Conway, M., Williams, J. S. & Zou, J. Large-quantity production of high-yield boron nitride nanotubes. *J. Mater. Res.* **17,** 1896–1899 (2002).
192. Han, W., Bando, Y., Kurashima, K. & Sato, T. Synthesis of boron nitride nanotubes from carbon nanotubes by a substitution reaction. *Appl. Phys. Lett.* **73,** 3085 (1998).
193. Bartnitskaya, T. & Oleinik, G. Synthesis, structure, and formation mechanism of boron nitride nanotubes. *JETP Lett.* **69,** 163–168 (1999).
194. Han, W. Q., Todd, P. J. & Strongin, M. Formation and growth mechanism of B 10 N nanotubes via a carbon nanotube–substitution reaction. *Appl. Phys. Lett.* **89,** 173103 (2006).
195. Ebbesen, T. W. & Ajayan, P. M. Large-scale synthesis of carbon nanotubes. *Nature* **358,** 220–222 (1992).
196. Iijima, S. & Ichihashi, T. Single-shell carbon nanotubes of 1-nm diameter. *Nature* **363,** 603–605 (1993).
197. Loiseau, a., Willaime, F., Demoncy, N., Hug, G. & Pascard, H. Boron Nitride Nanotubes with Reduced Numbers of Layers Synthesized by Arc Discharge. *Phys. Rev. Lett.* **76,** 4737–4740 (1996).
198. Golberg, D. *et al.* Nanotubes in boron nitride laser heated at high pressure. *Appl. Phys. Lett.* **69,** 2045 (1996).
199. Arenal, R., Stephan, O., Cochon, J. Lou & Loiseau, A. Root-growth mechanism for single-walled boron nitride nanotubes in laser vaporization technique. *J. Am. Chem. Soc.* **129,** 16183–16189 (2007).
200. Lin, H. *et al.* Combined STM/STS, TEM/EELS investigation of CNx-SWNTs. *Phys. Status Solidi* **245,** 1986–1989 (2008).
201. Enouz, S., Stéphan, O., Cochon, J. Lou, Colliex, C. & Loiseau, A. C-BN patterned single-walled nanotubes synthesized by laser vaporization. *Nano Lett.* **7,** 1856–1862 (2007).
202. Shimizu, Y. *et al.* Concurrent preparation of carbon, boron nitride and composite nanotubes of carbon with boron nitride by a plasma evaporation method. *Thin Solid Films* **316,** 178–184 (1998).
203. Lee, C. M., Choi, S. I., Choi, S. S. & Hong, S. H. Synthesis of boron nitride nanotubes by arc-jet plasma. *Curr. Appl. Phys.* **6,** 166–170 (2006).
204. Kim, K. S. *et al.* Large-scale production of single-walled carbon nanotubes by induction thermal plasma. *J. Phys. D. Appl. Phys.* **40,** 2375–2387 (2007).

205. Ostrikov, K. & Murphy, A. B. Plasma-aided nanofabrication: where is the cutting edge? *J. Phys. D. Appl. Phys.* **40,** 2223–2241 (2007).
206. Boulos, M. I. Thermal plasma processing. *IEEE Trans. Plasma Sci.* **19,** 1078–1089 (1991).
207. Eckert, H. Induction Arc - State of Art Review. *High Temp. Sci.* **6,** 99–134 (1974).
208. Boulos, M. I. Inductively Coupled R. F. (Radio Frequency) Plasma. *Pure Appl. Chem.* **57,** 1321–1352 (1985).
209. Proulx, P., Mostaghimi, J. & Boulos, M. I. Heating of powders in an r.f. inductively coupled plasma under dense loading conditions. *Plasma Chem. Plasma Process.* **7,** 29–52 (1987).
210. Swank, W. D., Fincke, J. R. & Haggard, D. C. Modular enthalpy probe and gas analyzer for thermal plasma measurements. *Rev. Sci. Instrum.* **64,** 56–62 (1993).
211. Chen, W. L. T., Heberlein, J. & Pfender, E. Diagnostics of a thermal plasma jet by optical emission spectroscopy and enthalpy probe measurements. *Plasma Chem. Plasma Process.* **14,** 317–332 (1994).
212. Fauchais, P. & Vardelle, A. Thermal plasmas. *IEEE Trans. Plasma Sci.* **25,** 1258–1280 (1997).
213. Shigeta, M. & Murphy, A. B. Thermal plasmas for nanofabrication. *J. Phys. D. Appl. Phys.* **44,** 174025 (2011).
214. Kim, K. S. *et al.* Synthesis of single-walled carbon nanotubes by induction thermal plasma. *Nano Res.* **2,** 800–817 (2009).
215. Esfarjani, S. A., Mostaghimi, J., Kim, K. S., Shahverdi, A. & Soucy, G. Radio Frequency Thermal Plasma: The Cutting Edge Technology in Production of Single-Walled Carbon Nanotubes. *J. Therm. Sci. Technol.* **6,** 307–322 (2011).
216. Alinejad, Y., Shahverdi, A., Faucheux, N. & Soucy, G. Synthesis of single-walled carbon nanotubes using induction thermal plasma technology with different catalysts: thermodynamic and experimental studies. *J. Phys. Conf. Ser.* **406,** 012019 (2012).
217. Esfarjani, S. A. *et al.* Detailed Numerical Simulation of Single-Walled Carbon Nanotube Synthesis in a Radio-Frequency Induction Thermal Plasma System. *J. Phys. Conf. Ser.* **406,** 012011 (2012).
218. Mao, M. & Bogaerts, A. Plasma chemistry modeling for an inductively coupled plasma used for the growth of carbon nanotubes. *J. Phys. Conf. Ser.* **275,** 012021 (2011).
219. Ventzek, P. L. G., Sommerer, T. J., Hoekstra, R. J. & Kushner, M. J. Two-dimensional for etching hybrid model of inductively coupled plasma sources for etching. *Appl. Phys. Lett.* **63,** 605–607 (1993).
220. Cumings, J. & Zettl, A. Mass-production of boron nitride double-wall

nanotubes and nanococoons. *Chem. Phys. Lett.* **316,** 211–216 (2000).
221. Nemanich, R. J., Solin, S. A. & Martin, R. M. Light scattering study of boron nitride microcrystals. *Phys. Rev. B* **23,** 6348 (1981).
222. Terrones, M. Synthesis, Properties, and Applications of Carbon Nanotubes. *Annu. Rev. Mater. Res.* **33,** 419–501 (2003).
223. Tang, C., Bando, Y., Ding, X., Qi, S. & Golberg, D. Catalyzed collapse and enhanced hydrogen storage of BN nanotubes. *J. Am. Chem. Soc.* **124,** 14550–14551 (2002).
224. Erickson, K. J. *et al.* Longitudinal splitting of boron nitride nanotubes for the facile synthesis of high quality boron nitride nanoribbons. *Nano Lett.* **11,** 3221–6 (2011).
225. Okamoto, K. *Phase diagrams for binary alloys*. (2000).
226. Krishnan, S., Ansell, S., Felten, J., Volin, K. & Price, D. Structure of Liquid Boron. *Phys. Rev. Lett.* **81,** 586–589 (1998).
227. Tavadze, F., Bairamas, I., Tsagarei, G., Tsomaya, K. & Zoidze, N. Structure of Boron Crystals Grown from Melt. *Sov. Phys. Crystallogr.* **9,** 768 (1965).
228. Krishnan, S. *et al.* Levitation apparatus for structural studies of high temperature liquids using synchrotron radiation. *Rev. Sci. Instrum.* **68,** 3512–8 (1997).
229. Yeh, C. L. & Kuo, K. K. Ignition and combustion of boron particles. *Prog. Energy Combust. Sci.* **22,** 511–541 (1996).
230. Mohan, G. & Williams, F. A. Ignition and Combustion of Boron in O2/Inert Atmospheres. *AIAA J.* **10,** 776–783 (1972).
231. Darwent, B. deB. *National Standard Reference Data Series*. (1970).
232. Cottrell, T. L. The Strengths of Chemical Bonds, 2nd Ed. **372,** 41–53 (1966).
233. Nozaki, H. & Itoh, S. Structural Stability of BC2N. *J. Phys. Chem. Solids* **57,** 41–49 (1996).
234. Cherrey, K. *et al.* Synthesis of BxCyNz nanotubules. *Phys. Rev. B* **51,** 11229 (1995).
235. Ebbesen, T. W., Ajayan, P. M., Hiura, H. & Tanigaki, K. Purification of nanotubes. *Nature* **367,** 519–519 (1994).
236. Hou, P. X., Liu, C. & Cheng, H. M. Purification of carbon nanotubes. *Carbon N. Y.* **46,** 2003–2025 (2008).
237. Zhi, C. *et al.* Purification of boron nitride nanotubes through polymer wrapping. *J. Phys. Chem. B* **110,** 1525–8 (2006).
238. Chen, H., Chen, Y., Yu, J. & Williams, J. S. Purification of boron nitride nanotubes. *Chem. Phys. Lett.* **425,** 315–319 (2006).
239. Vieira, S. M. C. & Carroll, D. L. Purification of Boron Nitride Multiwalled Nanotubes. *J. Nanosci. Nanotechnol.* **7,** 331803322 (2007).

240. Maguer, A. *et al.* Purification of Single-Walled Boron Nitride Nanotubes and Boron Nitride Cages. *J. Nanosci. Nanotechnol.* **7,** 3528–3532 (2007).
241. Koi, N., Oku, T., Inoue, M. & Suganuma, K. Structures and purification of boron nitride nanotubes synthesized from boron-based powders with iron particles. *J. Mater. Sci.* **43,** 2955–2961 (2008).
242. Choi, J. H., Kim, J., Seo, D. & Seo, Y. S. Purification of boron nitride nanotubes via polymer wrapping. *Mater. Res. Bull.* **48,** 1197–1203 (2013).
243. Weast, R. C., Lide, D. R., Astle, M. J. & Beyer, W. H. *CRC Handbook of Chemistry and Physics*. (1990).
244. Han, W. Q., Mickelson, W., Cumings, J. & Zettl, A. Transformation of BxCyNz nanotubes to pure BN nanotubes. *Appl. Phys. Lett.* **81,** 1110–1112 (2002).
245. Park, Y. S. *et al.* High yield purification of multiwalled carbon nanotubes by selective oxidation during thermal annealing. *Carbon N. Y.* **39,** 655–661 (2001).
246. Podobeda, L. T., Tsapuk, A. K. & Buravov, A. D. Bur. *Sov. Powder Met.* **9,** (1976).
247. Matsuda, T. Stability to moisture for chemically vapour-deposited boron nitride. *J. Mater. Sci.* **24,** 2353–2357 (1989).
248. Zhi, C. Y. *et al.* Chemically activated boron nitride nanotubes. *Chem. Asian J.* **4,** 1536–1540 (2009).
249. Zhi, C. *et al.* Phonon characteristics and cathodolumininescence of boron nitride nanotubes. *Appl. Phys. Lett.* **86,** 1–3 (2005).
250. Sainsbury, T. *et al.* Self-assembly of gold nanoparticles at the surface of amine- and thiol-functionalized boron nitride nanotubes. *J. Phys. Chem. C* **111,** 12992–12999 (2007).
251. Zhi, C. *et al.* Perfectly dissolved boron nitride nanotubes due to polymer wrapping. *J. Am. Chem. Soc.* **127,** 15996–7 (2005).
252. Chen, J. *et al.* Noncovalent engineering of carbon nanotube surfaces by rigid, functional conjugated polymers. *J. Am. Chem. Soc.* **124,** 9034–9035 (2002).
253. Star, A. *et al.* Preparation and properties of polymer-wrapped single-walled carbon nanotubes. *Angew. Chemie-International Ed.* **40,** 1721–1725 (2001).
254. Coleman, J. N. *et al.* Phase Separation of Carbon Nanotubes and Turbostratic Graphite Using a Functional Organic Polymer. *Adv. Mater.* **12,** 213–216 (2000).
255. Curran, S. a. *et al.* A Composite from Poly(m-phenylenevinylene-co-2,5-dioctoxy-p-phenylenevinylene) and Carbon Nanotubes: A Novel Material for Molecular Optoelectronics. *Adv. Mater.* **10,** 1091–1093 (1998).
256. Erickson, K. J. Synthesis and Functionalization of Carbon and Boron Nitride Nanomaterials and Their Applications. (University of California, Berkeley, 2012).
257. Li, F., Cheng, H. M., Xing, Y. T., Tan, P. H. & Su, G. Purification of single-walled carbon nanotubes synthesized by the catalytic decomposition of

hydrocarbons. *Carbon N. Y.* **38,** 2041–2045 (2000).
258. Dillon, A. C. *et al.* Simple and complete purification of single-walled carbon nanotube materials. *Adv. Mater.* **11,** 1354–1358 (1999).
259. Hou, P. *et al.* Purification of single-walled carbon nanotubes synthesized by the hydrogen arc-discharge method. *J. Mater. Res.* **16,** 2526–2529 (2001).
260. Chen, X. H. *et al.* Non-destructive purification of multi-walled carbon nanotubes produced by catalyzed CVD. *Mater. Lett.* **57,** 734–738 (2002).
261. Martinez, M. T. *et al.* Modifications of single-wall carbon nanotubes upon oxidative purification treatments. *Nanotechnology* **14,** 691–695 (2003).
262. Montoro, L. A. & Rosolen, J. M. A multi-step treatment to effective purification of single-walled carbon nanotubes. *Carbon N. Y.* **44,** 3293–3301 (2006).
263. Pederson, M. R. & Broughton, J. Q. Nanocapillarity in fullerene tubules. *Phys. Rev. Lett.* **69,** 2689–2692 (1992).
264. Ajayan, P. M. & Iijima, S. Capillarity-induced filling of carbon nanotubes. *Nature* **361,** 333–334 (1993).
265. Ajayan, P. M. *et al.* Opening carbon nanotubes with oxygen and implications for filling. *Nature* **362,** 522–525 (1993).
266. Saito, Y. & Yoshikawa, T. Bamboo-shaped carbon tube filled partially with nickel. *J. Cryst. Growth* **134,** 154–156 (1993).
267. Dujardin, E., Ebbesen, T. W., Hiura, H. & Tanigaki, K. Capillarity and wetting of carbon nanotubes. *Science* **265,** 1850–1852 (1994).
268. Tsang, S. C., Chen, Y. K., Harris, P. J. F. & Green, M. L. H. A simple chemical method of opening and filling carbon nanotubes. *Nature* **372,** 159–162 (1994).
269. Sloan, J., Hammer, J., Zwiefka-Sibley, M., Green, M. L. H. & Sloan, J. The opening and filling of single walled carbon nanotubes (SWTs). *Chem. Commun.* **1,** 347–348 (1998).
270. Monthioux, M. Filling single-wall carbon nanotubes. *Carbon N. Y.* **40,** 1809–1823 (2002).
271. Serp, P., Corrias, M. & Kalck, P. Carbon nanotubes and nanofibers in catalysis. *Appl. Catal. A Gen.* **253,** 337–358 (2003).
272. Tasis, D., Tagmatarchis, N., Bianco, A. & Prato, M. Chemistry of carbon nanotubes. *Chem. Rev.* **106,** 1105–36 (2006).
273. Monthioux, M., Flahaut, E. & Cleuziou, J.-P. Hybrid carbon nanotubes: Strategy, progress, and perspectives. *J. Mater. Res.* **21,** 2774–2793 (2006).
274. Eder, D. Carbon nanotube-inorganic hybrids. *Chem. Rev.* **110,** 1348–1385 (2010).
275. Monteiro, a. O., Cachim, P. B. & Costa, P. M. F. J. Mechanics of filled carbon nanotubes. *Diam. Relat. Mater.* **44,** 11–25 (2014).
276. Gao, Y. & Bando, Y. Carbon nanothermometer containing gallium. *Nature* **415,**

599 (2002).
277. Pan, X. *et al.* Enhanced ethanol production inside carbon-nanotube reactors containing catalytic particles. *Nat. Mater.* **6,** 507–11 (2007).
278. Che, G., Lakshmi, B. B., Martin, C. R. & Fisher, E. R. Metal-Nanocluster-Filled Carbon Nanotubes: Catalytic Properties and Possible Applications in Electrochemical Energy Storage and Production. *Langmuir* **15,** 750–758 (1999).
279. Korneva, G. *et al.* Carbon nanotubes loaded with magnetic particles. *Nano Lett.* **5,** 879–884 (2005).
280. Carter, R. *et al.* Correlation of Structural and Electronic Properties in a New Low-Dimensional Form of Mercury Telluride. *Phys. Rev. Lett.* **96,** 215501 (2006).
281. Grobert, N. *et al.* Enhanced magnetic coercivities in Fe nanowires. *Appl. Phys. Lett.* **75,** 3363 (1999).
282. Corio, P. *et al.* Characterization of single wall carbon nanotubes filled with silver and with chromium compounds. *Chem. Phys. Lett.* **383,** 475–480 (2004).
283. Kharlamova, M. V., Yashina, L. V. & Lukashin, A. V. Charge transfer in single-walled carbon nanotubes filled with cadmium halogenides. *J. Mater. Sci.* **48,** 8412–8419 (2013).
284. Han, W., Redlich, P., Ernst, F. & Rühle, M. Synthesizing boron nitride nanotubes filled with SiC nanowires by using carbon nanotubes as templates. *Appl. Phys. Lett.* **75,** 1875 (1999).
285. Golberg, D., Xu, F. F. & Bando, Y. Filling boron nitride nanotubes with metals. *Appl. Phys. A Mater. Sci. Process.* **76,** 479–485 (2003).
286. Man, W. Q., Chang, C. W. & Zettl, A. Encapsulation of one-dimensional potassium halide crystals within BN nanotubes. *Nano Lett.* **4,** 1355–1357 (2004).
287. Han, W. Q. & Zettl, A. GaN nanorods coated with pure BN. *Appl. Phys. Lett.* **81,** 5051 (2002).
288. Tang, C., Bando, Y., Golberg, D., Ding, X. & Qi, S. Boron Nitride Nanotubes Filled with Ni and NiSi 2 Nanowires in Situ. *J. Phys.Chem. B* **107,** 6539–6543 (2003).
289. Shelimov, K. B. & Moskovits, M. Composite nanostructures based on template-grown boron nitride nanotubules. *Chem. Mater.* **12,** 250–254 (2000).
290. Bando, Y., Ogawa, K. & Golberg, D. Insulating `nanocables': Invar Fe–Ni alloy nanorods inside BN nanotubes. *Chem. Phys. Lett.* **347,** 349–354 (2001).
291. Watts, P. C. P., Hsu, W. K., Kotzeva, V. & Chen, G. Z. Fe-filled carbon nanotube-polystyrene: RCL composites. *Chem. Phys. Lett.* **366,** 42–50 (2002).
292. Thamavaranukup, N., Höppe, H. A., Ruiz-Gonzalez, L., Costa, P. M. F. J. & Green, M. L. H. Single-walled carbon nanotubes filled with M OH ( M = K , Cs ) and then washed and refilled with clusters and molecules. *Inorg. Chem.* **1,**

1686–1687 (2004).
293. Shen, Z. Q. *et al.* Boron nitride nanotubes filled with zirconium oxide nanorods. *J. Mater. Res.* **17,** 2761–2764 (2002).
294. Golberg, D., Bando, Y., Fushimi, K., Mitome, M. & Bourgeois, L. Nanoscale Oxygen Generators: MgO2 -Based Fillings of BN Nanotubes. *J. Phys. Chem.* **107,** 8726–8729 (2003).
295. Loh, K. P., Lin, M., Yeadon, M., Boothroyd, C. & Hu, Z. Growth of boron nitride nanotubes and iron nanowires from the liquid flow of FeB nanoparticles. *Chem. Phys. Lett.* **387,** 40–46 (2004).
296. Koi, N., Oku, T. & Nishijima, M. Fe nanowire encapsulated in boron nitride nanotubes. *Solid State Commun.* **136,** 342–345 (2005).
297. Fathalizadeh, A., Pham, T., Mickelson, W. & Zettl, A. Scaled synthesis of boron nitride nanotubes, nanoribbons, and nanococoons using direct feedstock injection into an extended-pressure, inductively-coupled thermal plasma. *Nano Lett.* **14,** 4881–4886 (2014).
298. Ajayan, P. M., Stephan, O., Redlich, P. & Colliex, C. Carbon nanotubes as removable templates for metal oxide nanocomposites and nanostructures. *Nature* **375,** 564–567 (1995).
299. Datsyuk, V. *et al.* Chemical oxidation of multiwalled carbon nanotubes. *Carbon N. Y.* **46,** 833–840 (2008).
300. Ugarte, D., Stöckli, T., Bonard, J. M., Châtelain, A. & de Heer, W. A. Filling carbon nanotubes. *Appl. Phys. A Mater. Sci. Process.* **67,** 101–105 (1998).
301. Jana, N. R., Gearheart, L. & Murphy, C. J. Wet Chemical Synthesis of High Aspect Ratio Cylindrical Gold Nanorods. *J. Phys. Chem. B* **105,** 4065–4067 (2001).
302. Loubat, A. *et al.* Growth and self-assembly of ultrathin Au nanowires into expanded hexagonal superlattice studied by in situ SAXS. *Langmuir* **30,** 4005–12 (2014).
303. Yang, F., Taggart, D. K. & Penner, R. M. Fast, sensitive hydrogen gas detection using single palladium nanowires that resist fracture. *Nano Lett.* **9,** 2177–82 (2009).
304. Gao, Y., Bando, Y. & Golberg, D. Melting and expansion behavior of indium in carbon nanotubes. *Appl. Phys. Lett.* **81,** 4133 (2002).
305. Liu, Z. *et al.* Shape Anisotropy and Magnetization Modulation in Hexagonal Cobalt Nanowires. *Adv. Funct. Mater.* **18,** 1573–1578 (2008).
306. Wu, H. *et al.* Nanostructured Gold Architectures Formed through High Pressure-Driven Sintering of Spherical Nanoparticle Arrays. *J. Am. Chem. Soc.* **132,** 12826–12828 (2010).
307. Li, W., Fan, H. & Li, J. Deviatoric Stress-Driven Fusion of Nanoparticle

Superlattices. *Nano Lett.* **14,** 4951–4958 (2014).
308. Wu, H. *et al.* Pressure-driven assembly of spherical nanoparticles and formation of 1D-nanostructure arrays. *Angew. Chem. Int. Ed. Engl.* **49,** 8431–4 (2010).
309. Li, B. *et al.* Stress-induced phase transformation and optical coupling of silver nanoparticle superlattices into mechanically stable nanowires. *Nat. Commun.* **5,** 4179 (2014).
310. Yum, K. & Yu, M. F. Measurement of wetting properties of individual boron nitride nanotubes with the Wilhelmy method using a nanotube-based force sensor. *Nano Lett.* **6,** 329–333 (2006).
311. Lu, H. M. & Jiang, Q. Surface tension and its temperature coefficient for liquid metals. *J. Phys. Chem. B* **109,** 15463–15468 (2005).
312. Huang, Y. *et al.* Bulk synthesis, growth mechanism and properties of highly pure ultrafine boron nitride nanotubes with diameters of sub-10 nm. *Nanotechnology* **22,** 145602 (2011).
313. Chu, P. K., Zhi, C., Bando, Y., Tang, C. & Golberg, D. Boron nitride nanotubes. *Mater. Sci. Eng. R Reports* **70,** 92–111 (2010).
314. Huh, S., Kim, H., Park, J. & Lee, G. Critical cluster size of metallic Cr and Mo nanoclusters. *Phys. Rev. B* **62,** 2937–2943 (2000).
315. Yuvaraj, S., Lin, F. Y., Chang, T. H. & Yeh, C. T. Thermal decomposition of metal nitrates in air and hydrogen environments. *J. Phys. Chem. B* **107,** 1044–1047 (2003).
316. Zheng, Y., Guo, W., Bai, M. & Yang, X. Preparation of chloroauric acid and its thermal decomposition. *Chinese J. Nonferrous Met.* **16,** 1976–82 (2006).
317. Schweizer, A. E. & Kerr, G. T. Thermal decomposition of hexachloroplatinic acid. *Inorg. Chem.* **17,** 2326–2327 (1978).
318. Holleman, A. F. & Wiberg, E. *Inorganic Chemistry*. (Academic Press, 2001).
319. Mu, J. & Perlmutter, D. D. Thermal decomposition of metal nitrates and their hydrates. *Thermochim. Acta* **56,** 253–260 (1982).
320. Chen, Y. K. *et al.* Synthesis of carbon nanotubes containing metal oxides and metals of the d-block and f-block transition metals and related studies. *J. Mater. Chem.* **7,** 545–549 (1997).

# Appendix A

# Using the Attocube: Nanotube-AFM Tip Assembly

## A.1 Preparing nanotube substrates

1) Prepare a solution of CNTs in isopropyl alcohol.
2) Deposit 50 – 100 nm of Au on a SiN substrate.
3) Drop cast the CNT-IPA solution onto the gold coated SiN substrate.
4) Scribe one end a little bit and then crack the substrate by placing it over a wire.
5) The substrate you want to use is the one where the edge of the substrate has a slight overhang.

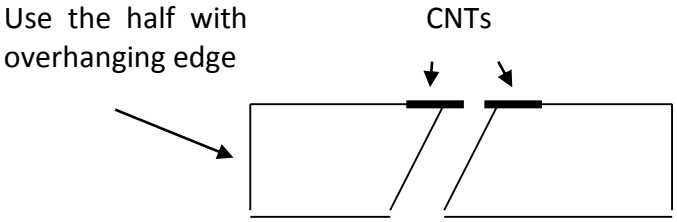

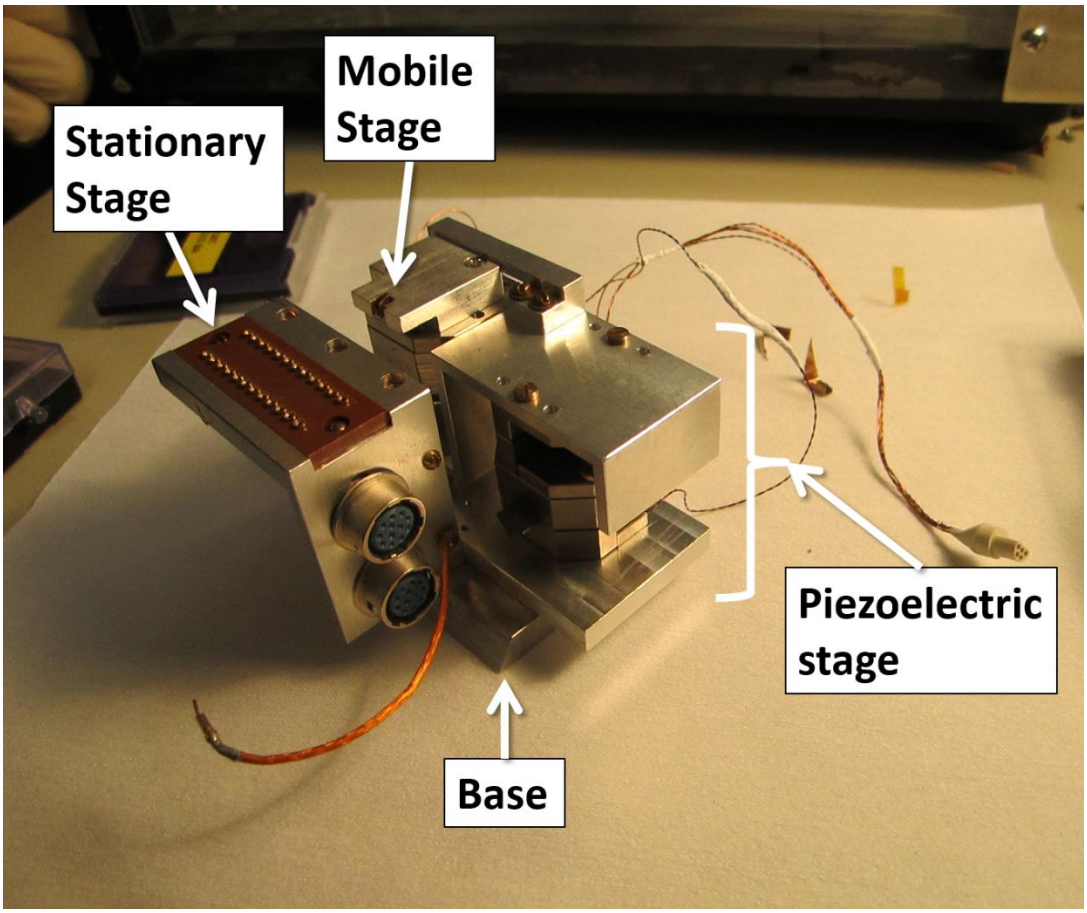


Figure A. 1: Picture of attocube with stages labeled.

## A.2 Preparing the attocube

1) Put on gloves before touching the attocube.
2) When handling the attocube, **always** pick it up from the base and **never** from the piezoelectric stage on the side.
   - Avoid pulling up or pushing down too hard on the piezoelectric stage as this will cause irreparable damage.
3) Attach the AFM stage on the top of the mobile piezoelectric stage.
   - Very gently unscrew the 2 screws on the top of the stage.

- Remove electrical connection from the mobile stage before lifting the stage.

4) Load the AFM chip into the AFM holder on the mobile stage.

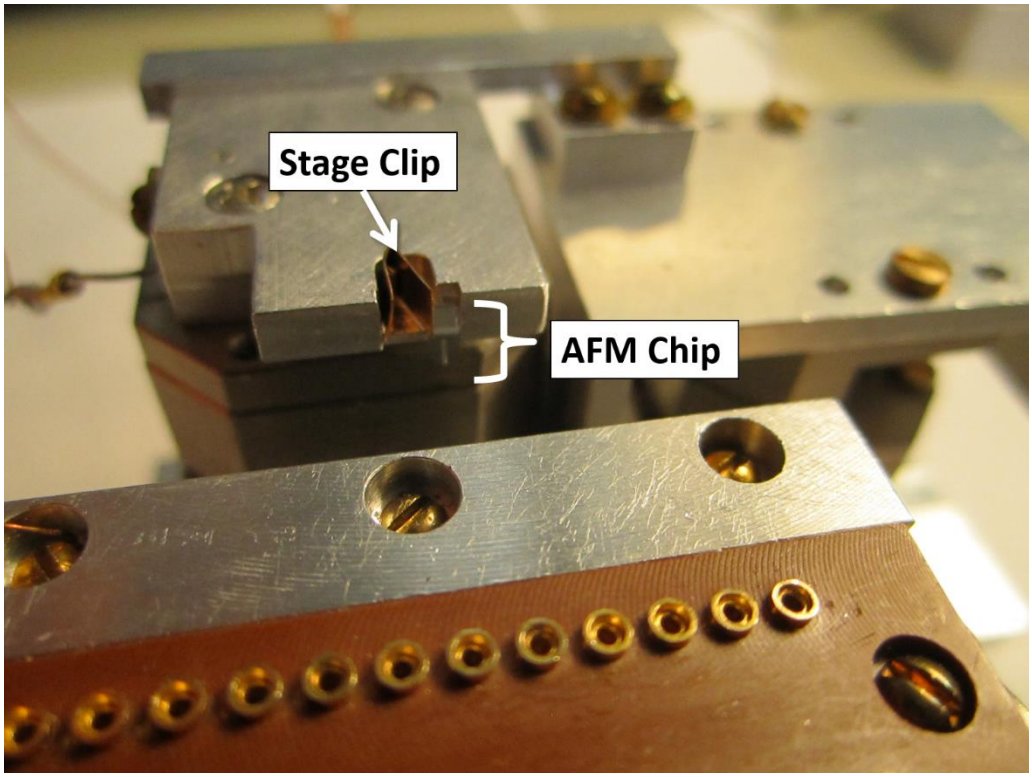


Figure A. 2: Top of attocube stage equipped for AFM chip mounting.

- Use a second pair of curved tweezers to very lightly open up the clip on the stage.
- Push lightly on chip so it lies flat on the angled recess of the holder.
- Load chip so that a little less than half of the chip is hanging below the holder. Be very careful when pushing down on the AFM chip as it may fling out.

5) Load the substrate containing nanotubes onto the stationary stage.
   - Use Kapton tape (Ted Pella Inc.) to attach substrate.

- Orient nanotube substrate edge as parallel as possible to the edge of the stationary stage.
- Attach the copper wire from the stationary stage to the top of the substrate to ensure that the top of the substrate is grounded (by simply slipping it under the Kapton tape).
- Using a multimeter, ensure that the top of the substrate is in good electrical contact with the stationary stage and not in electrical contact with the mobile stage.

6) Load the attocube into the SEM.
   - When transporting the attocube, support it by placing it on the palm of your hand and walking slow and carefully.
   - Make sure the SEM stage rotation has been zeroed
   - Load the attocube with blue electrical connections facing outward.
   - Attach the stage connection wires to those inside the SEM.
   - Check to make sure the stage height is okay by making sure everything is below the appropriate line on the SEM height measurement tool.
   - Watch using the CCD camera on the computer that the stage will not run into the pole piece as you close the SEM chamber door.

## A.3 Setting up measurements

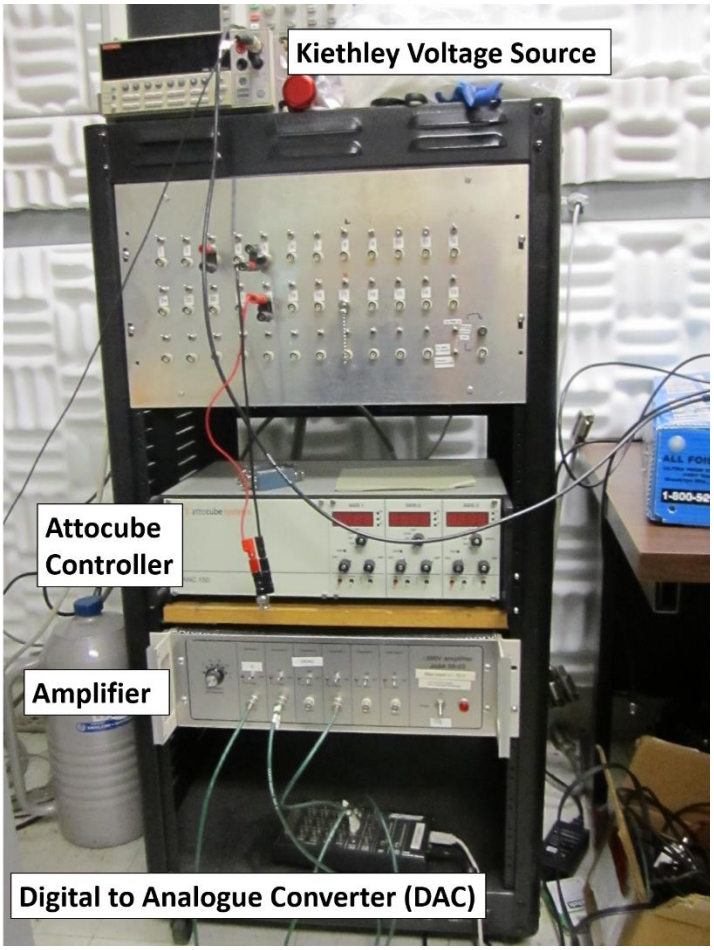


Figure A. 3: Electronics rack for attocube operation.

1) If not already connected, connect the external attocube feedthrough on the left side of the SEM chamber door.
   - If you want to do transport measurements, attach the additional feedthrough wire on the back of the SEM.
2) Turn on and attach the Keithley voltage source to the BNC cable labeled “V” which is feed to the SEM.

- If Keithley doesn't respond to the software, make sure it is in local mode and at zero volts.

3) Turn on the attocube controller (switch is on back) and amplifier.
   - Set amplifier signal gain (should be set at 15).
4) On the 2nd computer from the left, open the LabVIEW program entitled "Fowler Nordheim" or "Shortcut to Fowler Nordheim"
   - If initiated properly, running the program should read from the Keithley and you will hear a beep and it will begin taking data.
5) On the EDAX computer (to switch keyboard and mouse control over computers, push "Ctrl" key twice) and open the program entitled "attocube.exe."
   - Log in under the username "Attocube" and the password is the usual Zettl group password.
6) Get out the handle joystick and the smaller rotational mouse.
7) Turn on the "GIS" gas button on the GIS Manual Controller.
   - When the gas is warmed up and ready, the "READY" light will turn on.

# A.4 Using the attocube controller


Figure A. 4: Front panel of attocube controller.

- Note that “Axis 1” controls movement in the X – direction, “Axis 2” in the Y – direction, and “Axis 3” in the Z – direction.

| Axis 1 | Axis 2 | Axis 3 |
|---|---|---|
| X – direction | Y – direction | Z – direction |

These axes correspond to movement on the screen as:

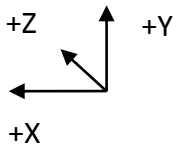

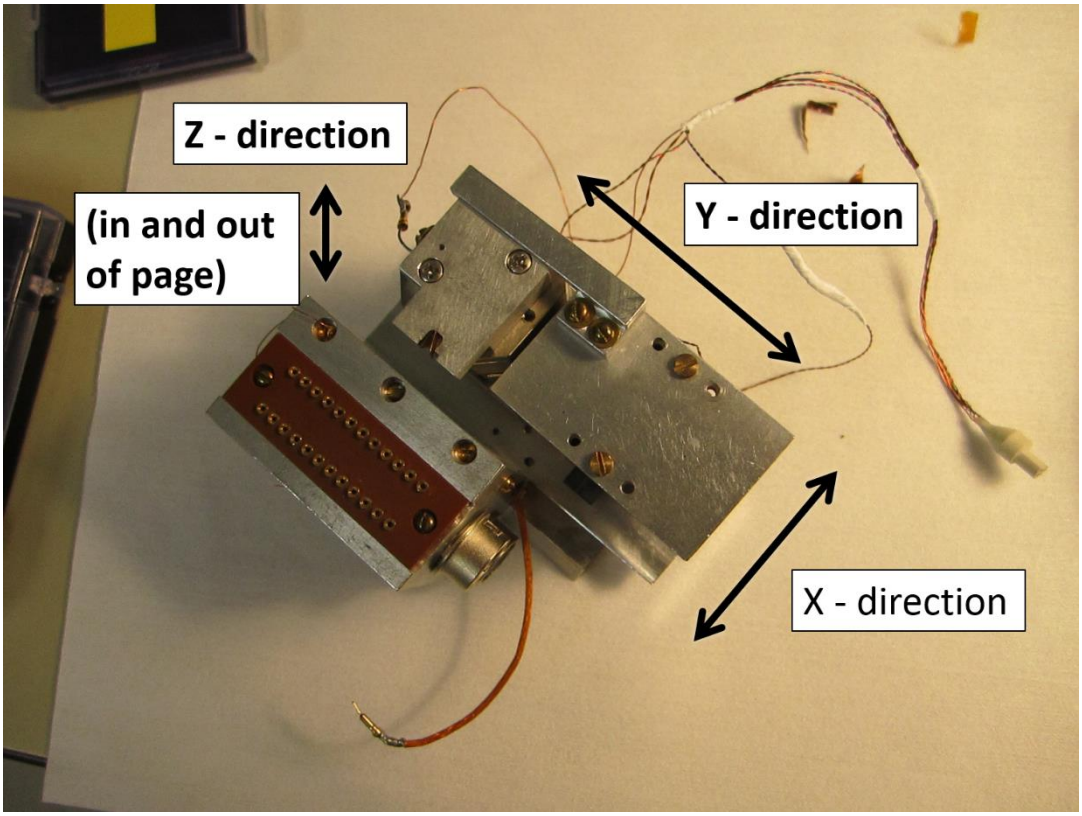


Figure A. 5: Attocube stage with piezo driven movements labeled.

- Controlling movement knob:
  - To turn OFF control of movement along an axis, turn its corresponding knob to “OFF”.
  - To control movement along an axis MANUALLY, turn its corresponding knob to “RUN”.
  - To control movement along an axis VIA THE COMPUTER, turn its corresponding knob to “CCON”.
- In order to move the piezoelectric stage, the attocube controller will send a saw tooth electrical signal to the piezos. The frequency and amplitude of these signals for the different axes can be set

independently, but usually a frequency of 100 Hz or 250 Hz and amplitude of 25 V is good.

- ❖ The three switches at the bottom enable the user to manually control the movement of the stage.
    - The “STEP” switch allows for movement in discrete steps in the + or – direction.
    - The “CONT” switch allows for continuous movement in the + or – direction.
    - The red “∞” switch, when flipped up or down, will keep the stage moving in the + or – direction until it is flipped back to neutral. Be careful when using this switch and keep an eye on how the stage is moving or it might crash into something.
- ❖ Use the joystick for finer movements once you are in the range of where you would like to move the tip. The “Attocube” program lets you know where in your range you can move the stage using the joystick. To move outside of this range, you must do so manually.
    - To use the joystick, make sure all axis knobs are set at “CCON” and the program “Attocube” is open.
    - Use the “sensitivity” on the joystick to adjust the speed of the movement.
    - Pressing the trigger moves the stage faster.
    - Use the small joystick on top labeled “Course Motion” for course motion and the larger joystick handle for fine motion.

1) Turn the knob for all axes on the attocube controller to “RUN” and use the switches to manually move the stage and AFM tip relatively close the edge of the carbon nanotube substrate.
2) Turn the knob for all axes on the attocube controller to “CCON” so that you can use the joystick to control the stage movement.
3) Find a nanotube on the substrate edge that is suitable (i.e. straight, at least 1 μm) and adjust the SEM controls until it is in focus.
    - To turn on the crosshairs, which are useful, hit Ctrl and x.

4) Without changing the focus on the SEM, now look at the AFM tip on the screen and adjust the Z – height of the stage using the metal rotational mouse until the tip too is in focus.
    - Alternatively, you can set the “Axis 3” knob to “RUN” and adjust the Z – height manually.
    - The nanotube and the AFM tip should roughly be at the same height now.
5) To attach a nanotube to the AFM tip, bring the AFM tip close to the desired nanotube and then make contact by bringing the AFM tip just under the height of the nanotube, then raise its Z – height a bit. Make sure there is sufficient overlap of the nanotube with the AFM tip.
6) To coat the nanotube with platinum and “weld” it onto the AFM tip, first zoom in on the screen on the part of the nanotube which overlaps the AFM tip.
    - The location of the electron beam is where the platinum particles will solidify.
7) Turn on the “VALVE” switch on the GIS Manual Controller to let in gas.
    - The valve can be opened a few times until you feel sufficient platinum has been deposited.
8) To check for electrical contact, run electricity through the AFM tip using the “Fowler Nordheim” software.
    - If a voltage bias is set, a current should flow through the tip-tube assembly.
    - Running current through will heat up the nanotube and can be used to anneal or burn off junk or break the tube.
9) To break the tube, gradually increase the amount of current running through the tube by increasing the bias voltage.
    - Tube is broken when the current value suddenly drops.
10) Move the AFM tip, with the attached tube, as far away from the substrate as possible.

11) Turn off the GIS Manual Controller by pushing the “HEAT” button again.
12) Begin procedures to open up the chamber by, for instance, first turning off the electron beam and then venting.
13) Set all of the knobs on the attocube controller to “OFF” and then proceed to turn off the attocube controller (switch is on the back), the amplifier, and the Keithley voltage source.

## A.5 Unloading from the attocube

1) After the SEM electron beam has been turned off and the chamber vented, carefully remove the attocube from the SEM chamber and handle it by the base or by placing it on the palm of your hands.
2) Strap yourself into a grounding wire in order to prevent electrostatic discharge from ruining your AFM tip-nanotube assembly.
3) If not already the case, push the AFM tip down a bit so that it protrudes from the bottom of the stage. This will make grabbing it easier.
4) Using straight tweezers to grab hold of the AFM tip and then use the curved tweezers to carefully unhinge the copper clip to loosen it up. Remove and store the AFM tip.

## Troubleshooting:

The Zettl Group contact for problems with the piezoelectric stage of the attocube is Rainer Goetz who can be contacted at: rainer.goetz@attocube.com.

# Appendix B

# EPIC Plasma System Parts

## B.1 RF Plasma Torch

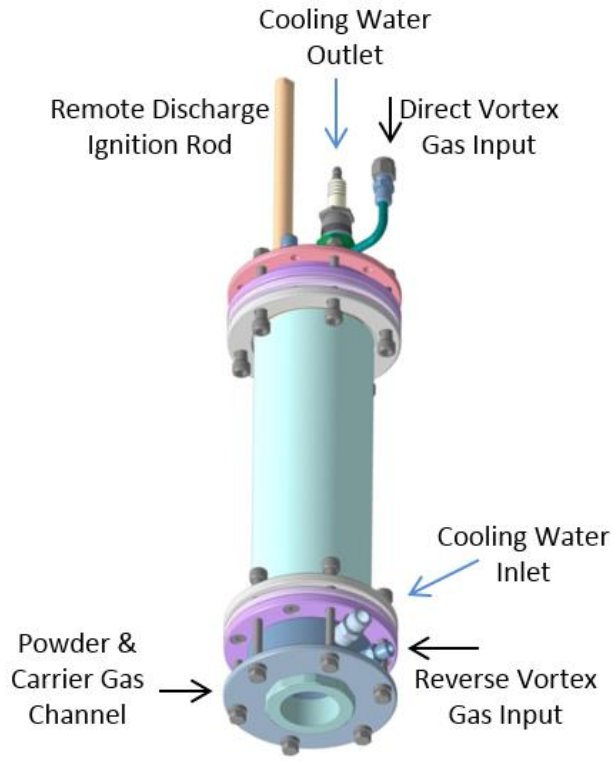


Figure B. 1: Labeled schematic of RF plasma torch body. Torch operates at 7.5 Mhz, has a length of 14.5” and an exit nozzle inner diameter of 1.38”. (3D-rendered image courtesy of I. Matveev)

## B.2 Synthesis Chamber

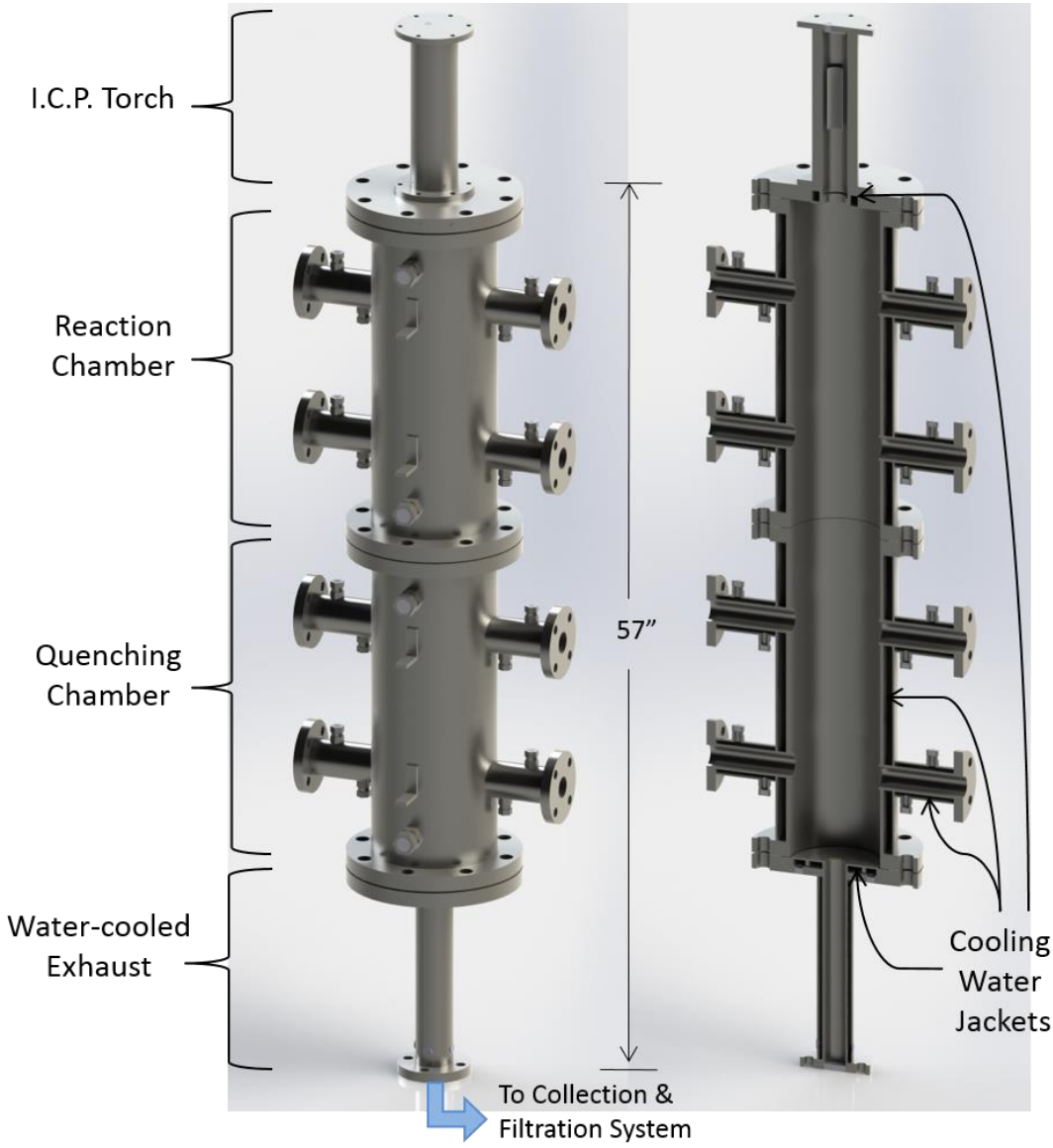


Figure B. 2: Front and cross-sectional schematic diagram of EPIC plasma system. Cooling water jackets are labeled in the cross-section image on the right. (3D-rendered images courtesy of G. Leyva)

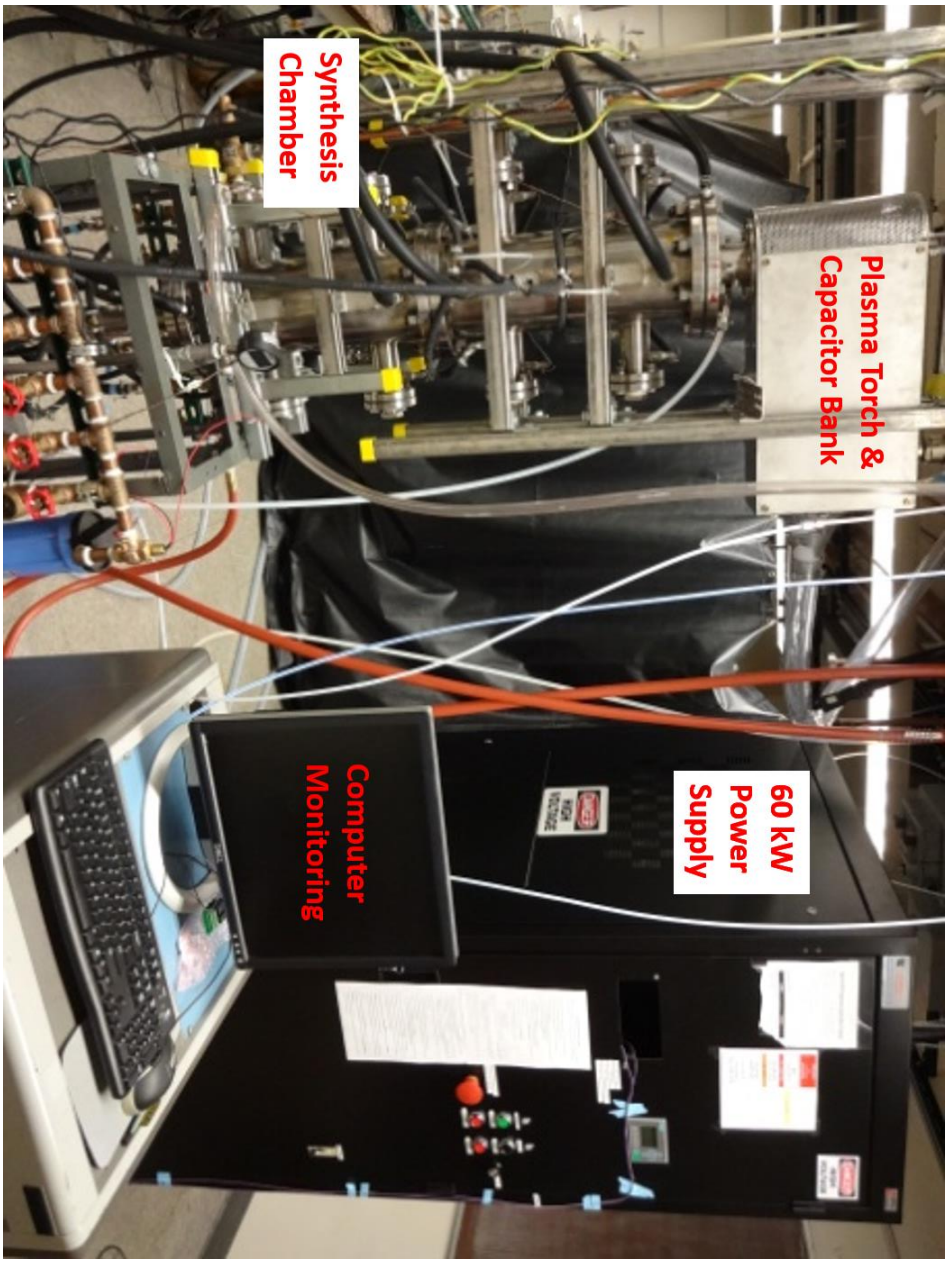


Figure B. 3: EPIC plasma system as viewed from the users' side.

# B.3 Synthesis Chamber Schematics

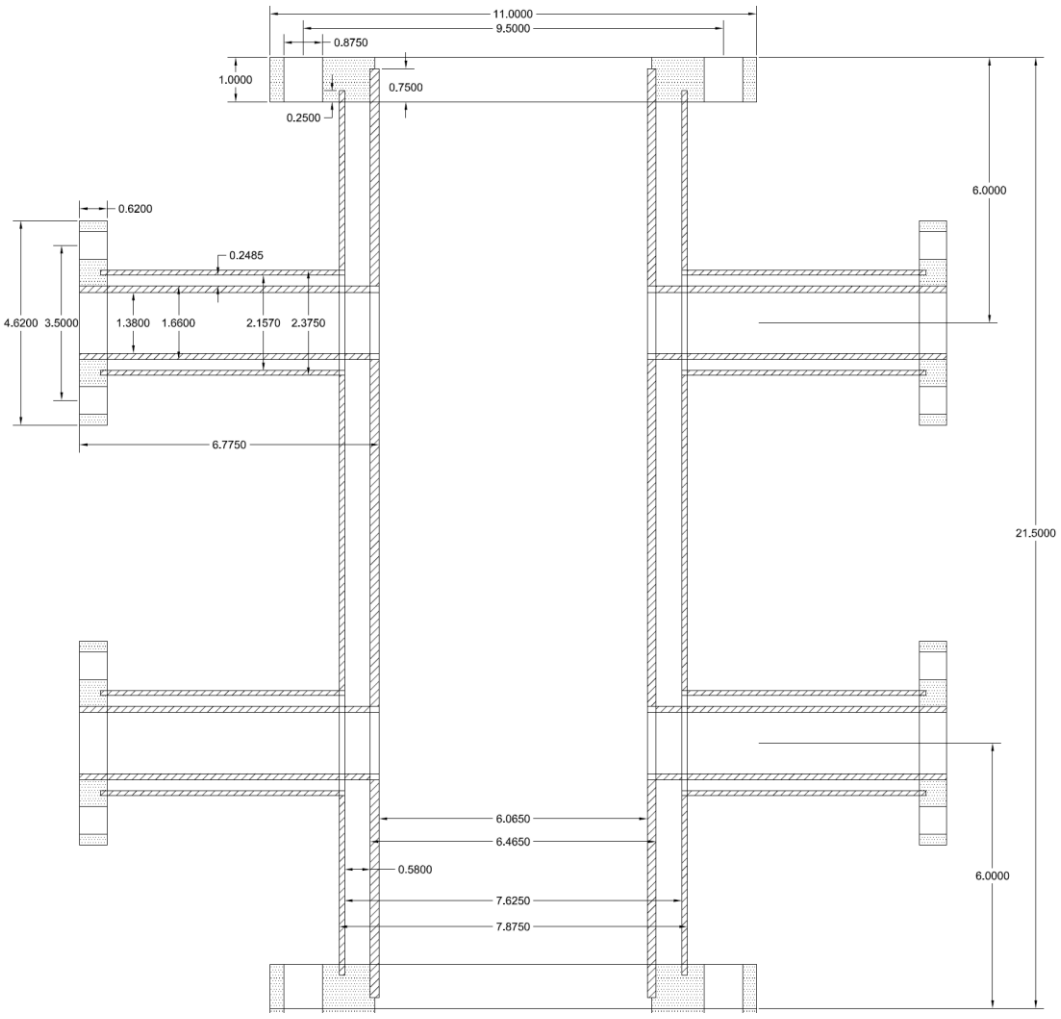


Figure B. 4: Cross-sectional schematic of synthesis chamber. In its original implementation, two such chambers are stacked atop one another.

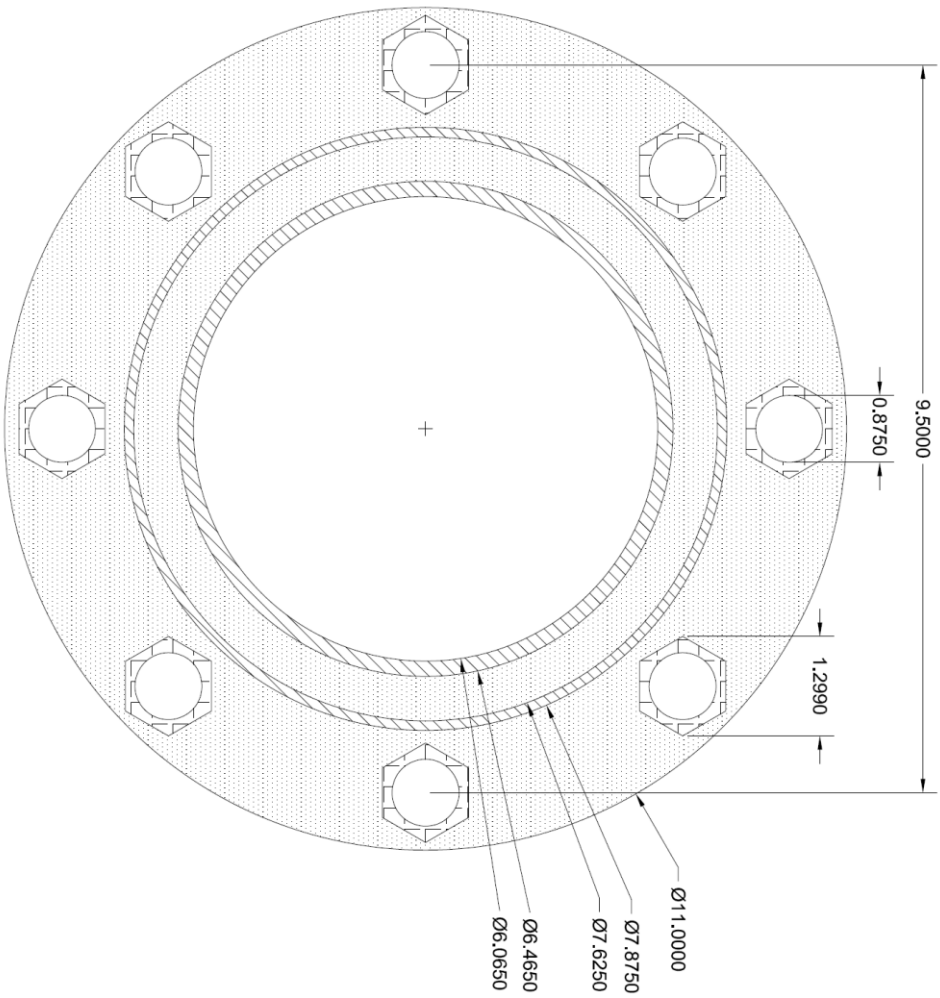


Figure B. 5: Schematic of top adaptor flange.

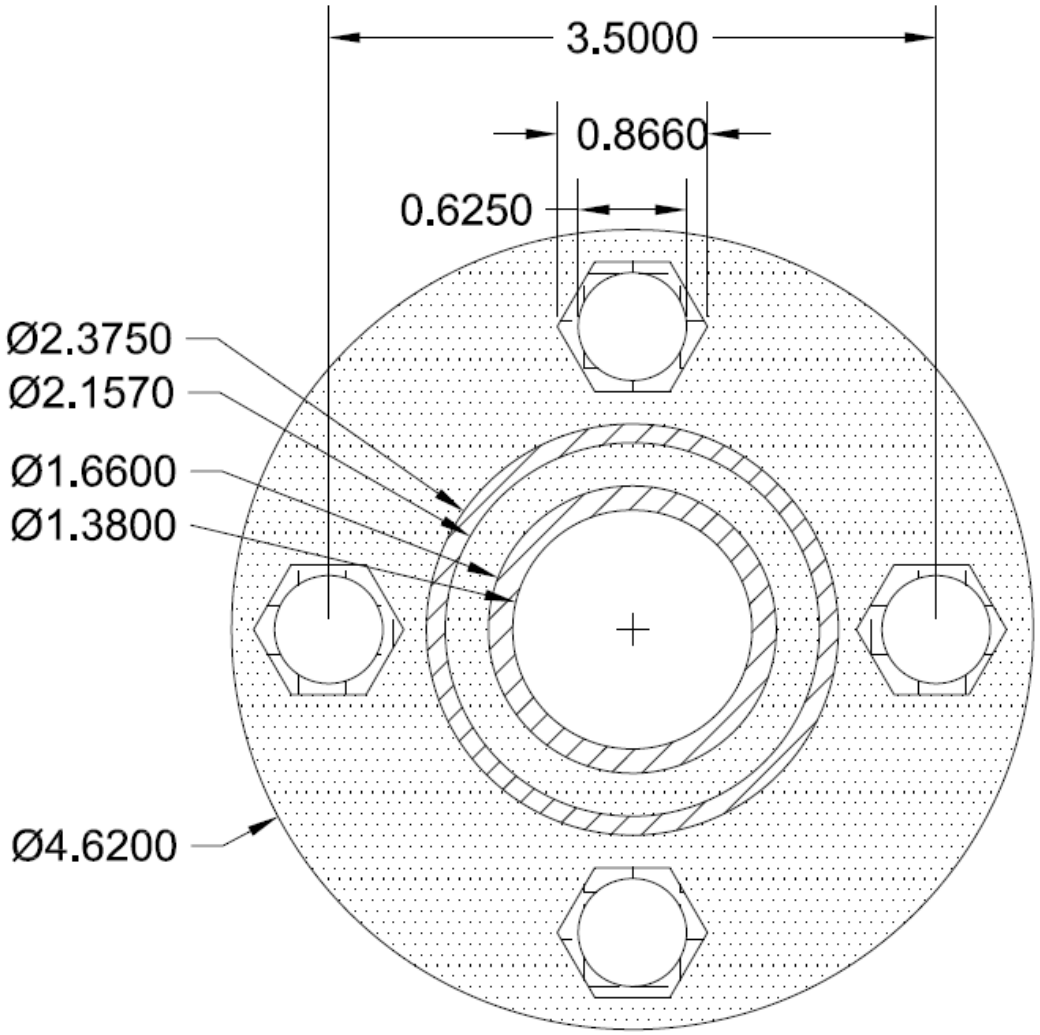


Figure B. 6: Schematic of side port flange.

# Appendix C

# RF Plasma Torch Diagnostics

In this appendix, some of the diagnostic results of operating the RF plasma torch under various parameters are presented.

In particular, the following parameters were varied:

- Plasma gas composition (Ar, $N_2$, or a combination of the two)
- Plasma gas injection point (direct or reverse vortex configuration)
- Synthesis chamber pressure (15 psia – 75 psia)
- Plasma gas flow rate (30 – 150 lpm)
- Power supply output power to the plasma torch (25 – 55 kW)

The following parameters were monitored and recorded:

- Power supply vacuum tube anode voltage
- Power supply vacuum tube anode current
- Power supply vacuum tube grid current
- Temperature of cooling water flowing into the power supply / plasma torch system
- Cooling water temperature returning from vacuum tube
- Cooling water temperature returning from inductor coil
- Cooling water temperature returning from plasma torch
- Mass flow rate of cooling water into the power supply / plasma torch system
- Mass flow rate of cooling water returning from the vacuum tube
- Mass flow rate of cooling water returning from the inductor coil
- Mass flow rate of cooling water returning from the plasma torch

From these measurements, the power dissipated by the vacuum tube, the inductor coil, and the plasma torch could be calculated from the temperature increase of the cooling water and its mass flow rate through these channels. The power of the plasma is then estimated by subtracting the power lost to heating the cooling water through these three branches from the power input as read and controlled by the power supply.

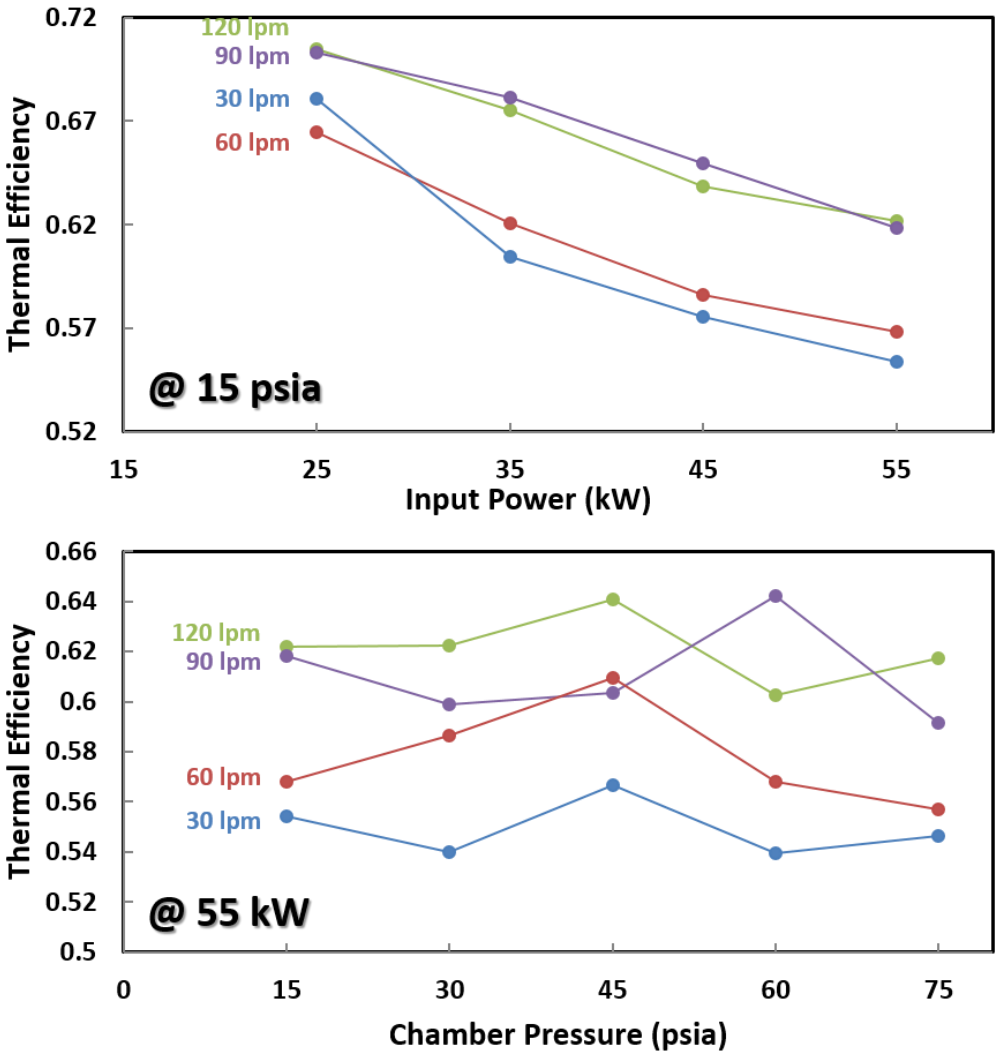


Figure C. 1: Thermal efficiency of RF plasma torch with Ar plasma gas in direct vortex configuration. (Top) Thermal efficiency at different powers as read on the power supply output for various Ar plasma gas flow rates. Synthesis chamber pressure is maintained at 1 atm. (Bottom) Thermal efficiency at various synthesis chamber pressures for several Ar plasma gas flow rates. Power supply output is maintained at 55 kW.

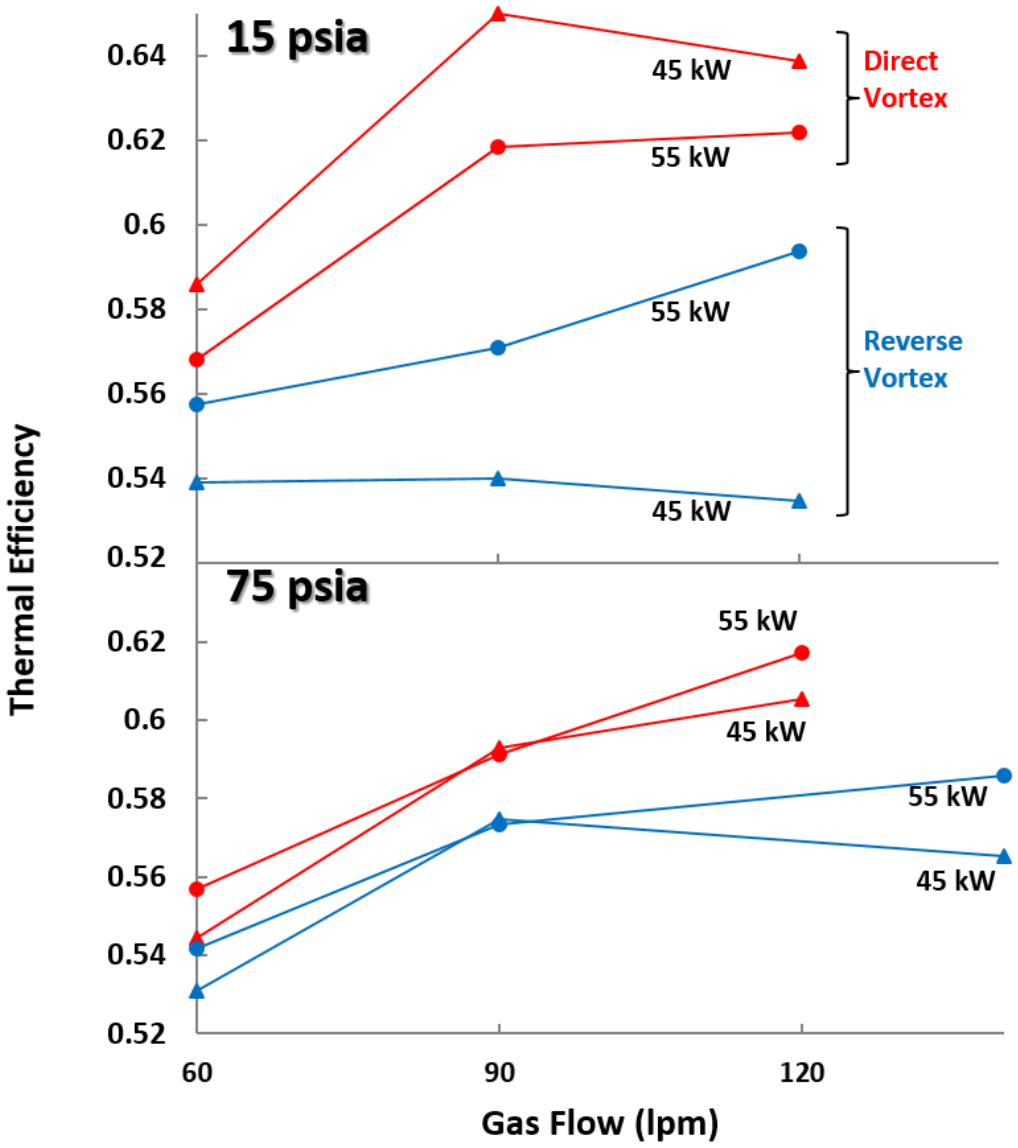


Figure C. 2: Thermal efficiency of plasma torch in direct and reverse vortex configurations using Ar as plasma gas at different flow rates. Synthesis chamber pressure is maintained at (top) 15 psia and (bottom) 75 psia. Ar is introduced into the plasma via the direct vortex (red) and reverse vortex (blue) at powers of 45 kW (triangles) and 55 kW (circles).

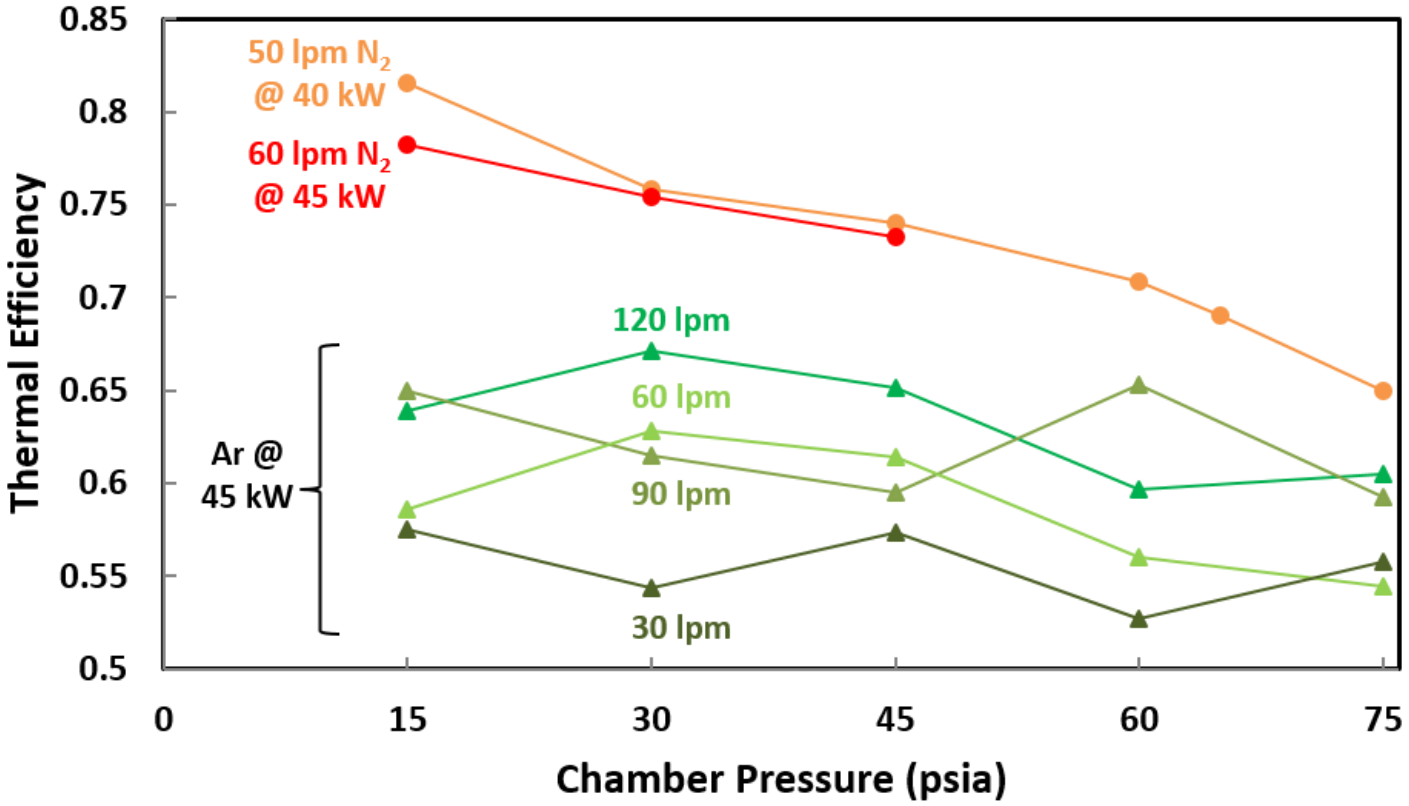


Figure C. 3: Thermal efficiency of RF plasma torch with $N_2$ plasma gas in direct vortex configuration (orange and red) at different synthesis chamber pressures. For comparison, the thermal efficiencies for Ar plasma gas at 45 kW power are also plotted (various shades of green).

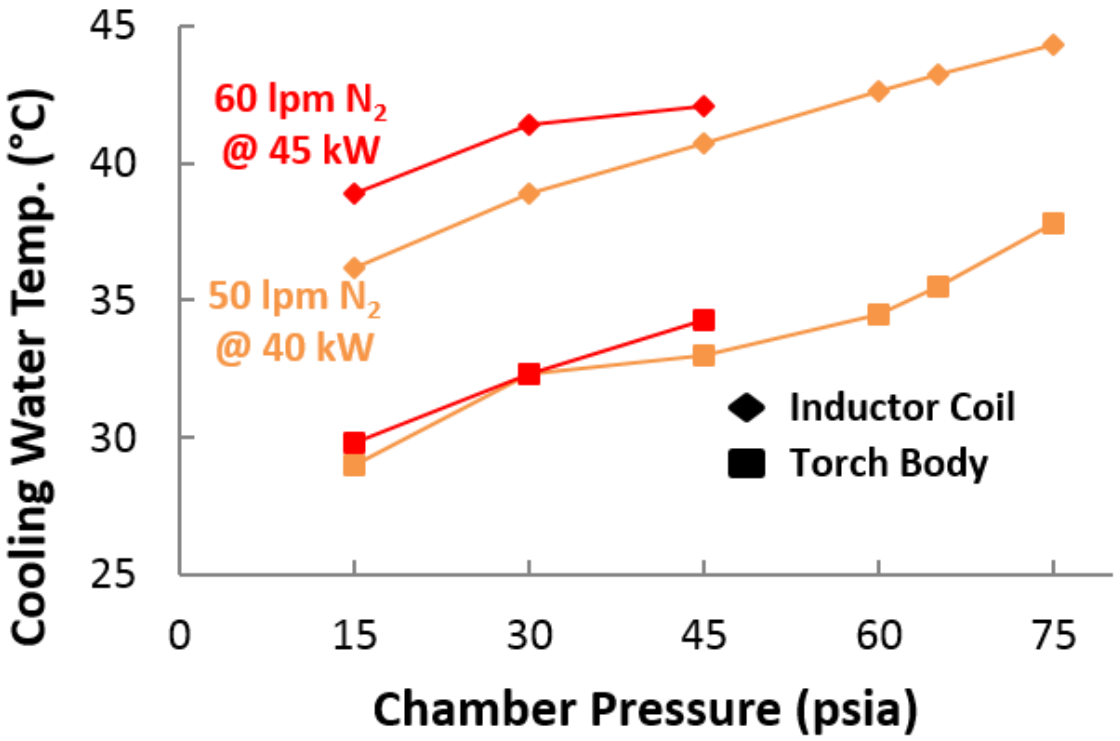


Figure C. 4: Returning cooling water temperatures through the inductor coil (diamonds) and plasma torch body (squares) when the EPIC system is operated using 60 lpm $N_2$ as plasma gas at 45 kW (red points) and at 50 lpm $N_2$ as plasma gas at 40 kW (orange points).

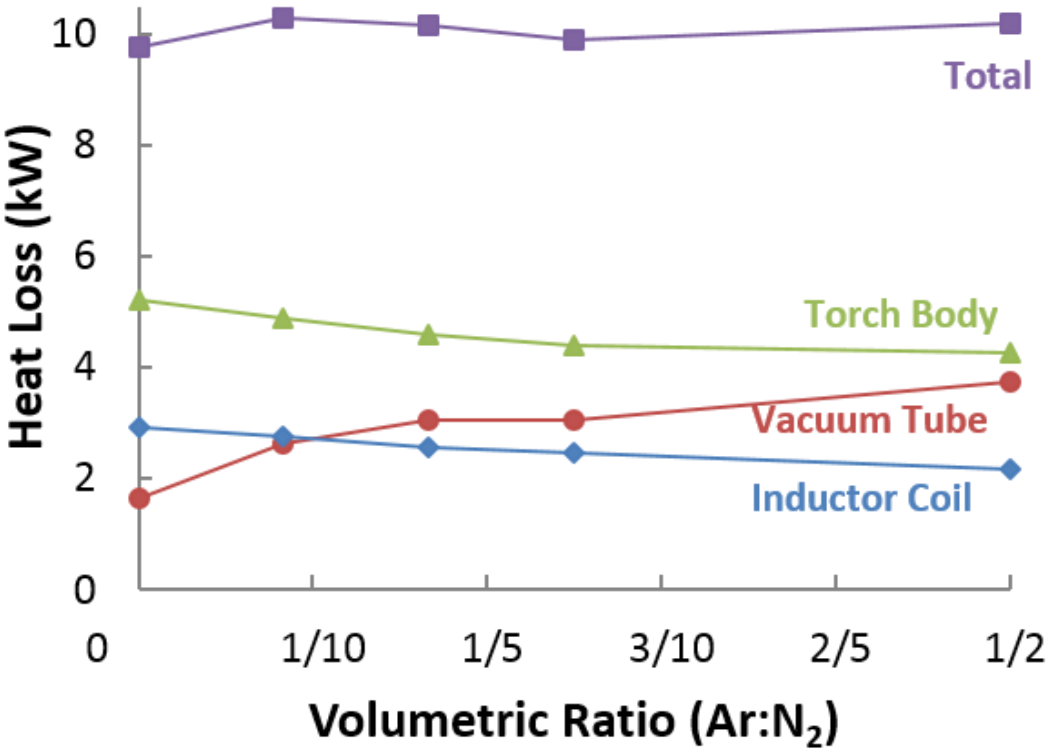


Figure C. 5: Heat loss through various parts of the plasma torch system, including the plasma torch body (green), the vacuum tube inside the power supply (red), and the inductor coil (blue) for various $Ar/N_2$ plasma gas compositions. Flow is 60 lpm, power supply output is maintained at 45 kW and synthesis chamber pressure is 15 psia.

# Appendix D

# EPIC Plasma System Operating Manual

Note: *All potential users must read and be familiar with the standard operating procedure for operating the Zettl group EPIC plasma system* ***before*** *they are permitted to run the equipment. Furthermore, only individuals who have been properly trained, qualified by the superuser, and whose names appear on the list of qualified users are permitted to operate the system.*

## D.1 Operating Procedure

1) Always wear proper personal protective equipment before you begin operating the ICP system. This includes but is not limited to safety glasses and full length lab coats. If handling powders or nanoparticles, also wear gloves and possibly respirators.

2) Open all of the relevant cooling water lines.
    a. First make sure both return line valves from the ceiling pipe (Fig. 1) are opened. Also make sure that the all of the relevant valves on the return

water cooling manifold located on the back of the cart supporting the chambers (Fig. 2) are opened.

b. With one hand on the copper pipe and the other on the valve so as not to torque the water piping, open the source line valve from the ceiling pipe (Fig. 1).


**Fig. 1** – Source and return valves near ceiling pipe for cooling water. *(Here return valve is open and source valve is closed.*)


**Fig. 2** – Return manifold for cooling water. (*Here all labeled valves are open and valve furthest left is closed.*)


**Fig. 3 –** Source manifold for cooling water. Blue water filter is seen on the right.

c. Open the valve labeled "**POWER SUPPLY**" on the source water cooling manifold located on the front of the cart supporting the chambers (Fig. 3). The pinwheel in the flow indicator should be rotating. The pinwheels in the 3 flow indicators located inside the back of the power supply should also be rotating (Fig. 5).
d. Open any other relevant valves on the water cooling manifold to supply cooling water to:
    - "**TOP BODY**" – the main water jacket of the top chamber
    - "**BOTTOM BODY**" – the main water jacket of the bottom chamber

- "**TOP PORTS**"& "**TOP ADAPTOR FLANGE**" – the feed-through side ports of the top chamber and the adaptor flange between the torch and the top of both chambers (the water flowing through the top ports subsequently flows through the adaptor flange)
- "**BOTTOM PORTS**" – the feed-through side ports of the bottom chamber
- "**EXHAUST**" – the flange and exit pipe at the bottom of both chambers

e. Check the entire system for potential water leaking. Areas worth checking include, but are not limited to:

- Hoses going from the water pipes on the ceiling to either the manifolds or the power supply
- The two water cooling manifolds
  - source manifold located on the front of the cart
  - return manifold located on the back of the cart
- The top and bottom chambers
  - all hose tee's
  - 8 chamber body water inlets and outlets
  - 16 feed-through side port water inlets and outlets
  - 6 exhaust flange and pipe water inlets and outlets
  - top adaptor flange water inlet and outlet

- The lines on the bottom of the back of the power supply (Fig. 4)
  - main water inlet and outlet
  - water lines going to and from the plasma torch
- Inside the back panel of the power supply (Fig. 5)
  - the water "**IN**" pipe which branches off into the "**INDUCTOR**", "**TORCH**", and "**TUBE**" pipes
  - the water "**OUT**" pipe which returns water from the three branches
- The plasma torch water lines
  - the ½" Swagelok water inlet on the bottom of the torch (Fig. 6)
  - the ½" Swagelok water outlet on the top of the torch (Fig. 7)
  - the ¼" Swagelok water inlet and outlet on the top of the capacitor bank box (Fig. 8)
- If sufficiently trained (i.e. the SUPERUSER), you may also want to occasionally check the water fitting lines visible when opening the side panels
  - left side of power supply – check lines to the vacuum tube (Fig. 9)
  - right side of power supply – check lines going to the capacitor bank box (Fig. 10)

f. Do not proceed until all leaks are sealed and water is flowing freely through all desired channels.


**Fig. 4** – Bottom of back panel of power supply. (From left to right: 480 V 3-phase cord, compressed air in from gas cylinder, compressed air out to ignition rod, main cooling water inlet, main cooling water outlet, cooling water from torch, cooling water going to torch)

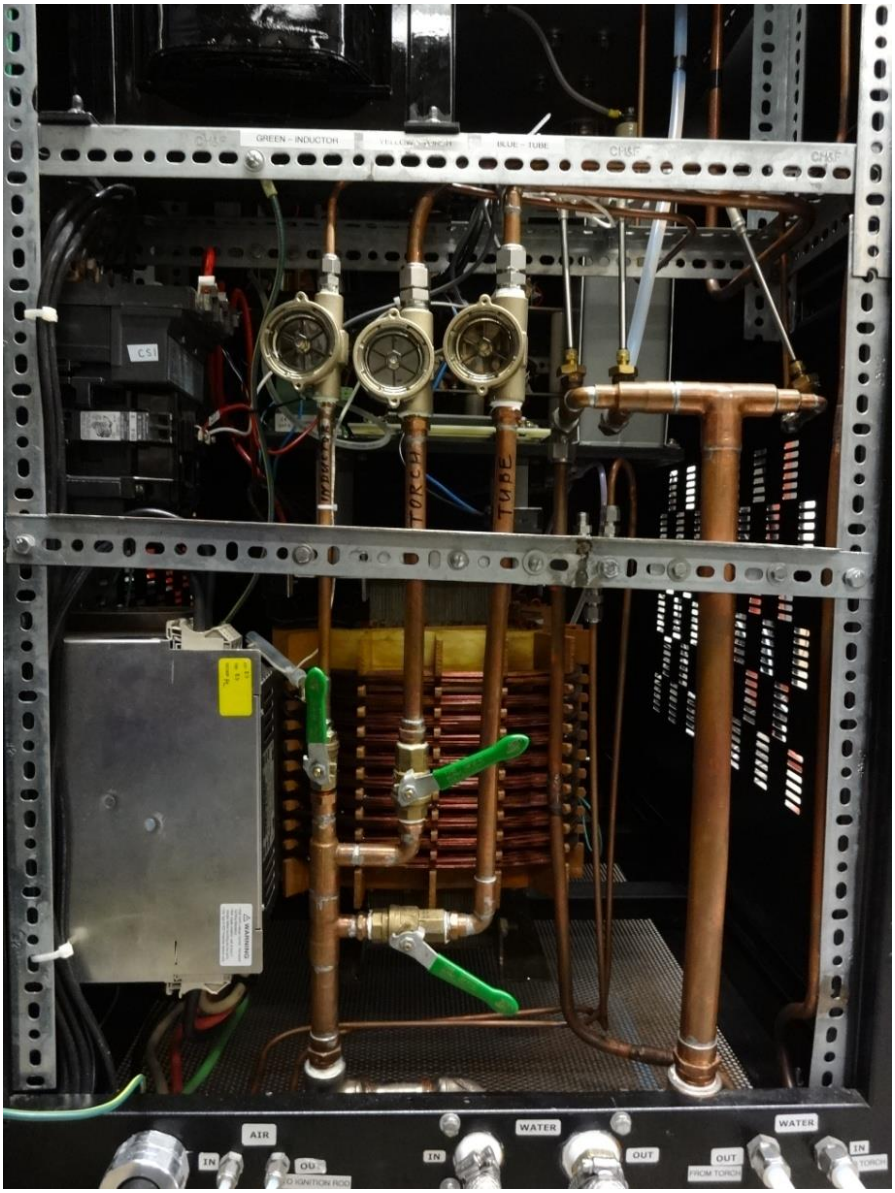


**Fig. 5** – Inside back panel of power supply. Cooling water inlet splits into three branches labeled “INDUCTOR”, “TORCH”, and “TUBE”, each with green flow control valves and flow indicators. Large copper pipe on right is cooling water return line coming from the three branches.

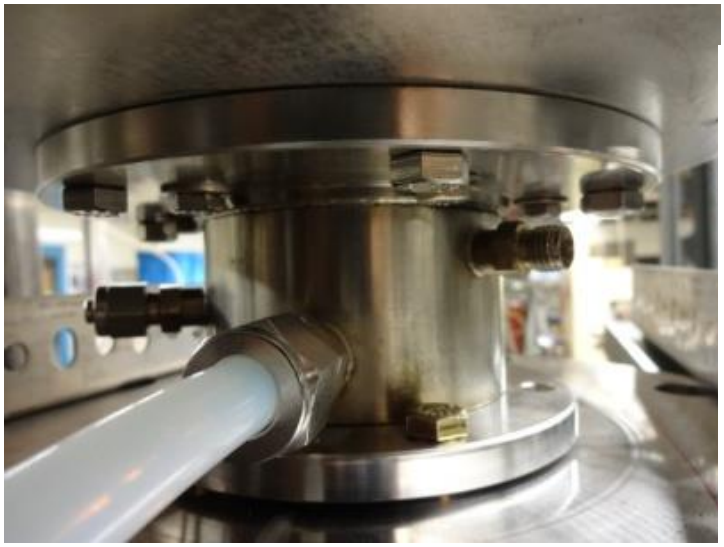

**Fig. 6** – Bottom of plasma torch. (From left to right: ¼" Swagelok fitting for feeding gas/powder into plasma plume, ½" Swagelok inlet for cooling water, ¼" Swagelok fitting for reverse vortex plasma gas)

**Fig. 7** – Top of plasma torch. (From left to right: ½" Swagelok outlet for cooling water, ¼" Swagelok fitting for direct vortex plasma gas inlet, ignition rod fitting the top of which has a ¼" Swagelok fitting for compressed gas)


**Fig. 8** – Top of capacitor bank box. (From left to right: ¼" Swagelok inlet for cooling water going into capacitor box, ¼" Swagelok outlet for cooling water exiting the capacitor box).

**Fig. 9** – Inside the left panel of power supply with vacuum tube. Cooling water lines are visible on left side with water inlets and outlets to the tube denoted by the arrow.

**Fig. 10** – Inside the right panel of power supply. Cooling water lines are visible on right side near the copper coil. The cooling water flowing to and coming from the capacitor bank box are visible at the very top center of the image.

3) Flip on the main circuit breaker labeled "**ICP SYSTEM CIRCUIT BREAKER**" which is located to the right of the door to the room (Fig. 11).
    a. The breaker should be locked out and must be opened by the equipment superuser.


**Fig. 11** – Main EPIC system circuit breaker. (*Here the breaker is switched off and has been locked out.*)

4) Turn on the power supply by flipping the switch/circuit breaker labeled "**MAIN POWER**" on the lower right of the front panel of the power supply (Fig. 12).
    a. Both of the front panel lamps "**FILAMENT**" and "**POWER**" will light red.
    b. After a few seconds of system initiation, the Siemens LOGO module screen on the front panel will indicate "*APT WELCOMES YOU*".


**Fig. 12** – Front panel of power supply. All screens, buttons, knobs, and switches are labeled.

5) Turn on the filament by pushing (do not hold) the green button labeled "**FILAMENT ON**".

a. The "**FILAMENT**" panel lamp will change color to green.
b. For a period of 90 seconds, the LOGO screen will indicate "*WARMING UP*".
c. Once the filament is warmed up, the LOGO screen will state "*READY FOR IGNITION*" and the system will allow further steps.
d. If the user decides to stop and abort warming up the filament, push the red button labeled "**FILAMENT OFF**".

6) Check that the power adjustment knob labeled "**POWER ADJUST**" is turned all the way counterclockwise to the zero position.

7) Turn on the high voltage power by pushing (do not hold) the black button labeled "**POWER ON**".
   a. Both the "**FILAMENT**" and "**POWER**" panel lamps should now be green.
   b. The LOGO screen will indicate the initial electrical parameters:

| |
|---|
| $U_a = 0$ |
| $I_a = 0$ |
| $I_{grid} = 0$ |
| $T_r$ = [X] hr. [Y] min. |

where $U_a$ = anode voltage (kV)
$I_a$ = anode current (A)
$I_{grid}$ = grid current (A)
$T_r$ = running time (hours and minutes)

8) Slowly ramp up the anode voltage, $U_a$, to **1 – 2 kV** by turning the "**POWER ADJUST**" knob clockwise.
    a. If the system was recently in operation, keep the voltage at this setting for at least 10 minutes. If the system has not been used for over a week, keep the voltage at this setting for at least 1 hour.

9) Check the water flow rates and temperatures by opening the front panel of the power supply (Fig. 13).
    a. The Siemens screen on the right will indicate the temperatures of the water into the power supply as well as the water flowing out of the torch, the inductor, and the vacuum tube. All water temperatures should not exceed 23°C.
    b. In order to check the water flows, flip down the switch on the left hand side labeled "**TOGGLE**". To ensure sufficient cooling, the water flow rates should be:

| | | |
|---|---|---|
| Tube flow | ≥ | 300 g/s |
| Inductor flow | ≥ | 40 g/s |
| Torch flow | ≥ | 100 g/s |

    c. If the water temperatures are too high or the water flow rates too low, you may have to adjust the cooling water flow rates to other parts of the system (such as the chamber) or the water inlet valves for the tube, inductor, and torch located inside the back panel of the power supply (Fig. 5). Do not proceed until you can ensure the necessary cooling water conditions are met.


**Fig. 13** – Inside the front panel of the power supply. The Siemens screen on the left is used to read $U_a$, $I_a$, $I_{grid}$, $T_r$ (and is duplicated on the LOGO module screen on the front panel). The Siemens screen on the right displays cooling water temperatures and flows. To change between the two, use the switch on the left labeled "**TOGGLE.**"

10) Open the gas cylinder that supplies the ignition rod with compressed gas of at least 50 psi.

11) Open and set outlet regulator pressures on all other necessary plasma and feeder gas cylinders (namely argon and nitrogen).


**Fig. 14** – MKS Type 247 controller box. (*Here the controller box has been switched on, the power to MFC #2 has been switched on, and the display is reading the real flow from MFC #2*)

12) Set and start the initial plasma gas of argon at 30 lpm.
   a. The MKS type 247 controller box located on the front of the main computer rack (Fig. 14) must be powered on.
   b. Flip on the switch labeled "**2**," which corresponds to the 2nd mass flow controller (MFC) for flowing argon (max flow: 200 lpm), so the green indicator light turns on and turn the "**Display Channel**" knob to position "**2**".

c. With the main computer on, open the latest LabVIEW VI which controls the MFCs (as of 7-17-2013, it is entitled "RAMP_UP_DOWN_IN_OUT_2_4"). Set the gas flow rate for MFC #2 (argon) to the desired value and monitor the real flow rate on both the LabVIEW VI and the digital display screen on the MKS type 247 controller box.
d. If the gas flow rate is too below or above the setpoint, the regulator outlet pressure on the gas cylinder may have to be increased or decreased respectively.

13) To strike a plasma, gradually ramp up the anode voltage, $U_a$, to **7.5 – 8.5 kV** by turning the "**POWER ADJUST**" knob clockwise.
a. It should take about 7 – 15 seconds to ramp up to this voltage. Ramping up too quickly could result in arcing!
b. Once you have reached **7.5 – 8.5 kV**, move onto the next step immediately and attempt ignition! Do not let the system stay in this high voltage mode for over 1 minute (the system is short circuited without ignition and staying in this mode for too long could result in overheating and damage).

14) Once you have reached an appropriate anode voltage for ignition, press and immediately release the "**F1**" button on the LOGO module screen.
a. You will hear a click at the torch as the ignition rod penetrates into the torch and recoils back. This

should then initiate an arc and radiofrequency discharge.

b. Never keep "**F1**" pressed as this will result in the ignition rod staying in the torch and potentially completely melting.

15) If after attempting ignition, no plasma is initiated, increase $U_a$ a bit more and retry igniting by pressing "**F1**" again.

a. Make sure $U_a$ stays within the 7.5 – 8.5 kV range.

b. If still no plasma is initiated, quickly ramp the anode voltage back to 0. Always remember: do not stay in the high voltage mode for too long!

16) Once a plasma is initiated, quickly increase the gas flow to at least 60 lpm. The higher gas flow will help keep the torch from overheating.

17) During operation with a plasma, the front panel "**POWER**" lamp will light red and you can monitor the parameters of the system with the LOGO module screen.

a. To display the total power input in kW, press and hold "**F2**". This is not the power in the plasma, but rather the total electrical power being put into the system. The maximum rated power input of the system is 60 kW.

b. The power can be adjusted by gradually turning the "**POWER ADJUST**" knob clockwise or counterclockwise. Be sure you never get close to 60 kW!

c. The flow rate of the plasma gas can be varied using LabVIEW.

18) To stop the plasma, push the red button labeled "**POWER OFF**." Turn the "**POWER ADJUST**" knob counterclockwise to the zero position.

19) Keep flowing water and leave the air fans on the top of the power supply on for at least 5-10 minutes to ensure all critical components of the system are sufficiently cooled.

20) To turn off the system, flip the "**MAIN POWER**" switch off.

21) Flip off the main electrical panel breaker switch labeled "**ICP SYSTEM CIRCUIT BREAKER**." Have the superuser lock it out once you are finished using the system.
    a. Flipping off and locking out the main circuit breaker will help protect the system from damage due to any incidental surges in the power grid and will also prevent untrained personnel from posing a threat to themselves and others.

22) The red mushroom-type button located on the front panel labeled "**EMERGENCY SHUT-OFF**" can be pressed at any time to disable the entire system and should only be used in cases of emergency.

23) To stop the flow of cooling water, first close the source valves located at the ceiling pipes. The valves located on the water cooling manifold can subsequently be closed. The return valves located at the ceiling pipes and at the return manifold can all be kept open.

24) Close all gas cylinders and “bleed” all the lines between the cylinders and the MFCs by flowing some gas until the regulator outlet pressure reads 0 psi.

## D.2 Changing Powder in Feeder

1) Always wear proper personal protective equipment before you begin dissembling the system. This includes but is not limited to safety glasses, full body Tyvek overalls, gloves, and respirator.

2) Unscrew the powder feeding line which feeds into the neck of the plasma torch.

3) Turn on the power to MARK XV powder feeder by pressing the "**POWER**" button on the front panel. See **Fig. 15.**
   - Whenever a button is depressed, its light will turn on. All other buttons should be off.


**Fig. 15** – Mark XV precision powder feeder front panel.

4) Depressurize the powder feeding canister.
   - Push in the "**DEPRESSURIZE**" button and wait until the pressure in the canister drops to **0** psi.

5) On the back side of the powder feeder, place a jar underneath and unscrew the "**CANISTER CLEANOUT**" as depicted in **Fig. 16**. Some powder may begin to flow out.


**Fig. 16** – Mark XV powder feeder lower back panel.

6) Turn on the canister vibration by pushing "**VIBRATE ONLY**" and setting the "**VIBRATION AMPLITUDE**" to some non-zero value.

7) Some powders, like boron, tend to agglomerate and won't flow out the back very quickly so it may be necessary to collect a lot of the material from the top of the powder feeding canister.
   - Turn off the "**VIBRATE ONLY**".
   - Open the top of the powder feeding canister by turning it **CLOCKWISE**.
   - Use a scoop, like an aluminum weigh boat, to scoop out as much powder from the canister as you can.

- When there is little powder left in the canister, you can turn on the "**VIBRATE ONLY**" and coax the powder down the "**CANISTER CLEANOUT**" shoot.

8) Once all of the powder has been removed, you can use spray IPA onto a techwipe and wipe the inside and bottom of the chamber.
   - CAUTION: Do not spray IPA directly into the bottom of the chamber as it will flow into the powder feeding lines and cause the remnants of the old powder to agglomerate and clog up the lines.

9) Before pouring in your new powder, cleanout what powder remains in the lines.
   - Screw the cap of the "**CANISTER CLEANOUT**" back on and close the top of the powder feeding canister by turning it **COUNTERCLOCKWISE**.
   - With the end of the powder feeding line (which was connected to the plasma torch) facing the shop vacuum (with the vacuum on), turn on the "**FEED AND VIBRATION**". What powder is being fed will now be directly vacuumed up and not dumped into the room.
   - To shoot out the last bits of powder out of the line, you can pressurized the canister and then hit "**FEED AND VIBRATION**".
     - To pressurize the canister, make sure all other buttons are turned off, the carrier gas flow is set to zero, and then vibration

amplitude is set to zero. Hit "**VIBRATE ONLY**" and then gradually increase the "**CARRIER GAS FLOW**". Gas will flow directly into the canister and pressure will build up.

10) Once the lines are sufficiently cleaned, set the "**CARRIER GAS FLOW**" to zero and turn everything off.

11) Pour in the new powder, being sure to fill up at least an inch above the top of the powder feeding screw.
    - It is recommended that the powder fill up at least an inch above the top of the powder feeding screw, but if this much precursor powder isn't available, it is sufficient to fill up to the top of the powder feeding screw.

12) Close the top of the powder feeding canister by turning it **COUNTERCLOCKWISE**.

13) Test that the new powder feeds properly.
    - This can be done by using a 5" glass tube and sealing one side with parafilm, the other with filter paper.
    - Stick the powder feeding line into the glass tube through the side with parafilm, using a clamp to hold up the line.
    - By hitting "**FEED AND VIBRATION**", the powder should start to feed out of the line into the glass tube.

- There may be a little bit of a delay in the powder feeding.
- You can use a flash light to clearly see the powder being sprayed out the nozzle end.
- For sticky powders, such as boron, when fed at low feed screw rates (such as 15 R.P.M.), the powder does not feed continually and actually spurts out periodically.
- Let it run for about 10 minutes to make sure the powder feeder does not eventually clog.

## D.3 Opening Chambers & Collecting Material

1) Always wear proper personal protective equipment before you begin dissembling the system. This includes but is not limited to safety glasses, gloves, full length Tyvek overalls, and face respirator.

2) Make sure that the power to the power supply is off (circuit breaker is in the **OFF** position and locked out), both water supplies to the power supply and the chamber are turned off, and all gas cylinders are closed.

3) Unbolt the top chamber from the bottom chamber by removing the 8 bolts (3/4" – 10 stainless steel 316) connecting the two. Keep the 8 bolts, nuts, washers, and lock washers together.

4) Disconnect the copper line (which is coiled around unistrut at the ceiling) from the emergency pressure relief pop valve by unscrewing the small clamp in **Fig. 17**. This is located at one of the bottom side ports of the bottom flange.

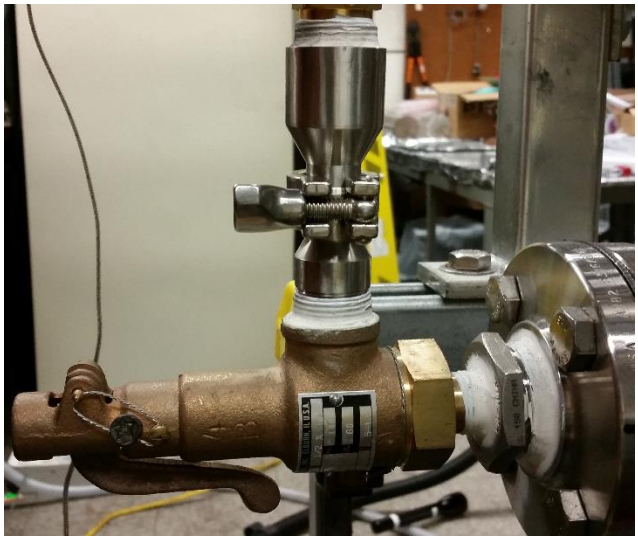

**Fig. 17** – Pressure relief pop valve (100 psi)

5) Very slowly raise the top chamber via the electric hoist just enough so that one can slide the bottom chamber from out under the top chamber. Raising the top chamber too much will put a lot of stress on the high voltage power line.

6) Carefully pull the cart supporting the bottom chamber to slide it completely out of the way of the top chamber. As you do this, be very careful not to get entangled in any of the water cooling lines of the top chamber.

7) When observed or collecting material from within the chambers, be sure to wear a respirator mask. Material from within the chambers can be conveniently collected with the pair of extra long tweezers.

- Material from chamber sidewalls may also peel off in sheets and can be collected

8) In order to clean the chambers, first use the HEPA shop vacuum to vacuum the chamber walls, top adaptor flange, and the powder feeding chamber at the torch exit nozzle. Follow this up by wiping everything down with IPA.

9) When ready to rebolt the two chambers, be sure to replace the gasket and carefully slide the bottom chamber underneath the top chamber.
   - In order to ensure the two are properly aligned, put a few bolts in and check to see whether they fall in place

10) Bolt the two chambers together with the 8 bolts (3/4" – 10 stainless steel 316), being sure to use a flat washer and lock washer along with the nut.
   - In order to ensure the gasket is not cracked during the bolting, tighten the nuts using the torque wrench in increments of 10 ft·lbs in the order labeled in **Fig. 18.**
   - Bolts tightened to 50 ft·lbs using a new gasket should ensure no gas leaks from the chamber at pressures up to 50 psig. If reusing a gasket, you may need to further tighten the bolts.

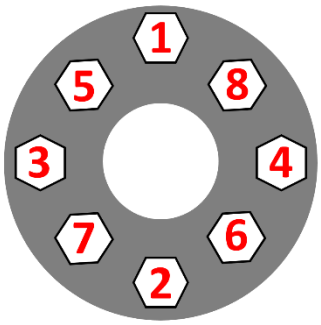


**Fig. 18** – 8-bolt tightening order.

11) Reconnect the copper line (which is coiled around the unistrut at the ceiling) to the emergency pressure relief pop valve by hand tightening the small clamp.

12) Run a “pressure test” by flowing gas into the chamber and sealing off the exit nozzle to the system until about 50 psi of pressure has built up. Turn off the gas and note how quickly the pressure drops.
    - A slow pressure drop of less than () psi per minute is typical and usual indicates proper sealing of the system.

## D.4 Removing and Disassembling Torch

1) Always wear proper personal protective equipment before you begin dissembling the system. This includes but is not limited to safety glasses and full length lab coats.

2) Make sure that the power to the power supply is off (circuit breaker is in the **OFF** position and locked out), both water supplies to the power supply and the chamber are turned off, and all gas cylinders are closed.

3) Disconnect the white plastic cone located at the end of the capacitor box from the capacitor box.

4) Close both the source and return valves for the water supply to the power supply, both located on the ceiling at the copper pipes.

5) Drain the water from the torch by disconnecting the cooling water lines to the torch and cooling water lines from the torch imaged on the far right in **Fig. 4** (labeled "**IN TO TORCH**" and "**OUT FROM TORCH**"). These are the two ½" Swagelok fittings located behind the power supply to the far right.

6) Disconnect the cooling water line going into the bottom of the torch. This is the ½" Swagelok fitting in **Fig. 6**. Wrap aluminum foil on both ends of this ½" tubing and place it to the side.

7) Disconnect the cooling water line coming from the top of the torch. This is the ½" Swagelok fitting in **Fig. 7**. Wrap aluminum foil on both ends of this ½" tubing and place it to the side.

8) Carefully disconnect the cooling water lines going into and out from the capacitor box. These are ¼" Swagelok fittings and are labeled "**IN**" and "**OUT**" in **Fig. 8**. Wrap aluminum foil on the ends of these two lines and over the inlet and outlet of the capacitor box.

9) Disconnect the "**Plasma Gas In**" line located on the top of the torch. This is the ¼" Swagelok fitting in **Fig. 7**.

10) Disconnect the powder feeding line connected to the bottom of the plasma torch. This is the ¼" Swagelok fitting on the left in **Fig. 6**.

11) Remove the ignition rod from the top of the plasma torch.
    - First disconnect the ¼" Swagelok fitting at the top of the ignition rod which connects it to the ¼" tubing extension.
    - Then carefully unscrew the ignition rod from the fitting at the top of the plasma torch, as imaged in **Fig. 7**. Cover the graphite end of the ignition rod with aluminum foil. Be sure to remove and hold onto the copper gasket as well.

12) Disconnect the high voltage power line from the capacitor box.
    - Remove the side panel of the capacitor box.
    - Disconnect the high voltage power line from the flat copper capacitor bank line, as seen at the bottom of **Fig. 19**. Due this by using a small pipe wrench to grip the power line and 3 washers above the flat copper capacitor bank line and then unscrew the large brass nut at the bottom with a 11/16" wrench. Do this carefully so as not to twist the entire high voltage power line as you are attempting to unscrew the nut.

**Fig. 19** – High Voltage Power Line connection to capacitor bank and torch. (*Located inside the capacitor bank box*).

- Disconnect the high voltage power line flange from the top of the capacitor bank by removing the four screws at the top of **Fig. 19**. These are 5/16 x 18 screws (316 ss). Three of them have a washer and a lock washer. The one at the back only has a lock washer.
- Using the yellow nylon lines or some other rope, secure the high voltage power line flange to the unistrut on the ceiling so that when the torch is eventually lowered, the high voltage power line will be supported and not lowered. See **Fig. 20**.

**Fig. 20** – High voltage power line secured to unistrut (*image taken after torch has been lowered*).

13) Unbolt the top chamber from the bottom chamber by removing the 8 bolts (3/4" – 10 stainless steel 316) connecting the two. Keep the 8 bolts, nuts, washers, and lock washers together.

14) Disconnect the copper line (which is coiled around unistrut at the ceiling) from the emergency pressure relief pop valve by unscrewing the small clamp in **Fig. 17**. This is located at one of the bottom side ports of the bottom flange.

15) Very slowly raise the top chamber via the electric hoist just enough so that one can slide the bottom chamber from out under the top chamber. Raising the top chamber too much will put a lot of stress on the high voltage power line.

16) Carefully pull the cart supporting the bottom chamber to slide it completely out of the way of the top chamber. As you do this, be very careful not to get entangled in any of the water cooling lines of the top chamber.

17) Slowly lower the top chamber all the way to the ground using the electric hoist.
    - As you do this, gradually remove the high voltage power line from the capacitor box. As you continue to lower the top chamber, be sure the high voltage power line flange does not get caught in the unistrut frame.

- Ensure there is enough room for the cooling water lines of the top chamber and that they are not hindered by the bottom chamber (and its cooling water lines).
- Place cardboard and bubble wrap underneath the 4 legs of the top chamber frame to keep the chamber level when it is seated on the ground. See **Fig. 21**.

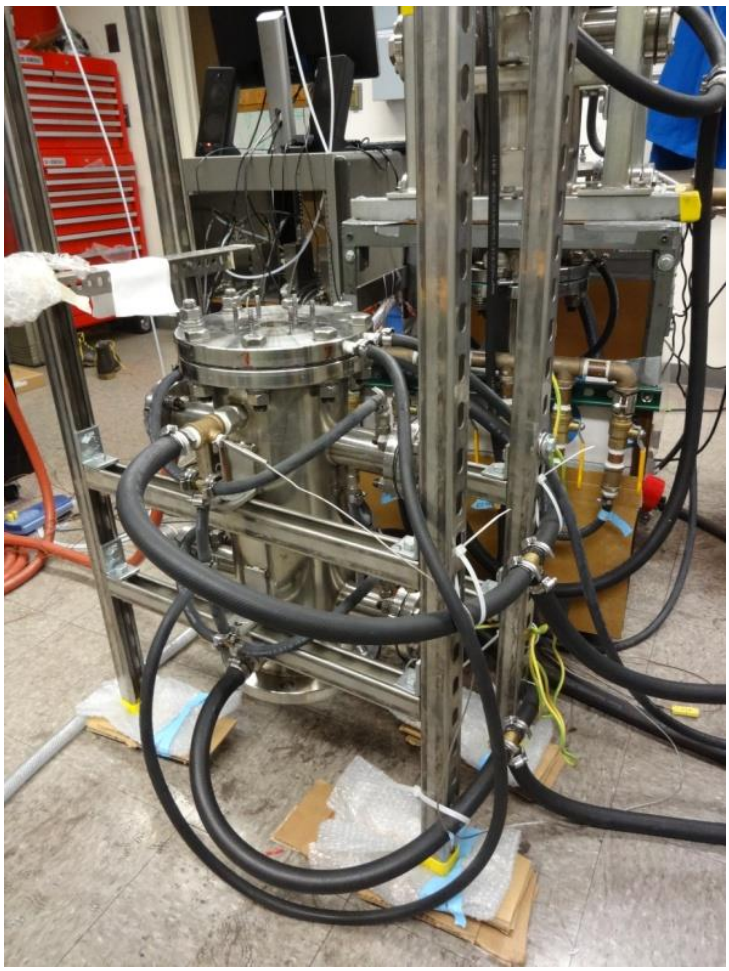

**Fig. 21** – Top half of synthesis chamber lowered to the ground (*torch has been removed in this picture*).

18) Unscrew the 6 nuts attaching the plasma torch to the adaptor flange.

19) Loosen the 4 bolts attaching the top of the frame of the top chamber to the 4 legs of the frame (located at the unistrut elbow joints). Use the electric hoist to raise the top of the frame. This is necessary in order to lift the plasma torch and capacitor bank box up out of the frame.

20) Attach the side panel back onto the capacitor bank box.

**Fig. 22** – Plasma torch and capacitor bank box horizontally mounted in between two tables.

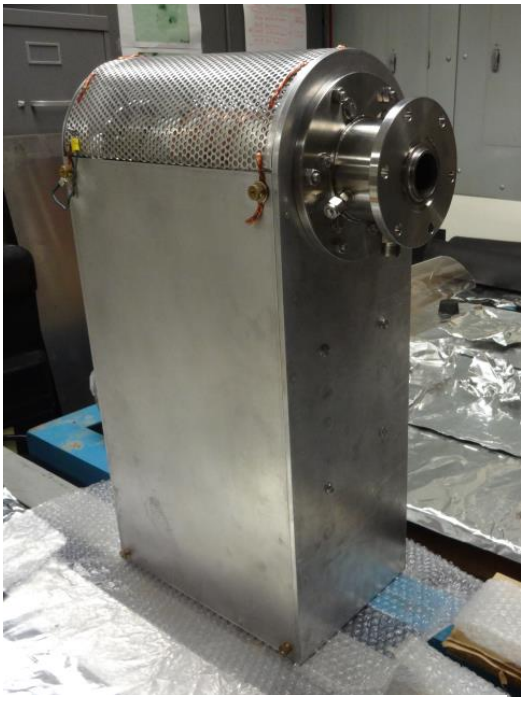

**Fig. 23** – Plasma torch and capacitor bank box vertically positioned.

21) Using at least two people, with a third as a guide, carefully lift the plasma torch and capacitor bank box up off of the top chamber. Keep in mind the weight is mostly distributed where the torch is and that most of the capacitor box is empty.

- Since the torch protrudes a bit beyond the bottom flange, you cannot place this torch on a flat surface. Typically, we place the removed torch/capacitor bank in between the two tables in 260 Birge such that the torch flange is rested

on the bubble wrap on the edge of the tables. See **Fig. 22**.

22) In order to detach the lower portion of the plasma torch, which is in fact the power feeding chamber and where the cooling water enters the copper body of the torch, it is necessary to sit the plasma torch / capacitor bank box vertically as in **Fig. 23**.

23) Position the yellow nylon straps so that the plasma torch is supported as in **Fig. 24**. This is necessary because when the torch is disconnected from the capacitor bank, it becomes loose and would otherwise fall.

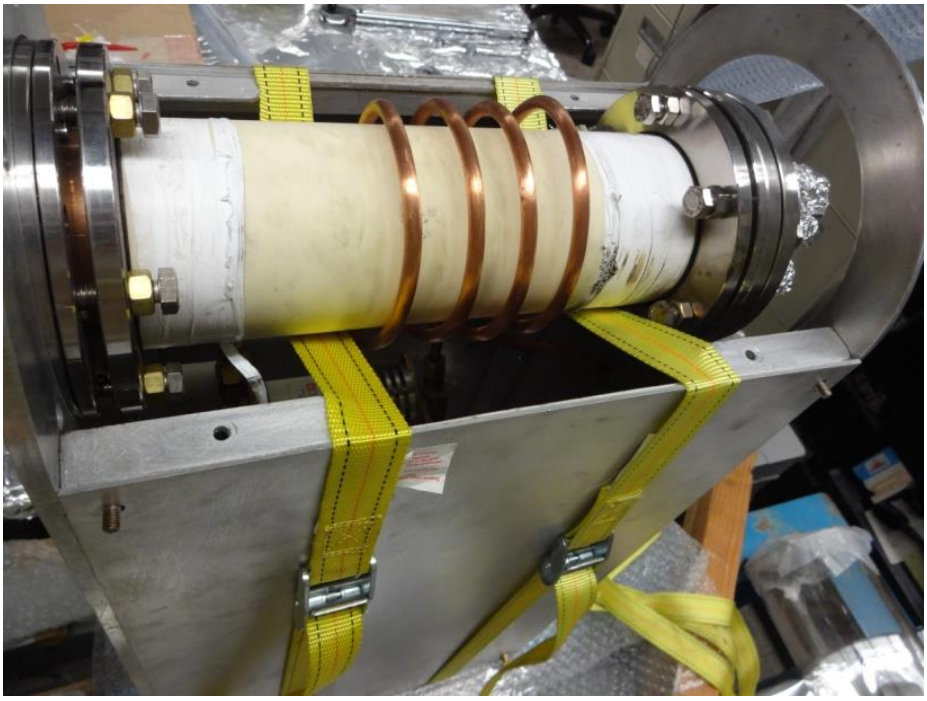

**Fig. 24** – Yellow straps supporting the plasma torch.

24) Looking upwards at the torch from the bottom, there are two concentric sets of screws, as denoted in **Fig. 25**. The outer six screws (5/16" x 18 stainless steel 316) attached the plasma torch to the aluminum capacitor bank box. Remove these first.

- NOTE: Once these are removed, the torch is free to move and rotate about, so it is critical that you have the plasma torch secured in place (for instance with the nylon straps) otherwise it will detach and fall.
- Then remove the inner set of six screws, being sure that you support the powder feeding chamber so it does not fall. You may need to exert a little force in pulling this bottom portion of off the rest of the plasma torch.

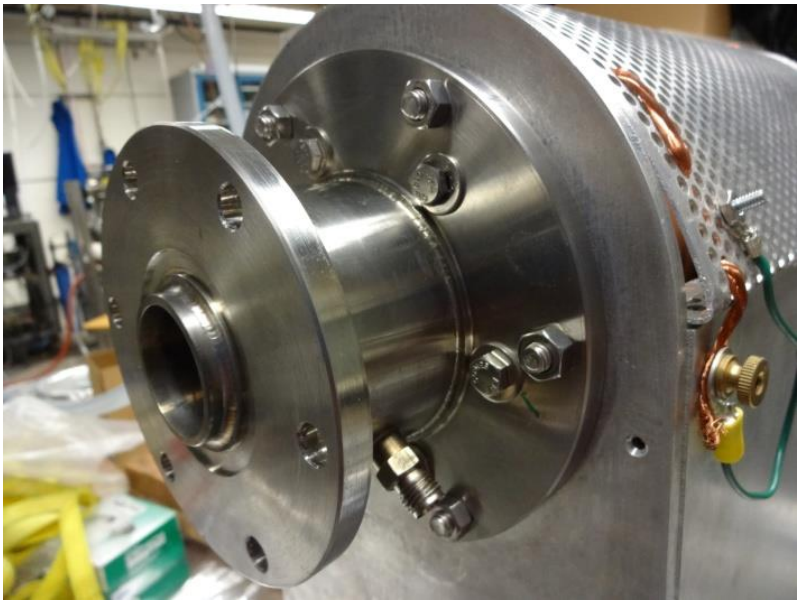

**Fig. 25** – Bottom portion of plasma torch (a.k.a. powder feeding chamber).

25) There are two elastic rings which form a seal between the bottom, powder feeding portion of the plasma torch, and the copper body of the plasma torch as seen in **Fig. 26**. The inner elastic ring is a “Double Seal Buna-N O-ring”, ID: 2 3/16” OD: 2 3/8” (McMaster Carr Part Number: 90025K451). The outer elastic ring is a “Square Buna-N O-ring”, ID: 2 ¾” OD: 2 15/16” (McMaster Carr Part Number: 4061T194).

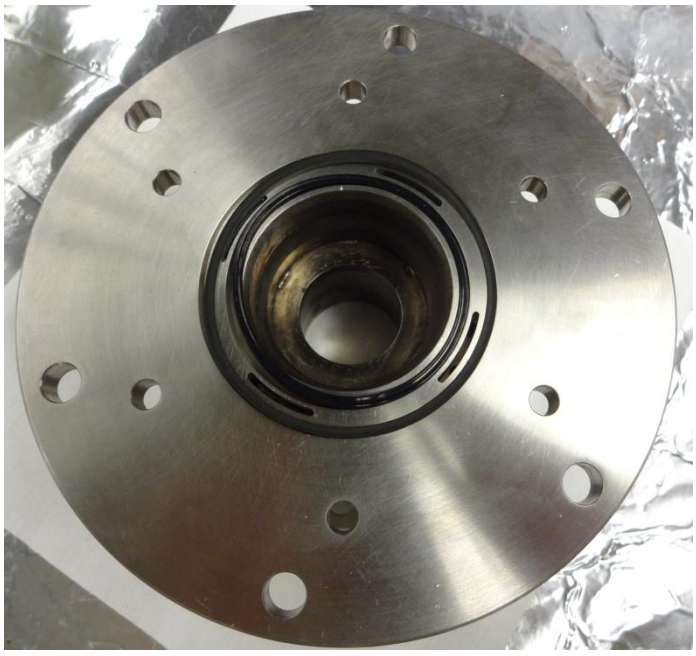

**Fig. 26 –** Powder feeding chamber, looking upward from the bottom.

26) The copper body of the plasma torch, which is encapsulated in a white ceramic cylinder, can be seen from a bottom-up view in **Fig. 27**. There are 8 slits in the copper body which allow for the induction of electromagnetic fields inside the torch and many small holes through which cooling water flows. Much of the thicker, inner copper layer has been eroded, but some of it remains.

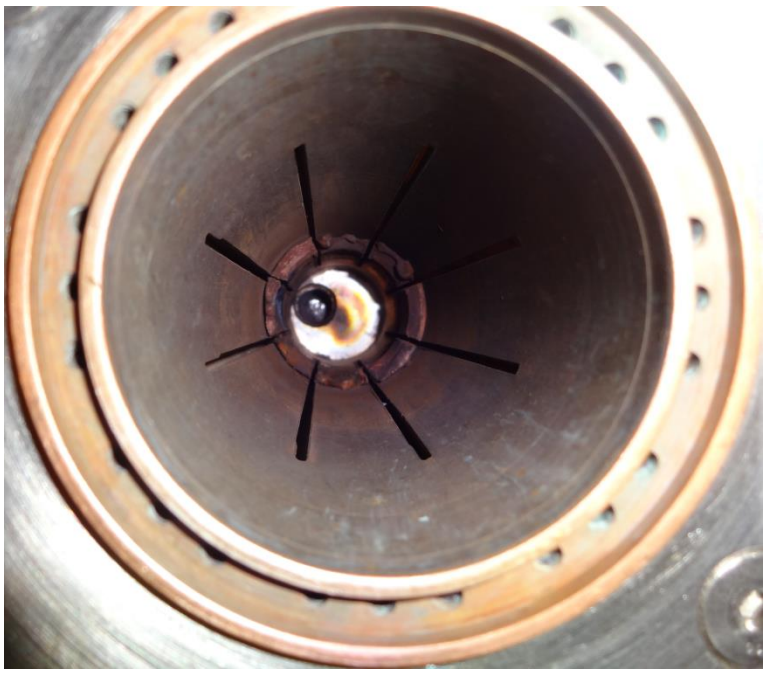

**Fig. 27** – Inside copper body of plasma torch.

## D.5 Hazards and Dangers

- Do not open the main circuit breaker labeled "**ICP SYSTEM CIRCUIT BREAKER**" without consulting an electrician or the superuser. There should be no need to open this unless one of the 100 A fuses have been blown, at which point an electrician should be contacted. There are spare 100 A fuses in the tool chest. The local electrician is Dennis Reeves (dennis.reeves@comcast.net).
- The side panels of the power supply should only be opened when the "**ICP SYSTEM CIRCUIT BREAKER**" is flipped off. Never open these panels when the power supply is on.
- Before, during, and after operation, always be aware and keep an eye out for any potential water leaks. Water will oftentimes leak very slowly so you may not see any leaks initially, but after a period of time, a small leak may result in a sizable puddle or stream of water. If a dangerous leakage of water is detected during operation, shut off the power supply immediately.
- Always monitor the internal pressure of the chamber and ensure that it never gets close to 100 psi. Pop-off valves will be attached to the chambers to prevent pressures from getting above 100 psi, but constantly keep an eye on the internal chamber pressure as well. This pressure is readout in the LabVIEW VI.
- Monitor all relevant water flow and temperatures to ensure proper cooling during operation. Interlocks will be put in place to ensure that the system will

automatically shut-off if proper water flow rates are not maintained or if water temperatures increase above a particular setpoint. Regularly check the water filter to ensure it is not close to becoming clogged.

- When operating the winch to raise or lower the top chamber, never allow anyone to get underneath the top chamber. Always raise or lower in a steady controlled fashion with one hand on the frame.

# Appendix E

# RF Plasma Torch Troubleshooting

## E.1 Water Jacket Sealing Rings

Sealing the water jacket of the copper torch body to the lower powder feeding chamber are two elastic rings, indicated by the red and yellow arrows of Figure E.1.

As designed, there are extensions of the inner and outer copper jacket of the torch (indicated by the red and yellow arrows of Figure E.2) which fit into the inner and outer grooves of the powder feeding chamber. These copper jacket walls fit snuggly into their respective grooves, with hardly any space for expansion of the elastic sealing rings. The elastic sealing rings are compressed in the groove when the torch and powder feeding chamber are bolted together. But the user must be careful not to under tighten the two fixtures together at the risk of a water leak, or over tighten at the risk of deforming the o-rings too much and damaging them.

Upon opening the torch for the first time after ~ 1 year of use, the outer elastic ring was melted and deformed onto the lip of the outer copper jacket of the torch. As manufactured, it was fabricated by custom cutting a square-profile O-ring stock to fit the circumference of the outer seal groove and then glued together to form one piece. The sealing integrity may be compromised by using adhesives to join the elastic seal. We thus replaced this damaged seal with a square profile o-ring (oil-resistant Buna-N, 3/32” thick) which fit in the outer grove. When the torch was most recently dismantled (June 2015), no melting or damage of this outer o-ring was observed (see red arrow of Figure E.1).

As manufactured, the inner elastic seal was a X-profile O-ring (double seal oil resistant Buna-N, 3/32” thick). Upon dismantling the torch after 1 year of use, there was no damage observed for this sealing ring (see yellow arrow of Figure E.1).

Both sealing o-rings are available from McMaster Carr.

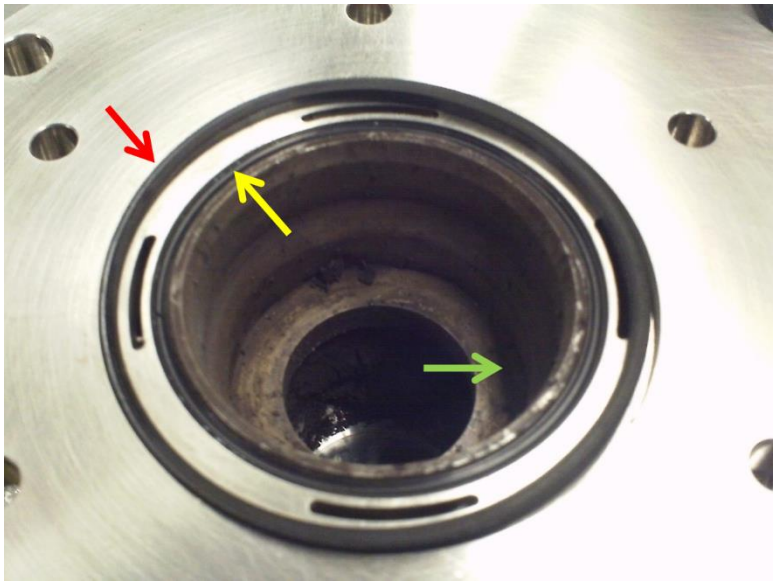

Figure E. 1: Sealing rings of water jacket between powder feeding chamber and plasma torch body. In this picture, the powder feeding chamber has been detached from the plasma torch body and image is taken looking down on the top of the former.

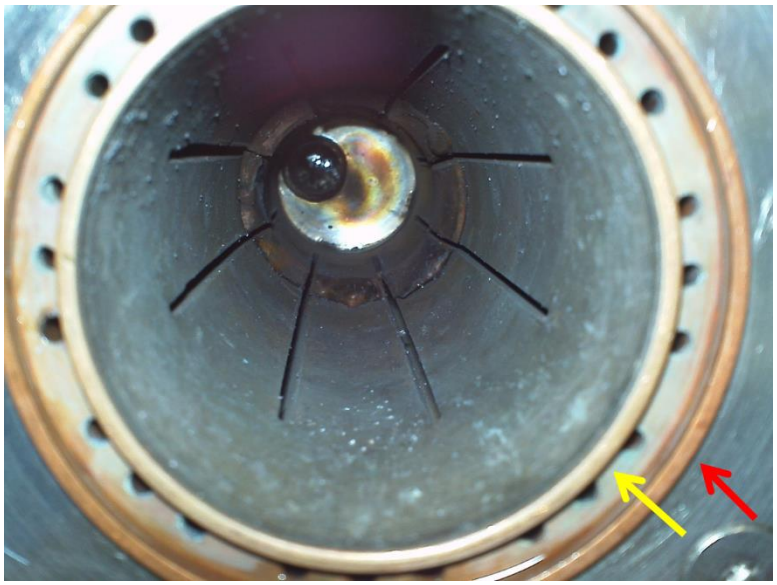

Figure E. 2: Inside of plasma torch body with metal sealing lips indicated by arrows. Picture is taken as seen looking up into the torch.

## E.2 Thermal Shock Damage

During regular use of the RF plasma system, standard procedure involves the turning off of the power to the torch when a run is complete. When the plasma power "OFF" button is hit at the conclusion of a run, the plasma within the torch is completely stopped. In this manner, there are several parts of the torch which experience thermal shock as parts of the torch are cooled down very quickly from a high temperature state when the power is abruptly cut off.

Several welded and sealed areas of the powder feeding chamber experience thermal shock which ultimately resulted in the formation of cracks in these seals. Some of these seals were compromised, leading to a host of problems, including water leakage from the water-cooled torch.

There are few tack welds which hold the lip of the reverse-vortex swirler to the inside of the powder feeding chamber, as denoted by the green arrow in Figure E.1. All of these welds have been comprised and are cracked. No water or gas leakage has occurred from these cracks as of yet.

The biggest problem, however, was the cracking and ultimately compromise of the weld near the exit of the torch nozzle between the flange and the tube extending from the powder feeder. This is indicated in Figure E.3 by a red arrow,

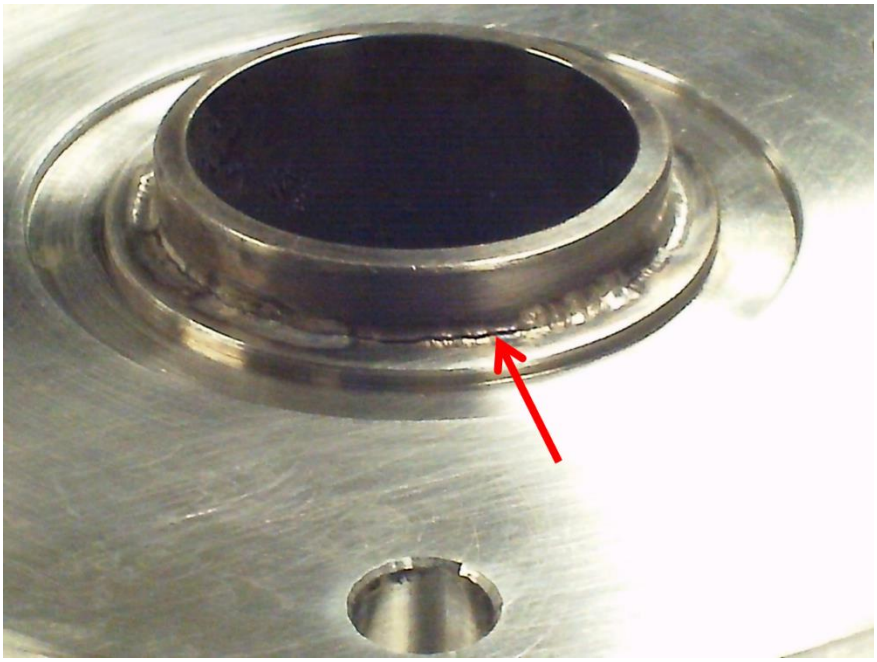

Figure E. 3: Plasma torch exit nozzle with crack indicated by red arrow.

where one can clearly see the presence of a large crack across a large portion of the seam. As manufactured, this seal was formed by welding the flange to the outside of the exit nozzle tube without any filler material. This results in an indentation across the entire seam which makes this sealing thinner, weaker, and more susceptible to damage. As manufactured, this weld was the only attachment between the flange, which itself is tightly bolted onto the top of the synthesis chamber, and the entire plasma torch.

After approximately 1 year of use, the users noticed that the synthesis chamber could no longer sustain a pressure of a ~ 25 psig (just under 3 atm). A clearly audible leak was heard coming from the region near between the flange and the powder feeding chamber. Ultimately, we discovered the sealing between the flange and the tube extending from the powder feeder had a crack in it. Upon dismantling the torch, the relatively small crack was sealed by the physics department machine shop with 316 SS filler material.

After fixing this initial leak and using the system for a few more months, a water leak developed from the powder feeding torch inside the synthesis chamber. Once again, the weld between the flange and the tube extending from the powder feeder had developed an even larger crack in it, as indicated by the red arrow of Figure E.3. In order to remedy the issue this time, the physics department machine shop welded this entire seam using 316 SS filling material. Furthermore, the entire

outside of the adaptor flange connection to the powder feeding chamber was also welded together with 316 SS. This additional welding is critical as it serves to provide further stability and strength to the flange / powder feeding chamber attachment.

## E.3 Copper Ablation from Torch

After several weeks of initial tests gauging and monitoring the plasma system's capabilities, when the synthesis chamber was opened up for the first time, a great deal of molten and fragmented bits of copper had accumulated throughout the bottom of the synthesis chamber. See Figure E.4.

We have also noticed an accumulation of copper, most likely from inside the copper cooled torch walls, which has melted off and deposited around the rim of the torch exit nozzle. In Figure E.5, this copper has accumulated around the region of the reverse vortex swirler in the lower part of the torch (the powder feeding chamber). This chunk of copper upon removing is visible next to the pen in Figure E.4 as well.

Upon looking inside the torch, there are many areas missing copper as well as some clearly damaged copper regions. This is clear in both Figure E.5 and Figure E.6.

It is still unclear why the copper from the inside of the torch was so damaged during the early lifetime of the plasma system. After many subsequent runs since initially cleaning out all these copper fragments, only very rarely did we notice any more copper appearing in the bottom of the synthesis chamber. The ablation of copper does not seem to be a result of normal operation of the system, but it is still unclear exactly why there was so much damage to the inside of the torch following initially testing of the system. I suspect some damage may have resulted when the plasma torch was operated flowing gasses in through both the direct as well as reverse vortex swirlers. In this mode, a distinctly new color was observed from the region of the plasma which may have been the result of copper ablation. In particular, a greenish hue was observed from the top chamber viewport during certain runs, which we suspect is due to the melting and copper from inside the plasma torch.

Upon consulting with the manufacturer of the plasma torch, it seems the copper ablation is indeed a result of operation using both gas injection systems (direct vortex and reverse vortex). When working with two swirlers, a region of turbulent gas flow is created somewhere in the middle of the torch in the most narrow zone, where there is almost no gas flow along the torch wall. This leads to local overheating and melting. Hence operating the torch with one gas injection port or using only one swirler will not lead to copper ablation.

Figure E. 4: Copper pieces collected from inside the synthesis chamber and near the plasma torch exit nozzle.

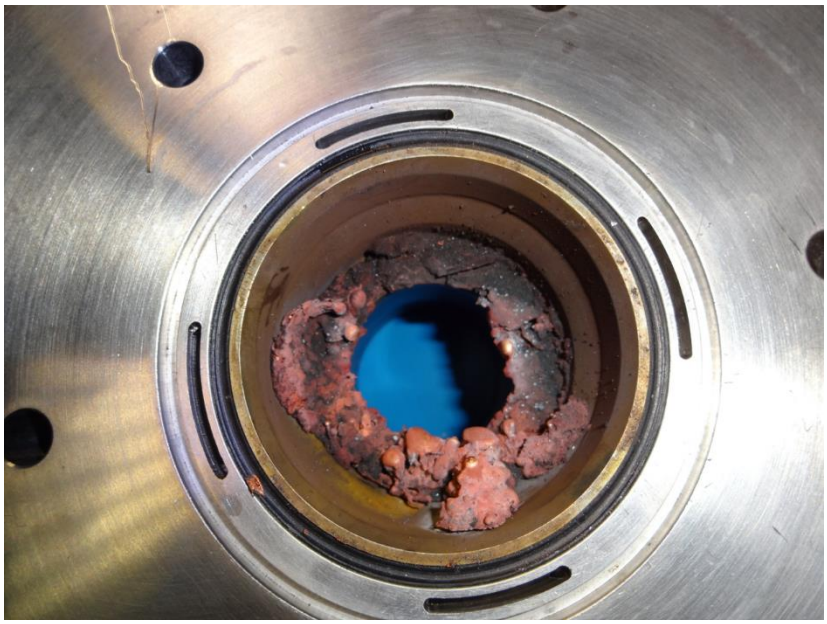

Figure E. 5: Copper collected in powder feeding chamber. Powder feeding chamber is detached from the plasma torch body and is pictured looking down.

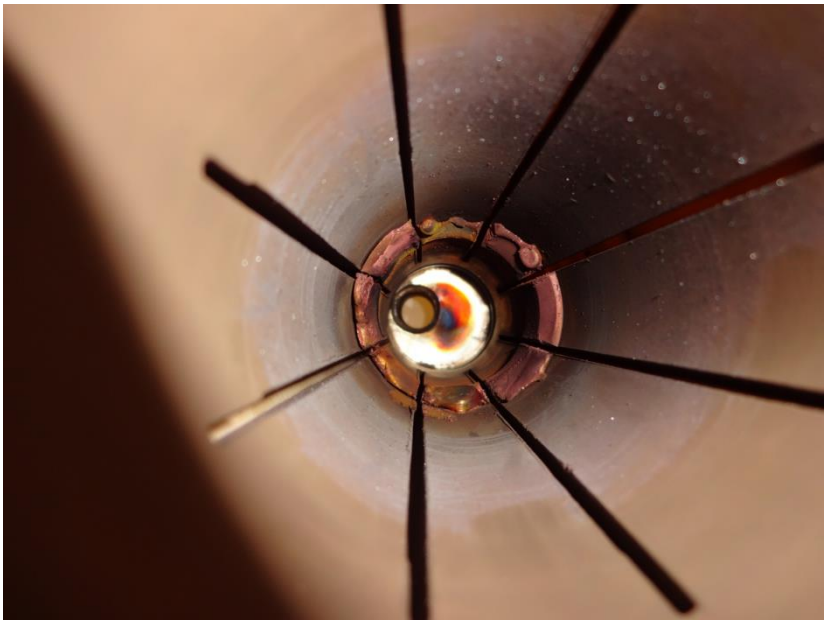

Figure E. 6: Inside of plasma torch with inner copper layer ablated.

## E.4 Torch Overheating

House water flowing into the 60 kW power supply is used to cool several parts of the system. The cooling water branches off into three regions: (1) vacuum tube, (2) inductor coil, (3) plasma torch. Levers in the back panel of the power supply can be adjusted to vary the flow of water into each branch. After hours of operation, we have noticed that both the vacuum tube and plasma torch are sufficiently cooled and water returning from these branches during operation never reaches high enough temperatures to be of concern. The cooling water to the inductor coil, however, does approach critically high temperature levels near 45°C under some normal operating conditions. In particular, when pure nitrogen is used as the plasma gas at 50 lpm and as the synthesis chamber pressure is increased above 35 psig, the temperature of the cooling water flowing through the inductor coil does creep towards 42 – 44 °C. This could possibly be remedied by increasing the flow of cooling water to this branch by reducing the water flow to the other two branches (note that the lever controlling water flow to the inductor coil is always completely open). As manufactured, the cooper tubing carrying the cooling water to the inductor coil is also ¼" in diameter and could potentially be replaced with larger diameter tubing.

We also note that in its current state of operation, the cooling water is house supplied, i.e. from the building itself. As such, we do not have control over the maximum total flow of water into the power supply. This is problematic as sometimes, the total water flow has noticeably decreased, leading to insufficient cooling of parts of the power supply (namely the inductor coil).

# Appendix F

# EPIC Plasma System Abridged Standard Operating Procedure

## EPIC System Standard Operating Procedure

(*Note: This is an abridged form of the SOP for this equipment. All users must have read through and become completely familiar with the full operating manual before using this equipment*)

1. Open all cooling water to chambers and power supply. Check for leaks.
2. Open all gas cylinders (ignition rod, carrier, and plasma gases).
3. Turn on the main circuit breaker and power switch to the power supply.
   - Both lamps will light red
   - After the PLC initiation (takes several seconds), LOGO text module screen on the front panel will indicate "*APT WELCOMES YOU*"
4. Push and release the green "**FILAMENT ON**" button.
   - "**FILAMENT**" lamp will turn green

- Screen will indicate "*WARMING UP*" for a 90 second period
- After warming, screen will show "*READY FOR IGNITION"*

5. Check that power adjustment knob "**POWER ADJUST**" is turned all the way counterclockwise to zero.
6. Turn on high voltage power by pushing "**POWER ON**".
   - Both panel lamps should light green
   - The LOGO screen will indicate the initial electrical parameters:

| | |
|---|---|
| $U_a = 0$<br>$I_a = 0$<br>$I_{grid} = 0$<br>$T_r$ = [X] hr. [Y] min. | $U_a$ = anode voltage (kV)<br>$I_a$ = anode current (A)<br>$I_{grid}$ = grid current (A)<br>$T_r$ = running time (hr. min.) |

7. Test that the ignition rod works *before* ramping up the voltage by pressing "**F1**".
8. Slowly ramp up the anode voltage, $U_a$, to **1 – 2 kV** by turning the "**POWER ADJUST**" knob clockwise.
   - If the system was recently in operation, keep the voltage at this setting for at least 10 minutes. If the system has not been used for over a week, keep the voltage at this setting for at least 1 hour.
9. Check the water flow rates and temperatures.

   (Tube flow $\geq$ 300 g/s, Inductor flow $\geq$ 40 g/s, Torch flow $\geq$ 100 g/s, Temp. < 23°C)

10. Set initial argon flow for ignition at about **30 lpm**.
11. To strike a plasma, gradually ramp up the anode voltage, $U_a$, to **7.5 – 8.5 kV** by turning the "**POWER ADJUST**" knob clockwise.
    - Take about 7 – 15 seconds to ramp up voltage. Ramping up too quickly could result in arcing!
    - Once you have reached **7.5 – 8.5 kV**, move onto the next step immediately and attempt ignition! Do not let the system stay in this high voltage mode for over 1 minute (the system is in a short circuited mode).
12. Once ignition voltage is reached, press and immediately release the "**F1**" button on the LOGO screen.
    - Do not keep "**F1**" pressed!
    - You will hear a click and this should initiate an arc and RF discharge.
13. If after attempting ignition, no plasma is initiated, increase $U_a$ a bit more and retry igniting by pressing "**F1**" again.
    - Make sure $U_a$ stays within the 7.5 – 8.5 kV range.
    - If still no plasma is initiated, quickly ramp the anode voltage back to 0. Always remember: do not stay in the high voltage mode for too long!
14. Once a plasma is initiated, quickly increase the Ar gas flow to **60 lpm**.
15. During operation with a plasma, the front panel "**POWER**" lamp will light red and you can monitor the parameters of the system with the LOGO module screen.

- To display the total power input in kW, press and hold "**F2**". The maximum rated power input of the system is 60 kW!

16. To stop the plasma, push the red "**POWER OFF**" button.

    Turn the "**POWER ADJUST**" knob counterclockwise to the zero position.
17. Keep flowing water and leave the air fans on the top of the power supply on for at least 5-10 minutes to ensure all critical components of the system are sufficiently cooled.
18. To turn off the system, flip the "**MAIN POWER**" switch off.
19. Flip off the main electrical panel breaker switch labeled "**ICP SYSTEM CIRCUIT BREAKER**."
20. Close gas cylinders and stop the flow of cooling water by closing the source valves located at the ceiling pipes and near the sink.